Tracking Efficiency of the HERA-B First Level Trigger in the Single Lepton Mode

Dissertation
zur Erlangung des Doktorgrades
des Fachbereichs Physik
der Universität Hamburg

vorgelegt von
Michael Nörenberg
aus Hamburg

Hamburg
2002

Tracking Efficiency of the HERA-B First Level Trigger in the Single Lepton Mode

Dissertation
zur Erlangung des Doktorgrades
des Fachbereichs Physik
der Universität Hamburg

vorgelegt von
Michael Nörenberg
aus Hamburg

Hamburg
2002

Gutachter der Dissertation:	Dr. A. Schwarz Prof. Dr. W. Schmidt-Parzefall
Gutachter der Disputation:	Dr. A. Schwarz Prof. Dr. B. Naroska
Datum der Disputation:	19.2.2003
Dekan des Fachbereichs Physik und Vorsitzender des Promotionsausschusses:	Prof. Dr. F.-W. Büßer

Spurfindungseffizienz der ersten Triggerstufe von HERA-B im Einzel-Lepton Modus

Kurzfassung

Das Experiment HERA-B wurde mit dem Ziel gebaut, CP-Verletzung in Zerfällen von neutralen B Mesonen zu messen. Um Zerfälle in dem sogenannten Goldenen Zerfallskanal $B^0 \to J/\psi K_S^0$ zu untersuchen, wurde die erste Triggerstufe (**F**irst **L**evel **T**rigger, FLT) entwickelt, die in der Lage ist, $J/\psi \to l^+l^-$ Zerfälle zu selektieren. Sie bietet einen Unterdrückungsfaktor von 200 gegenüber dem hadronischen Untergrund.
Der FLT besteht aus einem Netzwerk von etwa 80 dedizierten Prozessoreinheiten, welche die Rekonstruktion von $\mathcal{O}(10^7)$ Spuren pro Sekunde während der Datennahme erlaubt. Die Rekonstruktion beinhaltet die Bestimmung der Spurimpulse und der invarianten Massen von Spurpaaren.
Diese Arbeit behandelt die Leistungsfähigkeit des FLT während der Datennahme im Jahr 2000. Sie umfasst die Analyse des Detektorverhaltens und der Datenübertragung, soweit es die Funktionalität des FLT betrifft. Darauf aufbauend werden Kanalmasken erstellt, welche in der FLT Simulation verwendet werden.
Die Übereinstimmung zwischen dem FLT System und deren Simulation wird auf der Basis von einzelnen Ereignissen untersucht. Hierzu werden Spuren verglichen, welche vom FLT System und der Simulation rekonstruiert worden sind. Die korrekte Beschreibung des FLT Algorithmus in Hardware und Simulation wird gezeigt. Probleme in der Übertragung der Detektorinformationen werden untersucht.
Die Spurfindungseffizienz des FLT für einzelne Spuren wird mit Monte Carlo Ereignissen untersucht. Neben der intrinsischen Effizienz des FLT für einen idealen Detektor werden auch die Einflüße betrachtet, die sich bei dem realen Detektor ergeben. Dies beinhaltet sowohl die Treffereffizienzen und die Alignierung der Spurkammern als auch fehlerhaft arbeitende Kanäle in den Spurkammern.
Zusammenfassend wird die Einzelspureffizienz des FLT für Elektronen angegeben. Die Rekonstruktionseffizienz des FLT für ein Elektron aus einem $J/\psi \to e^+e^-$ Zerfall, welches die Akzeptanz des FLT in den äußeren Spurkammern passiert, beträgt

$$\epsilon = \left(26.3 \pm 0.5\,(\text{stat}) \,{}^{+0.9}_{-1.2}\,(\text{syst})\right)\%$$

Dieses Ergebnis berücksichtigt alle untersuchten Effekte. Es beinhaltet die Simulation des auf dem elektromagnetischen Kalorimeter basierenden Pretriggers mit einem Schnitt auf die transversale Energie auf die Energiedeposition von $E_\mathrm{T} > 1.0\,\mathrm{GeV}$.

Abstract

The experiment HERA-B has been designed to measure CP violation in the decay of neutral B mesons. In order to collect B decays in the gold-plated channel $B^0 \to J/\psi K^0_S$, the First Level Trigger (FLT) is designed to select $J/\psi \to l^+l^-$ decays. It reduces the hadronic background by a factor of 200.
The FLT is built from a network of about 80 custom designed processor boards which allow an online reconstruction of $\mathcal{O}(10^7)$ tracks per second, including the calculation of momenta of tracks and invariant masses of track pairs.
This thesis is about the performance and efficiency of the HERA-B FLT during the data taking of the year 2000. The analysis describes the detector performance and the data transmission, as it concerns the FLT. Based on that results, channel maskings are generated, which are applied in the simulation of the FLT.
The correspondance between the FLT hardware and simulation is investigated by comparing tracks which are reconstructed by the FLT hardware and simulation on a event-by-event basis. The agreement between FLT hardware and simulation is shown. Limitations on the correspondance, which are introduced by the hit data transmission, are demonstrated.
The FLT single track efficiency is analyzed using Monte Carlo. Besides investigating an idealized detector for the estimation of the intrinsic efficiency of the FLT algorithm, the influences of the real detector on the efficiency are analyzed. This comprises hit efficiencies and misalignment as well as defective channels of the detector.
Concluding, the single track efficiency of the FLT for electrons is calculated. The efficiency that the FLT triggers on an electron which originates from a $J/\psi \to e^+e^-$ decay and which passes the FLT outer tracker acceptance is

$$\epsilon = \left(26.3 \pm 0.5\,(\text{stat}) \,{}^{+0.9}_{-1.2}\,(\text{syst})\right)\,\%$$

This takes into account all effects which are investigated. It includes a simulation of the ECAL pretrigger with a cut on the transverse energy of a cluster in the ECAL of $E_\text{T} > 1.0\,\text{GeV}$.

Contents

Introduction

The analysis of symmetries is one of the most powerful methods for the discovery of laws of nature. Continuous symmetries are linked to principles of conservation as expressed in Noether's theorem [noe16]. For example, the symmetry under time and space translation corresponds to the conservation of energy and momentum, respectively.

Besides the continuous symmetries, there are the discrete symmetries of charge conjugation C, space inversion (parity) P, and time reversal T. It was long believed that the laws describing the interaction of elementary particles are invariant under each of these operations. However, it was experimentally shown that both C and P are violated in weak interactions [gol58, wu57]. The combined symmetry CP was then thought to be conserved in weak interactions, until CP violation was found in the system of neutral K mesons [chr64]. In the K system, the effect of CP violation is small. The corresponding asymmetry of decay probabilities is of the order $\mathcal{O}(10^{-3})$. The Standard Model of elementary particles predicts CP violation also in the system of neutral B mesons. Contrary to the K system, large effects are expected in this case.

Several experiments have been planned and built to investigate the system of neutral B mesons: the BaBar [bou95] and Belle [che95] collaborations use dedicated electron-positron colliders to produce B mesons. The HERA-B experiment [loh94] uses the proton storage ring of the existing HERA collider. The B mesons are produced by moving wire targets into the outer regions of the 920 GeV[1] proton beam.

Due to many technical challenges involved in the measurement of heavy flavor decays in a huge hadronic background, the ambitious time schedule of HERA-B could not be met, and the detector was still in its commissioning phase during the data taking of the year 2000.

This thesis is about the performance and efficiency of the HERA-B **F**irst **L**evel **T**rigger (FLT) during the data taking of the year 2000. The first chapter deals with the physical motivation of the construction of the experiment HERA-B. The detector components are described and an overview of the trigger and data acquisition system is given.

The second chapter describes in detail the design of the FLT. The tracking algorithm, the realization of the FLT hardware, and the simulation of the system are the subject of that chapter.

The analysis of the thesis is contained in the remaining three chapters. In Chapter 3 the

[1] Throughout this thesis, we use $\hbar = c = 1$ and multiples of electronvolts (eV) as units for energies, momenta, and masses. In particular, $1\,\mathrm{GeV} = 10^9\,\mathrm{eV}$.

detector performance and the data transmission is investigated, as far as it concerns the FLT. Not only the performance of the system is reported, but also channel maskings are developed which are used for simulating the FLT in a realistic way.
Chapter 4 describes the correspondence of the FLT algorithm in hardware and simulation. The tracks which are reconstructed by the FLT during data taking are compared with the simulation on an event-by-event basis. Erroneous behavior of the hardware in different areas of the acceptance is demonstrated. The principle agreement between the FLT in hardware and simulation is shown, and the limitations due to technical problems in the system are reported.
In the last Chapter the FLT single track efficiency is analyzed using Monte Carlo. Besides investigating an idealized detector for the estimation of the intrinsic efficiency of the FLT algorithm, the influences of the real detector on the efficiency are analyzed. This comprises hit efficiencies and misalignment as well as defective channels of the detector. Finally, the single track efficiency of the FLT for electrons is calculated.

Chapter 1

The Experiment HERA-B

The original goal of the experiment HERA-B was the measurement of CP-Violation in the system of B-Mesons. Because of various problems in the development and during the commissioning of the detector, this aim has not been met. Thus, an additional physics program was proposed in order to make use of the detector in its current state.
This chapter begins with a short historical overview of the developments in the field of symmetry-breaking in the Standard Model of particle physics. This leads to the phenomenon of CP-Violation in the B-system, which has motivated the construction of the HERA-B detector. From this, the requirements are derived which lead to the design of the detector. Finally, the updated physics program is described that is the goal for the future data taking.

1.1 The Standard Model of Particle Physics

The best description of the phenomenona of particle physics is summarized in the *Standard Model*. The foundations of the Standard Model are given in [gla61] and [wei67]. The model proposes the existence of a set of fundamental fermions, i.e. particles of spin $\frac{1}{2}$. These are divided into two types, the *leptons* and the *quarks*. There are three *generations* — or *families* — of each type, leading to twelve particles as shown in Table 1.1. Using the charge of the particles, one can divide them into 'up'- and 'down'-like particles.
The interactions between these fundamental particles are mediated by a set of bosons, which are particles of integer spin. They can be associated to the fundamental interactions as shown in Table 1.2. The theory describing the strong interaction is called *quantum chromodynamics* (*QCD*), while the electromagnetic and the weak interactions are combined in the theory of the *electroweak interaction*.
The bosons which mediate the electroweak interaction, as well as the fermions, are a priori massless since the theory of electroweak interaction is a local gauge theory which can be only applied to massless particles. However, it is proven by experimental data that there are both, massive (the $W^{\pm}$ and Z^0) and massless (the photon) bosons involved in the electroweak interaction. To introduce mass into the theory the mechanism of

	charge	generation		
		first	second	third
quarks	$+\frac{2}{3}$	u (up)	c (charm)	t (top)
		$1-5\,\mathrm{MeV}$	$1.15-1.35\,\mathrm{GeV}$	$174.3\pm5.1\,\mathrm{GeV}$
	$-\frac{1}{3}$	d (down)	s (strange)	b (bottom)
		$3-9\,\mathrm{MeV}$	$75-170\,\mathrm{MeV}$	$4.0-4.4\,\mathrm{GeV}$
leptons	0	ν_e (electron neutrino)	ν_μ (muon neutrino)	ν_τ (tau neutrino)
		$<3\,\mathrm{eV}$	$<0.19\,\mathrm{MeV}$	$<18.2\,\mathrm{MeV}$
	-1	e (electron)	μ (muon)	τ (tau)
		$0.511\,\mathrm{MeV}$	$105.658\,\mathrm{MeV}$	$1777\,\mathrm{MeV}$

Table 1.1: The two kinds of fundamental fermions in the Standard Model of particle physics, leptons and quarks. The fermions are grouped by their generation and charge. Moreover, the masses are given [gro00].

spontaneous symmetry-breaking is established which allows for the assignment of mass to both the mediating bosons and the fermions. This mechanism is connected with the prediction of at least one Higgs-particle, which introduces mass in the theory. There is presently no direct evidence for the existence of this particle. The discovery of the Higgs-particle would be one important proof of the Standard Model.

1.1.1 Discrete Symmetries in the Standard Model

Studying the behavior of a physical system in terms of symmetries has often revealed new aspects of the essence of physical laws. In quantum field theory, which is the basis of the Standard Model, there are three fundamental discrete symmetry-transformations:

interaction	couples to	gauge boson	mass	charge	spin
strong	color charge (quarks)	g (gluon)	0	0	1
weak	flavor (quarks, leptons)	W^+, W^-	$80.419\,\mathrm{GeV}$	$+1$, -1	1
		Z^0	$91.188\,\mathrm{GeV}$	0	1
electromagnetic	electric charge (el. charged part.)	γ (photon)	0	0	1
gravitation	mass (all particles)	graviton (not yet observed	0	0	2

Table 1.2: The fundamental interaction together with their mediating gauge bosons and their masses and electrical charge [gro00].

Charge Conjugation	(C)	exchange of particles with antiparticles
Parity	(P)	inversion of spatial coordinates: $\vec{x} \rightarrow -\vec{x}$, this also inverts other vectors as the momentum, while axial vectors, such as angular momentum, are unchanged
Time Reversal	(T)	inversion of time: $t \rightarrow -t$, this inverts both momentum and angular momentum

A physical system is called *invariant under a certain symmetry-transformation* if the observables are not changed by the application of the corresponding transformation on the system. A symmetry is commonly called a *good symmetry* if it is not violated. The CPT theorem [lue57] predicts that any local, causal, relativistic field theory is invariant under the combined application of the three transformations C, P and T. However it is experimentally proven that the transformations C, P and the combined transformation CP are violated in weak processes, as discussed in the following.
The violation of the parity symmetry was observed in 1957 by Wu et al. [wu57] who found that electrons from the decay of ^{60}Co

$$^{60}\mathrm{Co}(J=5) \longrightarrow {}^{60}\mathrm{Ni}^{*}(J=4) + e^{-} + \bar{\nu}_e$$

are emitted preferentially in the direction opposite to the nuclear spin, J. Parity violation and the characteristic property of neutrinos and antineutrinos to exist only in left- and right-handed states, respectively, led to the formulation of the V-A-theory of weak interactions.
The violation of the charge conjugation C becomes visible in the weak decay of π^+

$$\pi^{+} \longrightarrow \mu^{+}_{\mathrm{R}} + \nu_{\mu,\mathrm{L}} \quad \stackrel{C}{\Longrightarrow} \quad \pi^{-} \longrightarrow \mu^{-}_{\mathrm{R}} + \bar{\nu}_{\mu,\mathrm{L}}$$

The charge conjugated process yields a left-handed $\bar{\nu}_{\mu,\mathrm{L}}$ which is not observed in nature. However, the process after the combined application of C and P is realized in nature:

$$\pi^{+} \longrightarrow \mu^{+}_{\mathrm{R}} + \nu_{\mu,\mathrm{L}} \quad \stackrel{CP}{\Longrightarrow} \quad \pi^{-} \longrightarrow \mu^{-}_{\mathrm{L}} + \bar{\nu}_{\mu,\mathrm{R}}$$

Although it was believed that CP is a good symmetry in weak interactions, in 1964 CP was found to be violated as well [chr64]. The long-lived neutral kaon K^0_L decays to final states with two (CP-eigenvalue $+1$) and three (dominantly CP-eigenvalue -1) pions. Therefore, the mass eigenstate K^0_L cannot be simultaneously an eigenstate of CP. However, CP-Violation in the kaon-system is a small effect since the branching ratio to the two-pion states is about 10^{-3} of the branching ratio to the three-pion state. In contrast, CP-violation in the B-meson system is expected and was indeed proven to lead to a much larger effect than in the kaon-system.

1.1.2 CP-Violation in the Standard Model

In the Standard Model, CP-violation occurs in the charged current weak interactions of quarks. The mass eigenstates of the quarks do not coincide with the eigenstates

of the weak interaction. Conventionally, the weak eigenstates of down-type quarks are constructed by applying a unitary transformation matrix V_{CKM}, the *Cabbibo-Kobayashi-Maskawa matrix* (*CKM matrix*), on the mass eigenstates:

$$\begin{pmatrix} |d'\rangle \\ |s'\rangle \\ |b'\rangle \end{pmatrix} = V_{\mathrm{CKM}} \begin{pmatrix} |d\rangle \\ |s\rangle \\ |b\rangle \end{pmatrix} = \begin{pmatrix} V_{ud} & V_{us} & V_{ub} \\ V_{cd} & V_{cs} & V_{cb} \\ V_{td} & V_{ts} & V_{tb} \end{pmatrix} \begin{pmatrix} |d\rangle \\ |s\rangle \\ |b\rangle \end{pmatrix}$$

For example the transition of a down-type quark j into an up-type quark k involves the matrix element V_{jk}, see Fig. 1.1. In order to conserve probability, V_{CKM} has to be unitary. Therefore nine of the eighteen parameters (from nine complex parameters) are constrained by the condition $V_{\mathrm{CKM}}^{\dagger} V_{\mathrm{CKM}} = 1$, and there remains three real angles and six phases.

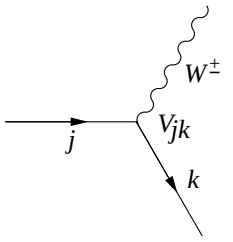

Fig. 1.1: The weak transition of quark j to quark k has to take into account the element V_{jk} of the CKM matrix.

The absolute phases of all quark fields are arbitrary, unmeasurable quantities. There exist five phase differences between the six quark fields. By the convention to use the minimal number of phases, one can remove five phase differences of the quark fields by redefinition of the elements of the CKM matrix, for example, V_{jk} is replaced by $e^{i(\phi(k)-\phi(j))}V_{jk}$. In this way, one phase remains which is the single source of *CP*-violation in the Standard Model [nir99].
The CKM matrix is commonly written in the Wolfenstein parameterization, which is an expansion in powers of $\lambda = |V_{us}| = \sin\theta_C \approx 0.22$, where θ_C is the Cabbibo angle known from the mixing of the first two quark generations:

$$V_{\mathrm{CKM}} \approx \begin{pmatrix} 1-\frac{\lambda^2}{2} & \lambda & A\lambda^3(\rho - i\eta) \\ -\lambda & 1-\frac{\lambda^2}{2} & A\lambda^2 \\ A\lambda^3(1-\rho-i\eta) & -A\lambda^2 & 1 \end{pmatrix} + \mathcal{O}(\lambda^4)$$

Using the unitarity condition $V_{\mathrm{CKM}}^{\dagger} V_{\mathrm{CKM}} = 1$, relations between the parameters of the CKM matrix can be obtained. Among these the relation

$$\begin{array}{ccccccc} V_{ud}V_{ub}^* & + & V_{cd}V_{cb}^* & + & V_{td}V_{tb}^* & = & 0 \\ (1-\frac{\lambda^2}{2})(A\lambda^3(\rho+i\eta)) & + & (-\lambda)(A\lambda^2) & + & (A\lambda^3(1-\rho-i\eta))(1) & = & 0 \end{array}$$

deserves special attention because all terms of the sum are proportional to λ^3 and are hence of similar magnitude. After dividing by $V_{cd}V_{cb}^*$

$$\frac{V_{ud}V_{ub}^*}{V_{cd}V_{cb}^*} + \frac{V_{cd}V_{cb}^*}{V_{cd}V_{cb}^*} + \frac{V_{td}V_{tb}^*}{V_{cd}V_{cb}^*} = 0$$

and using the relation

$$\frac{V_{ud}V_{ub}^*}{V_{cd}V_{cb}^*} = \frac{(1-\lambda^2)(A\lambda^3(\rho+i\eta))}{A\lambda^3} = \rho\left(1-\frac{\lambda^2}{2}\right) + i\eta\left(1-\frac{\lambda^2}{2}\right)$$

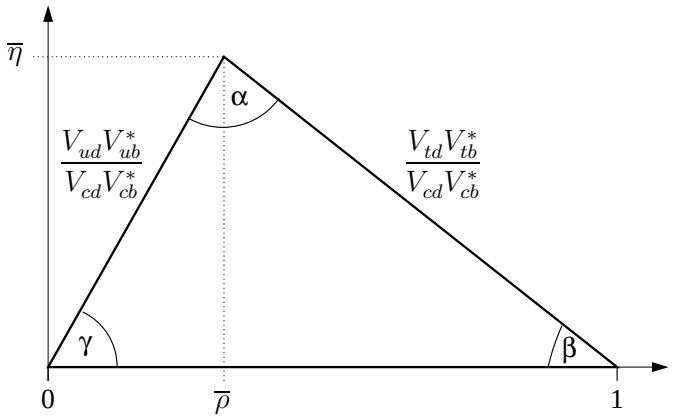

Fig. 1.2: The Unitarity Triangle represents one of the unitarity relations of the CKM matrix.

we are able to visualize the relation by a triangle in the complex plane. The triangle shown in Fig. 1.2 is called *Unitarity Triangle* in which the top is given by the point $(\bar{\rho}, \bar{\eta})$ using the definition

$$\bar{\rho} = \left(1-\frac{\lambda^2}{2}\right)\rho \qquad \bar{\eta} = \left(1-\frac{\lambda^2}{2}\right)\eta$$

The triangle contains the following angles

$$\alpha = \arg\left(-\frac{V_{td}V_{tb}^*}{V_{ud}V_{cb}^*}\right) \qquad \beta = \arg\left(-\frac{V_{cd}V_{cb}^*}{V_{td}V_{tb}^*}\right) \qquad \gamma = \arg\left(-\frac{V_{ud}V_{ub}^*}{V_{cd}V_{cb}^*}\right)$$

The angles α, β and γ are observables and can be measured independently through *CP*-asymmetries in particle-decays, especially in B-decays because of the favorable ratio of the CKM matrix elements which are associated to the b-quark. If *CP* were conserved, the quark mixing matrix would be real and the triangle collapses to a line. However, recent measurements prove that *CP* is not conserved in B-decays [aub02, aba02]. Future measurements are intended to overconstrain the unitarity triangle by measuring as many parameters as possible, especially all three angles and sides, in order to determine if *CP*-violation as observed in nature can be described by the Standard Model, i.e. whether the three angles do add up to π. If the unitarity relation is violated, it may point to physics beyond the Standard Model.

1.1.3 *CP*-Violation in the B^0-System

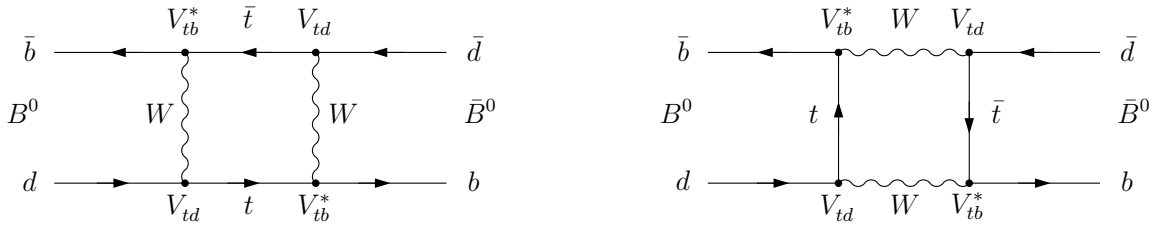

Fig. 1.3: Lowest order Feynman diagrams describing the mixing of $B^0 \leftrightarrow \bar{B}^0$. At the vertices the involved elements of the CKM-matrix are given. The contribution of the t-quarks in the loops dominates since $V_{tb}^* \approx 1$.

Like the system of $K^0 - \bar{K}^0$, where mixing has first been observed, also the neutral B-mesons can mix via weak interactions as shown in the Feynman diagrams in Fig. 1.3 [ale99a]. The description for B^0 and $\bar{B}^0$ mesons given here can be generalized to other neutral mesons like B_s, K^0 and D^0 and their antistates. Any arbitrary state is a superposition of the flavor eigenstates. We denote such a state $a|B^0\rangle + b|\bar{B}^0\rangle$ by a two-component vector

$$\psi = \begin{pmatrix} a \\ b \end{pmatrix} \tag{1.1}$$

which obeys the time-dependent Schrödinger equation

$$i\frac{d}{dt}\psi = \mathbf{H}\psi = \left(\mathbf{M} - \frac{i}{2}\mathbf{\Gamma}\right)\psi = \begin{pmatrix} M_{11} - \frac{i}{2}\Gamma_{11} & M_{12} - \frac{i}{2}\Gamma_{12} \\ M_{21} - \frac{i}{2}\Gamma_{21} & M_{22} - \frac{i}{2}\Gamma_{22} \end{pmatrix}\psi \tag{1.2}$$

The Hamiltonian $\mathbf{H}$ consists of the following terms:

- M_{11} and M_{22} take into account the mass of the constituent quarks of the B^0- and $\bar{B}^0$-mesons and their binding energy.
- M_{12} and M_{21} reflect transitions $B^0 \leftrightarrow \bar{B}^0$ involving virtual processes as shown e.g. in Fig. 1.3.
- Γ_{11} and Γ_{22} correspond to the decays $B^0 \to f$ and $\bar{B}^0 \to \bar{f}$, respectively.
- Γ_{12} and Γ_{21} reflect transitions $B^0 \leftrightarrow f \leftrightarrow \bar{B}^0$ where f is a real state common to both B^0 and $\bar{B}^0$.

Because of CPT-conservation we require $M_{11} = M_{22} = M$ and $\Gamma_{11} = \Gamma_{22} = \Gamma$. Moreover $\mathbf{H}$ has to be hermitian which demands $M_{21} = M_{12}^*$ and $\Gamma_{21} = \Gamma_{12}^*$. The diagonal elements of the Hamiltonian $\mathbf{H}$ describe the time evolution of the states $|B^0\rangle$ and $|\bar{B}^0\rangle$ of mass M and decay width Γ. In contrast, the weak transition of neutral mesons as indicated in

Fig. 1.3 is described by the off-diagonal elements of the Hamiltonian which correspond to the elements of the CKM matrix given in the Feynman diagrams. By diagonalization of the Hamiltonian one gets the eigenvalues

$$\begin{aligned} M_L - \tfrac{i}{2}\Gamma_L &= \left(M - \tfrac{i}{2}\Gamma\right) + \tfrac{q}{p}\left(M_{12} - \tfrac{i}{2}\Gamma_{12}\right) \\ M_H - \tfrac{i}{2}\Gamma_H &= \left(M - \tfrac{i}{2}\Gamma\right) - \tfrac{q}{p}\left(M_{12} - \tfrac{i}{2}\Gamma_{12}\right) \end{aligned} \tag{1.3}$$

where

$$\frac{q}{p} = \sqrt{\frac{M_{12}^* - \frac{i}{2}\Gamma_{12}^*}{M_{12} - \frac{i}{2}\Gamma_{12}}} \tag{1.4}$$

The corresponding eigenstates yield

$$\psi_\pm = \begin{pmatrix} p \\ \pm q \end{pmatrix} \tag{1.5}$$

which represent a heavy and a light mass eigenstate

$$\begin{aligned} |B_L\rangle &= p|B^0\rangle + q|\bar{B}^0\rangle \\ |B_H\rangle &= p|B^0\rangle - q|\bar{B}^0\rangle \end{aligned} \tag{1.6}$$

The Schrödinger equation (Eq. 1.2) leads to the following time evolution

$$\begin{aligned} |B_L(t)\rangle &= e^{-i(M_L - \frac{i}{2}\Gamma_L)t}\ |B_L(0)\rangle \\ |B_H(t)\rangle &= e^{-i(M_H - \frac{i}{2}\Gamma_H)t}\ |B_H(0)\rangle \end{aligned} \tag{1.7}$$

The difference in the width between the physical states is negligible compared to the mass difference

$$\frac{|\Delta\Gamma_{L/H}|}{\Delta M_{L/H}} \approx 0 \tag{1.8}$$

From this follows that one can set $\Gamma_H = \Gamma_L$ while the masses differ by the magnitude ΔM_B so that $M_H = M_B + \frac{1}{2}\Delta M_B$ and $M_L = M_B - \frac{1}{2}\Delta M_B$. With this notation we get

$$\begin{aligned} |B^0(t)\rangle &= \tfrac{1}{2p} e^{-i(M_B - \frac{i}{2}\Gamma_B)t}\left(e^{-\frac{i}{2}\Delta M_B t}|B_H\rangle + e^{+\frac{i}{2}\Delta M_B t}|B_L\rangle\right) \\ &= e^{-i(M_B - \frac{i}{2}\Gamma_B)t}\left(\cos\left(\tfrac{1}{2}\Delta M_B t\right)|B^0\rangle + i\tfrac{q}{p}\sin\left(\tfrac{1}{2}\Delta M_B t\right)|\bar{B}^0\rangle\right) \end{aligned} \tag{1.9}$$

and correspondingly

$$|\bar{B}^0(t)\rangle = e^{-i(M_B - \frac{i}{2}\Gamma_B)t}\left(\cos\left(\tfrac{1}{2}\Delta M_B t\right)|\bar{B}^0\rangle + i\tfrac{p}{q}\sin\left(\tfrac{1}{2}\Delta M_B t\right)|B^0\rangle\right) \tag{1.10}$$

Thus an initially pure $|B^0\rangle$ state which is created at time $t = 0$, for example, by a strong interaction, propagates through the vacuum and has a non-zero probability to be a $|\bar{B}^0\rangle$ after a given time t.

Using $|\Gamma_{12}| \ll |M_{12}|$ and the CKM-matrix elements as depicted in Fig. 1.3 the ratio of (Eq. 1.4) can be approximated by [nir99]

$$\frac{q}{p} = \sqrt{\frac{M_{12}^* - \frac{i}{2}\Gamma_{12}^*}{M_{12} - \frac{i}{2}\Gamma_{12}}} \approx \sqrt{\frac{M_{12}^*}{M_{12}}} = \frac{M_{12}^*}{|M_{12}|} = \frac{(V_{tb}^* V_{td})^2}{|V_{tb}^* V_{td}|^2} = \frac{V_{tb}^* V_{td}}{V_{tb} V_{td}^*} = e^{-2i\beta} \tag{1.11}$$

where β is one of the angles defined in the Unitary Triangle, see Fig. 1.2. Since $\frac{q}{p} \approx e^{-2i\beta}$ is just a phase, it is necessary to regard the interference of $|B^0\rangle$ and $|\bar{B}^0\rangle$ states in order to get a measurable effect. A final *CP* eigenstate can be reached by direct decay or by a previous mixing, see Fig. 1.3. This gives the chance to measure *CP* violation by the interference of these two possibilities. Both B^0 and $\bar{B}^0$ can decay into the same final state f_{CP} which is a *CP* eigenstate. The decay of a B^0 can either take place directly, $B^0 \to f_{CP}$, or the B^0 first oscillates into a $\bar{B}^0$ which leads to the decay $B^0 \to \bar{B}^0 \to f_{CP}$. The two amplitudes for the two decays interfere. If a complex matrix element of the CKM-matrix occurs in the mixing, the two decay rates are not the same and *CP* is violated. This type of *CP* violation is called *CP* violation in the interference between decays with and without mixing [hq98].
Such an interference is observable by comparing the decay rates into final *CP* eigenstates of a time-evolving $|B\rangle$ state that begins at time $t = 0$ as a B^0 to those of the state that begin as a $\bar{B}^0$

$$\begin{aligned} a_{f_{CP}} &= \frac{\Gamma(B^0(t) \to f_{CP}) - \Gamma(\bar{B}^0(t) \to f_{CP})}{\Gamma(B^0(t) \to f_{CP}) + \Gamma(\bar{B}^0(t) \to f_{CP})} \\ &= \frac{(1 - |\lambda_{f_{CP}}|^2)\cos\Delta M_B t - 2\mathrm{Im}\lambda_{f_{CP}} \sin\Delta M_B t}{1 + |\lambda_{f_{CP}}|^2} \end{aligned} \tag{1.12}$$

Here the parameter $\lambda_{f_{CP}}$ indicates whether *CP* is violated. It is defined as the ratio of the decay amplitudes into the final state f_{CP}

$$\lambda_{f_{CP}} = \frac{q}{p}\frac{\langle f_{CP}|H|\bar{B}^0\rangle}{\langle f_{CP}|H|B^0\rangle} \tag{1.13}$$

The cleanest decay modes are those where one *CP* violating phase dominates. For those modes the hadronic uncertainties in λ cancel.

1.1.4 Measurement of *CP* Violation in the B^0-System

The decay $B^0/\bar{B}^0 \to J/\psi K_S^0$ offers a very clean measurement of *CP* violation due to the following reasons:

- The final state is a *CP* eigenstate.
- *CP* violation is expected to be large in B^0-$\bar{B}^0$mixing, thus the effect is measurable in an easy way.

- The contamination from penguin diagrams is small.
- It has a clear signature which allows an efficient trigger strategy.

Because of these favorable conditions this channel has been called the *gold-plated decay* for measuring $\sin 2\beta$.

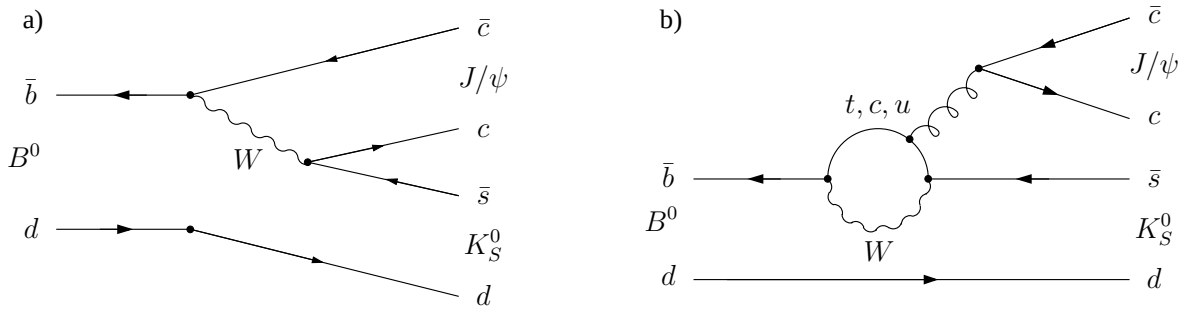

Fig. 1.4: The major contribution to the gold-plated decay is the tree diagram a) while the penguin diagram b) is suppressed.

The decay diagrams are shown in Fig. 1.4. The amplitude of the tree diagram is proportional to $A_{\text{tree}} = V_{cb}V_{cs}^* = A\lambda^2 + \mathcal{O}(\lambda^4)$. There are three types of penguin contributions, each with a t-, c- or a u-quark in the loop. All penguin diagrams are suppressed due to this loop. The amplitude of the t-quark diagram is proportional to $V_{tb}V_{cs}^* = -A_{\text{tree}} + \mathcal{O}(\lambda^4)$. With the c-quark the amplitude is proportional to A_{tree} and with the u-quark to $V_{ub}V_{us}^* = \mathcal{O}(\lambda^4)$. Hence all penguin diagrams contribute with the same weak phase as the tree diagram up to corrections of order $\lambda^4 \approx 10^{-3}$. The hadronic uncertainties are only of that order.
Recently both BaBar and Belle reported measurements of $\sin 2\beta$ using the gold-plated decay. Their results are

$$\sin 2\beta = 0.741 \pm 0.067\,(\text{stat}) \pm 0.034\,(\text{syst}) \qquad \text{BaBar [aub02]}$$
$$\sin 2\beta = 0.719 \pm 0.074\,(\text{stat}) \pm 0.035\,(\text{syst}) \qquad \text{Belle [aba02]}$$

1.1.5 Measurement of *CP* Violation at HERA-*B*

The measurement of *CP* violation at HERA-*B* consists in counting how many B^0s and how many $\bar{B}^0$s decay into the *CP* eigenstate $J/\psi K_S^0$. The resulting asymmetry is connected to the angle β of the unitarity triangle [loh94]

$$\frac{N(B^0 \to J/\psi K_S^0) - N(\bar{B}^0 \to J/\psi K_S^0)}{N(B^0 \to J/\psi K_S^0) + N(\bar{B}^0 \to J/\psi K_S^0)} = \sin 2\beta \sin \Delta M_B t \tag{1.14}$$

ΔM_B indicates the mass difference of B^0 and $\bar{B}^0$and t the time which has elapsed since the production of the two B mesons. Besides reconstructing the decay of the B meson

it is also needed to determine whether a B^0 or a $\bar{B}^0$ has decayed. This can be done by *tagging*, which is the detection of the flavor of the other B meson containing the other produced b-quark. In HERA-B, this flavor is determined by the charge of a lepton or kaon produced in the decay, see Fig. 1.5.

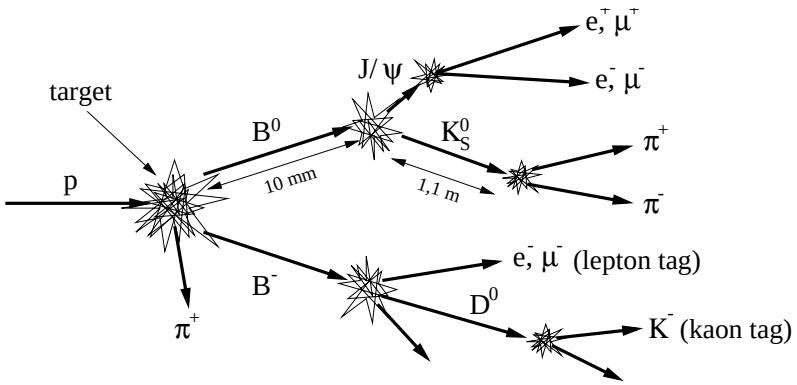

Fig. 1.5: The decay chain of the gold-plated decay intended for HERA-B including the second B meson that is used for the tagging. Both the lepton tag and the kaon tag are shown.

The experimental challenge to measure $\sin 2\beta$ in the gold-plated decay at HERA-B is defined by the vast difference between the expected rate of events containing the gold-plated decay compared to all inelastic interactions. With a beam momentum of 920 GeV the total inelastic cross section for proton-nucleon scattering is of the order 13 mb/nucleon while the production cross section of a $b\bar{b}$ pair is only about $10 - 20$ nb/nucleon. The branching ratio into the gold-plated decay mode is only $\Gamma(B^0/\bar{B}^0 \to J/\psi K_S^0) = 8.9 \cdot 10^{-4}$ [gro00]. Together with the branching ratio $\Gamma(J/\psi \to \mu^+\mu^-) = 0.059$ and trigger and reconstruction efficiencies about 10^{11} interactions result in one triggered and reconstructed gold-plated decay written to tape. For a significant measurement of $\sin 2\beta$ about 1000 events were needed. If these are to be collected within one year of running (with 10^7 s of usable beam time) this implies a mean interaction rate of about 40 MHz.

1.2 HERA-B Physics Program for 2002

Since the primary goal of HERA-B — the first measurement of CP-violation in the B-system — was not met, an alternative physics program was developed in order to make use of the detector in its state in the year 2002 [zoc01]. Some of these topics are discussed in the following.

$b\bar{b}$ Cross Section

The measurement of the $b\bar{b}$ cross section provides a good test for perturbative QCD predictions at **N**ext-to-**L**eading **O**rder (NLO). The results obtained by other fixed tar-

get experiments [ale99b, jan95] are qualitatively comparable with theoretical predictions. However, both theoretical and experimental errors are large.
At HERA-B, two methods to determine the $b\bar{b}$ cross section have been applied. One way is to reconstruct exclusive $b\bar{b} \to \mu\mu + X$ double semileptonic decays i.e. decays in which the b as well as the $\bar{b}$ decay with the emission of a single muon. The other method utilizes the inclusive $B \to J/\psi + X$ channel with $J/\psi \to \mu^+\mu^-$, the cross section can then be obtained by scaling the ratio $N_{B\to J/\psi X}/N_{\mathrm{prompt}J/\psi}$ with the cross section for prompt J/ψ production. HERA-B can use both methods [hb00].
The measurement of the $b\bar{b}$ cross section is first, an interesting measurement in itself. Second, it constrains perturbative QCD calculations which are needed for the understanding of heavy quark production.

Nuclear Dependence of Charmonium Production

The production of bound $c\bar{c}$-states is described by different models like the *color singlet model* and the *color octet model*. The models differ in their predictions on the angular distribution of the final states and in the dependence on nuclear effects. The color singlet model is based on the hypothesis that the $q\bar{q}$ pair is directly generated in a color singlet state while the color octet model assumes that a primary color octet state turns into a singlet state by emitting gluons. More information about these models can be found in [bra96].
At present a distinction between these models is not possible, and so a combination of both mechanisms has to be taken into consideration.
Existing measurements mainly cover the region with $x_F > 0$, while HERA-B covers the range of $-0.4 < x_F < 0.3$, extending the range where model predictions can be tested. The possibility to measure simultaneously the production of J/ψ, ψ', $\chi_{c1,2}$, and Υ allows the determination of relative suppression factors which are almost completely free of systematic effects. Interactions on two or more target wires with different atomic number can be measured simultaneously. In this way systematic effects of the detector can be controlled more easily.

Open Charm Production

The accumulation of a large open charm sample could be obtained, for example, with a single lepton trigger and would provide the possibility to measure properties of charm decays. In particular, $D^0 - \bar{D}^0$ mixing, which can be observed in the lifetime ratio of $D^0 \to K^-\pi^+$ to $D^0 \to K^-K^+$ and the lifetime difference between D^0 and $\bar{D}^0$ is expected to be small. Thus, the observation of $D^0 - \bar{D}^0$ mixing would point to new physics. Furthermore, recent results from CLEO and FOCUS [ber00] do not agree well and show only an agreement at a level of around two sigma.
Another channel suitable for the search for new physics is the rare decay $D^0 \to \mu^+\mu^-$. The Standard Model predicts a branching ratio of $\mathcal{O}(10^{-19})$ and the experimental signature is very clean.

1.3 The Proton Storage Ring of HERA

HERA-*B* is one of four high energy physics experiments which are located on the storage ring **H**adron-**E**lectron-**R**ing-**A**ccelerator (HERA) at **D**eutsches **E**lektronen-**SY**nchrotron (DESY) in Hamburg. HERA is the world's only lepton-proton collider. The electrons or positrons have an energy of 27.5 GeV, and the protons, 920 GeV. The storage ring has a circumference of 6.3 km. It is shown in Fig. 1.6 together with the contributing pre-accelerators.

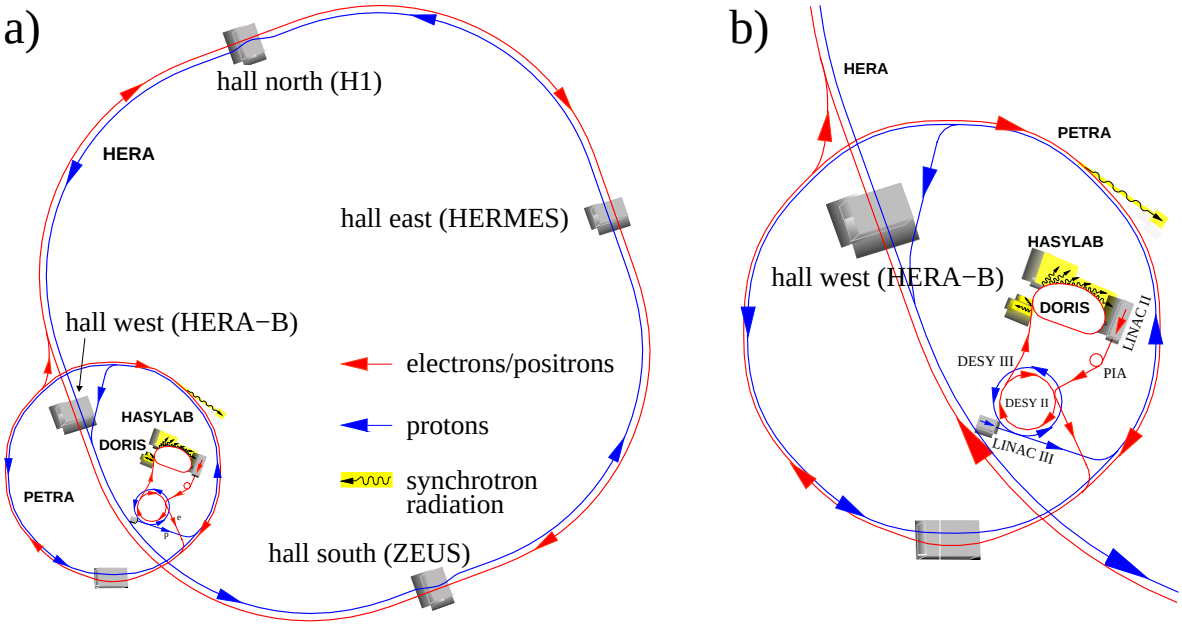

Fig. 1.6: Fig. a) shows the HERA accelerator and the location of the four experiments as well as the pre-accelerators. Fig. b) shows the pre-accelerator complex in more detail.

The two beams are brought to collision in two interaction regions where the experiments H1 [abt97] and ZEUS [zeu93] are situated. Their physics program comprises the measurement of the proton structure with a resolution varying over more than five orders of magnitude. Studies of the hadronic final state include jet physics, diffractive scattering in deep inelastic scattering, and the photoproduction of jets.
The experiment HERMES [ack98] is located in the east experimental area. It uses only the electron beam of HERA which is transversly polarized in the accelerator and longitudinal polarized at the experiment by means of spin rotators. Using an internal polarized gas target, HERMES investigates the spin structure of protons and neutrons.
HERA-*B* is located in the west experimental area. It uses the protons in the outer regions of the proton beam which are brought to collision with thin wires. With this type of target high interaction rates are possible with only a minimal disturbance of the operation of the other experiments.
Fig. 1.6 b) shows the pre-accelerators of HERA. The proton beam is generated in the

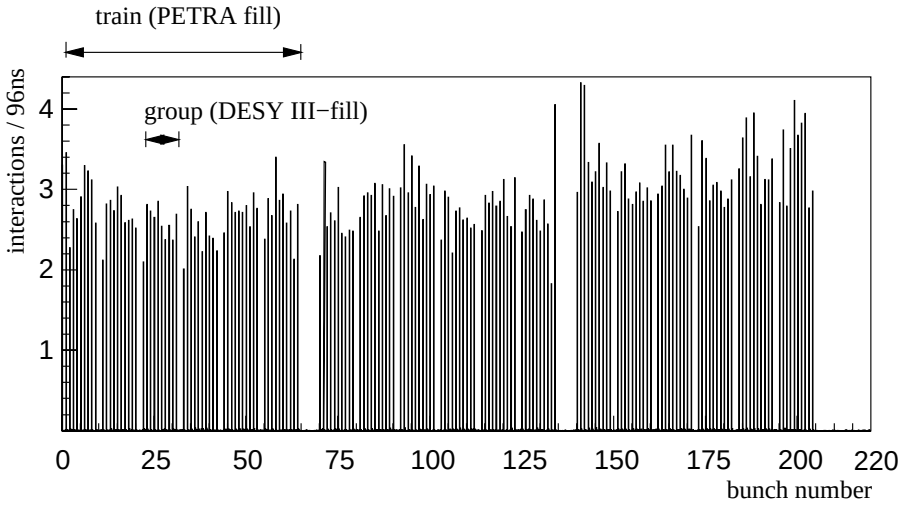

Fig. 1.7: The HERA bunch structure [scha98]. A HERA fill consists of three PETRA fills (trains). Each PETRA fill is made of six DESY III fills.

following way: first negative hydrogen ions are accelerated to an energy of 50 MeV by a **LIN**ear **AC**celerator (LINAC III). The ions pass a stripping-foil, which removes the electrons. The resultant protons are collected in *bunches* of about 10^{11} protons each. Ten bunches are accumulated in the DESY III pre-accelerator at an energy of 7.5 GeV and then transfered to PETRA[1]. PETRA collects six DESY III fills which makes up a PETRA train of 60 bunches. After acceleration to 40 GeV, the protons are transfered to HERA. HERA takes three PETRA trains and accelerates them to the final energy of 920 GeV. Combining the time interval between two bunches of 96 ns with the circumference of HERA leads to 220 *buckets* which can be filled by protons. 180 of the 220 buckets are filled with proton bunches. A typical fill of HERA is shown in Fig. 1.7.

1.4 The HERA-B Spectrometer

In this section, we will discuss the design of the HERA-B-spectrometer. An overview is shown in Fig. 1.8. The spectrometer covers the full azimuthal and polar angles between 10 mrad and 250 mrad in the bending and between 10 mrad and 160 mrad in the non-bending plane. The angular coverage corresponds to about 90% of 4π in the center of mass system [alb95].
HERA-B is using a right handed coordinate system. The z-axis is defined by the proton beam direction, the x-axis points to the center of HERA and the y-axis points upwards. The spectrometer consists of an internal wire target and a vertex detector system which are

[1]Before being used as pre-accelerators, **D**eutsches **E**lektronen-**SY**nchrotron (DESY) and **P**ositron **E**lectron **T**andem **R**ing **A**ccelerator (PETRA) were used as electron accelerator and electron-positron-collider, respectively.

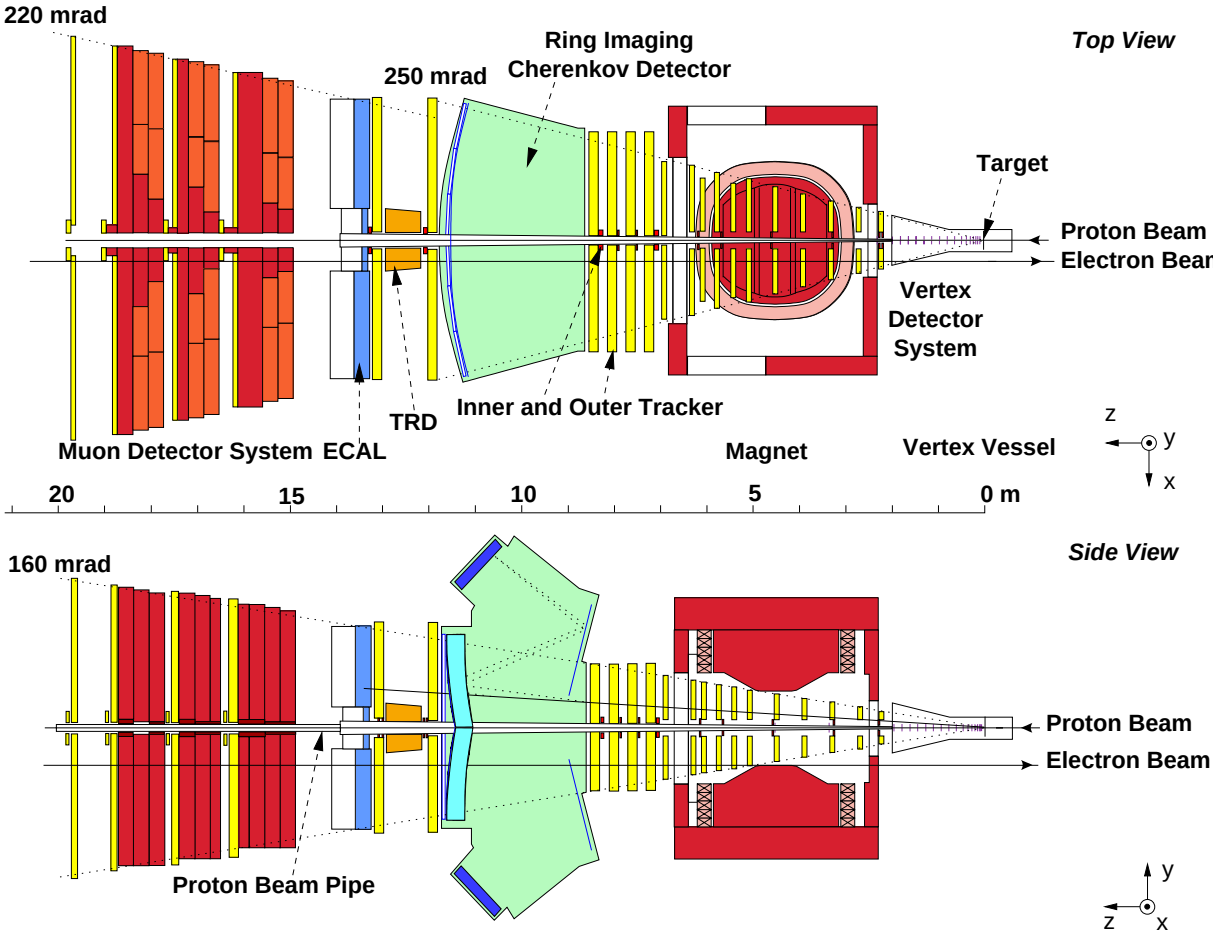

Fig. 1.8: Overview of the HERA-B spectrometer as it was used in the 2000 run [pyr98].

housed in the *vertex vessel*. Immediately downstream a normal-conducting spectrometer magnet of a field integral of 2.2 Tm enables the determination of the momentum of tracks with the help of the tracking system. For particle identification, a ring imaging Cherenkov detector, a transition radiation detector, an electromagnetic calorimeter, and a muon system are available. The different subdetectors are discussed in the following.

1.4.1 Internal Wire Target

The interactions in HERA-*B* are produced by inserting target wires into the outer regions of the HERA proton beam [ehr00]. By removing protons from the outer regions of the beam by collisions with the target wires, HERA-*B* is able to achieve high interaction rates without seriously affecting the proton beam and therefore the other experiments at HERA. The target wires are contained in the same vacuum vessel that is used for the vertex detector system, see Fig. 1.10.

The design interaction rate for HERA-*B* is 40 MHz, but filled proton bunches only pass

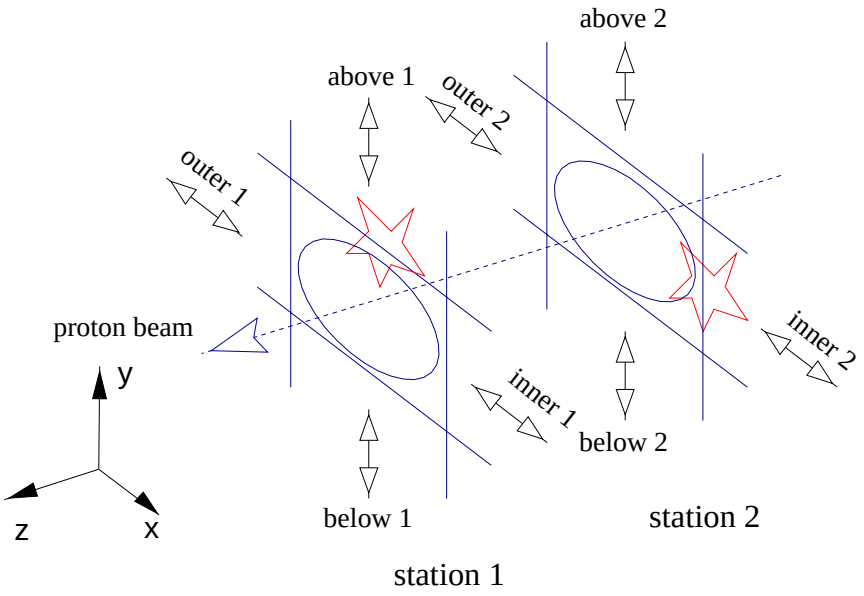

Fig. 1.9: Overview of the HERA-*B* target system. The positions of the eight target wires around the proton beam are shown [sym99].

the target with a rate of 8.5 MHz. This value is obtained by combining the bunch time interval of 96 ns and the ratio of 180 filled of the total 220 buckets: $180/220 \cdot 1/96\,\text{ns} = 8.5\,\text{MHz}$. An average of 4.7 interactions per bunch crossing is therefore needed for an interaction rate of 40 MHz. To be able to distinguish between the different interactions, the HERA-*B* target system uses up to eight target wires simultaneously. The eight wires are mounted in two stations, separated by approximately 4 cm in z, see Fig. 1.9. Each wire is attached to its own target fork and is able to be moved independently of the others. Typically the wires are operated at a distances of $5-6$ beam sigma away from the beam center, where the beam sigma is typically around 400 μm.

Four scintillating counter pairs placed behind the RICH (11.5 m downstream) are used to monitor the interaction rate. If a too high rate is observed, the target wires are retracted slightly, and vice versa. The wire position adjustments are done ten times per second and the stepping motors are able to move a wire by as little as 50 nm. To distribute the interactions equally between the different target wires, each wire is equipped with a charge integrator which measures the charge produced by δ electron generation inside the target wires. In this way, only the wires producing too many or few interactions are adjusted and the number of interactions on each wire can be kept equal, to within 10%.

In the 2000 setup, most of the target wires were ribbons with widths of 500 μm along the beam axis and 50 μm perpendicular to the beam. Different target materials are used, including carbon, aluminum, titanium, and tungsten. By using different target materials, HERA-*B* is able to measure nuclear effects in, for instance, prompt charmonium production.

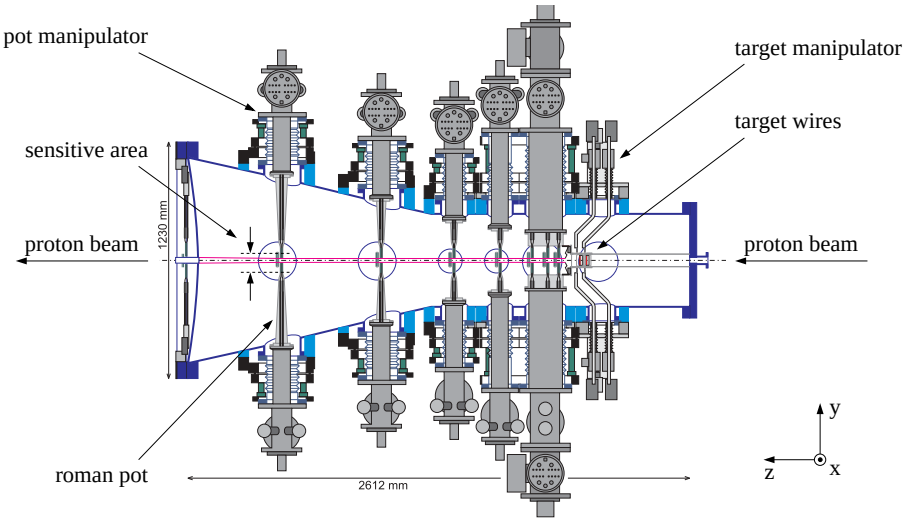

Fig. 1.10: Schematic overview of the vertex vessel containing the target wires and the VDS [bräu01].

1.4.2 Track Reconstruction

Vertex Detector

The **V**ertex **D**etector **S**ystem (VDS) allows for the reconstruction of primary and secondary vertices, as well as the determination of impact parameters of tracks. This is needed for selecting long lived particles, like $B^0 \to J/\psi K^0_S$ or $K^0_S \to \pi^+\pi^-$.
The VDS is built of 64 double-sided silicon micro-strip detectors. They are arranged in eight superlayers which are divided into four quadrants as shown in Fig. 1.11. In order to reconstruct the primary and secondary vertices with high precision, the detectors need to be as close to the target as possible and to have the largest possible angular coverage. In addition, the amount of material is kept as low as possible in order to minimize multiple scattering which limits the spatial resolution of the VDS.
In order to fulfill these requirements the first seven superlayers are located inside a vacuum vessel which is part of the HERA proton storage ring. The vessel also contains the target system and is shown in Fig. 1.10.
The detector modules in each quadrant of each superlayer consist of two double-sided silicon layers which are situated in *Roman pots*. The first three superlayers are housed in the same Roman pot. In the year 2000, one layer in each of the three superlayers only had single-side readout. The Roman pot system allows the silicon detectors to be retracted during injections. During data taking the detectors are moved within 10 mm of the beam, giving an angular coverage from 10 to 250 mrad. The steering system allows the detector modules to be repeatedly placed at the same position with a high precision of about 1 μm. This precision is high enough that the VDS does not need to be re-aligned after each insertion. Since the superlayers have similar sizes while being located at different z-positions along the beam, the superlayers have different angular acceptances.

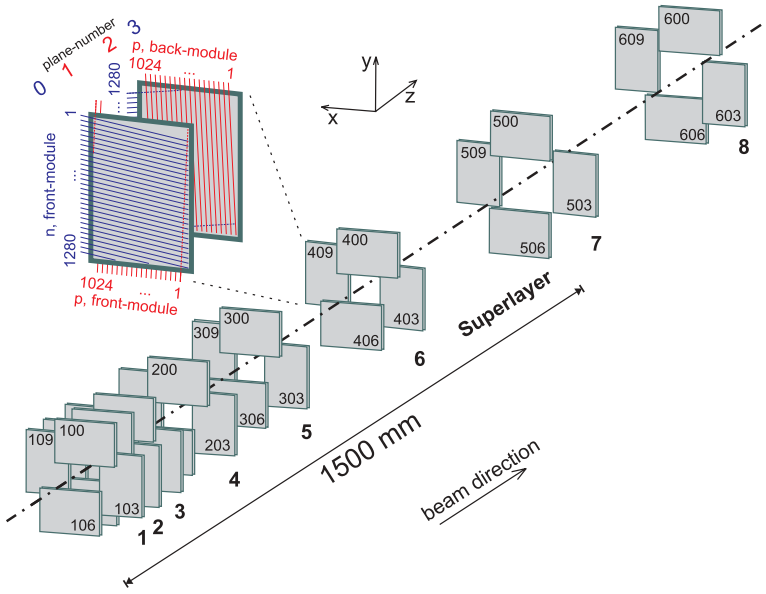

Fig. 1.11: Schematic overview of the VDS [knö01].

Typically a charged track passes through sensitive areas in three of the superlayers. The last superlayer (SI08) is not movable and housed outside of the vertex vessel.
The silicon layers are made from 280 μm thick n-type material and have an active area of $50 \cdot 70\,\mathrm{mm}^2$. The strips on the two sides are orthogonal and, with a readout pitch of 50 μm, the two sides have 1024 and 1280 readout strips, respectively. To facilitate pattern recognition the strips are tilted by $\pm 2.5°$ relative to the coordinate axis in the two layers of a superlayer. A single superlayer, therefore, provides measurements with stereo angles of $-2.5°$, $+2.5°$, $-87.5°$ and $+92.5°$ relative to the y-axis. A charged track usually produces a signal in more than one strip in a layer and using a clusterization algorithm a hit resolution of 12 μm is achieved with a hit efficiency above 98%. With this performance, primary and secondary vertices can be reconstructed with a resolution along the z-axis of about 500 μm and $700 - 800\,\mu$m, respectively

Inner Tracker

The **I**nner **TR**acker (ITR) covers angles from 10 mrad up to about 100 mrad (corresponding to a radial distance to the proton beam of approximately 30 cm). It is designed to withstand the high radiation dose of up to $10^5\,\mathrm{mm}^{-2}\mathrm{s}^{-1}$ charged particles in the inner acceptance of the HERA-B detector.
The positioning of the chambers is shown in Fig. 1.13. Each superlayer contains several layers in four quadrants. The stripes of the layers are oriented with respect to the vertical axis at angels of 0° and ±5°. This results in a spatial resolution of better than 100 μm in the horizontal and of 1 mm in the vertical direction. This design is used because the magnetic field bends charged particles in the horizontal plane and precision is needed for the momentum measurement.

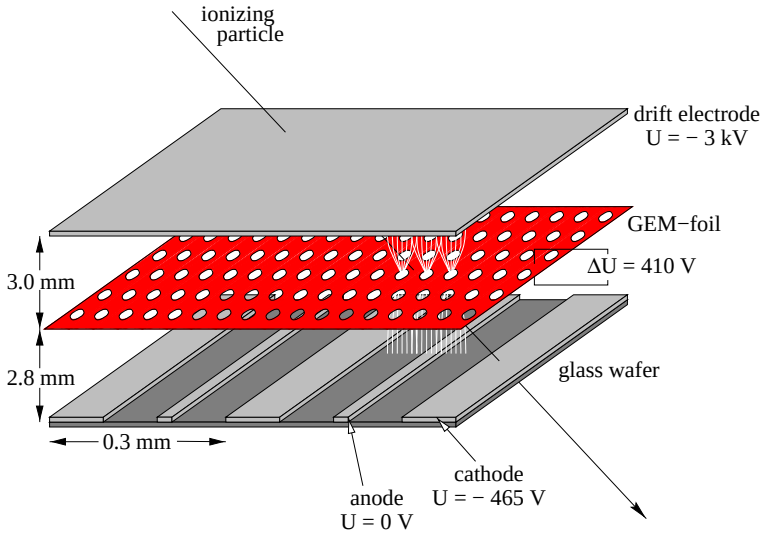

Fig. 1.12: Schematic overview of a GEM-MSGC [str98].

Each layer of the ITR is a **M**icro **S**trip **G**as **C**hamber (MSGC) [zeu00]. The principle of a MSGC detector is shown in Fig. 1.12. It consists of a thin glass wafer of 400 μm with anode and cathode strips of gold in a gas filled volume (70%Ar and 30%CO_2). A large drift voltage is applied between the anode and the top of the chamber (-3 kV) and the cathode strips (-465 V). The passage of a charged particle ionizes the gas and the electrons drift to the anode strips. The large electric field around the 10 μm wide anode strips provides a strong gas amplification of the primary electrons and a large signal can be read out from the anode strip.
During the design phase it was found that if the field strength is adjusted to provide sufficient signals for minimum ionizing particles, heavy ionizing particles, such as α particles, will often lead to sparks destroying the delicate structure of a chamber. Therefore, an intermediate gas amplification is introduced by the **G**as **E**lectron **M**ultiplier (GEM) layer, which allows for a reduction of the voltage of the cathodes. The GEM layer is a 50 μm thick Kapton foil which is clad with copper on both sides. The layer is provided with holes of 55 μm diameter and a 140 μm pitch. By applying an electrical potential between the copper layers a gas amplification of a factor 15-100 takes place in the holes.
The output of the ITR for the FLT was not used during the year 2000 data taking. Because of a feedback loop in the electronics that was discovered in 2000, the threshold settings were put on a higher level. This decreased the hit efficiency to a level that was not useful for the FLT. A summary of the ITR performance in 2000 can be found in [kra01].

Outer Tracker

The **O**uter **TR**acker (OTR) has an angular acceptance overlapping slightly with the inner tracker and extending to 250 mrad in the horizontal and 160 mrad in the vertical direction. In the magnet the outer tracker has three more superlayers than the inner tracker, see

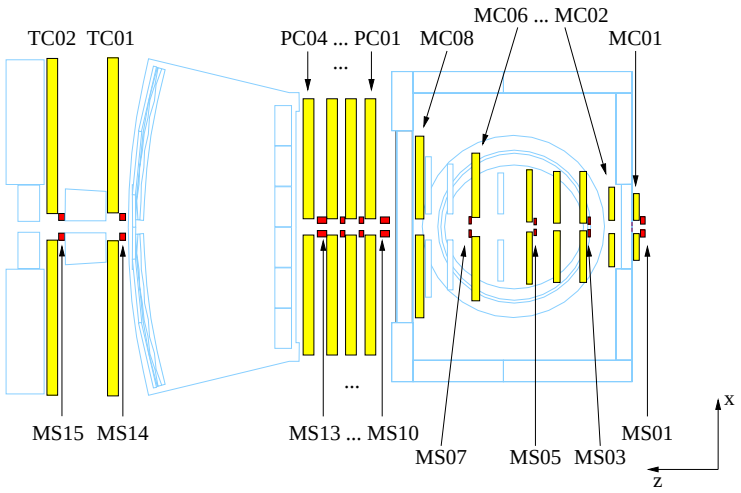

Fig. 1.13: Positions and nomenclature of the inner (MS01-MS15) and the outer (MC01-MC08, PC01-PC04, TC01, TC02) tracker superlayers.

Fig. 1.13. Behind the magnet the outer tracker has six superlayers at approximately the same z-positions as the inner tracker. The four layers in front of the RICH are labeled PC01-PC04 (**P**attern **C**hambers) and the two behind the RICH TC01 and TC02 (**T**rigger **C**hambers). The names refer to the first four being the main chambers for pattern recognition (i.e. track finding), while the last two are mainly used by the tracking of the first level trigger.

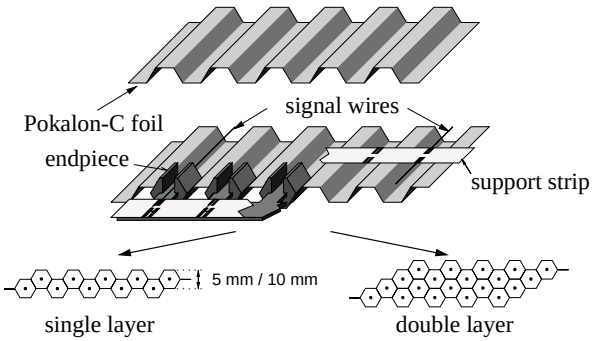

Fig. 1.14: The honeycomb structure of the outer tracker drift chambers [per98]. The upper part of the figure shows the composition of the honeycomb structure of folded Pokalon-C foils, the lower part the structure of the single and double layer.

Similar to the ITR, each superlayer in the OTR contains three different stereo layers with angles of 0° and ±5° with respect to the vertical axis. Due to the large size (up to $6 \cdot 4\,\mathrm{m}^2$ in TC02), the OTR is built from many modules. Chambers used by the first level trigger (PC01, PC04, TC01 and TC02) all have double layers to achieve a high hit efficiency, while the other chambers use singe layered modules, see Fig. 1.14.
The OTR layers are built from Honeycomb drift cells [ste00]. Fig. 1.14 shows the layout of both a single and double layered OTR module. A 25 μm gold-plated tungsten wire is used as anode wire in a honeycomb shaped drift cell. The drift cell, which serves as cathode, is made of 50 μm polycarbonate (Pokalon-C), coated on the inside by a thin gold layer.

The drift gas used is a mixture of $Ar/CF_4/CO_2$ which keeps the drift time below the time interval between two bunch crossings and minimizes aging effects. Due to the high flux of charged particles, aging was a major concern during the design of HERA-*B* and the OTR design had to be changed several times due to problems with aging. The cell size is 5 mm in modules closest to the beam pipe and 10 mm further away, which keeps the occupancy at 40 MHz interaction rate below 20%. In order to increase the spatial resolution, the drift time is measured. The drift time measures how far from the anode the charged particle has passed. This measurement involves an ambiguity whether the particle traversed the wire on the left or on the right side. From this, a hit resolution of about 215 μm is achieved for the 5 mm chambers [zim99]. The hit efficiencies in 2000 were between 90% and 95% [hul02]. This is well below the design value of 98% and was caused by noise in the readout, which forced a higher signal threshold to be used.

Another problem which occurred during the data taking in 2000 was the failure of high voltage groups at a rate of about one per five hours during which high voltage was applied. It was found that these failures were due to soldering faults involving two specific capacitors on the high voltage boards. This lead to a low overall tracking efficiency since the affected high voltage groups had to be switched off.

1.4.3 Particle Identification

Ring Imaging Cherenkov Detector

The **R**ing **I**maging **CH**erenkov detector (RICH) is used to identify charged kaons and protons. It exploits the Cherenkov effect: a charged particle traveling through a medium with a velocity higher than the velocity of light in the medium emits photons in a cone around the charged particle. The angle θ_C of the emitted photons with respect to the particle direction is given by

$$\cos\theta_C = \frac{1}{\beta n}$$

where n is the refraction index of the medium and β is the velocity of the particle divided by the speed of light in vacuum. By measuring the Cherenkov angle, the velocity can be determined and by comparing it to the measured momentum, the mass, and thus the particle type, can be identified.

The radiator medium is perfluorobutane gas (C_4F_{10}), leading to a Cherenkov angle of 51.5 mrad for particles of a velocity $\beta = 1$ [kri00]. The photons are reflected to multichannel photomultipliers by spherical and planar mirrors. In this way the cones of emitted photons are transformed to rings, see Fig. 1.15. The momentum threshold for Cherenkov light is 2.6 GeV for pions, 9.0 GeV for kaons and 17.2 GeV for protons. Pions and kaons can be separated up to momentum of about 60 GeV, protons up to 80 GeV and electrons up to 15 GeV.

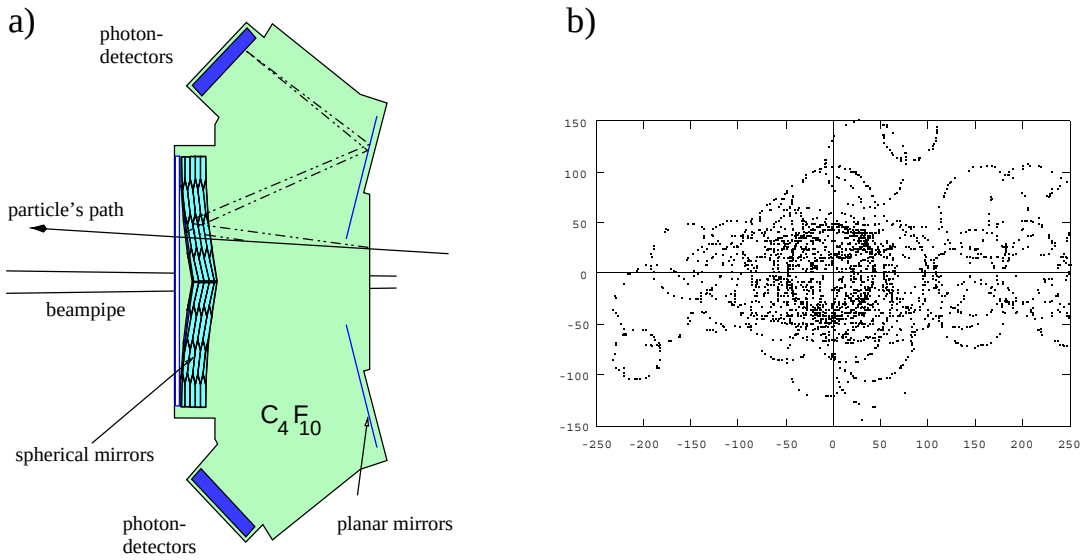

Fig. 1.15: Schematic overview of the RICH vessel a) and example of the observed RICH hits in an inelastic event b) [duj01].

Transition Radiation Detector

The **T**ransition **R**adiation **D**etector (TRD) is intended to complement the ECAL in the task of electron-hadron separation in the inner part of the detector. The TRD is built of interleaving radiator material with straw tubes. If a charged particle traverses media with different dielectricity constants it emits x-rays, the *transition radiation*. While in the RICH particles of different velocities β can be separated, the radiation emitted in the TRD scales with the Lorentz-factor $\gamma = \frac{E}{mc^2}$ and is therefore much more energetic for electrons.
In HERA-*B*, the TRD is placed between the OTR superlayers TC01 and TC02 and has 32 layers of radiator material and straws [sav98]. The radiator consists of polypropylene fibers with a 20 μm diameter and each layer has a thickness of 1.6 cm. The straws are made from thin multi-layered (Kapton and aluminum) cylindrical drift tubes with a diameter of 6 mm and are tilted by $\pm 30°$ relative to the horizontal axis. The gas used is 70% Xe, 20% CF_4 and 10% CO_2. The Xenon gas is used to detect the x-rays, while the other gases adjust the drift time so that a signal is collected within a single bunch crossing. The TRD gives a good electron-pion separation in the energy range from 1 to 100 GeV. During the running in the year 2000 the TRD was not used.

Electromagnetic Calorimeter

The **E**lectromagnetic **CAL**orimeter (ECAL) is used to identify electrons and photons by measuring the energy which is released in electromagnetic showers. Photons do not leave a track in the tracker such that the ECAL provides the only possibility for photon detection. For electrons the measured momentum p by the tracking system should match the

measured energy E. Within measurement uncertainties one expects $E/p \approx 1$. Moreover, the ECAL is responsible for providing the electron pretrigger signals that initiate the FLT algorithm.

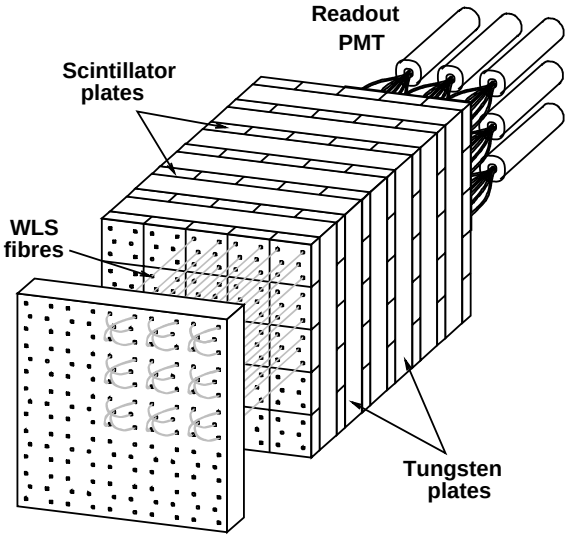

Fig. 1.16: The shashlik structure of the ECAL [loh94].

The ECAL is built as a sampling calorimeter with a *shashlik structure*, as shown in Fig. 1.16, where absorber plates are interleaved with plastic scintillator layers [zoc00]. Electrons and photons hitting the absorber produce bremsstrahlung photons and electron-positron pairs, respectively, and a shower of secondary electrons, positrons and photons develops. The number of particles in a shower is proportional to the total energy of the original electron or photon. The electron and positron are detected in the scintillator plates, whose light is collected by wavelength-shifting fibers inserted in the calorimeter parallel to the beam. The photons are measured in photomultipliers located behind the calorimeter.

The calorimeter is divided into modules with a front face of $11.2 \cdot 11.2\,\mathrm{cm}^2$. In total, it has 56 (in the horizontal direction) times 42 modules (in the vertical) resulting in the full acceptance of the inner and outer tracker. Like almost all HERA-B subdetectors, the ECAL addresses the variation in occupancy as a function of distance from the proton beam pipe by dividing the ECAL modules further into cells of varying size. In the most inner part (inner ECAL), a module consists of 25 cells, in the middle ECAL of four cells and in the outer ECAL a module is a single cell. The division is shown in Fig. 1.17. To keep the shower of an electron or photon confined laterally to a few cells, the inner ECAL uses a tungsten-alloy as absorber material which has a Molière radius of 1.42 cm, while the middle and outer ECAL use lead with a Molière radius of 4.15 cm, see [bru01].

Since a shower typically deposits energy in several neighboring cells the reconstruction combines cells with energy depositions into clusters, which are used as candidates for electrons and photons. In the inner ECAL, the expected energy resolution $\sigma(E)$ is given

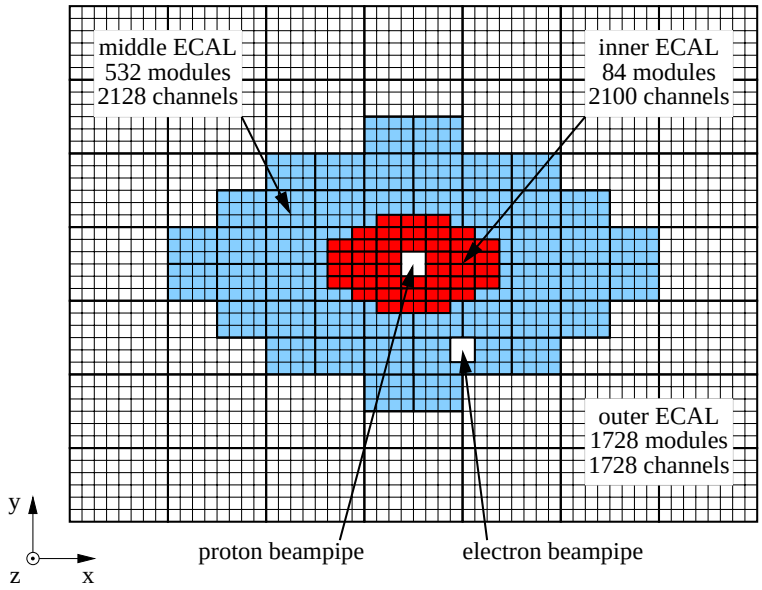

Fig. 1.17: The regions of different granularity of the ECAL [alb97].

by

$$\frac{\sigma(E)}{E} = \frac{17\%}{\sqrt{E/\mathrm{GeV}}} \oplus 1.6\%$$

while for the middle and the outer ECAL it is given by

$$\frac{\sigma(E)}{E} = \frac{9.5\%}{\sqrt{E/\mathrm{GeV}}} \oplus 1.0\%$$

During the 2000 run the energy resolution was significantly worse because of noise in the readout electronics.

Muon Detector

The **MU**on **D**etector (MUD) provides the information necessary for the reconstruction of muon tracks, as well as the muon pretrigger signals to the FLT. It consists of four tracking stations (MUD1-MUD4) behind the calorimeter that are separated from each other by one meter. In front of the first three stations there are thick absorber walls of concrete and iron as shown in Fig. 1.18. The absorber walls stop all hadrons and only muons with a momentum larger than 5 GeV are able to penetrate all walls and leave signals in all four tracking stations.
The inner part of the tracking stations (± 42 cm in x and ± 33 cm in y) is constructed from gas-pixel chambers [tit00]. The structure of such a chamber is illustrated in Fig. 1.19. A square cell of $9 \cdot 9\,\mathrm{mm}^2$ is formed by four potential wires and a sense wire in the middle. The wires are 3 cm long, oriented parallel to the proton-beam and surrounded by gas

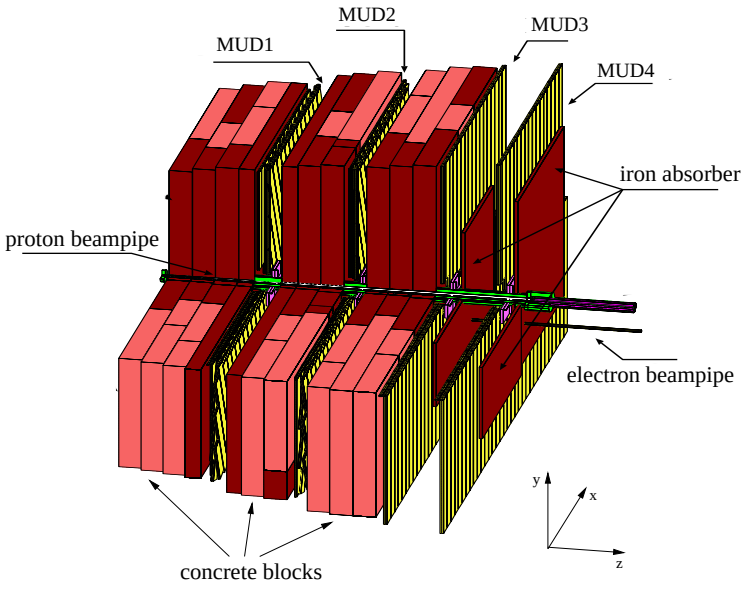

Fig. 1.18: The four tracking stations of the muon system and the concrete absorber separating them [tit00]. The last two stations are only separated by about 5 cm iron.

(80%Ar, 20%CF_4). A charged particle passing the cell ionizes the gas and the electrons drift to the anode wire and induce a signal. To limit the amount of readout channels the signals from $2 \cdot 2$ cells in MUD1 and MUD2 and $1 \cdot 4$ cells in MUD3 and MUD4 are combined together in the readout.
The outer part of the muon detector is made of proportional tube chambers. The tubes are 16 mm wide and in order to have high hit efficiency all layers are implemented as double layers with the second layer shifted by half a cell size with respect to the first as shown in Fig. 1.20. A digital hit readout is used. The tracking stations in MUD1 and MUD2 have three double layers with the tubes oriented at angles of 0° and ±20° with respect to the vertical axis. MUD3 and MUD4 only have a vertical oriented double layer, which is equipped with segmented cathodes (pads). The pads are $12 \cdot 10\,\mathrm{mm}^2$ large

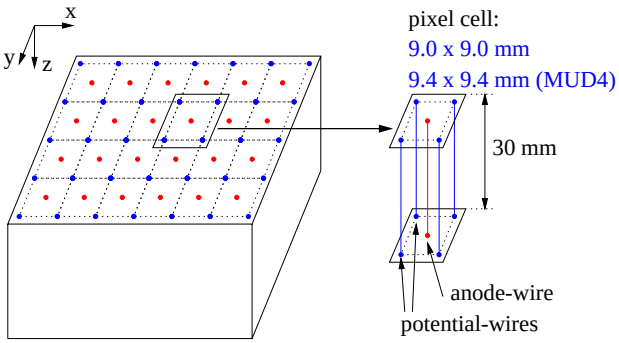

Fig. 1.19: Part of a pixel-chamber of the muon system. One pixel is built by four potential wires and a central signal wire acting as anode [ada02].

and provide the initial measurements of x and y coordinates of a muon-candidate for the trigger system. The signals from two pads in a double layer are combined into a single measurement.

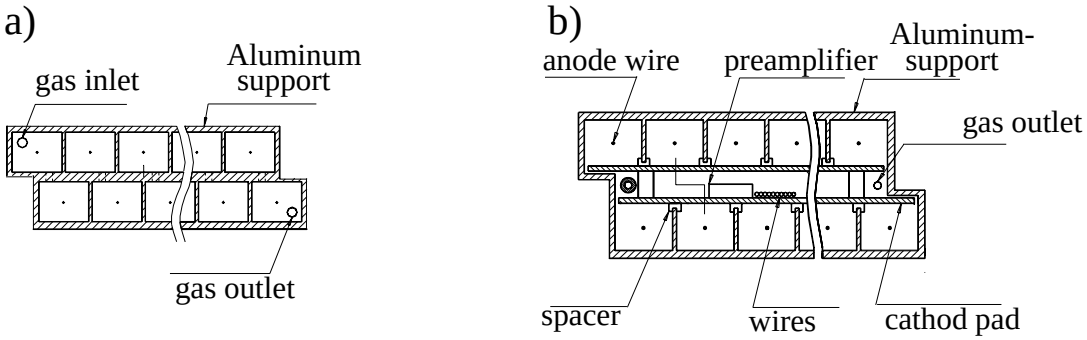

Fig. 1.20: a) Tube structure in a double layer of the muon system in superlayer MUD1 and MUD2 and b) the structure of a double layer tube and pad combination in superlayer MUD3 and MUD4 [loh94].

High-p_{T} chambers

To allow fast recognition of hadrons with high transverse momentum ($p_{\mathrm{T}} > 2.0\,\mathrm{GeV}$) in the trigger system, three special tracking chambers called high-p_{T} chambers are installed in the magnetic field. This permits studies of final states that do not include a dilepton pair, such as the decay $B^0 \to \pi^+\pi^-$.
The high-p_{T} chambers measure the position of charged tracks with a pad-type readout. The chambers have a projective segmentation, where the high p_{T} particles, which have almost straight trajectories in the magnet, leave a characteristic pattern in the three stations.
The inner part of the high-p_{T} chambers is constructed from chambers similar to the gas-pixel chambers in the muon detector. The outer part uses straw tubes which are positioned against printed circuits with a pad pattern, see [schwa99]. A signal in the straw tube induces an image charge on the pads, which can be read out. The straw tubes themselves are not read out. Due to commissioning studies they were not used by the FLT during the data taking of the year 2000.

1.5 Trigger System and Data Acquisition

In this section the trigger and data acquisition system of the HERA-B experiment are described. Since the trigger system has to be designed with respect to the intended physics goals, first the requirements on the trigger system are summarized.
The design of HERA-B was motivated by the aim to measure CP violation in the $B^0/\bar{B}^0$-system by exploiting the gold-plated decay $B^0/\bar{B}^0 \to J/\psi K^0_S$. To get enough precision

one has to collect about 1000 reconstructed gold-plated events within one year which would yield a precision of $\sigma(\sin(2\beta)) \approx 0.1$, see [loh94]. This number follows from the assumption of an effective beam time of 10^7 s and an average interaction rate of 40 MHz. In addition, one has to take into account the cross sections and branching ratios shown in Table 1.3. The tag efficiencies represent the probability for the correct determination of the flavor of the B-meson which decayed in the gold-plated channel, see Sect. 1.1.5.

$\sigma_{b\bar{b}}/\sigma_{\text{inelastic}}$	$\approx 10^{-6}$
$2 \cdot \text{probability}(b \to B^0)$	≈ 0.8
$\Gamma(B^0/\bar{B}^0 \to J/\psi K_S^0)$	$\approx 5 \cdot 10^{-4}$
$\Gamma(J/\psi \to l^+l^-)$	≈ 0.06
$\Gamma(K_S^0 \to \pi^+\pi^-)$	≈ 0.69
trigger and reconstruction efficiency	≈ 0.15
kaon tag efficiency	≈ 0.45 (incl. fakes)
lepton tag efficiency	≈ 0.15 (incl. fakes)

Table 1.3: Overview of the cross sections, branching ratios, and efficiencies which are used to calculate the amount of interactions which are necessary to obtain a significant measurement of $\sin 2\beta$. The numbers are taken from [loh94].

The demand on the data acquisition is defined on one hand by the bunch crossing rate of 10.4 MHz and on the other hand by the finely segmented detector with more than 500000 channels. The numbers of channels and bit-width per channel is given in Table 1.4. In total, 470 kByte of data are produced per bunch crossing which, at the 10.4 MHz bunch crossing rate, yields almost 5 TByte/s. Since no system which is currently available can read out and store that amount of data at that rate, the data has to be filtered.

subcomponent	channels		
	number	bitwidth	bandwidth per event
VDS	176000	8 bit	$\approx$ 172 kByte
ITR	135000	8 bit	$\approx$ 132 kByte
OTR	120000	8 bit	$\approx$ 117 kByte
High-p_T	8736	1 bit	$\approx$ 1 kByte
RICH	27520	1 bit	$\approx$ 3 kByte
TRD	16000	2 bit	$\approx$ 4 kByte
ECAL	5800	16 bit	$\approx$ 11 kByte
MUD	30814	1 bit	$\approx$ 4 kByte

Table 1.4: The number of channels and bitwidth per channel for each subdetector of HERA-B. The numbers are taken from [ress97]

In contrast to the huge amount of data that is produced by the detector, the rate of the interesting channels is comparatively low. Only about one out of $\mathcal{O}(10^6)$ inelastic events contains b-hadrons and just one out of $\mathcal{O}(10^4)$ such b-hadrons decays in the gold-plated decay. Other interesting b-hadron decays occur at the same or lower rates. The tiny ratio ($\mathcal{O}(10^{-10})$) of the signal event rate compared to the inelastic event rate has to be compensated by a high input rate in order to achieve the desired number of signal events. Moreover, the input data has to be filtered in order to reduce the input event frequency of 10.4 MHz to a value of about $20 - 50$ Hz which can be stored permanently. The filtering is performed in four sequential trigger levels since the necessary suppression can not be achieved by a single system. Therefore the suppression is factorized into four trigger levels. The trigger systems at each level work on a decreasing event rate and an increasing amount of data per event from one trigger level to the next.

1.5.1 Trigger Overview

The trigger system of HERA-B is designed for the selection of the gold-plated decay $B^0/\bar{B}^0 \to J/\psi K_S^0 \to l^+l^-\pi^+\pi^-$. While the the decay of the K_S^0 into pions does not provide a usable signature for a trigger in the hadronic background, the decay of the J/ψ meson into an electron or muon pair is well suited for that purpose. Because of the high mass of the J/ψ, the leptons of its decay have a high *transverse momentum*

$$p_{\mathrm{T}} = \sqrt{p_x^2 + p_y^2} \tag{1.15}$$

where p_x and p_y are the x- and y-component of the momentum, respectively. This allows a selection since the background contains leptons mainly of small transverse momenta. Moreover, the reconstruction of the invariant mass of the leptons makes it possible to select J/ψ decays.

After the selection of the J/ψ, the background of the gold-plated decay can be further reduced by exploiting the relatively long lifetime of b-mesons which is approximately $\tau \approx 1.5$ ps. With help of the Lorentz boost of HERA-B this leads to an average distance between the production and decay point of 1.1 cm for b-mesons. Thus, by reconstruction of the decay vertex it is possible to select b-mesons because almost all other particles are produced in the primary vertex at the target wires.

The HERA-B trigger system consists of four trigger levels. The design is illustrated in Fig. 1.21. The event data has to be read out at the bunch crossing frequency of 10.4 MHz. Since it is not possible to analyze the event data at this frequency it is necessary to store the event data during the evaluation by the trigger system. The time which is allocated to the different trigger levels is defined by the number of events which can be stored during the trigger decision. The usage of several trigger levels allows for the use of fast trigger systems which perform a rough trigger decision, making it possible to use more elaborate trigger systems afterwards, which perform at a slower rate.

The first level trigger uses a limited set of detector channels which allows both the fast transfer of the information from the detector to the trigger and a fast evaluation of the

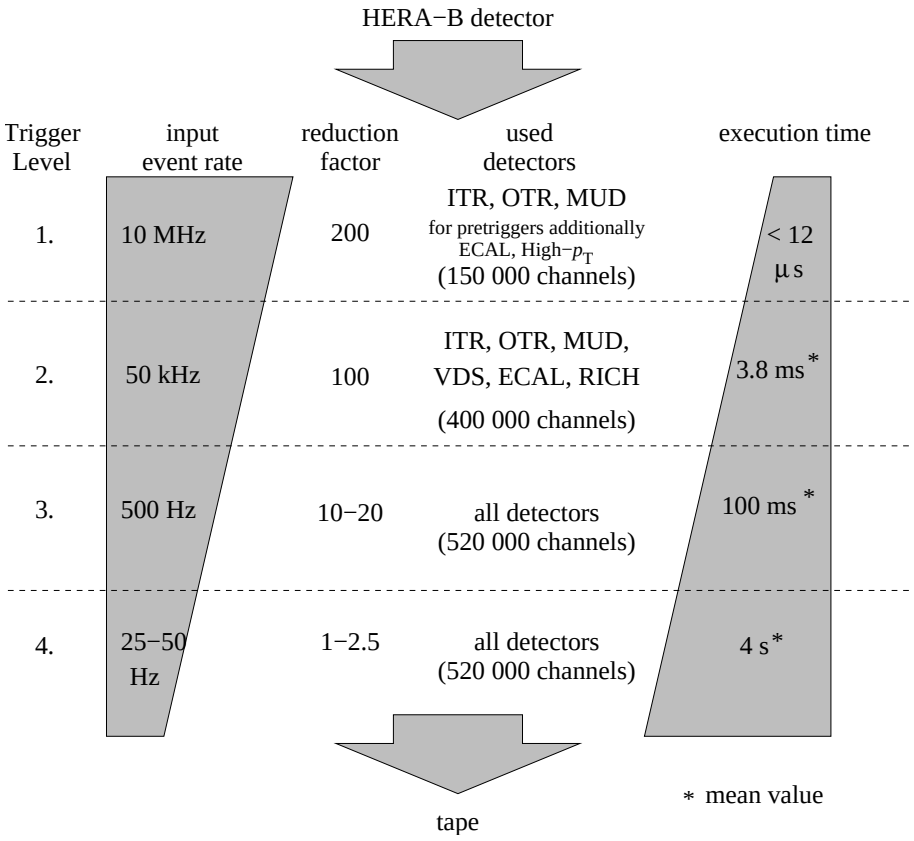

Fig. 1.21: The four trigger levels of HERA-*B* with the design values for events rates, suppression and latency [wag00].

data. The time allocated to the FLT trigger decision is 12.3 μs. This time interval is defined by the depth of the ring-buffers of the front end drivers, which allow for the storage of information of 128 consecutive events. After $128 \cdot 96\,\text{ns} = 12.3\,\mu\text{s}$, the information is overwritten by the data of new events, and so the FLT trigger decision has to come to its decision before that time. The FLT performs a track search in selected superlayers of the ITR, OTR, and muon detector using seeds that are generated by the *pretriggers*. The ECAL and muon systems are able to provide pretrigger signals. The tracks which are reconstructed by the FLT undergo a cut on the momentum and transverse momentum. Moreover, invariant masses of track pairs are calculated. This makes it possible to trigger on the decay of massive particles as, for example, that of the J/ψ. By design, the FLT reduces the input rate of 10.4 MHz by a factor of up to 200.

The **S**econd **L**evel **T**rigger (SLT) refines the tracks which are found by the FLT in order to suppress *ghost tracks*. Ghost tracks are reconstructed tracks which arise from hits in the detector which are not associated to a real track. Rather, hits of different tracks and noise hits are combined to a track by mistake. The tracks are projected through the magnetic field into the VDS. There the track search is continued in order to obtain the

vertices of the J/ψ decays that were found by the FLT. The cut on the distance of the decay vertex and the primary interaction region allows for the selection of J/ψ mesons which stem from the decay of B mesons. In this way, the SLT is able to select b meson decays. The SLT reduces the rate of the FLT further by a factor of 100.

Assuming the design suppression factors of the FLT and SLT, respectively, the input rate of the **T**hird **L**evel **T**rigger (TLT) is about 500 Hz [schwa00]. At this input rate it is possible to acquire the complete detector information and not — as it is done in the first two trigger levels — only the information of selected regions of dedicated subdetectors. The primary and secondary vertices are reconstructed on the TLT. The requirement of the existence of a detached secondary vertex reduces the event rate by an additional factor of 10. The TLT was not used during the data taking of the year 2000 that was mainly allocated to detector commissioning.

The **Fourth L**evel **T**rigger (4LT) is not primarily used for triggering, but for complete event reconstruction. This makes it possible to perform an immediate physics analysis and event classification. In this way, certain event classes can be selected in an offline analysis [her01]. The 4LT is designed to deliver an event rate of 20 Hz for permanent storage. Since network and storage technology have improved compared to the design, it is now possible to store events at a rate of up to 1 kHz.

Since this thesis deals with the performance of the FLT, which is described in Chapter 2, in the remainder of this chapter the SLT, TLT, and 4LT, as well as the data acquisition system, is discussed in more detail.

1.5.2 Second Level Trigger

The SLT consists of a farm of 240 diskless PCs which are called *SLT nodes*. 100 nodes run at a clock frequency of 300 MHz (Pentium II CPU) and 140 nodes run at 450 MHz (Pentium III CPU). Each node has 64 MBytes RAM and is based on a simplified version of the Linux operating system. One process exists on each node which carries out the processing of the events. This process is called the **S**econd **L**evel **P**rocess (SLP). The event data is stored in the **S**econd **L**evel **B**uffer (SLB) which is part of the data acquisition system, see below. The SLT nodes receive the event data from the SLB using a large switch. Each node is working on one event that has been assigned to it.

In order to be able to cope with the high input rate of up to 50 kHz the SLT is not able to take the information of the complete detector acceptance into consideration. It has to restrict the track search to a **R**egion **o**f **I**nterest (RoI). This is an area of the detector acceptance which is defined by track candidates. Based on the knowledge of the track candidates, the tracking algorithm can be restricted to these areas. This limits the data transfer from the SLB to the SLT nodes.

The SLT algorithm is split into several consecutive steps of increasing complexity. At each step only the data from the detector inside the RoIs under investigation are requested from the SLB. The consecutive steps which are applied on the found FLT tracks by the SLT algorithm are [slt02]:

- **Slicer**
  Performs a fast ghost removal by applying a discrete Hough transformation on the hits that are found in the RoI.

- **RefitX** and **RefitY**
  The track parameters in the xz- and yz-planes are refined using a simplified Kalman filter algorithm. Tracks with too few hits or too poor χ^2 are rejected.

- **L2Magnet**
  The RoIs are projected through the magnetic field based on a momentum estimation using the track slopes after the magnet. Moreover, hits are searched for in the MS01/MC01 superlayer of the ITR and OTR, respectively. The hits are used to refine the RoIs.

- **L2Sili**
  The RoIs are confirmed by VDS hits using a Kalman filter algorithm and refitted.

- **L2Vertex**
  A track pair is ensured to originate from the same target wire. Moreover a cut on the vertex position of the track pair is performed.

During the data taking of the year 2000 not all of these steps were used since the FLT was still in the commissioning phase and could not provide the tracks which are the basis of the original SLT algorithm. The pretrigger informations were forwarded by the FLT, and the SLT has emulated the FLT functionality.

1.5.3 Third Level Trigger

The third level trigger runs on the same nodes and in the same process as the SLT. In contrast to the SLT, the algorithm is not restricted to RoIs but requests the entire detector information from the SLB. In the design, the TLT has to perform a complete reconstruction of the event which allows for the application of a flexible suite of trigger scenarios [schwa00].
During the data taking in the year 2000, the suppression factor of the FLT and SLT was not large enough to allow for the execution of a complex TLT algorithm. The only purpose of the TLT algorithm was the *event building*. All detector information that is given for an event is collected by the SLT node that has come to a positive trigger decision. The complete data is then transferred to the 4LT.

1.5.4 Fourth Level Trigger

The 4LT consists of 100 PCs which contain two 500 MHz Pentium III CPUs and 256 MB RAM each. The event reconstruction software which is used on the 4LT nodes is identical to the software used in the offline analysis. It is based on the framework ARTE [art96]

which provides structured access to the full information of detector data as well as of the event reconstruction. The event reconstruction on the 4LT serves two purposes. First, the reconstruction allows an event classification. Moreover, the data quality can be based on a set of physics signals. Second, the event is written together with the information of the reconstruction to tape. This allows a quick offline analysis since the reconstructed event is directly available.
The 4LT farm offers in addition the possibility to repeat the event reconstruction at a later time. This gives the opportunity to use a refined detector calibration and alignment compared to the first reconstruction during the data taking.

1.5.5 Data Acquisition System

The **D**ata **A**c**Q**uisition system (DAQ) controls the data readout. It is closely interweaved with the trigger system, as shown in Fig. 1.22. The readout of the detectors is steered by the **F**ast **C**ontrol **S**ystem (FCS). The FCS makes sure that the readout is synchronized to the bunch crossing timing. The untriggered event rate at HERA-B is 10.4 MHz, such that every 96 ns the data of all subdetectors has to be stored. During the time which is allocated to the FLT trigger decision the data is stored in the buffers of the **F**ront **E**nd **D**rivers (FEDs). They are capable of storing the detector data of 128 consecutive events which makes up the maximal decision time of $128 \cdot 96\,\text{ns} = 12.3\,\mu\text{s}$ that the FLT must not exceed. As soon as the FCS receives the trigger signal from the FLT, it distributes the *trigger accept* signal to all FEDs, which then send the data to the SLBs.
Besides the storage of the detector data, the FEDs have the task of amplifying, shaping and digitizing the raw signals. The front end electronics in HERA-B is highly unified and only a few different readout chips are used.
The VDS and the ITR use the *HELIX chip* [bre94] for the readout. It handles 128 input channels and stores the event data using a pipeline of 141 capacitors for each channel. On a trigger accept from the FCS, the data is read out sequentially via an analog multiplexer and transmitted using an optical fiber to the electronics hut.
For the ECAL the signals of the photomultipliers are transmitted via coaxial cables into the electronics hut. There the signals are digitized and stored in dual ported memories which are read out in case of a FCS trigger accept.
The remaining subdetectors use the *ASD8 chip* for the readout [kol99]. The ASD8 chip provides preamplification, pulse shaping, and discrimination for eight channels. The signals which are prepared by the ASD8 chip are then transferred to the TDC boards. They contain a **T**ime-to-**D**igital **C**onverter (TDC) which translates the drift time information of the OTR into an 8 bit digital value. Except for the OTR, the other detectors use only the hit information. As in the ECAL readout, the data is stored in a dual ported memory during the FLT processing.
On an FCS trigger accept the detector data is sent from the FEDs to the SLB. The SLB is built of 140 **S**uper-**H**arvard-**AR**chitecture-**C**omputer (SHARC) modules, each with six digital signal processors of the type ADSP-21060 running at 40 MHz. Each module receives and stores the data from up to six FEDs until an SLT node has decided whether

to discard the corresponding event or not. Meanwhile, parts of the data are requested by the SLT in order to perform the trigger algorithm.
After a positive trigger decision of an SLT node, the entire event data is acquired from the SLB. The event data is collected and then sent to the 4LT using an Ethernet connection. The 4LT farm performs the event reconstruction and adds the corresponding data to the detector information. The complete data is then sent to the computing center using a gigabit Ethernet. In the computing center the data is buffered on the logging machine (in 2000 an SGI server). This has the advantage that the data can first be stored on a large hard disk before it is written to tape. Thus data taking is decoupled from the logging procedure.

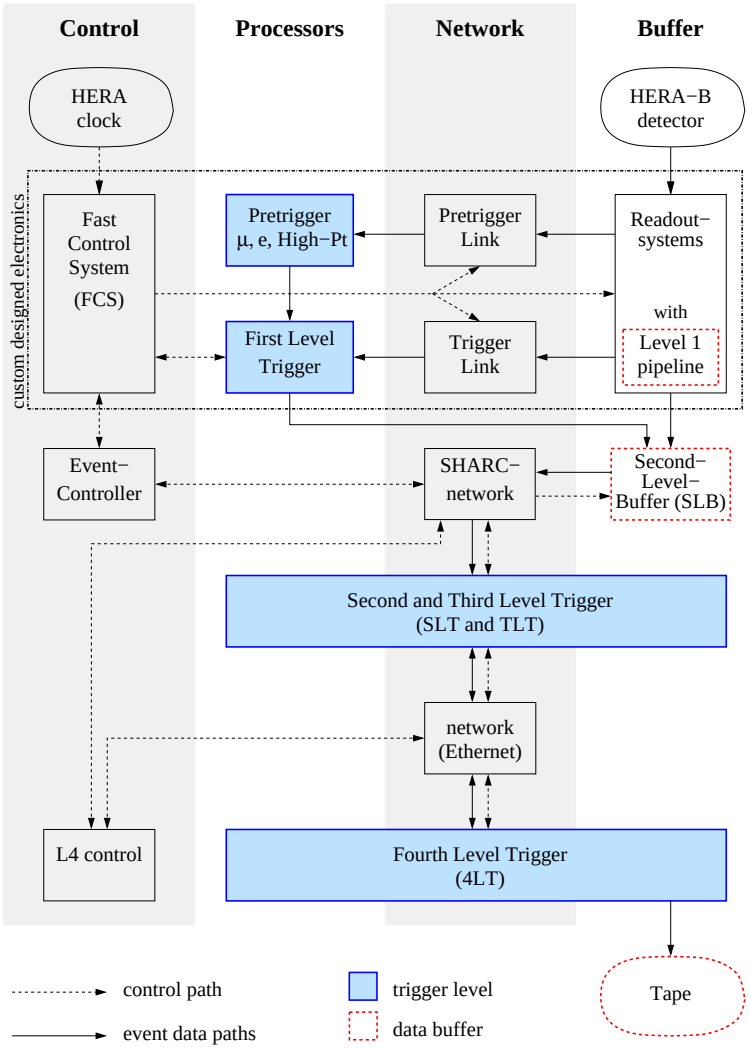

Fig. 1.22: Overview of the data and control paths in the HERA-*B* DAQ system [wag00].

Chapter 2

The First Level Trigger

In this chapter, we give an overview of the **F**irst **L**evel **T**rigger (FLT) hardware, algorithm and simulation. After considering the pretrigger system, we discuss the readout of the outer tracker and muon tube system, which was used by the FLT in the running of the year 2000, and the technique used for the transmission and preparation of the hit information. The inner tracker and the muon pixel system readout will not be mentioned here. After this description we introduce the FLT tracking algorithm and the three kinds of dedicated processor boards which carry out the algorithm in the hardware: the TFU, the TPU, and the TDU. The last section of this chapter deals with the FLT simulation and its embedding in HERA-B's common analysis framework, ARTE.

2.1 Tracking in the First Level Trigger

The FLT tracking algorithm is said to be inspired by the *Kalman Filter* technique. The Kalman Filter provides an efficient iterative way to perform a least-squares fit [kal60] on systems, which are described by time-discrete *state vectors*. In order to estimate the evolution of the system, two iterative steps are applied: based on the previous measurements the state and error estimates are predicted for the next measurement (*prediction step*); then the next measurement is incorporated for an improved estimation of the state of the system (*correction or filtering step*). For starting this iterative method, a first estimation of the system is needed (*seeding*).
The Kalman Filter has proven to be an effective tool in high energy physics. It allows for the implementation of tracking algorithms using a progressive least-square fitting in an iterative process, in contrast to a time-consuming global fit. Track finding and parameter fitting in, for example, consecutive detector planes go hand in hand [frü87].
The first level trigger of HERA-B uses an algorithm similar to the Kalman Filter technique. The FLT receives hit information from a subset of the tracking superlayers, namely PC01, PC04, TC01, and TC02 of the outer tracker, and from the muon tube chambers in the layers MUD1, MUD3, and MUD4. All these layers are situated after the magnet in the field-free region. Therefore, the tracks are straight lines.

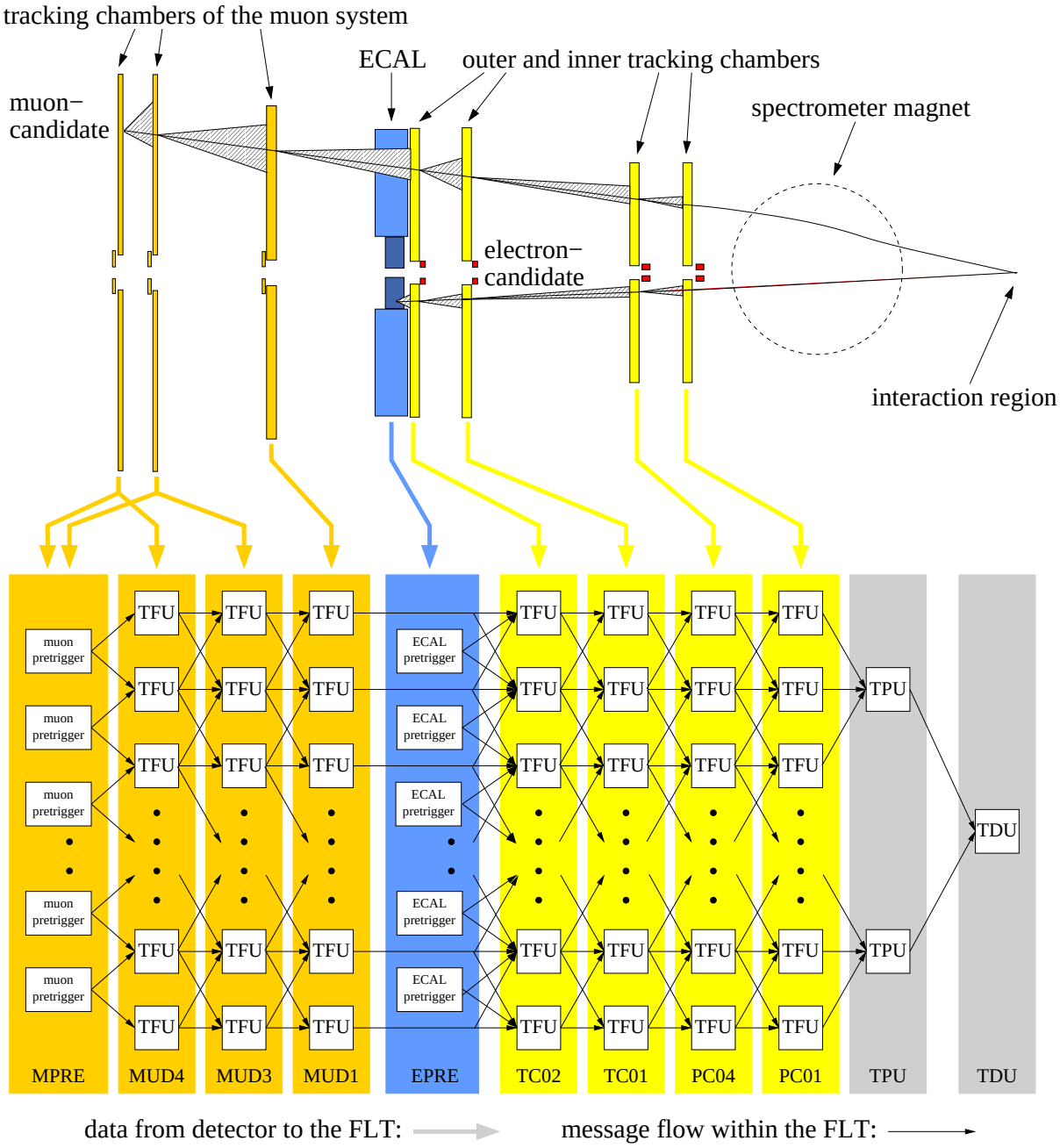

Fig. 2.1: Overview of the FLT network. The information flow within the network is twofold. On one hand, the hit data is sent via optical fibers from the TLB which are mounted next to the front end drivers of the tracking chambers to the TFUs which cover the corresponding region. On the other hand, the track candidates which are given by the FLT messages are sent from TFUs from one superlayer to the next and, finally, to the TPUs and the TDU. The high-p_{T} pretrigger is not shown in this figure.

The tracking algorithm starts from *track seeds*, corresponding to the seeding used in the Kalman Filter. Since the evaluation of all combinations possible of hit coincidences in the tracking devices is too time consuming, the FLT has to rely on external starting points for the track search. The pretriggers use information of the ECAL and the muon detector in order to provide electron and muon track candidates[1]. In this way, not only starting points for the tracking but also a particle identification is provided to the FLT. The track candidates are defined by *regions of interest* (RoIs). A region of interest is a geometrically defined part of the detector acceptance in which the track candidate is assumed to be, corresponding to the state vectors of the Kalman Filter algorithm.
Based on the RoIs, the hit information of the tracking chambers is used to search for hit coincidences in the next layer upstream towards the target (corresponding to the correction of filtering step of the Kalman Filter). By incorporation of the hit information, a new RoI is calculated and sent to the next tracking layer (the analog to the prediction step of the Kalman Filter algorithm). In this way, the RoIs of successive updates are similar, but gain in precision. Track candidates which are generated by noise hits are not updated at some point, since there are most likely not noise tracks in a straight line in all superlayers.
At the last superlayer in front of the magnet, the track candidates are known with an accuracy which allows the FLT to estimate their momentum using the hypothesis that the tracks have originated from an average target position at $(x, y, z) = (0, 0, 0)$. The knowledge of their momenta allows to perform kinematical cuts and to reject clones. *Clones* are several similar tracks which are associated to the same hits in the detector. They can be suppressed by exploiting the fact that they have similar kinematical parameters. Using the kinematical information of the tracks, it is possible to reconstruct invariant masses of all combined track pairs of one event. This allows the FLT to trigger on decays of massive mother particles as, for example, the J/ψ.
One can obtain the necessary computing speed for a system such as the HERA-B FLT only by using hardware specifically designed for this purpose. In particular, the large amount of input data (about 1 TB/s) cannot be handled during the required 12 μs allocated to the FLT to take the trigger decision. Therefore, the FLT is built as a network of three kinds of custom-designed processor boards, as shown in Fig. 2.1. The **T**rack **F**inding **U**nits (TFU) combine the hit data with the messages which represent the track candidates and perform the track reconstruction. In total, about 80 TFUs are used in the FLT network. Each of them handles a specifically assigned part of the tracking system. The **T**rack **P**arameter **U**nits (TPU) calculate the momenta of the found tracks and are able to reject tracks based on kinematical cuts and on comparison of tracks of one event (for clone removal). The last step is carried out on the **T**rigger **D**ecision **U**nit (TDU) which can base the trigger decision on simple counting of tracks or on the calculation of the invariant masses of all possible track pairs of each event.
In case of a positive trigger decision, the TDU notifies the fast control system, which

[1] Moreover, pretriggers which provide track candidates based on high-p_T hadron tracks (using the high-p_T chambers) and candidates based on high-energetic photon clusters in the ECAL are planned. Since they were not used during the data taking of the year 2000, they are not discussed in the following.

then initiates the read out of the entire system to the second level buffer as described in Sect. 1.5. After this procedure, the event is passed to the second level trigger.
In the following, the FLT trigger algorithm is described in more detail.

2.2 Pretriggers

The tracking algorithm of the FLT is based on track seeds. Rather than combining hits of the tracking devices, which would be by far too time consuming on the level of the first level trigger, external sources — the pretriggers — provide starting points for the track search. Either clusters in the ECAL or hit coincidences in the muon pad system are used to form a track seed. They define the region of interest in the first superlayers where the search of a track is to be performed, TC02 in the case of the ECAL and MUD4 in the case of the muon pretrigger. The high-p_{T} and hard photon trigger are not discussed here since they were not used during the data taking of the year 2000.
In this section, a short survey of the pretriggers is given.

2.2.1 The ECAL Pretrigger

The ECAL pretrigger bases its track seeds for the FLT on high energetic clusters in the calorimeter. For each cell in the calorimeter, an individual energy threshold $E_{\mathrm{thres}}^{\mathrm{cell}}$ can be set and, if the energy in a cell exceeds that threshold a cluster search around that cell is started. The energy in the surrounding eight cells is added to the energy of the central cell and, if the total energy exceeds a second threshold $E_{\mathrm{thres}}^{\mathrm{cluster}}$ a pretrigger seed is generated and sent to the FLT. This method is called the *nonett-scheme*.
To avoid generating several seeds for the same physical cluster, the energy in the central cell is required to be the largest of the cluster. For the year 2000 running a slightly different configuration was used, which only considers the cells in a cross around the central cell. This alternative algorithm is called the *cross-scheme*, see Fig. 2.2.
Both thresholds for the pretrigger cells are position dependent and can be set individually for each cell. By default, the pretrigger uses $E_{\mathrm{thres}}^{\mathrm{cell}} = 0.5 \cdot E_{\mathrm{thres}}^{\mathrm{cluster}}$. The threshold reflects the transverse momentum of the electron generating the cluster. This is complicated by the magnetic field in front of the calorimeter, which bends the electron trajectory either outward or inward in x depending on the charge. The simplest approach is to ignore the magnetic field and use the *transverse energy* instead,

$$E_{\mathrm{T}} = E_{\mathrm{cluster}} \frac{\sqrt{x^2 + y^2}}{\sqrt{x^2 + y^2 + z^2}} \tag{2.1}$$

where E_{cluster} is the cluster energy and x, y and z are the coordinates of the cluster in the calorimeter. A cut on the transverse momentum $E_{\mathrm{T}}^{\mathrm{cut}}$ can then be achieved by setting the threshold to

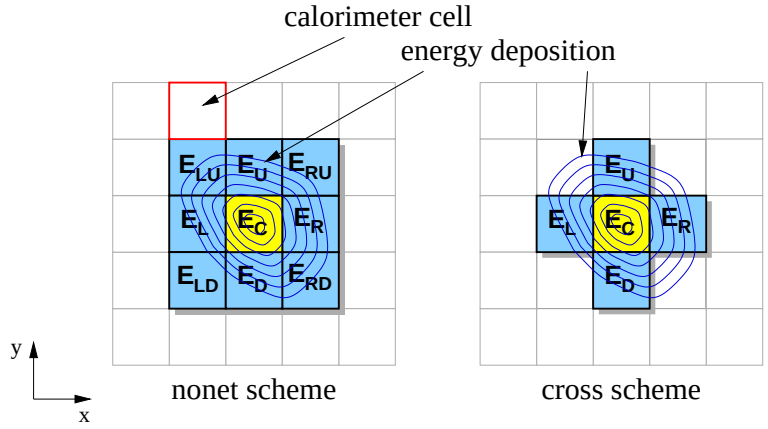

Fig. 2.2: Two two cluster types possible in the ECAL pretrigger. The central cell has to have to largest energy deposition. Figure based on [fla01c].

$$E_{\text{thres}}^{\text{cluster}} = E_{\text{T}}^{\text{cut}} \frac{\sqrt{x^2+y^2+z^2}}{\sqrt{x^2+y^2}} \tag{2.2}$$

This definition favors electrons which are bent away from the center of the detector as their E_{T} will be overestimated. Empirically, a better definition of the threshold was found to be

$$E_{\text{thres}} = K_{\text{trig}} \left(\frac{1}{\sqrt{x^2+y^2}} + \frac{1}{\sqrt{x^2+|y|^3}} \right) \tag{2.3}$$

where the design proposed a value of $K_{\text{trig}} = 700\,\text{GeV} \cdot \text{cm}$ [loh94]. In the data taking of the year 2000 only the E_{T} threshold has been used.
An extra feature of the ECAL pretrigger is its ability to recover bremsstrahlung. This makes it possible to correct for the energy which electrons emit while traveling through matter. When electrons pass through material, they emit bremsstrahlung photons in approximately the same direction as the electrons are traveling. These photons are not affected by the magnetic field and if they are emitted before the magnetic field, they will be visible as a cluster with the same y-position as the electron cluster but separated in x. The separation depends on the momentum of the electron as it passes through the magnetic field and, therefore, on the measured electron cluster energy. The pretrigger is able to search for such bremsstrahlung clusters. If a bremsstrahlung cluster is found for a pretrigger seed, its energy is forwarded together with the track seed to the FLT. The FLT uses this to correct its estimate of the electron momentum in front of the magnet and, therefore, increases the value of p_{T} and the invariant mass of possible electron pairs. As the spectrometer contains a significant amount of material, this correction is important to achieve good trigger efficiency for electrons, depending of the p_{T} thresholds used in the FLT. However, the bremsstrahlung recovery was not used during the data taking of the year 2000.

2.2.2 The Muon Pretrigger

The muon pretrigger uses the hit information from the MUD3 and MUD4 superlayers at the very end of the spectrometer, see Fig. 1.18. Essentially, only muons with momentum larger than 5.0 GeV are able to penetrate the thick absorbers in front of these two layers. The outer part of the layers MUD3 and MUD4 contains pads of $12 \cdot 10\,\mathrm{cm}^2$ size which are used by the muon pretrigger. In the inner part, the pixel readout is combined into pseudo pads consisting of $6 \cdot 4$ pixel cells. If any of the pixels in a pseudo pad receives a hit, the pseudo pad signals a hit.

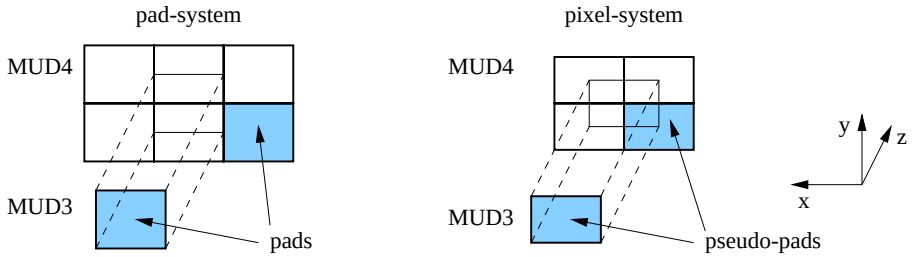

Fig. 2.3: Coincidence schemes for the muon pretrigger in the pad and pixel system. In the pad system, coincidences of one pad in MUD3 with six pads in MUD4 are taken into consideration. In the pixel system, one pseudo-pad in MUD3 is able to coincide with four pseudo pads of MUD4. Figure based on [böck01].

A muon track seed is defined as a hit coincidence between pads in two muon chambers which are placed behind the absorber planes and are separated by 1 m from each other. The coincidence is searched between every single pad in the layer MUD3 and six or four pads or pseudo pads in the outer and inner part, respectively, of the layer MUD4. The possible pad and pseudo pad coincidences are shown in Fig. 2.3. During the data taking of 2000, only pad coincidences in the outer part were used by the muon pretrigger.

2.3 Readout and Transmission of Hit Information

This section describes the basics of the detector readout of the tracking devices which were used by the FLT during the running of 2000. Here, we focus only on the description of the outer tracker and the muon tube system readout, as the inner tracker and the muon pixel system were not used in that running period.
Additionally, we discuss the rearrangement of hit data (the mapping), which is especially elaborate in the outer tracker case, and the transmission of the hit information via optical links.

2.3.1 Outer Tracker Readout

The design of the outer tracker detector has been described in Sect. 1.4.2. In this section, the readout of the outer tracker drift cells is discussed.

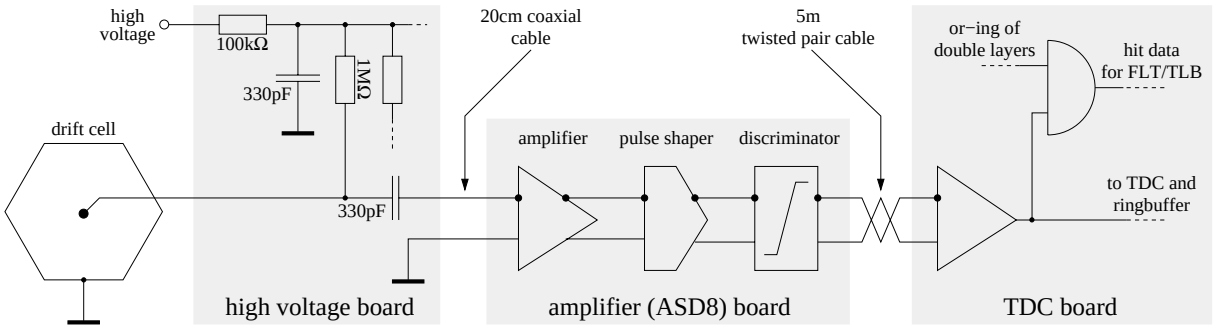

Fig. 2.4: Outer tracker readout. The high voltage boards are mechanically connected to the drift cells and both deliver the high voltage and pick up the signals. They are transfered via coaxial cables to the amplifier boards and, after this, sent using twisted pair cable to the TDC boards, which provide the hit output for the trigger link boards of the FLT. Figure based on [zim99] and [hul02].

The high voltage supply and the read out of signals from each wire of the outer tracker modules is performed using three types of electronic boards: the high voltage board, the amplifier (ASD8) board, and the TDC board, as shown in Fig. 2.4.
The high voltage board is placed on the base-plate of the module and is connected via coaxial cables to the amplifier board. Each amplifier board has two ASD8-chips. Each chip amplifies, shapes, and discriminates the signals of eight channels. Therefore, the amplifier boards are also called ASD8-boards, see Fig. 2.4. The differential signal is connected via twisted pair cables of about 5 m length to the TDC boards. It contains 8 bit **T**ime-to-**D**igital-**C**onverters (TDCs) for measuring the drift time and pipelined memories for 128 consecutive events which allows for the storage of information of about 12.3 μs of data taking. This corresponds to the maximal time allocated to the FLT to take a decision. Each TDC board is able to handle 128 input channels.
In order to optimize the hit efficiency, the outer tracker layers which are used for the FLT tracking are realized as double layers, as can be seen in Fig. 1.14. As we will see below, the FLT tracking algorithm requires a hit in each superlayer and in each stereo view, adding up to twelve hits in total. Assuming the outer tracker cell efficiency to be $\epsilon_{\text{single cell}} = 98.0\%$, the upper limit of the FLT tracking efficiency $\epsilon_{\text{FLT, OTR}}$ in the OTR is

$$\epsilon_{\text{FLT, OTR}} = \epsilon_{\text{single cell}}^{12} = 78.5\% \tag{2.4}$$

The usage of double layers reduces this efficiency loss by combining the hit information of the two double layers using a logical or-operation. This operation is carried out on the TDC boards, see Fig. 2.4. In this way, the effective cell efficiency is increased to

$$\epsilon_{\text{double cell}} = 1 - (1 - \epsilon_{\text{single cell}})^2 \tag{2.5}$$

This enhances the upper limit of the FLT tracking efficiency due to the cell efficiency to

$$\epsilon_{\mathrm{FLT,\,OTR}} = \epsilon^{12}_{\mathrm{double\,cell}} = (1-(1-\epsilon_{\mathrm{single\,cell}})^2)^{12} = 99.5\% \tag{2.6}$$

Please note that this is just a rough estimation. The dependence of the tracking efficiency on the hit efficiency of the cells will be discussed in Sect. 5.4 in more detail.

2.3.2 Muon Tube System Readout

In addition to the general description of the muon system in Sect. 1.4.3, we take a look at the readout electronics of the muon tube system which is used in the FLT tracking.
The readout electronics for the muon tube system — as well as for the pad system — are placed directly at the anode wire feedthroughs of the chambers. Each anode wire is connected to a *tube card*. The tube card contains the high voltage distribution and the ASD8-chips which are used for amplification, shaping, and discrimination of the signal, as shown in Fig. 2.5. Each tube card serves 32 wires.

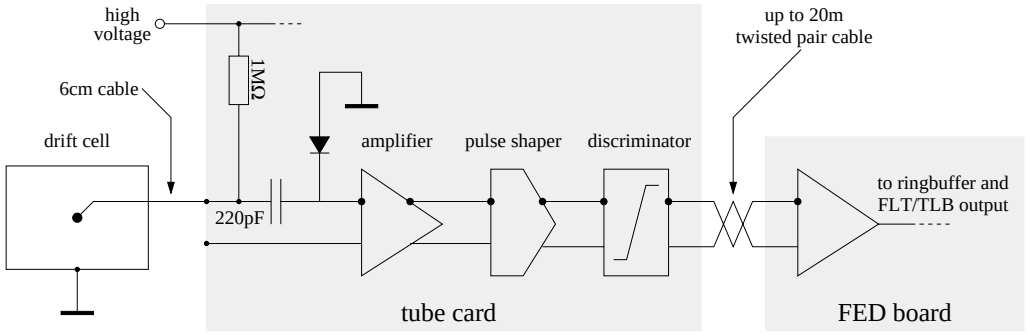

Fig. 2.5: Muon tube system readout. In contrast to the OTR readout the high voltage and the amplification, pulse shaping and discrimination of the signals are done on the same printed circuit boards, the tube cards. Figure based on [buc99].

The ASD8 output is transferred via a twisted pair cable up to 20 m long to the front end driver (FED) which uses a ring buffer for storing the hit information until the FCS requests it to be sent to the SLBs. The hit information is also transferred to the trigger link boards to make the data available for the FLT.
An or-ing of double layers as performed in the outer tracker is not provided for the muon tube chambers. The double layer structure in the muon tube system is necessary because of the noticeable gap of adjacent cells. The gaps are due to the separating wall between neighboring rectangular cells, see Fig. 1.18. In order to optimize the efficiency in case of particles traversing just through that wall, a second layer is situated behind the first layer, shifted by half of the cell size. The hit information of the double layer is mapped into the FLT processors, such that each wire of the double layer is treated separately. Although not or-ed, the overlap of the cells of the two layers results in enhanced efficiency, since most of the particles traverse two cells of the double layer.

2.3.3 Trigger Link Boards

The hit information of the outer tracker and of the muon tube system are sent to the **T**rigger **L**ink **B**oards (TLBs), which rearrange the hit data and forward it to the FLT processor network using optical fibers. Moreover, the TLBs provide a time stamp to the hit data by associating the bunch crossing (BX) number, as distributed by the fast control system.

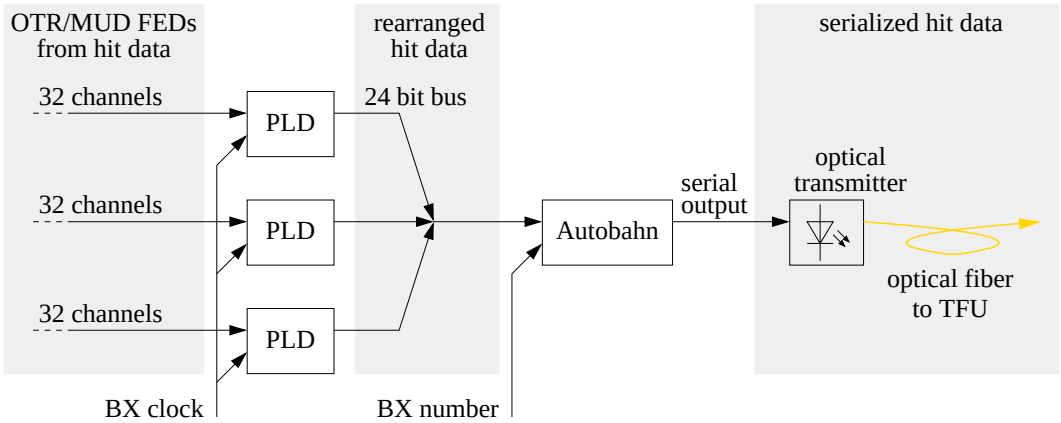

Fig. 2.6: Overview of the functionality of a trigger link board (TLB). The figure shows the data path from three input connectors of 32 bit each to one optical transmitter. One TLB contains eight such devices. Figure based on [bru02].

The setup of a trigger link board is depicted in Fig. 2.6. A TLB has 24 inputs each carrying 32 bits of hit information from the front end drivers of the outer tracker or the muon tube system. Three inputs are treated together and belong to one optical link. The 32 channels of one input are fed into one **P**rogrammable **L**ogic **D**evice (PLD). Any required logical operation can be programmed in a PLD such that the 32 input channels are read in synchronously with the BX clock and mapped to an intermediate data format of 24 bit. This mapping comprises, in particular, the or-ing of channels and the distribution of one input to several output channels, as will be discussed in the upcoming Sect. 2.3.6.
The outputs of three PLDs which belong together are combined and two times 24 bits of information are given to the Autobahn chip in every bunch crossing. The Autobahn Spanceiver, which was built by Motorola[2], is able to serialize or deserialize a data stream of $32s$ bit reaching a maximum effective transfer rate of 900 Mbit/s [bru98]. The two times 24 bits of hit data are joined with the bunch crossing number adding up to two times 32 bits per bunch crossing and are serialized and transfered to the optical transmitter.
It is possible to reprogram the TLBs in the crate where they are installed. The link boards may have to be reprogrammed to fix errors in the mapping or to mask non-working channels for efficiency optimization.
There are 105 TLBs designated for the outer and inner tracker and 51 TLBs for the muon

[2]The production of that chip has been discontinued.

tube and pixel system. A more detailed description of the trigger link boards is given in [bru98].

2.3.4 Optical Data Transmission

The hit information which is rearranged by the trigger link boards is sent to the TFUs by use of optical fibers. After the serialization of the hit data by the Autobahn chips, the data is fed into optical transmitters which are directly mounted on the TLBs. About 2500 optical fibers carry the signal over a distance of $\sim$50 m to the TFUs in the electronics hut. In the TFUs, the optical signals are converted back to electrical signals and are parallelized back again by an Autobahn chip.
The data is stored according to the bunch crossing number in the wire memories of the TFUs, see Fig. 2.7. The purpose of the wire memories will be discussed later in Sect. 2.3.5.

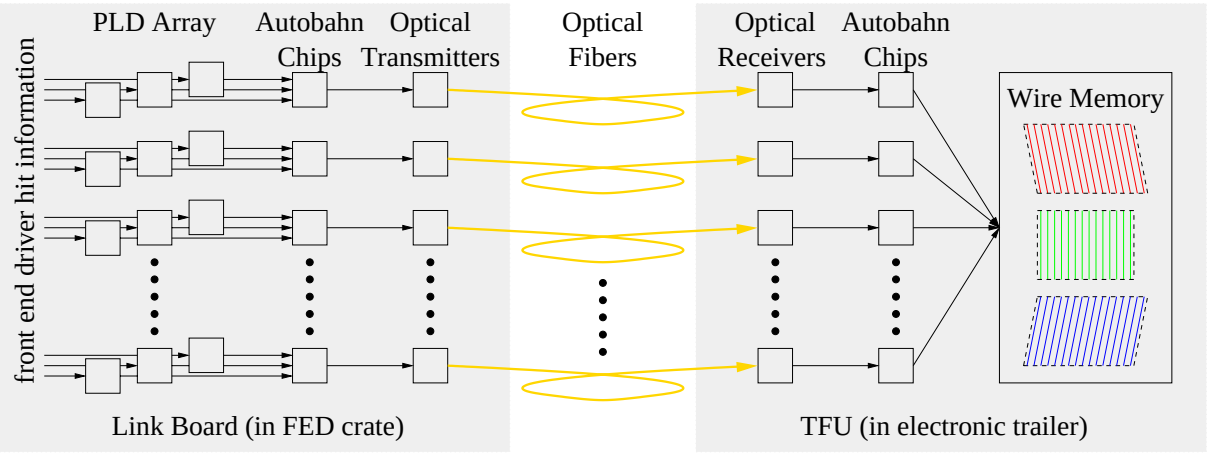

Fig. 2.7: Optical transmission of hit information. After the rearrangement of the hit information using PLD arrays the data is serialized and sent via optical links to the TFUs. There the hit information is deserialized and fed into the wire memories.

The serial data is sent in packages of two 32 bit words which contain, besides 48 bit hit information, twice the 8 bit bunch crossing (BX) number. The redundant transmission of the BX number allows for the estimation of an upper limit on the bit error rate by comparing two successive bunch crossing identifiers which should be identical by definition of the protocol. A deviation in the two values increments the error counter associated to the link. This makes it possible to monitor the link reliability.
The optical receivers digitize the incoming light signals by generating a positive signal as soon as the light exceeds an adjustable threshold. The link performance depends strongly on the chosen threshold of the receiver, and a stable operation depends on a proper adjustment. A dedicated setup procedure varies the threshold of each receiver and monitors simultaneously the error rate. The range of the threshold, the *offset range*, for which the measured error rate is within an acceptable level is used to judge whether the link in question works reasonably. If the offset range is too small, the link is not used and

the corresponding 48 wire memory channels are set to one in order to keep the efficiency at a high level.[3] The links which were switched off are stored, for each run, in the FLT database in order to be able to treat the corresponding channels in the simulation in the same way as during the data taking (see Fig. 2.21). In the following, we call this the *link masking*.

2.3.5 Wire Memory and TFU Geometry

Inside the TFUs, which carry out the tracking algorithm and which will be described in more detail in Sect. 2.4.3, the hit information is stored in the **Wi**re **M**emories (WiMs). The deserialized hit information provided by the optical receiver is stored according to the bunch crossing number in the WiMs. The WiMs are actually dual-ported memories which allow for concurrent writing and reading of the memory cells. In this way, the hit information of 128 events can be stored.

On one side, the hit patterns which are sent through the optical fibers together with the corresponding bunch crossing number are written into the memory. On the other side, the process logic of the TFU requests hit information for events specified by the BX number in order to search for hits during the track finding algorithm.

Each bit in the wire memory is associated to one or more detector cells. In order not to mix up the wires of the detector and the memory cells of the WiMs, we call the bits in the wire memories *wire memory channels* rather than wires in the following.

The wire memory channels represent an idealized view of the detector consisting of consecutive and equidistant cells. This idealization is needed by the FLT tracking algorithm. Although the wire memory channels represent the wires in the real detector, the mapping of the detector cells on the channels of the wire memories is non-trivial, as we will see in Sect. 2.3.6.

The wire memory channels of a given TFU are assigned to a rectangular area. Each wire memory consists of 384 channels in each of the three stereo views: minus (−), zero (0) and plus (+). Due to mapping issues in general, not all of these 384 channels are used. Therefore there are *hard coded zero* (hc0) channels at the beginning and the end of the 384 channels which are not set by the TLBs. In the geometry description of the TFUs this is taken into account by the variables *Nzero*, which denotes the number of leading hard coded zero channels and *Nx*, which denotes the number of channels before the closing hard coded zero channels, see Fig. 2.8.

[3] This was done during the data taking in 2000, which is regarded here. For the future, it is intended not to change this kind of masking so often because it entails an unstable behavior of the system, which makes the analysis needlessly difficult.
Moreover from the 2002 data taking period onward, it is possible to adjust the light output of the optical transmitters remotely, which enhances the availability of the system.

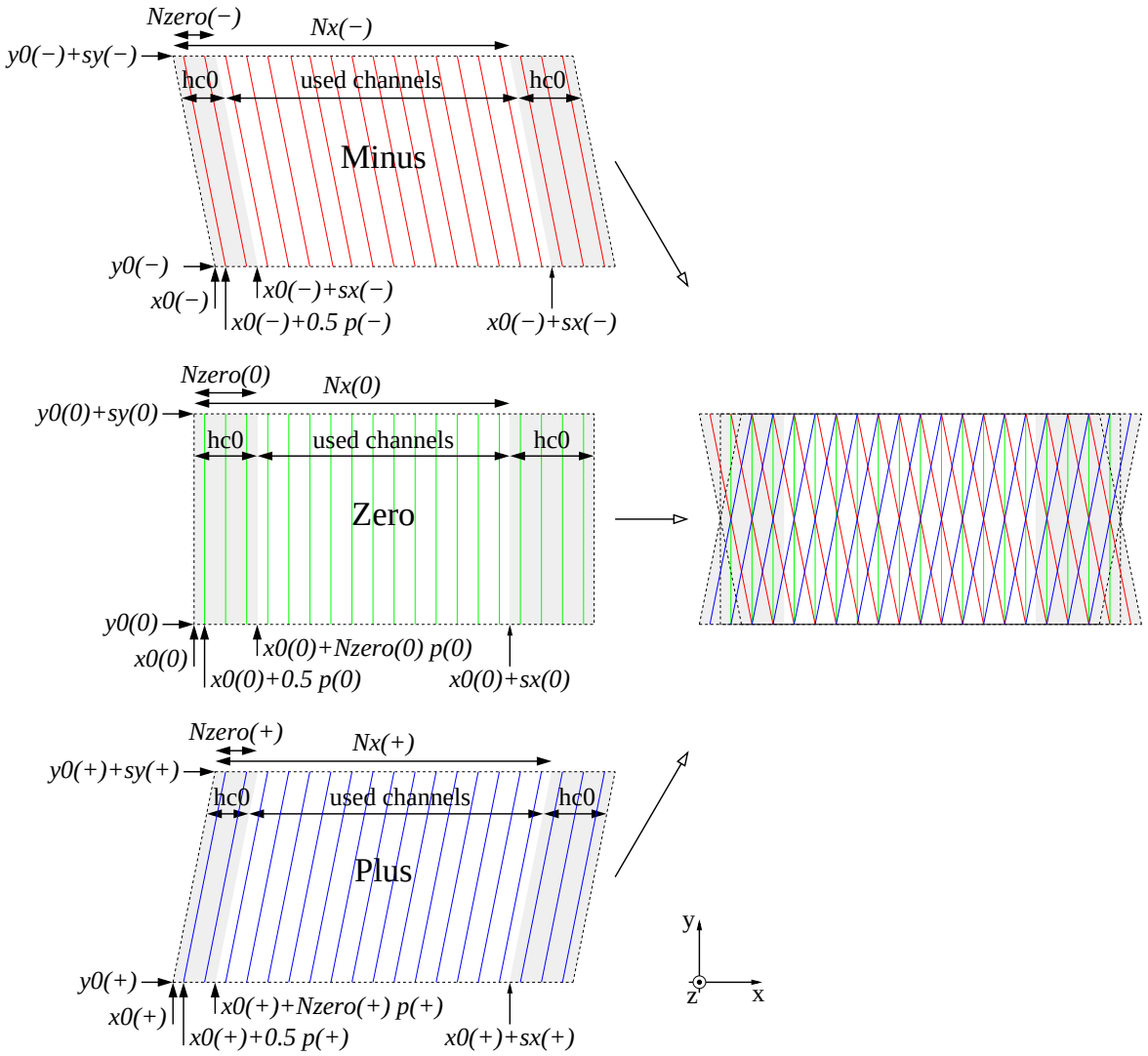

Fig. 2.8: Wire memory- or TFU-Geometry. The figure illustrates the meaning of the parameters $x0$, $y0$, sx and sy which denote the area which is virtually covered by the corresponding wire memory. Nx specifies the number of wires which correspond to the extension in the x-direction sx. Thus $p = sx/Nx$ is the pitch of the logical channels. $Nzero$ is the number of not-used channels at the beginning of the wire memory which are hard coded zero, like the channels following the channel of number Nx. Please note the all the variables depend on the stereo view $-$, 0, or $+$.

The geometry of the parallelograms which are assigned to each wire memory of each of the three stereo views is defined by the lower left corner $(x0, y0)$, the width sx and the height sy, see Fig. 2.8. Due to the stereo angle α, the upper left corner is shifted with respect to the lower left corner by $\tan(\alpha) \cdot sy$. By convention, the sign of the angle is just opposite to the notation of the stereo view:

stereo view		α
minus	$(-)$	$+5°$
zero	(0)	$0°$
plus	$(+)$	$-5°$

The pitch p, which is the virtual distance of two neighboring channels of a WiM, is given by the ratio of the width sx and the number of channels Nx:

$$p = \frac{sx}{Nx} \tag{2.7}$$

Because of the rotation of the virtual channels in the minus and plus stereo view, the pitch, as seen in the x-direction, is enlarged with respect to the pitch in the zero stereo view by the factor $1/\cos(\alpha)$. The left edge of the first wire has the x-position of $x0$, while the center of the first wire lies at $x0 + p/2$. The width of the area of hard coded zero channels at the beginning of the WiM is $Nzero \cdot p$. Taking everything together, the nominal x-position x of the logical cell of the 'wire memory detector', corresponding to channel n at the y-position y, is given by

$$x = x0 + \left(\frac{1}{2} + n\right)\frac{sx}{Nx} + \tan(\alpha)(y - sy) \tag{2.8}$$

Please note that all the values which specify the geometry are dependent upon on the stereo view.

Nominal and Aligned Geometry

In the analysis presented in this thesis two versions of the FLT geometry, nominal and aligned, are used.
The *nominal FLT geometry* is produced assuming that the chambers of the OTR and the muon tube system are situated at their nominal positions. This version of the geometry is used for running the FLT simulation in Monte Carlo studies.
The *aligned FLT geometry* takes the alignment constants of the OTR and muon chambers into account. The OTR alignment and corresponding aligned FLT geometry which is used in this thesis is based on the data taking of the year 2000. The way this is done is described in Sect. 5.3. The aligned geometry is used for the production of the lookup tables which were loaded to the TFUs since 29.6.2000 for the outer tracker, and since 18.8.2000 for the muon tube system, both until the end of the data taking of the year 2000. This geometry has to be used for the FLT simulation on real data of the corresponding run period.

2.3.6 The Mapping

The trigger link boards perform the mapping of physical wires in the tracking chambers to the logical channels of the wire memories of the TFUs, see Fig. 2.6. This is necessary since

the TFUs are designed to work on a rectangular area containing consecutive equidistant channels, while the detector setup is in general more complicated. The wires in the detector are grouped in non rectangular sectors including gaps (e.g., between the left and the right half of the detector) and different wire spacings (e.g., between 5 and 10 mm cells in the OTR). The mapping of the OTR is described in more detail in [neg00]. We cite some of the constraints which have to be taken into account:

- In order to increase the hit efficiency, the OTR uses double layers in the superlayers which are used by the FLT. The hit information of both layers is or-ed on the TDC boards as described in Sect. 2.3.1.

- The efficiency of the coincidence-finding in the TFUs can be improved by or-ing the hit information in one stereo view. For the OTR +5°-channels (which correspond to the minus degree layer in the FLT notation) the information of a hit is distributed not to one, but two adjacent channels in the wire memory, see Fig. 2.9.

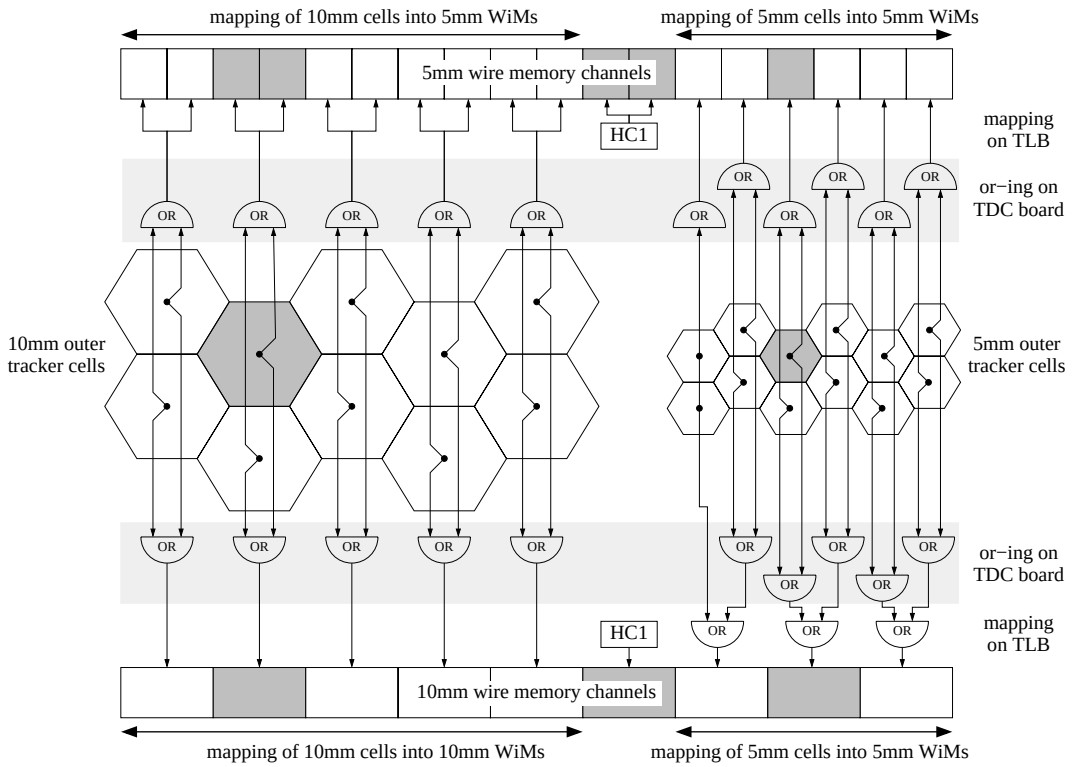

Fig. 2.9: Mapping of 5 mm and 10 mm cells. Both the mapping of 5 mm outer tracker cells into 10 mm wire memory channels and of 10 mm outer tracker cells to 5 mm wire memory channels is illustrated. Also visible is the or-ing of the double layers which is carried out on the TDC boards and hard coded one (HC1) channels which do not have corresponding detector cells.

- The OTR is composed of overlapping modules which contain either 5 mm- or 10 mm-cells. Since each TFU requires a single cell spacing, the TFUs are assigned either to 5 mm- or 10 mm-cells. Due to the actual geometry of the outer tracker, the 5 mm and 10 mm segmentation of the TFUs cannot directly be mapped to the segmentation of the OTR modules. Therefore, it is necessary to combine adjacent OTR 5 mm-cells by logical or-ing and to map them into 10 mm-WiM regions, and to distribute 10 mm-cells on two adjacent wire memory channels if situated in 5 mm-regions of the WiM, see Fig. 2.9. A corresponding procedure is not necessary for the muon tube or pixel system or the inner tracker since both provide only a single granularity.

- The separation in the left and right half of the outer tracker, which is constrained by the position of the electron beam pipe, does not match the separation of the TFUs, which is situated roughly at $x = 0$.

- All channels in the wire memory have to be assigned to consecutive cells in the detector. A gap or an overlap in the detector cells has to be treated accordingly by setting hard coded one (HC1) channels in order to close gaps, or by or-ing the hit data of overlapping detector cells, see Fig. 2.9.

The mapping of wires in the OTR (similar to the ITR and the muon system) to the channels in the wire memories is a many to many relation, i.e., at the same time one wire of the OTR may be mapped to several channels of the wire memory and a wire memory channel may receive the hit information from several OTR cells.

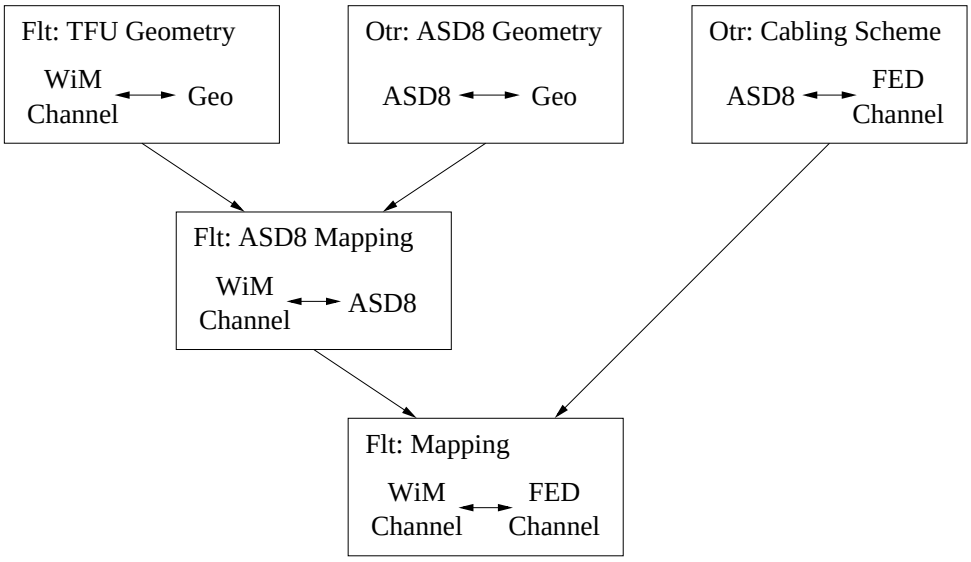

Fig. 2.10: Creation of the mapping. In a first step, the TFU geometry and the OTR ASD8 geometry are combined to get a mapping of wire memory channels to ASD8 chips (ASD8 mapping). In a second step, this result is combined with the OTR cable scheme which relates the ASD8 chips to the front end drivers.

Fig. 2.10 gives an overview of the production of the mapping which is done in two steps: The TFU geometry (the assignment of wire memories to geometrical regions in the detector) and the geometry of the ASD8 chips (the set of wires covered by a given chip), provided by the OTR data base, are combined to obtain a mapping from wire memory channels to ASD8 chips.
In a second step, resulting in the *OTR cabling scheme*, the mapping from wire memory channels to ASD8 chips is combined with the mapping from ASD8 chips to OTR front end drivers and channels. The result is the mapping from wire memory channels to OTR front end drivers and the corresponding channels. This information is used both for programming the trigger link boards and for the reconstruction of the wire memory content in the FLT simulation.
As is discussed in Sect. 5.2, the mapping has an important influence on the tracking efficiency.

2.4 The FLT Network

After a discussion of the pretriggers and the data transmission, in this section the hardware of the FLT and the trigger algorithm are discussed.

2.4.1 Realization of the FLT Hardware

In this section, the implementation of the FLT processor boards is discussed. In order to simplify the complex calculations which are necessary for the tracking algorithm such that they can be implemented in dedicated processor boards, more elementary units are put together. These units, namely the pipelined processor, lookup tables, and programmable logic devices, are the subject of this section.

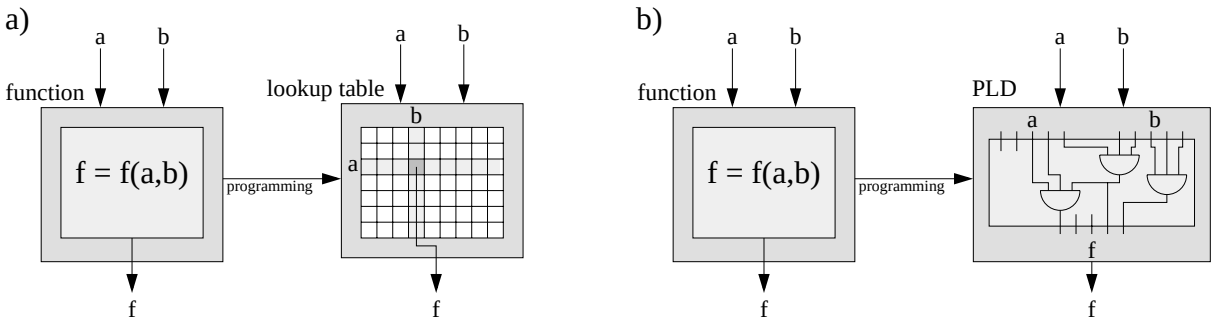

Fig. 2.11: Principle of lookup tables and programmable logic devices. Figure a) shows the idea of a lookup table. Instead of calculating the function $f = f(a, b)$ all possible results of the function for a finite set of input values are stored in a table which is simply to be 'looked up' on demand. Figure b) depicts a programmable logic device which represents the function $f = f(a, b)$ by a set of logical operations.

The central element of the FLT processor boards are operations on digital data. An input pattern of a certain number of bits has to be mapped to an output pattern. There are two possibilities to realize this functionality: the first is the **L**ook**U**p **T**able (LUT), the second is the usage of **P**rogrammable **L**ogic **D**evices (PLD). Both allow for a mapping of a set of input bits to an output pattern, see Fig. 2.11.

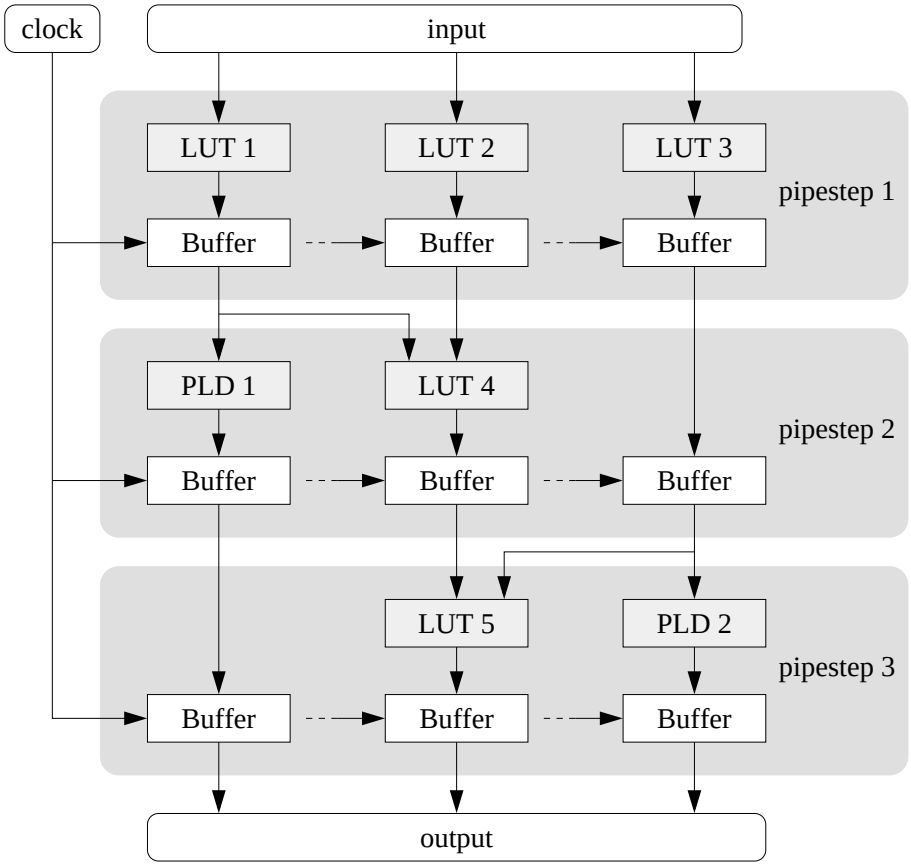

Fig. 2.12: View of a pipelined system of three pipeline steps. The clock controls the buffers which store the output of the lookup tables or simply forward a message that will be needed in a following pipe step. On a clock signal, the input of the buffers is transfered to their outputs and the next pipe step can perform its operation.

A lookup table uses RAM chips which store the desired output data for each possible input pattern. This has the advantage that an arbitrary function can be realized and that the reprogramming can be done easily by writing the corresponding values into the RAM chip. The disadvantage is that the number of input channels is limited by the fact that a lookup table of n input and m output bits has to store information of $2^n \cdot 2^m$ bits. In the case of the FLT, RAM chips of a maximal 18 bit address space are used.
In contrast, a PLD can handle many more input channels, but the process logic is limited to a predefined set of operations which can be used for the mapping of input to output data. Due to their orthogonal advantages, both LUTs and PLDs are used on the FLT

processor boards. The LUTs are used for calculations of the track parameters while PLDs serve for simple, such operations as for addition of parameters and the overall process logic of the boards.
The concept which connects input and output of the LUTs and PLDs is the pipelined processor. The FLT boards are organized by pipe steps which represent, for example, the data of one message or track candidate, respectively. In each pipe step, a set of operations on this data is carried out in each clock cycle of the board electronics. All processor boards are clocked with 50 MHz. The full operation which is performed on an incoming message is composed of the successive executions of the pipe steps. Fig. 2.12 depicts an example for such a system. The pipeline is controlled by a clock signal which steers the transmission of the information from one pipe step to the next. On a clock signal, the output of the lookup tables of pipe step i is transfered to the input of pipe step $i + 1$. In this way, a system of n pipe steps needs n clock cycles to perform the full operation. A system of n pipe steps is able to handle n such operations at the same time since each pipe step contains the information of a different incoming message. On each clock signal the system reads one incoming message and provides one resulting message at the output. The result appears at the output with a delay of the number of pipe steps times the clock interval. This delay is also called the *latency* of the pipeline processor.

board type	number of LUTs	number of pipe steps	latency
TFU	38	22	≥ 400 ns
TPU	54	12	≥ 260 ns
TDU	$4 \cdot 16 + 1$	27	$540 - 2120$ ns

Table 2.1: Some characteristics of the FLT processor boards. The clock frequency is 50 MHz for each board type. The TDU contains four modules of 16 LUTs each for the invariant mass calculation plus one additional LUT for the board logic. Only five pipe steps of the TDU are assigned to the calculation of invariant masses of track pairs, the remaining pipe steps are dedicated to the process logic. The latency numbers are based on [ger00].

Depending on the functionality of the board some additional clock cycles are needed to perform the full calculations which may also depend on the actual data which is processed. If, for example, the TFU finds more than one coincidence in a given region of interest, the board logic has to introduce an additional clock cycle to produce additional output messages. Since the rest of the system has to wait in this case, the additional clock cycles are called *stall cycles*. If stall cycles are possible in the system, the latency becomes variable and depends on the actual input data.
For controlling purposes, each FLT processor board hosts an on-board CPU[4]. The CPU

[4] **C**entral **P**rocessing **U**nit. Main processing unit of a microcomputer. In the FLT processor boards the MC 68020 from Motorola with 4 MByte RAM is used.

makes it possible to communicate to the board via a VME[5] bus. The loading of lookup tables and the setting of registers in the process logic of the boards is also done using the CPU. Moreover, there is a monitoring of voltages and temperatures of the boards in order to ensure safe operation conditions.

2.4.2 The Message Transmission within the FLT Network

Fig. 2.1 shows that messages have to be transmitted from processor boards of one superlayer to those of the next superlayer starting at the pretriggers and ending at the TPUs and at last reaching the TDU. The messages contain 80 bits of information each. The actual meaning of these bits varies depending on which kind of processor receives the messages. An overview of the information given in the messages is shown in Table 2.2.

messages to TFUs, TPUs and TDU		
variable	description	bits
$n\xi$	two messages	1
ξ	x-coordinate at reference superlayer	10
$d\xi$	minimal track slope	8
η	slope in y	9
w	cluster width in TC02	2
BX	bunch crossing number	8
ID	pretrigger identifier	2
messages to TFUs and TPUs		
$dd\xi$	size of region of interest	8
P	ECAL estimated nominal momentum	7
E^+	ECAL bremsstrahlung energy (positron hypothesis)	7
E^-	ECAL bremsstrahlung energy (electron hypothesis)	7
messages to TFUs		
TDI	destination identifier	8
messages to TDUs		
$dd\xi'$	new size of region of interest	8
P_z	z-component of momentum	7
$\hat{P}_x$	x-component of momentum divided by P_z	10
$\hat{P}_y$	y-component of momentum divided by P_z	9
q	charge of track	1

Table 2.2: FLT message definition for messages sent from the pretriggers to the TFUs and from TFUs to TFUs of the next superlayer [ger98].

[5] **V**ersa **M**odule **E**urocard. Standardized 64 bit interface.

The FLT processor boards do not send and receive the messages directly, but by means of the *message boards*, see [glae02]. They contain input and output buffers which allows for an asynchronous message transfer while providing a continuous message input to the corresponding processor board. These buffers are realized by FIFOs, (**F**irst **I**n **F**irst **O**ut buffer), which transfers the data which is received first, preserving the order of the incoming data. Moreover, message boards which are assigned to TFUs make it possible to by pass parts of the message that are not needed for the calculations of the TFUs. For example, the information of the cluster energy of an ECAL pretrigger message, as well as the energy of hypothetical bremsstrahlung clusters, are not used inside the TFU and, therefore, stored by the message board and put again into the messages which are sent to the next superlayer.
The message boards which are assigned to TFUs have six input channels (*receivers*) while the message boards which are used for the TPUs and TDUs have four receivers. Each message board has one *transmitter* which serves as output for the messages. In order to distribute the output to several TFUs of the next superlayer the output of the message boards is multiplexed by the *repeater boards*.
In order to minimize the load of the TFUs, the messages should only be sent to TFUs which are assigned to the detector region which covers the region of interest that is defined by a given message. On one hand, TFUs are either assigned to the $+y$-half or the $-y$-half of the detector and, therefore, the messages do not cross from the upper half to the lower or vice-versa. On the other hand, the messages contain the *destination identifier* (*TDI*) which is a pattern of eight bits that indicates which TFUs of a superlayer should use the messages.
In Table 2.2 an overview of the meaning of the different parameters which are transferred by the 80 bit message is given. The most meaningful parameters in terms of the tracking algorithm are ξ, $d\xi$, $dd\xi$ and η. They represent the analog of the state vectors used in the Kalman Filter algorithm as they give the best estimate of the track parameters at a given point. These parameters are used in the extrapolation scheme which is described in Sect. 2.4.3 in more detail. The extrapolation describes the transition from a reference plane to the extrapolation plane. A cluster of up to four adjacent hits is described by the position ξ of the upper edge (more positive x-values) and the width of the cluster w, see Fig. 2.13. The track slope in the xz-plane is defined by $d\xi$ which is the angle between the track slope and the trajectory of a particle of infinite momentum traversing the position ξ in the reference plane. In this way, the parameter $d\xi$ is related to the momentum and the charge of the described track. The track slope is also defined by a window in the extrapolation plane of the width $dd\xi$.
In the *swap extrapolation scheme* the window in the extrapolation plane is enlarged by the width w of the cluster in the reference plane. The swap scheme is used in the muon layers and in superlayer TC02, as well as for the pretrigger messages. In contrast, the TFUs of the superlayers TC01, PC04, and PC01 use the *no swap extrapolation scheme*.
In the case that the region of interest in the extrapolation plane exceeds 32 wires, the RoI can be enlarged by setting the bit $n\xi$. This is necessary since the TFU can handle only RoIs of 32 wires width within one clock cycle. If $n\xi$ is set, an additional clock cycle will

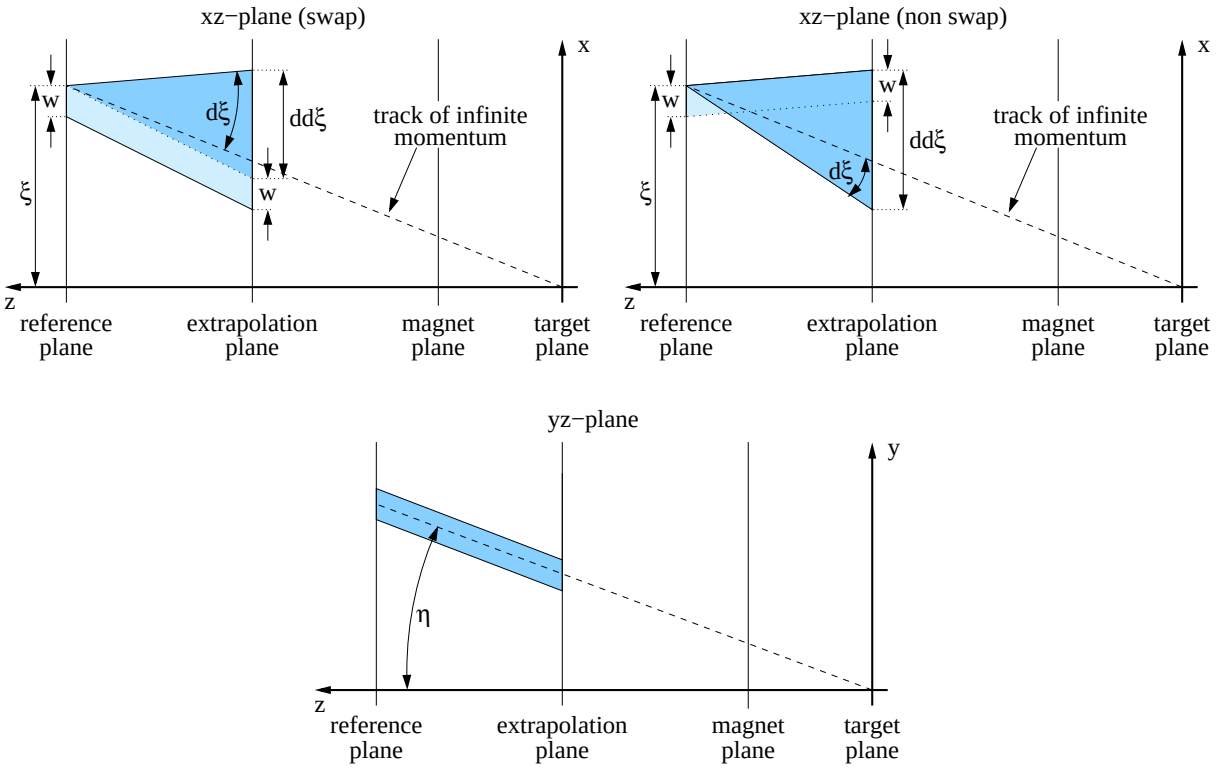

Fig. 2.13: Definition of the track parameters ξ, $d\xi$, $dd\xi$ and η. While the track definition in the yz-plane is simply given by the track slope assuming that the tracks are not bent by the magnetic field in the yz-plane, the parameterization in the xz-plane is more detailed and oriented by the extrapolation from a reference to an extrapolation plane. ξ denotes the upper (at more positive x-values) edge of the cluster (of with w) in the reference plane. The track slope is enclosed by a window. The upper edge is defined by the slope $d\xi$ of the upper edge in the reference plane to the upper edge in the extrapolation plane with respect to the track slope of a track of infinite momentum. The width of the window in the extrapolation plane is given by the parameter $dd\xi$. Please note that there are two extrapolation schemes (swap and no swap) with slightly different definition of the parameters.

be performed to treat the large RoI.

Since the tracks are not bent in the yz-plane inside the magnetic field, the track parameterization in that plane is simply given by the track slope η in that plane.

Additional parameters that are sent from TFUs to TFUs are the bunch crossing number BX, the pretrigger identifier ID which differentiates between tracks seeded by the electron or muon pretrigger. The ECAL pretrigger provides information of the cluster energy which is used in the TPU to perform an E/p-cut. In addition, the cluster energies of hypothetical bremsstrahlung photons can be taken into account in the TPU as soon as the charge of the track is known.

The TPU uses the track parameters for the calculation of the momenta of the tracks. It

inserts values of the track momentum into the 80 bit message comprising the z-component of the momentum P_z and the the x- and y-component relative to the z-component $\hat{P}_x = P_x/P_z$ and $\hat{P}_y = P_y/P_z$. The latter values correspond to the track slopes $t_x = P_x/P_z$ and $t_y = P_y/P_z$ before the magnet. Moreover, the charge of the track q is deduced from the track slope.
All these parameters are stored within the 80 bit message. The continuous variables are binned such that the accuracy loss due to the binning does not affect the functionality of the system.

2.4.3 The Track Finding Unit and the Tracking Algorithm

The purpose of the TFUs is to receive messages with track candidates from the previous superlayer and to refine or reject those by searching for triple coincidences in the region of interest.
If coincidences are found within the RoI, new messages with updated track parameters are calculated and sent to the next processing units. The algorithm used in the TFUs is described in detail in [fle01]. A rough overview of the functionality of the TFUs is depicted in Fig. 2.14.
The TFU receives two types of information: the hit data from the detector and the messages from the previous superlayer, which define the regions of interest. Each TFU covers a specific part of the tracking system in which it looks for coincidences. The detector data is stored in the **Wi**re **M**emory (WiM) already mentioned in Sect. 2.3.5. The WiM stores the hit information of the last 128 events and, for each event, up to 384 detector channels for each of the three stereo views.
First, the RoIs are calculated in the local TFU frame using the track parameters given by the message. For each of the three wire memories, the RoIs are expressed in terms of the first wire n and the range of wires l. These values are used together with the bunch crossing number (BX) to address the hit pattern in the wire memory. The BX number of each message provides the information which hit data has to be used. The hit patterns of the three wire memories are directed to the *coincidence matrix*, which uses the hit patterns to find triple coincidences in the RoI. Fig. 2.15 shows the coincidence schemes which are accepted by the coincidence matrix.
The set of accepted coincidences also takes into account the uncertainty on the vertical slope of the track. A small deviation in the vertical direction would change the relative position of the positive and negative stereo angles with respect to the zero degree layer. The TFU internal parameter h (height) indicates the magnitude of such a deviation. The set of coincidences centered around the extrapolated vertical position are the six with $h = 0$. A positive or negative shift in the vertical direction would give rise to the possible extra coincidences of $h = 1$ or $h = 2$, respectively. In case $h = 3$ all twelve possible patterns which are shown in Fig. 2.15 are used.
For each of the coincidences which is found in the RoI, the coordinates are calculated and a new message is created. The parameters of the new message are calculated in the remaining pipeline steps of the TFU. During this time, the TFU is not able to handle

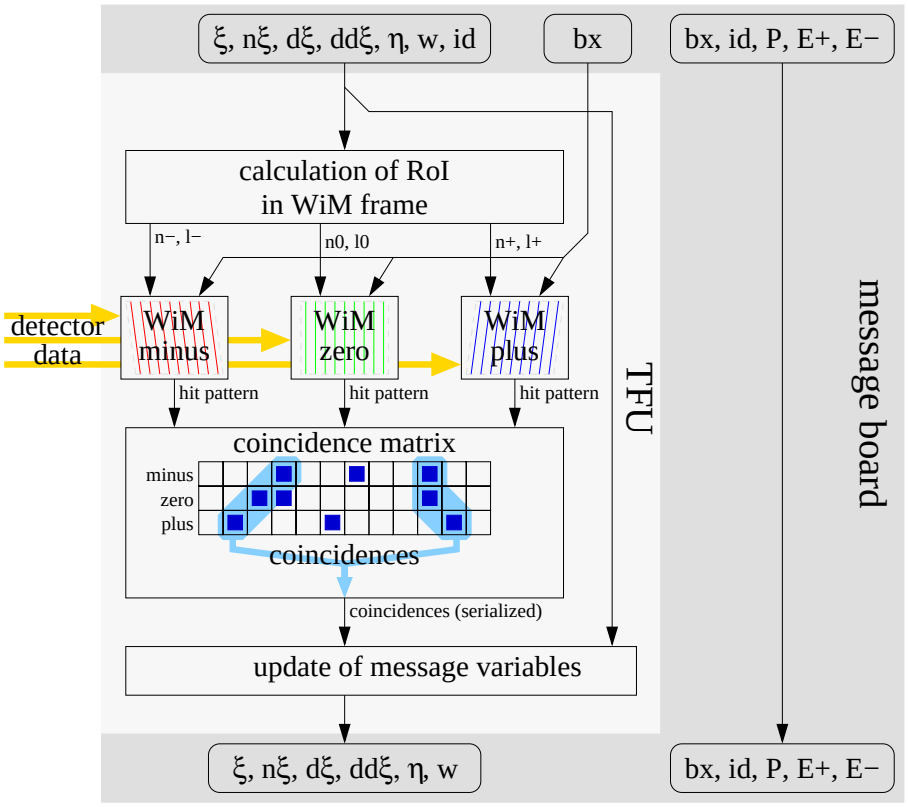

Fig. 2.14: Overview of the TFU functionality. Using the parameters of the incoming track candidate, the TFU calculates the region of interest (RoI) in the frame of the wire memory (WiM). The hit information which is sent by the detector is stored in the WiM. The RoI and the bunch crossing number address the regions in the WiM which are transferred to the coincidence matrix for the search for triple hits. Finally, the found coincidences are combined with the incoming parameters in order to obtain the updated track candidate which is sent to the next superlayer. Parameters which are not updated in the TFU are by passed by the message board.

new messages. Therefore, the pipeline processing is stalled until all found coincidences are processed.

With the coordinates of the space point found, the track parameters are refined and an updated message is generated. The TFU determines the target TFUs in the following superlayer and codes this in the message variable *TDI*. The whole FLT tracking in the outer tracker is depicted in Fig. 2.16.

Fig. 2.16 a) illustrates the extrapolation from superlayer TC02 to superlayer TC01. The RoI in TC01 is defined by the 'upper edge' ξ (more positive x-values) of the cluster of hits found in TC02 and the width w of the cluster. Moreover, the slope $d\xi$ defines the 'upper edge' of the RoI in TC01 and the width of the RoI is given by $dd\xi$ minus the width of the cluster in TC02 w. This extrapolation scheme is called the swap case, see also Fig. 2.13.

In the next step, see Fig. 2.16 b), the found cluster in TC01 is used for the extrapolation

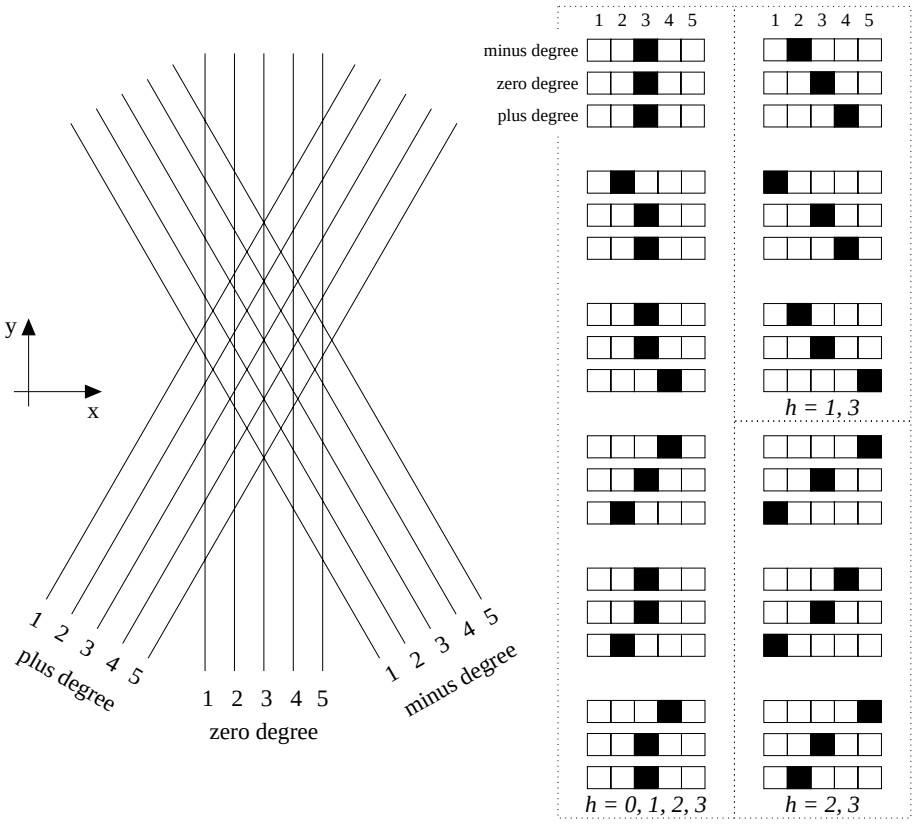

Fig. 2.15: Coincidence Schemes. On the left side, the assignment from wire memory channels to the cells on the right part is illustrated. The schemes which are recognized by the coincidence matrix are indicated by the patterns on the right side. Depending on the TFU internal parameter h which indicates the height in y-direction of the RoI, different coincidence schemes are taken into consideration.

in superlayer PC04. For simplicity, we regard only the hits in the zero degree stereo view. Since the extrapolation scheme is the non-swap case, the line connecting the upper edge of the cluster in TC02 and the lower edge of the cluster in TC01 is extended into superlayer PC04, defining the lower edge of the RoI. The upper edge of the RoI in PC04 is obtained similarly. Again, the RoI is defined by the upper edge ξ of the cluster in TC02 and the corresponding width w, while the slope $d\xi$ of the extrapolation from the upper edge in TC02 to PC04 and the width $dd\xi$ of the RoI in PC04 are updated.

The extrapolation from PC04 to superlayer PC01 is similar to the extrapolation from TC01 to PC04. At last, the TFUs of superlayer PC01 generate messages which define a region of interest in the magnet plane at $z_{\mathrm{magnet}} = 450\,\mathrm{cm}$. The final track candidate is defined by the hit clusters in TC02 and PC01, independent of the pretrigger source. The track parameters are sent to the TPU for the calculations of the kinematical parameters.

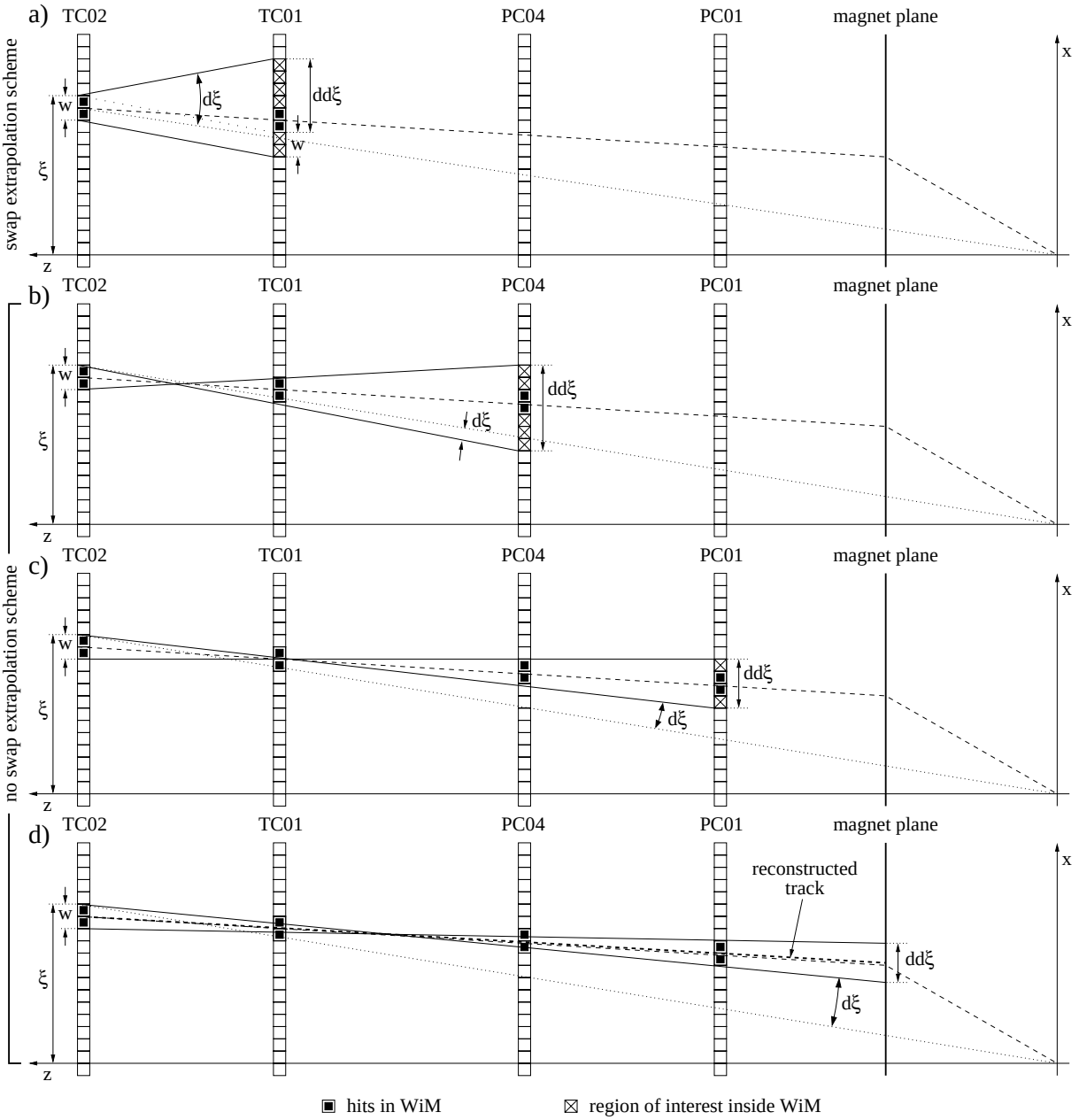

Fig. 2.16: Tracking algorithm of the FLT depicting the tracking through the outer tracker system from superlayer TC02 up to the extrapolation into the magnet plane, which is sent to the TPU. The figure is not to scale.

The tracking in the muon system is similar, besides the fact that the MUD4 and MUD3 superlayers contain only one stereo view. Moreover, the parameter η is updated in superlayer MUD1. For details of the muon tracking please refer to [fle02].

2.5 Kinematical Cuts and Trigger Decision

Apart from the track finding based on the pretrigger seeds, the FLT provides some further functionality which is needed for a trigger decision. First, the momenta of the tracks are calculated and a ghost rejection is performed. Second, two strategies of triggering are applied, the count and the pair trigger, which are the basis of the trigger decision of the FLT. This functionality is the subject of this section.

2.5.1 The Track Parameter Unit

The TPUs get the track candidates from the TFU network and calculate the kinematical parameters of the tracks. They extract the momentum and the charge of the tracks which is given by the track parameters of the TFU tracking. The momentum calculation is based on the x-position of the track in the magnet plane x_{magnet} and the impact point of the extrapolation of the straight track in the field-free region into the target plane x_{impact}, see Fig. 2.17 a).

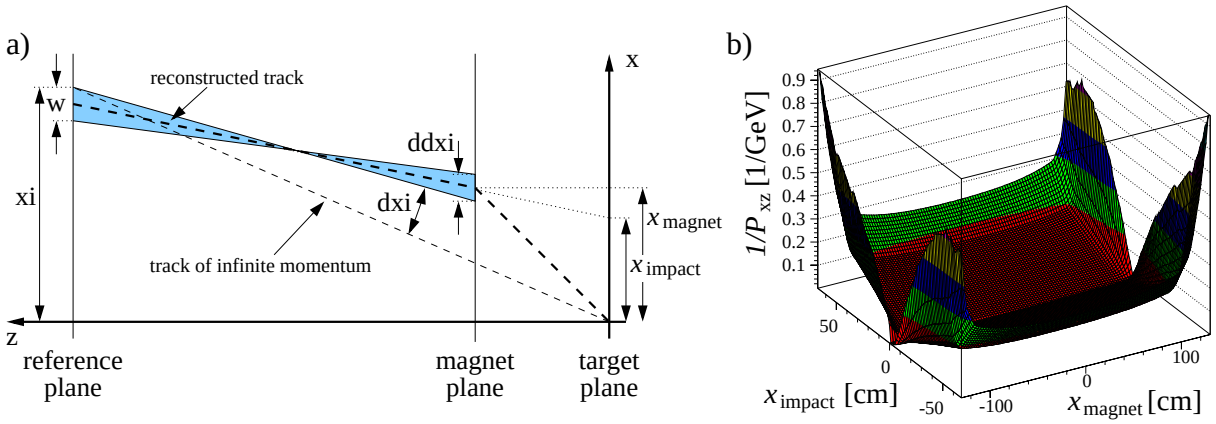

Fig. 2.17: Calculation of the momentum of a track by the TPU. Figure a) illustrates the x-position of the reconstructed track in the magnet plane x_{magnet} and the impact point of the extrapolation of the track behind the magnet into the target plane x_{impact} which are used to calculate the momentum of the track. Figure b) shows the parameterization of the momentum of the track in the xz-plane depending on the the values x_{impact} and x_{magnet}, see [rat96].

Using the estimation sketched in Fig. 2.18 a particle carrying an elementary charge receives a momentum kick of

$$P_{\text{kick}} = \frac{0.3\,\text{GeV}}{\text{m}\cdot\text{T}} \cdot B \cdot l \approx 0.672\,\text{GeV} \tag{2.9}$$

in the transverse direction using the magnetic field of $B = 0.8\,\text{T}$ and the diameter of the HERA-B magnet of $l = 2.8\,\text{m}$. The deflection angle α as shown in Fig. 2.18 is $\alpha = P_{\text{kick}}/P$, assuming α to be small. By projecting this angle into the target plane using the distance

from the middle of the magnet to the target plane, $z_{\text{magnet}} = 450\,\text{cm}$, the impact point of the extrapolated track in the target plane x_{impact} is $x_{\text{impact}} = \alpha \cdot z_{\text{magnet}}$. Thus the relation of the impact point x_{impact} and the momentum P of the track at first order is given by

$$P = \frac{302.4\,\text{GeV} \cdot \text{cm}}{x_{\text{impact}}} \tag{2.10}$$

This relation holds at the center of the magnet. Tracks which traverse the magnet more peripherally 'feel' a lower magnetic field integral. In order to take this into account the dependence of the momentum not only on x_{impact} but also on x_{magnet} was studied using the parameterization of the magnetic field as available in the HERA-B analysis software ARTE, see [rat96]. A table of the dependence $P_{\text{xz}}^{-1}(x_{\text{impact}}, x_{\text{magnet}})$ was built and is used for the lookup table generation for the TPU, see Fig. 2.17 b).

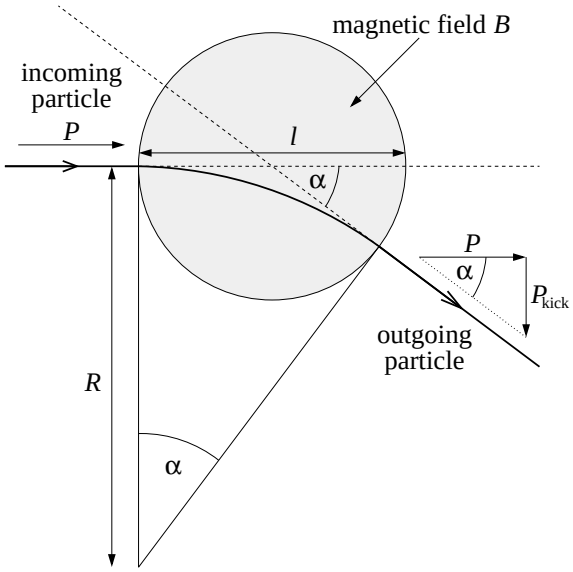

Fig. 2.18: Illustration for the estimation of the magnet kick. The incoming particle of momentum P travels in the magnetic field of strength $B\,[\text{T}]$ on a circular path of radius $R\,[\text{m}]$ obeying $P = 0.3\,\text{GeV} \cdot \text{m}^{-1} \cdot \text{T}^{-1} \cdot B \cdot R$. For small angles α one obtains the ratio $P_{\text{kick}}/P = l/R$ having the diameter of the magnet l and the momentum kick P_{kick} that the particle receives by traversing the magnetic field. Hence the momentum kick is $P_{\text{kick}} = 0.3\,\text{GeV} \cdot \text{m}^{-1} \cdot \text{T}^{-1} \cdot B \cdot l$.

Assuming the magnetic field to have no extension in z, the ratio of the momentum components P_x/P_z is given by the x- and z-position of the track in the magnet plane $P_x/P_z = x_{\text{magnet}}/z_{\text{magnet}}$. Using $P_{\text{xz}}^{-1}(x_{\text{impact}}, x_{\text{magnet}})$ one obtains P_z and P_x. Finally, the ratio of the momentum components in the non bending plane is calculated by neglecting the magnetic field in the yz-plane which yields $P_y/P_z = dx/dy = \eta$. Using these ingredients, the total momentum

$$P = \sqrt{P_x^2 + P_y^2 + P_z^2} \tag{2.11}$$

and the transverse momentum

$$P_{\text{T}} = \sqrt{P_x^2 + P_y^2} \tag{2.12}$$

can be calculated using the track parameters.

Track candidates that do not satisfy a cut on the transverse momentum are rejected. To reduce the hadronic background for electron candidates, moreover, a cut on the ratio of the measured cluster energy and the momentum, E/p, can be applied. A hadron which overlap a photon has a similar signature as an electron as it deposits energy in the calorimeter and hits in the tracking chambers. Nevertheless, the hadron deposits less energy in an electromagnetic calorimeter than an electron of the same momentum. In this way, the requirement to measure a cluster energy that is comparable to the momentum of the associated track is able to reduce such a background.
Another feature of the TPU is the bremsstrahlung recovery, although it was not used during the running of the year 2000. Since the charge of the track is known to the TPU it can decide which of the hypothetical bremsstrahlung clusters (electron of positron hypothesis) provided by the ECAL pretrigger is valid. The energy of the bremsstrahlung cluster is added to the momentum of the electron track. This procedure enhances the efficiency of the cut on the invariant mass in the TDU.
In order to reduce the number of clones which can cause stall cycles in the TDU and thus lead to an increased latency of the FLT, the TPU compares tracks found in one event and rejects tracks with almost identical parameters. The last 20 messages that are accepted by the TPU are compared to each incoming track. A track is discarded if the track slopes P_x/P_z and P_y/P_z are the same but for one bin for a track of the same event and the same pretrigger source. Such tracks are regarded as clones, i.e. two or more messages which could be ascribed to the same physical track. This happens if a track hits the acceptance of two neighboring TFUs or if there are two or more adjacent coincidences in one TFU. Further information about the TPU can be found in [fla01b].

2.5.2 The Trigger Decision Unit

Finally, the track candidates of the TPU are sent to the TDU. The TDU decides if a given event is to be accepted or not, based on the found tracks and their momenta. On one hand, a threshold of a number of certain track types can be specified. These tracks are differentiated by their pretrigger source and by the exceeding an adjustable cut on the transverse momentum. One the other hand, the invariant masses of all possible track pairs are calculated and the excess of a mass cut can also trigger an event. An overview of the TDU process logic is shown in Fig. 2.19.
The first possible trigger condition is subject of the *count trigger*, which simply counts the number of track candidates. The trigger condition is defined by the minimum numbers of different kinds of tracks. As soon as one of these thresholds is reached for one particle kind, the corresponding event is accepted.
There are eight message kinds which are distinguished by the count trigger. The four different pretrigger sources for electron, muon, high-p_{T}, and hard photon seeds[6] are combined with a flag indicating tracks of high transverse momentum. Based on the momentum cal-

[6]The high-p_{T} and hard photon pretrigger are not discussed in detail since they were not used during the data taking of the year 2000.

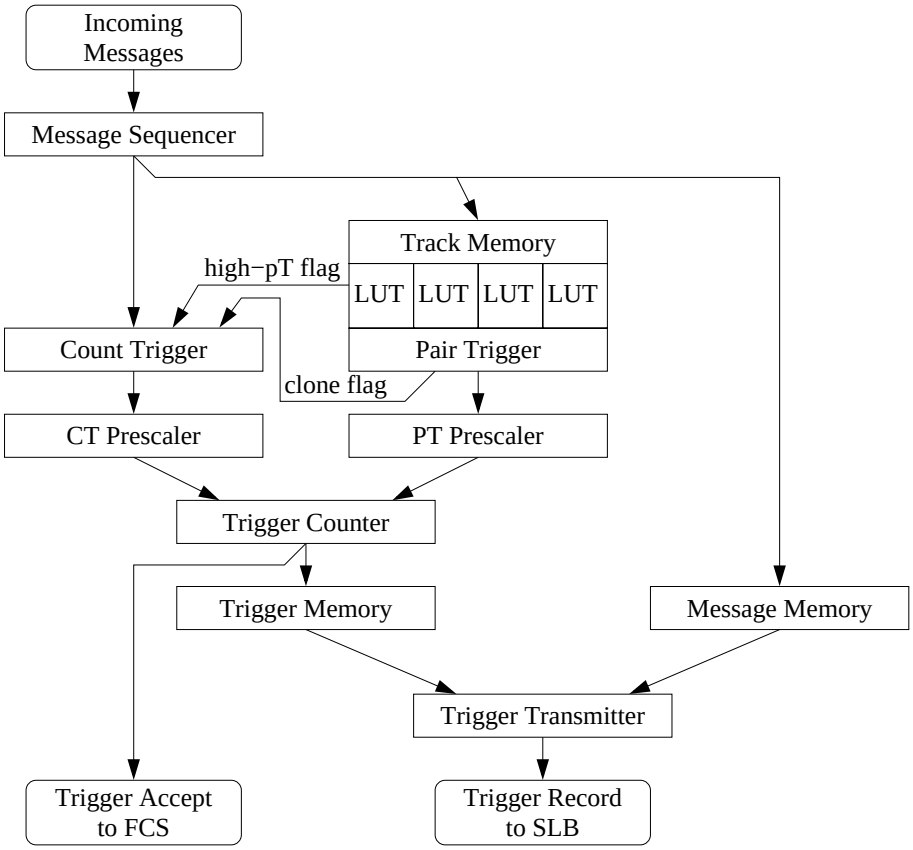

Fig. 2.19: Flow chart of the TDU. The message sequencer distributes the incoming messages to the count trigger, the track memory and the message memory. The track memory is used to feed the lookup tables (LUT), which perform the calculation of the invariant mass of track pairs. Moreover, tracks of high transverse momenta and clone tracks are detected, and the information is taken into account in both the count and the pair trigger. After the prescaling of the found triggers, they are stored in the trigger memory and the FCS is notified about the trigger decision. On demand of the FCS, the TDU provides the information about the found triggers and the stored messages to the SLB.

culations of the TPU, the TDU determines the transverse momentum. A threshold for the flag of high transverse momentum can be set for each pretrigger source individually.

Besides the eight count trigger, it is also possible to trigger on a combination of k high-p_{T} (i.e. messages of the high-p_{T} pretrigger) and n messages of other pretrigger sources requiring (or not) the high-p_{T} flag. This sums up to $8 + 6 = 14$ different count trigger patterns.

During the running of the year 2000, the FLT was still not fully commissioned and therefore mainly running using the count trigger for triggering. This mode can be realized either using the FLT tracking algorithm or, alternatively, by directly using the pretrigger messages as input to the TDU. In that mode, the FLT just counts the number of pretrig-

ger messages for the trigger decision. In the 2000 data taking period the pretriggers were used for the enhancement of events containing J/ψ mesons. The tracking of the FLT was used only for the very last runs of 2000.
The second type of trigger condition is the *pair trigger*. Each incoming message can be combined to each message of the same event that has already been received by the TDU. A maximum of 24 messages for each event can be stored and combined pairwise. Combining each message pair, two calculations are carried out. First, a clone removal is performed, based on the comparison of the energy and slope difference of the tracks. Second, the invariant mass of both tracks is calculated. Besides the mass calculation, a positive trigger decision is based on the pretrigger types, charges, and transverse momenta of the tracks, as well as the energy asymmetry of both tracks. Because of the usage of lookup tables in the TDU the conditions of the trigger decision allow for a fine tuning. Taking all information together, 255 different pair trigger conditions can be defined. During the commissioning phase in the year 2000, a trigger requirement of an invariant mass of 2.0 GeV of unequal charged tracks of the same particle type was used.

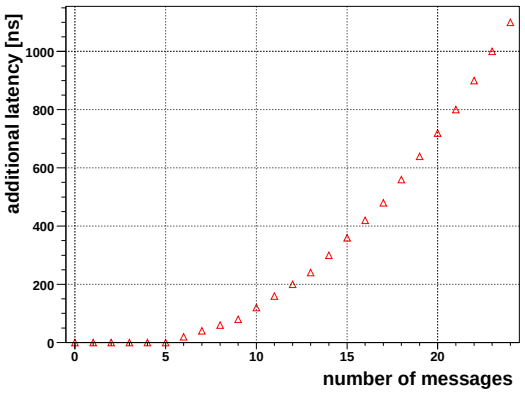

Fig. 2.20: Additional latency introduced by stall cycles which are necessary for the TDU to perform the calculation of the invariant mass for all possible message combinations [noe99].

The pair trigger is realized such that a maximum of four tracks can be compared to the last incoming track in one clock cycle since there are four *pair trigger modules* which carry out the comparison in parallel. Thus, if more than five tracks are received by the TDU for one event, stall cycles have to be introduced to carry out all calculations sequentially in bundles of four. Fig. 2.20 gives an impression of the non-linear increase of additional latency as function of the number of messages that the TDU has to deal with.
Both the trigger decisions of the count trigger and from the pair trigger differentiating the 14 count patterns and 255 pair trigger possibilities can be scaled separately. This makes it possible to down-scale the frequencies of the trigger types by factors varying from 1 to 65535.
The TDU stores up to 24 messages for each event in the *message memory* and up to 16 *triggers*, i.e. the conditions which lead to a trigger, in the *trigger memory*. As soon as one trigger is found, the TDU notifies the fast control system, which then distributes the *trigger accept* signal to the entire readout electronics of the detector. Thereupon, the complete detector data is sent to the second level buffer (SLB) and the SLT starts to

process the event data, as described in Sect. 1.5.2. Also, the TDU sends the information which is stored in the message and trigger memory to the SLB within a record of 300 bytes. The SLT can use this information, for example, to refine the tracks which were found by the FLT tracking. A more detailed description of the TDU can by found in [noe99].

2.6 The FLT Simulation

In this section, an overview of the simulation of the FLT is given and its relation to the FLT hardware and the data taking is described. This helps us to understand the problems which are discussed in the remaining chapters of this thesis. They contain the analysis of the reliability of the simulation in comparison to the performance of the hardware. Moreover, the simulation is used to determine the efficiency of the system.
Fig. 2.21 illustrates the data flow, both in the FLT hardware and the simulation. For real data, the hit information from the tracking devices splits into two distinct paths at the level of the front end driver, as discussed in Sect. 2.3.1 and Sect. 2.3.2. On one side, the hit and — in the OTR case — the timing information is kept by the data acquisition (DAQ) in the **D**ata **S**ummary **T**apes (dst-files). We denote this path as *common data stream*.
On the other side, the hit information is transfered to the trigger link boards (TLB) which collect the hit information and apply the mapping procedure as discussed in Sect. 2.3.3 and Sect. 2.3.6. Via optical fibers, the data is transfered to the electronics hut and received by the TFUs. The hit data is stored in the wire memories of the TFUs, see Sect. 2.3.5, and is used by the tracking algorithm which is carried out by the TFUs.
The hit information can be reconstructed in the simulation by using the data which is stored in the common data stream for real data. Alternatively, the simulation can be run using Monte Carlo events. Since the HERA-*B* analysis framework, **A**nalysis and **R**econstruction **T**ool and **E**nvironment (ARTE), does not provide the hit information in the same format as it is delivered by the data acquisition, an intermediate step has to be performed. The software package DaqIf reads the digitized hit information which is provided by ARTE in the Monte Carlo simulation and converts it to the same format that is given by the data acquisition and which is needed by the FLT simulation [söz01].
As soon as the hit information is given in the format of the data acquisition, the simulation of the FLT for real data and Monte Carlo becomes similar. In order to make the simulation realistic, different versions of the TFU geometry and maskings of defective channels can be applied. The mapping, which is done on the TLBs in the hardware, is provided by the corresponding functions of the FLT software that use the mapping as it is stored in the FLT database. The same mapping is used to program the trigger link boards, which assures that the mapping in the hardware and the simulation are the same (exceptions to this are discussed below). The mapping delivers the wire memory hits and can be used by the simulation of the FLT network, which consists of the pretrigger simulations and the simulation of the TFU network and the TPUs and the TDUs.
However, one has to take into account the imperfections of the detector and the read out

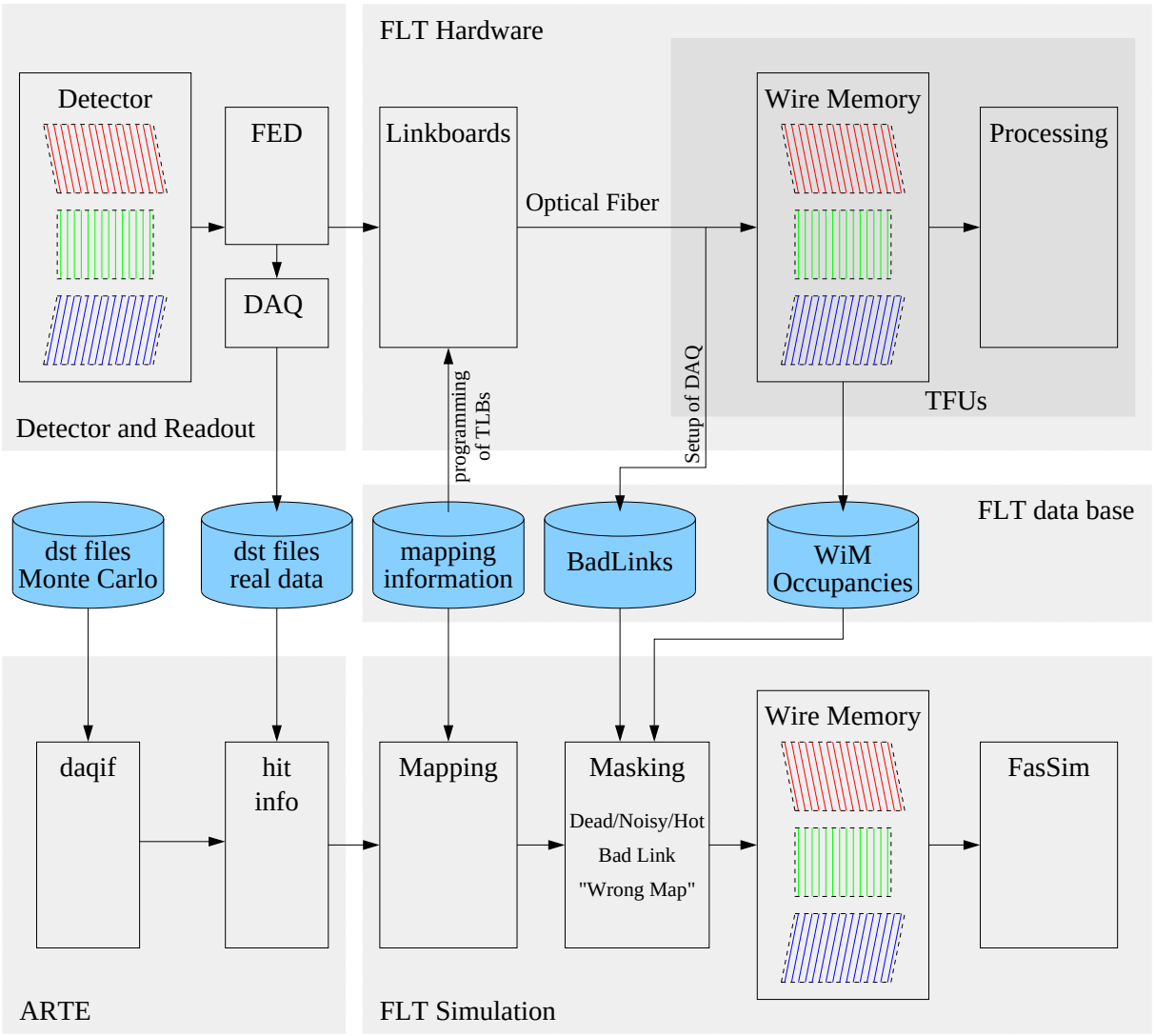

Fig. 2.21: Data flow in the FLT hardware and the simulation. The source of the hit information is either the detector which is read out by the FEDs or Monte Carlo. The detector hit information can be directly sent via the optical fibers to the TFUs in the hardware, or by producing dst files in the simulation. The hit data from these dst files, containing real data or Monte Carlo events, are made available to the FLT simulation by means of the simulation framework, ARTE. Although the usage of ARTE is not necessary, all analysis done in this thesis was done in this way.

and FED electronics if one wants either to reproduce the results of the FLT hardware or to have a realistic simulation of the system for efficiency estimations. To take that into account, in the simulation, a masking may be applied in order to take the defects of the hardware into account. The maskings are treated in Chapter 3.
Defects in the detector cells, the readout or front end electronics, as well as defective programming or malfunctions of the link boards may result in wire memory channels

which behave erroneous. It is possible to keep track of them by monitoring the occupancy of the wire memories. These occupancies can be used with or without the combination of the hit data of the common data stream to produce maskings which can be applied to the wire memory content in the simulation.
A similar procedure is used to detect problems in the correspondence of the mapping as it is performed by the link boards and as it is given in the simulation. To account for this effect, an additional masking is used.
Moreover, the performance of the optical data transmission from the linkboards to the TFUs is monitored and optical links are switched off in case of poor performance. The corresponding wire memory areas are set to one in order not to lose efficiency. This is also done in the simulation in order to obtain realistic results by setting the corresponding wire memory regions to one. The links which are not used for a given run are stored in the FLT data base.

2.6.1 ECAL and Muon Pretrigger Simulation

For the simulation of the ECAL and the muon pretrigger, dedicated software packages are available. Both serve, not only for simulation purposes, but also for the debugging of the corresponding hardware and for efficiency studies [fla01c, ada02]. In contrast to the hardware system, both simulations have access to the internal steps of the operations allowing for an optimization of the lookup tables.
The EcalSIM package is used for the simulation of the ECAL pretrigger and is embedded in the ARTE framework for event processing in HERA-*B*. It reads the digitized calorimeter information which corresponds to the ADC outputs of the photomultipliers. For real data, the values that were found by the readout system are used. For Monte Carlo, the energy depositions are converted to the corresponding ADC values. The output are ECAL pretrigger messages, given in the format described in Table 2.2. They can be directed to the FLT simulation. EcalSIM reproduces the functionality of the ECAL pretrigger logic on the bit-level. In this way, the comparison of the hardware and software results can be directly compared for debugging. The simulation uses the same lookup tables as those used in the hardware. The set of installed components, the masking and calibration of individual channels, as well as the cuts on the cluster energy can by specified by the user.
Likewise, the MUPRESIM package simulates the muon pretrigger system. This simulation is based on the bit-level description of the pretrigger using the same lookup tables that are loaded into the hardware. Defective and masked channels of the muon system are specified by the run number. The input is the hit information of the muon pad chambers or the muon pixel chambers which are combined to pseudo pads, see Sect. 2.2.2. Both real data and Monte Carlo contain this hit information, making the operation of the simulation similar in both cases.

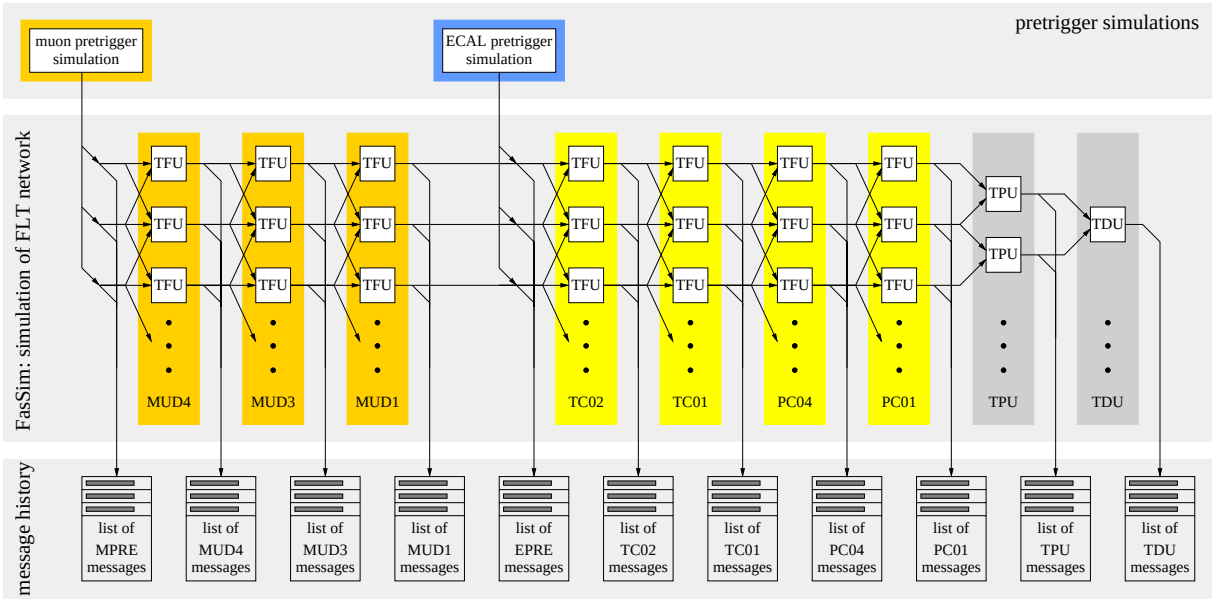

Fig. 2.22: Overview of the functionality of FasSim. The messages which are generated are made available to the network simulation. The request of the TDU messages triggers the computation of the entire network chain for the given pretrigger messages since all processor board inputs are calculated recursively up to the pretrigger messages. The messages which are sent from the processor of one superlayer to the next are stored in the message history. Moreover, the wire memories of the TFUs in the simulation have to be filled with the corresponding hit information.

2.6.2 Simulation of the FLT network

The TFU network is simulated by the **Fas**t **Sim**ulation (FasSim) package. It is part of the FLT software and is closely connected with the lookup tables which are used in the processor boards and has access to the FLT data base, which provides the mapping and geometry information. It has not only the purpose — as used in this analysis — to simulate the FLT as one complete unit, but also to simulate it in detail at the bit-level, which allows for a direct comparison and debugging of the hardware, see [mic02].
Based on a connection scheme which is defined in the FLT data base, a set of TFU, TPU, and TDU processors is simulated, as well as the message transfer among them. In order to obtain the output of the TDU one has to provide the pretrigger messages. After this, the value of each parameter can be calculated on request. Parameters at the output or inside of a certain processor board can be requested. All parameters which are needed for computing the desired parameter are recursively computed, too.
Fig. 2.22 illustrates the usage of FasSim for the analysis of this thesis. In a first step, the pretrigger simulations are processed. Additionally, the hit information of the outer tracker and the muon system has to be loaded into the simulated wire memories. After this step, the output of the TDU is requested and all messages which emerge in the data transmission from the processors of one superlayer to the next are stored in the *message*

history. The primary purpose of the message history is to store the messages which are calculated by the simulation on the recursive request, in order to avoid that they are calculated multiple times. The messages which occur in the different superlayers are stored and undergo further processing depending on the focus of the analysis.

Chapter 3

Channel Masking

After the discussion of the functionality of the FLT in Chapter 2 we investigate the reliability of the hit data transfer from the detector to the wire memories in the TFU network.
The analysis used in this chapter is based on statistical methods. This means that the data transfer is not investigated separately for each event but only the sum of hits in certain detector channels over a given amount of time are regarded. In contrast, the event-by-event comparison, which needs a dedicated setup of the FLT, allows for the investigation of the data transfer differentiating each event. Since this method was not available for the running in the year 2000 it is not used in this analysis.
The analysis follows a 'phenomenological approach'. The hit information which is observed in data and Monte Carlo is the basis for the investigations of this chapter. The design of the involved hardware components is not analyzed in order to trace back the origin of the problems of the data transmission. Rather, the emphasis is placed on the requirement to take the defects of the data transmission into account in the simulation of the FLT on data and Monte Carlo. Thus, the result of this chapter is not the uncovering of the origin of the detector defects but the means to simulate them as realistically as possible using the information at hand.

3.1 Wrongly Mapped Channels

In Sect. 2.3.6 the mapping of detector cells to the wire memory channels of the TFUs was introduced. Here the test of the correct realization of the mapping is regarded. One has to differentiate between the correctness of the mapping as obtained by the procedure that was described in Sect. 2.3.6 and the correct implementation of the mapping in the hardware. Unfortunately, the terminology is confusing. In the case of an incorrectly implemented mapping the term *wrongly mapped channels* is used. In contrast, a mapping that assigns detector cells to wire memory channels in a wrong way due to incompatible cabling and geometry information of the FLT and the detector is called *wrong mapping*.
From the simulation point of view the difference of wrongly mapped channels and wrong

mapping is that the wrongly mapped channels have to be measured in the hardware and explicitly simulated using a corresponding masking. The wrong mapping in contrast is already taken into account if the simulation uses the same ASD8 geometry and cabling scheme of the OTR as for the production of the lookup tables which were used in the running of the FLT during the data taking. The wrong mapping will be regarded in Sect. 5.2. The wrongly mapped channels and the corresponding masking will be discussed in the following.

Testing of the Wrongly Mapped Channels

The programming of the link boards which perform the mapping in the hardware was tested in two steps. First, several link boards were tested using characteristic test patterns at the input which evoke defined output patterns. This test showed that the programming of the link boards works generally in the expected way. However, it is not possible to test all used link boards like this since this test is first, rather elaborate, and second, it does not cover all possible problems of the data transmission.
For that reason a second test was done: during a dedicated run the ASD8 thresholds are lowered. In this way the noise level is enhanced such that a characteristic occupancy pattern can be observed. This pattern can be measured in two ways. On one hand, the wire memory contents of the TFUs are directly read out. On the other hand, the hits in the OTR are stored. The hits are accumulated for a certain amount of time such that statistically significant occupancy patterns can be obtained. After applying the mapping of the FLT to the outer tracker data, the resulting occupancy patterns should be equal for the wire memory read from the hardware (which has undergone the mapping in the linkboards) and the expected wire memory content from the outer tracker (after applying the mapping in the software). The characteristic shape of the occupancies allows for a rough validation of the mapping, see Fig. 3.1.
The similarity of the shapes proves the mapping to work in the same way in both cases. However, there are individual channels which show a significantly different occupancy in the wire memories and in the outer tracker data. These differences were used to trace back erroneous programming of the link boards in the commissioning phase in the year 2000. However even after this debugging procedure there remains a set of wire memory channels which still shows a different behavior than the expectation seen in the outer tracker data. These channels are denoted as *wrongly mapped channels*. There were 341 such channels detected during the test in year 2000. The observed occupancy of these channels in the wire memories is kept and applied in the simulation in the case of real data or Monte Carlo with realistic masking. The denotation *wrongly mapped channels* was motivated by the notion that an error in the link board programming leads to a quasi random occupancy in the wire memories as expected for getting the hit information from an arbitrary region of the detector. The test described in this section is on the one side also sensitive to defects arising from other stages of the data transmission as, for example, from the front end drivers to the link boards or during the optical data transmission.
On the other side, programming errors (and other defects) may not be discovered by this

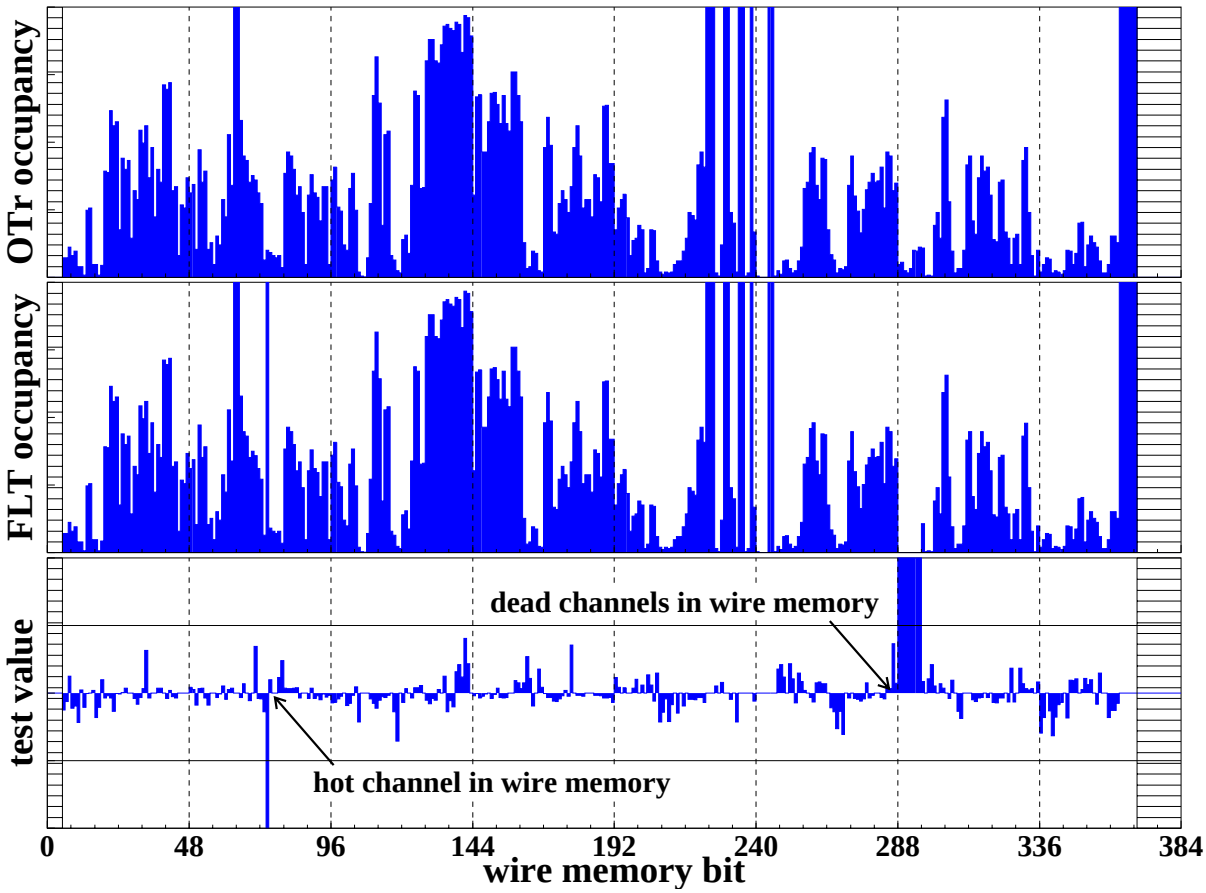

Fig. 3.1: Example for the validation of the programming of the link boards using characteristic occupancy patterns gained by a lowered ASD8 threshold [per01]. The topmost plot (OTR occupancy) shows the occupancy of the recorded outer tracker data after exercising the mapping in software. The next plot (FLT occupancy) shows the wire memory occupancy in the FLT hardware which has undergone the mapping in the link boards. The lower plot shows the difference (OTR occupancy) − (FLT occupancy). The differences (here denoted as hot and dead channels) point to problems in the mapping procedure of the link boards.

test since it depends on the randomly shaped occupancies caused by the lowered ASD8 threshold. A wrongly mapped channel may be not discovered if the ASD8 noise happens to be at a low or high level for that specific channel. Moreover, the set of channels which show an erroneous behavior changes over time. Therefore, additional effects have to be regarded in the following.

3.2 Stability of the Optical Data Transmission

The transmission of the data which is gained by the trigger links boards (TLBs) which apply the mapping procedure on the detector hit information was described in Sect. 2.3.4. The transmission is done using optical links which carry the signals of 48 wire memory channels each. One problem during the operation of the FLT in the year 2000 was the unstable performance of these optical links. It was necessary to test the transmission quality at the beginning of each run. In this section the evolution of the link behavior over several runs of the year 2000 data taking is analyzed.

runs	rate	date	run type
16993, 16995-16999, 17002, 17004	5 MHz	11.8.00	
17026-17032, 17034-17038	4 MHz	13.8.00	
17068, 17070-17074	5 MHz	15.8.00	pretrigger only run
17116, 17127, 17129-17134	2 MHz	17.8.00-18.8.00	first part of single lepton triggered runs
17154, 17155, 17157	5 MHz	19.8.00	
17160, 17163 17164, 17165 17166	5 MHz 10 MHz 15 MHz	19.8.00	FLT efficiency run
17168-17173	5 MHz	19.8.00	
17178-17181, 17183, 17184	5 MHz	20.8.00	
17185, 17187	4 MHz	21.8.00	

Table 3.1: List of runs which provide information about the link masking and wire memory occupancies. The runs are grouped according to HERA fills.

The transmission performance of the optical links is tested using redundant information in the data which is sent by the TLBs. The bunch crossing number, which provides a time stamp to the transferred hit information, is sent twice. In case the two bunch crossing numbers are not identical, the error counter is incremented. After a defined amount of time the error counters are read out and the number of errors is used as a measure of the link reliability. Links which show a significant above average error rate are not used and the corresponding wire memory channels are switched to one in order not to lose efficiency. This procedure is called *link masking*. Tracks which pass such regions of the wire memory are accepted if hits coincide in the remaining two stereo views. The information about the links which were not used is stored. For the runs shown in Table 3.1 this information

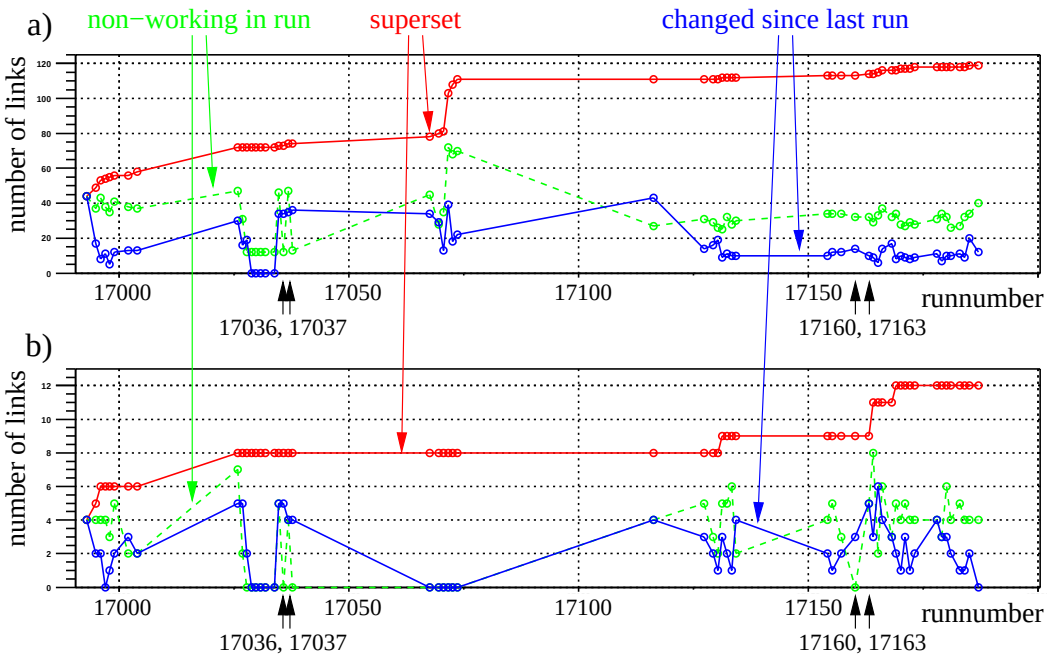

Fig. 3.2: Number of bad links versus the run number for a) OTR links and b) muon tube links. The uppermost line denotes the number of links which are in the superset of all links which are non-working in at least one run. Therefore the line represents a monotonic increasing function of the run number. The dashed line indicates the number of non-working links in a given run and the remaining line shows the number of links which have changed their status from working to non-working or vice versa. There are in total 764 links used in the outer tracker and 245 links in the muon tube system.

is available.

In order to investigate the stability of the link masking the number of non-working links is plotted versus the run number. In addition, the superset which accumulates the non-working links and the links which have changed from one run to the next are plotted. The results are shown in Fig. 3.2 a) for the links used for the OTR and in Fig. 3.2 b) for the links of the muon tube system.

One observes that despite the fact that the superset of all links which appear non-working in at least one run is quite high (about 120 links which is roughly 16% of all 764 used links of the outer tracker), the average number of non-working links in a given run is noticeably lower at a level between 15 and 40 links (which is 2% to 5% of all used channels). In contrast, it is worrisome to see the relatively high amount of links which change their status from one run to the next, even if they belong to the same fill and are timewise immediately consecutive. The quantity of changing links varies from zero to about 40 links. The four runs, however, which are analyzed in the next chapter reveal a more stable behavior. But still, for the runs 17160 and 17163 the amount of changing links is about a quarter of all non-working links.

For the links used for the muon pad system the results shown in Fig. 3.2 b) are similar to the outcome of the outer tracker links although on a lower level. The number of links in the superset of all links which show up non-working in at least one of the regarded runs is 12 which is just 5% of all 245 links used in the muon tube system.
As an example, Fig. 3.3 shows for run 17163 the found non-working links. It is taken care during the data taking that the non-working channels are not used and the corresponding wire memory channels[1] are set to one during the run. Since the links which were masked in that way during a given run are stored in the FLT data base the same method can be applied in the simulation. The relatively huge fluctuations of the links which are regarded as non-working from one run to the next may indicate that the same links do not work reliably even if they are not detected as non-working for a given run. This can explain discrepancies comparing FLT records gained by the FLT hardware to records obtained by running the FLT simulation on the same data.

3.3 Defective Channels and Generation of Masking

When simulating the FLT, either on real data or on Monte Carlo, one has to make sure that the wire memory content which is used by the simulation of the TFUs is as realistic as possible. The method which takes into account channels which behave erroneously is the *channel masking*. The masking contains the information about malfunctioning channels and is applied during the simulation of the FLT. We differentiate between *dead*, *noisy*, and *hot* channels. Dead channels show below-average occupancy while noisy and hot channels are characterized by an above-average occupancy. A more precise definition of these three categories will be given in the following. The channel masking is based on the statistical information about the wire memory occupancies. One one hand, the wire memory occupancy is taken into account that is directly measured in the hardware of the FLT. On the other hand, the hit information of the common data stream is used. Before going into more detail, the overall strategy of the masking is presented.
For the generation of the channel masking two different strategies are used depending upon whether the FLT simulation is supposed to run on Monte Carlo or on data. The masking which is used for Monte Carlo is based only on the wire memory occupancy which can be measured in the FLT hardware. The masking which is used for data additionally takes into account the occupancies as given in the common data stream.
Fig. 3.4 illustrates the strategy for the masking which is used for Monte Carlo. The measured WiM occupancies as given in the hardware are analyzed and the dead, noisy, and hot channels are extracted. The channel masking contains not only the location of the defective channels but also the measured occupancies. During the simulation of the FLT, first the Monte Carlo hit information of an event is loaded into the simulation. Then the masking is taken into account: the hit information of channels which are dead or hot is discarded. Instead the occupancies which are stored in the masking for that channels

[1] One link corresponds to up to 48 channels of the wire memory. However, if the link is assigned to the first or last part of the wire memory acceptance it may represent a smaller number of channels.

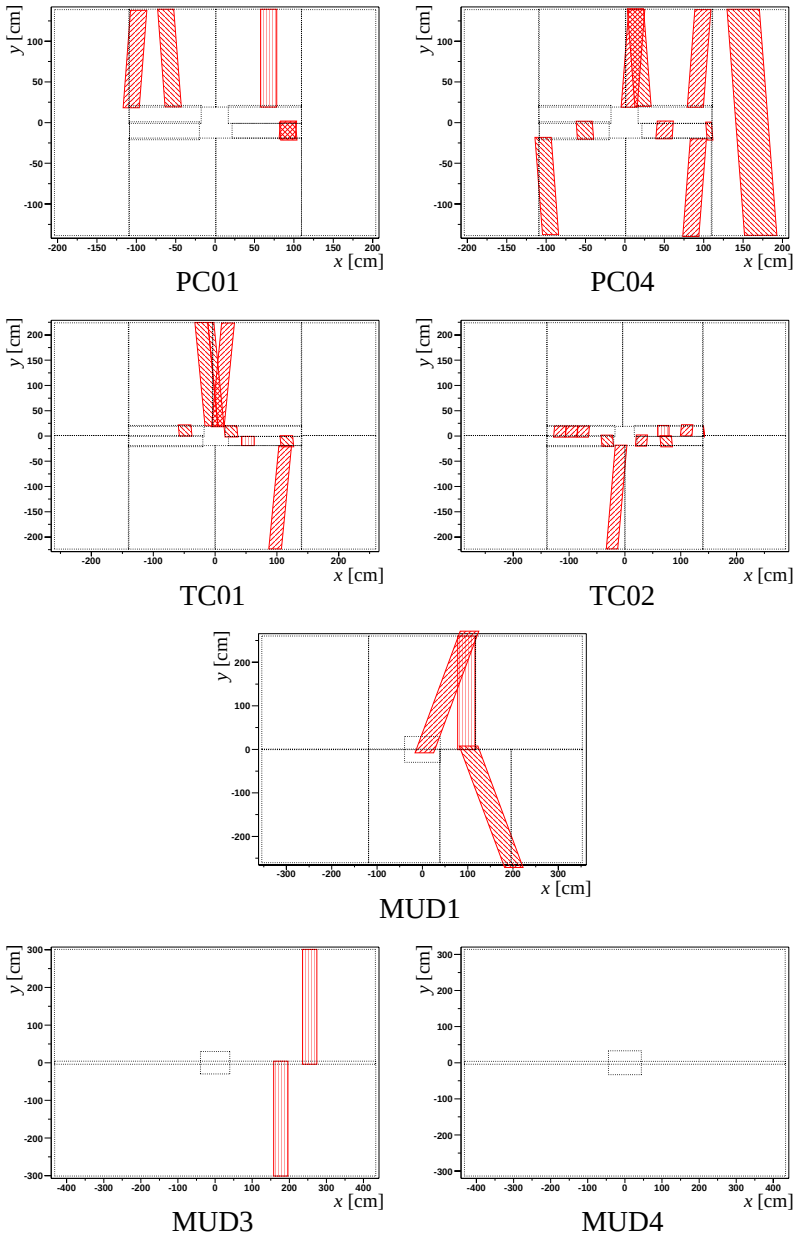

Fig. 3.3: Map of masked links in run 17163. Each optical link carries the hit information of at maximum 48 channels (with exception to those which are assigned to the boarders of used range of the wire memory). Thus each masked link is represented in this plot by a shaded area that covers the acceptance of the corresponding channels. There is no geometrical accumulation visible and only few regions which are covered by non-working links in more then one stereo view.

are used to randomly generate hits such that on average the same occupancy is obtained as measured in the hardware. Noisy channels are treated slightly differently. The Monte

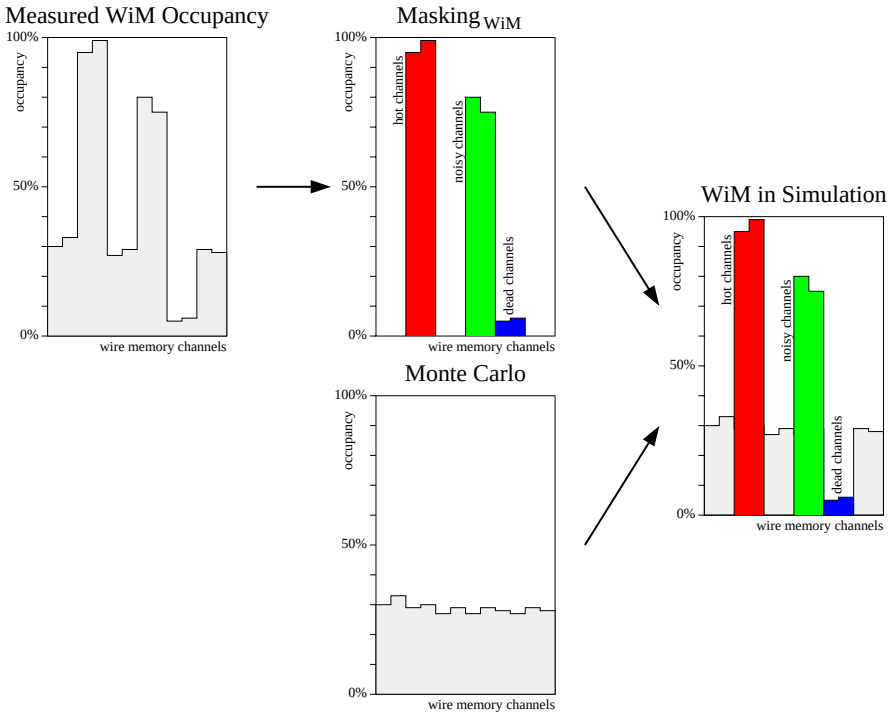

Fig. 3.4: Generation of the channel masking which is used for running the FLT simulation on Monte Carlo. The masking is based on the measured WiM occupancies. It contains the information of the defective channels. In the simulation the Monte Carlo hit data is combined with the masking such that the occupancies of the simulated WiM is similar to the measured WiM occupancies.

Carlo hit information is not discarded. Instead, additional hits are randomly generated such that again the same occupancy as observed in the hardware is obtained.

The situation changes slightly when the FLT simulation is used on real data as indicated in Fig. 3.5. First the same channel masking as in the Monte Carlo case is generated. Additionally a similar masking is obtained by applying the mapping procedure on the hit information which is given in the common data stream for the same period of data taking.

The masking which is based on the wire memory measurements contains defects which arise from both detector defects and data transmission defects. The masking which uses the hit information of the common data stream only contains defects of the detector. In contrast, it does not contain the channels which behave erroneously due to the data transmission which is specific to the FLT.

This difference was already presented in Fig. 2.21. The transfer of the hit information is split up at the stage of the front end drivers. The hit information is sent to the linkboards which apply the mapping procedure. After this the data is forwarded to the TFUs via optical links. The data which is stored in the common data stream is, in contrast, read out by the data acquisition system.

Taking these two maskings together allows for the generation of a third masking which

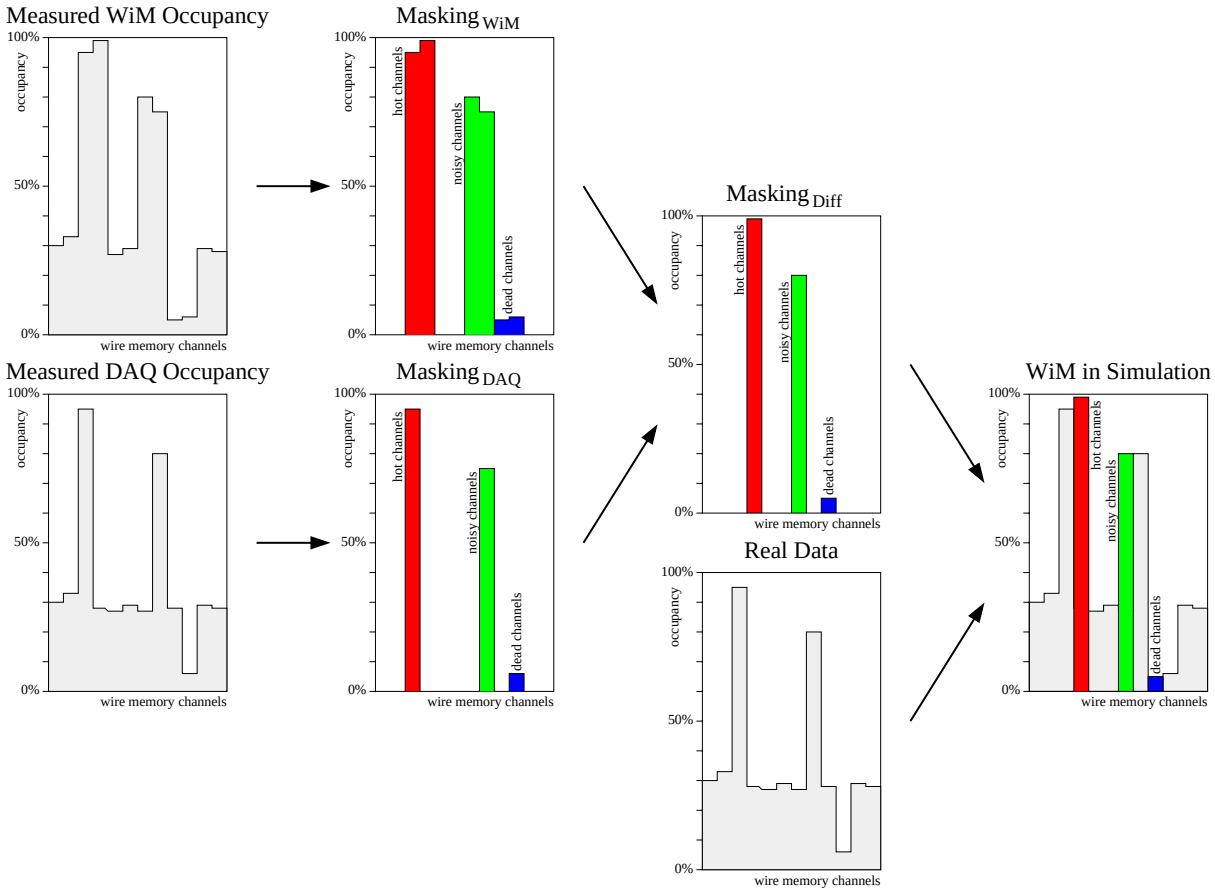

Fig. 3.5: Generation of the channel masking which is used to run the FLT simulation on data. First, the maskings which are based on the measured WiM occupancies and on the occupancy as given in the common data stream (DAQ) are built. Second the differential masking is generated which contains the channels which are contained in the WiM masking but not in the DAQ masking. This differential masking is then used for running the simulation on data.

is based on the difference of the two maskings. Only channels which are reported to be defective in the measured wire memory occupancies but not in the common data stream are included in this combined masking. When using this masking in the simulation of data the detector defects are taken into account since they are present in the hit data of the common data stream. The defects of the data transfer (and only those defects) are taken into account by the combined masking.

In the following the analysis of the occupancies of the wire memories is described and the results and the generation of the maskings are presented.

Wire Memory Occupancies

In the following the wire memory occupancies are used for the generation of the masking. In this section the methods are described which are used to get them. Both methods that are used only provide a statistical information about the wire memory occupancy. The hit information could not be regarded on an event by event level. In contrast, the hits are accumulated over a certain time and the frequency of hits during that period is the basis of the analysis[2].

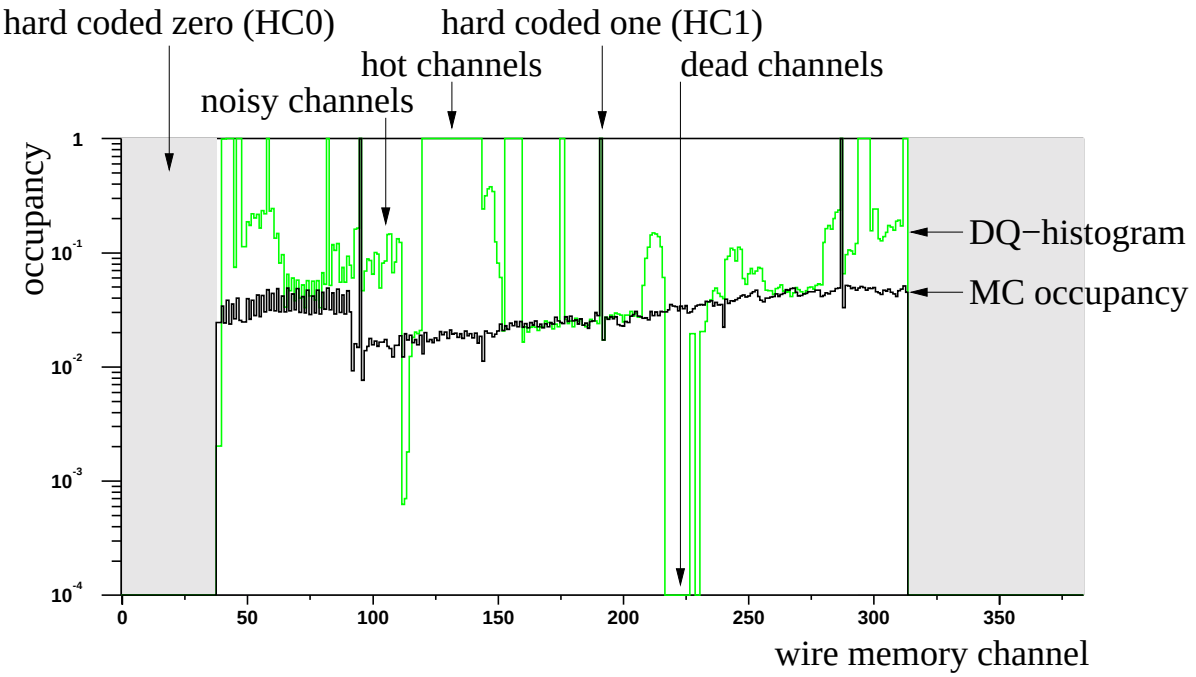

Fig. 3.6: Example of the occupancy (green) of a wire memory as recorded at the start of a run in the data quality histograms. For comparison the occupancy (black) as expected by Monte Carlo is also given. The three kinds of defective channels — dead, noisy and hot — are indicated. The shaded areas indicate the hard coded zero channels which are not used in that particular wire memory. The hard coded one channels are always one due to mapping reasons.

One source of information is the direct readout of the wire memories of the TFUs in the hardware. For bandwidth reasons this is unfeasible during common data taking. In contrast, before the start of a run it is possible to take a dedicated set of 2560 minimum bias events and to store the resulting wire memory occupancies in the *data quality histograms*[3] (DQ-histograms). The complete set of runs in the year 2000 for which this information is

[2]Future plans aim for a comparison of the wire memory content in the TFUs and the hit information of the data acquisition on an event basis, the *Event By Event Comparison*.

[3]During the running of 2000 it was the common method to log the condition of the detector in histograms which are stored in ROOT-files (one per run). The wire memory occupancies of the OTR TFUs are stored since run 16993.

available is shown in Table 3.1. This occupancy information was stored in 2000 only for the TFUs assigned to the outer tracker.
Alternatively, the occupancies of the common data stream hit information is used. In order to be able to compare the hit information of the common data stream to the occupancies which are gained by the readout of the TFUs in the hardware the mapping procedure has to be done in software. For this purpose the FLT simulation is run on the data which has to be analyzed. The FLT simulation applies the same mapping procedure on the hit information which is stored in the common data stream which is applied by the trigger link boards to the hit information of the front end drivers. The wire memory contents which are in this way reconstructed are accumulated over the full run and the occupancies are stored. These reconstructed occupancies are similar to those which are generated at the beginning of the runs. The only difference is that they only contain defects which arise in the detector and the front end electronics, while the occupancies which are stored in the data quality histograms also contain the effects of the link boards and the optical data transmission.
Fig. 3.6 depicts an example of the occupancy of a wire memory and compares it to the occupancy which is expected by Monte Carlo. Occupancy plots which are based on the common data stream look similar. The three kinds of defective channels are indicated. While the noisy channels show an occupancy which is by a factor of at least two higher than the Monte Carlo expectation, the dead and hot channels have an occupancy of almost zero or one, respectively.

Definition of Dead, Noisy, and Hot Channels

Malfunctioning channels in the detector or problems during the transmission of the hit information lead to an obviously incorrect behavior of wire memory contents. Looking into the wire memory occupancies one can distinguish channels which have an occupancy of almost zero (*dead channels*), channels where the occupancy is too high compared to the Monte Carlo expectation (*noisy channels*), and channels which have an occupancy of almost one (*hot channels*). We denote them in summary as *defective channels*.
In order to quantify these categories the channel occupancies are compared to Monte Carlo. The actual channel occupancies strongly depend on the position in the detector acceptance. The density of charged tracks follows roughly a $1/r$ distribution, where r is the distance to the proton beam. Therefore the occupancies of channels is higher the closer they are situated to the proton beam. Because of this it is not possible to establish common occupancy cuts for all channels for the definition of defective channels. The alternative is to compare the occupancies to the Monte Carlo expectation.
A Monte Carlo reference sample is generated by running the FLT simulation on 10000 Monte Carlo generated minimum bias events. The simulated wire memory contents are accumulated during the simulation and provide the expected occupancy for each single wire memory channel. In this way not only the occupancy dependence on the location of the corresponding detector cells is taken into account but also the impact of the mapping procedure is included. For example the channels of the minus stereo view have a higher

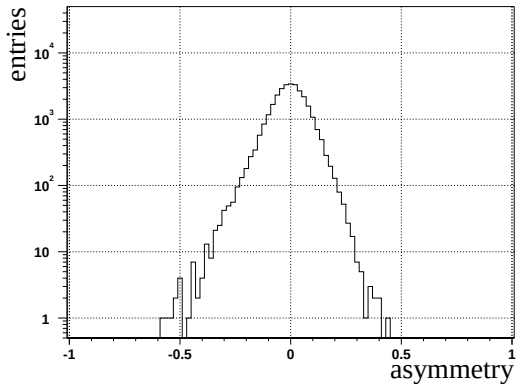

Fig. 3.7: The asymmetry $a = (occ_{\mathrm{MCII}} - occ_{\mathrm{MC}})/(occ_{\mathrm{MCII}} + occ_{\mathrm{MC}})$ of channel occupancies of two distinct Monte Carlo samples of minimum bias events.

occupancy than channels of the other stereo views because of the or-ing of adjacent channels which is applied in that stereo view.
The occupancies which are gained in this way are object of statistical fluctuations. In order to estimate the amount of the fluctuations a second Monte Carlo sample is used. This second sample is distinct to the first and is generated using a different random seed. The two resulting occupancy sets (for each wire memory channels two occupancy values for the two Monte Carlo sets each) are compared. For each wire memory channel the asymmetry a of the two occupancies occ_{MC} and occ_{MCII} of the two Monte Carlo sets is calculated

$$a = \frac{occ_{\mathrm{MCII}} - occ_{\mathrm{MC}}}{occ_{\mathrm{MCII}} + occ_{\mathrm{MC}}} \tag{3.1}$$

The asymmetries of the wire memory channels of the two Monte Carlo sets are histogramed in Fig. 3.7. The distribution peaks at zero indicating that on average the occupancies are the same in both Monte Carlo sets as expected. Due to the fluctuations in the occupancies the distribution has a certain width. As is visible from Fig. 3.7 the distribution is spread from asymmetry values of $a = -0.5$ to $a = +0.5$. This values will be used in the following to define dead and noisy channels. Channels of an occupancy of less than a third (corresponding to an asymmetry of $a = -0.5$) of the expected Monte Carlo occupancy will be counted as dead channels. Channels of an occupancy of more than three times (which is equivalent to an asymmetry of $a = +0.5$) of the expected Monte Carlo occupancy are counted as noisy channels. In addition, hot channels are defined as having an occupancy of more then 98% which will be motivated in the following. Channels which are hot are of course not additionally accounted to the noisy channels. The definitions of the defective channels are summarized in Table 3.2.
In the following these cuts are applied to the occupancies which are available from the direct readout of the wire memories in the hardware and from the reconstruction of wire memories which is based on the hit information of the common data stream.
The evaluation of the occupancies of the readout of wire memories in the hardware using the data quality histograms is shown in Fig. 3.8. The histogram of the measured occu-

dead channels			occ	$<$	$\frac{1}{3} \cdot occ_{\mathrm{MC}}$
noisy channels	$3 \cdot occ_{\mathrm{MC}}$	$\leq$	occ	$<$	0.98
hot channels	0.98	$\leq$	occ		

Table 3.2: Definition of dead, noisy, and hot channels. The Monte Carlo occupancy occ_{MC} is the occupancy that is expected from a Monte Carlo data set.

pancies of the wire memory channels shows a peak for occupancies above $occ > 98\%$, see Fig. 3.8 a). Most entries of this peak are at an occupancy level of exactly $occ = 100\%$, indicating that they deliver always a signal. This observation motivates the definition of the hot channels which was already given in Table 3.2.

Fig. 3.8 b) shows the asymmetry of the measured wire memory occupancies to the expected wire memory occupancies. In order to be able to compare the measured and the Monte Carlo generated occupancies the occupancies which are gained by Monte Carlo are scaled such that the average occupancy is the same as in the measured occupancies. Therefore the distribution shows a central peak at an asymmetry of $a = 0$.

For a better comparison the asymmetry distribution of Fig. 3.7 which is obtained by the two distinct Monte Carlo data sets is overlayed in Fig. 3.8. The distribution of the measured asymmetry is broader compared to the Monte Carlo generated distribution. This is due to the influence of noise and defective behavior in the hit data transmission.

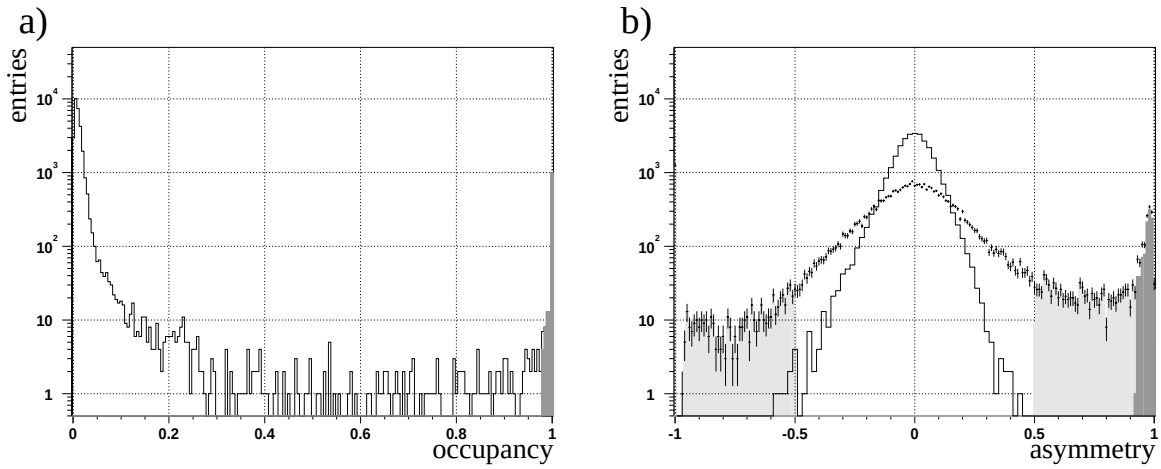

Fig. 3.8: Figure a) shows the histogram of the occupancies of the wire memories as measured in run 17116. The shaded peak at $occ = 1.0$ indicates the hot channels. In figure b) the entries carrying error bars depict the asymmetry of the measured occupancies and the occupancies as expected by Monte Carlo. For comparison the asymmetry of the two distinct Monte Carlo sets is given by the solid line (same as in Fig. 3.7). The defective channels are shaded. In the interval $a = -1.0.. - 0.5$ the dead channels can be seen. In the interval $a = +0.5.. + 1.0$ the noisy (light shaded) and the hot channels (dark shaded) are visible.

The dead, noisy, and hot channels are marked according to Table 3.2.

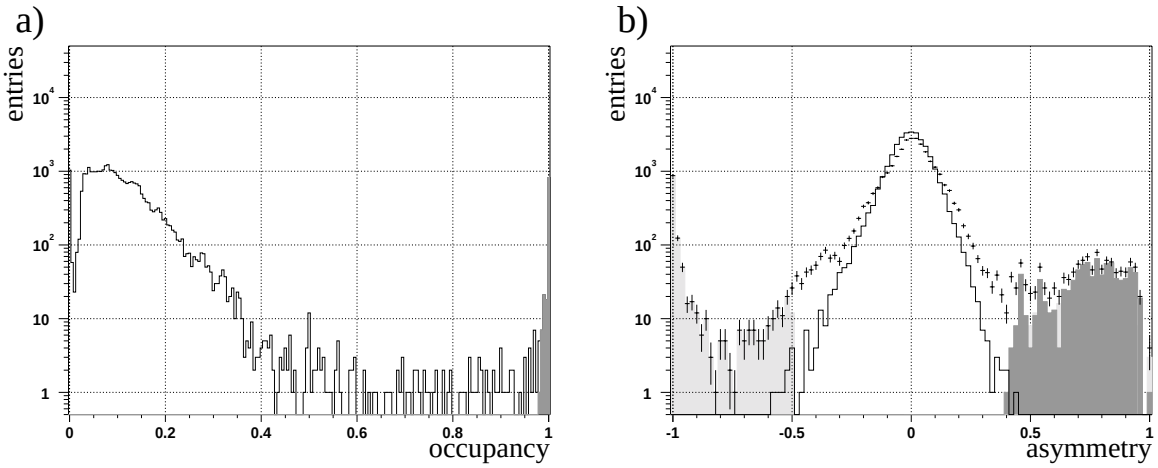

Fig. 3.9: Figure a) shows the histogram of the reconstructed occupancies of the wire memories using the hit information of the common data stream of run 17116. The shaded peak at $occ = 1.0$ indicates the hot channels. In figure b) the entries carrying error bars depict the asymmetry of the reconstructed occupancies and the occupancies as expected by Monte Carlo. For comparison the asymmetry of the two distinct Monte Carlo sets is given by the solid line (same as in Fig. 3.7). The defective channels are shaded. In the interval $a = -1.0..-0.5$ the dead channels can be seen. In the interval $a = +0.5..+1.0$ the noisy (light shaded) and the hot channels (dark shaded) are visible. The hot channels overlap the noisy channels almost completely.

Fig. 3.9 shows similar plots for the case of the reconstructed wire memory occupancies based on the hit data which is stored in the common data stream. The main difference is that the events are triggered while the events which are used during the direct readout of the wire memory channels are minimum bias events. Therefore in case of the reconstructed occupancies the average wire memory occupancy is higher. This can be seen when comparing the histogram of the occupancies of both cases, Fig. 3.8 a) and Fig. 3.9 a). Nevertheless, the behavior of the channels which have an occupancy close to unity has not changed.

The asymmetry of the reconstructed and the Monte Carlo generated wire memory occupancies are given in Fig. 3.9 b). Again the Monte Carlo occupancies are scaled such that the average occupancies match resulting in the peak at $a = 0$. Due to the larger statistics the central part of the distribution is more narrow. The dead channels show, in contrast to Fig. 3.8 b), a pronounced peak at $a = -1.0$. This indicates that in the case of the direct measurement even dead channels show an occupancy slightly above zero. This can only be explained by additional noise in the data transmission via the optical links. On the other side the hot channels cover the same region as the noisy channels. This can be understood by the fact that the average occupancy is significantly higher during the direct readout of the wire memories since triggered events are used.

The information which is stored in the masking, besides the identifier of the defective channel, is the observed occupancy. As discussed in the case of dead and hot channels the hit information which is given to the FLT simulation is not used. Instead the occupancy which is measured in the direct readout of the wire memories is the basis of a randomly generated hit. In this way the channels in the simulation are not simply switched to zero or one if they are dead or hot due to the masking but rather the measured hit probability is reproduced.
For the noisy channels both the measured and Monte Carlo generated channel occupancy are stored by the masking. The difference of these two values is then used to generate hits such that, first, hits which are given to the simulation are used and, second, the measured wire memory occupancies are reproduced.
In order to give an impression of the amount of defective channels Fig. 3.10 shows the positions of dead, noisy, and hot channels in TFUs of the four outer tracker superlayers. The figure makes clear that during the data taking of the year 2000 there is almost no area of the FLT acceptance which does not contain some defective channels in one of the used superlayers. This is especially a problem in the case of the noisy channels since it is not possible to reconstruct using the hit information whether a wire memory channel was active or not in a certain event. This will limit the possibility to match the recorded FLT tracks to the reconstructed FLT tracks which are gained by running the simulation of the same data which is the subject of Chapter 4.

Stability of Defective Channels in the Data Quality Histograms

In this section the the stability of the defective channels will be investigated as they appear in the direct readout of the wire memory channels. Therefore we have to survey the defective channels in the runs which are listed in Table 3.1. We use the following criterion for the stability of dead, noisy, and hot channels, respectively: For each run the dead, noisy and hot channels are determined. In order to judge the stability of the defective channels the channels which appear defective in the runs are compared. In a second step we scan these sets of channels for all runs of Table 3.1 and calculate the superset of all defective channels in each category of the run of interest and all preceding runs. The superset registers all channels which are defective in at least one run and gives an impression of the quantity of channels which tend to behave erroneously. Moreover, we select the channels which have changed their status from defective to non-defective or vice versa, which reveals the short-term stability. Channels that belong to a non-working link are not taken into consideration.
An overview of the development of the defective channels as measured in the wire memories of the TFUs in the hardware is given in Fig. 3.11. The number of defective channels, the number of channels in the accumulated superset and the number of channels which have changed their status since the last regarded run are shown.
It is remarkable that within a series of runs of the same HERA fill the defective channels stay relative constant but vary from one series of runs within one fill to the next. There is only one exception to this observation; namely, in the dead channels during the runs from

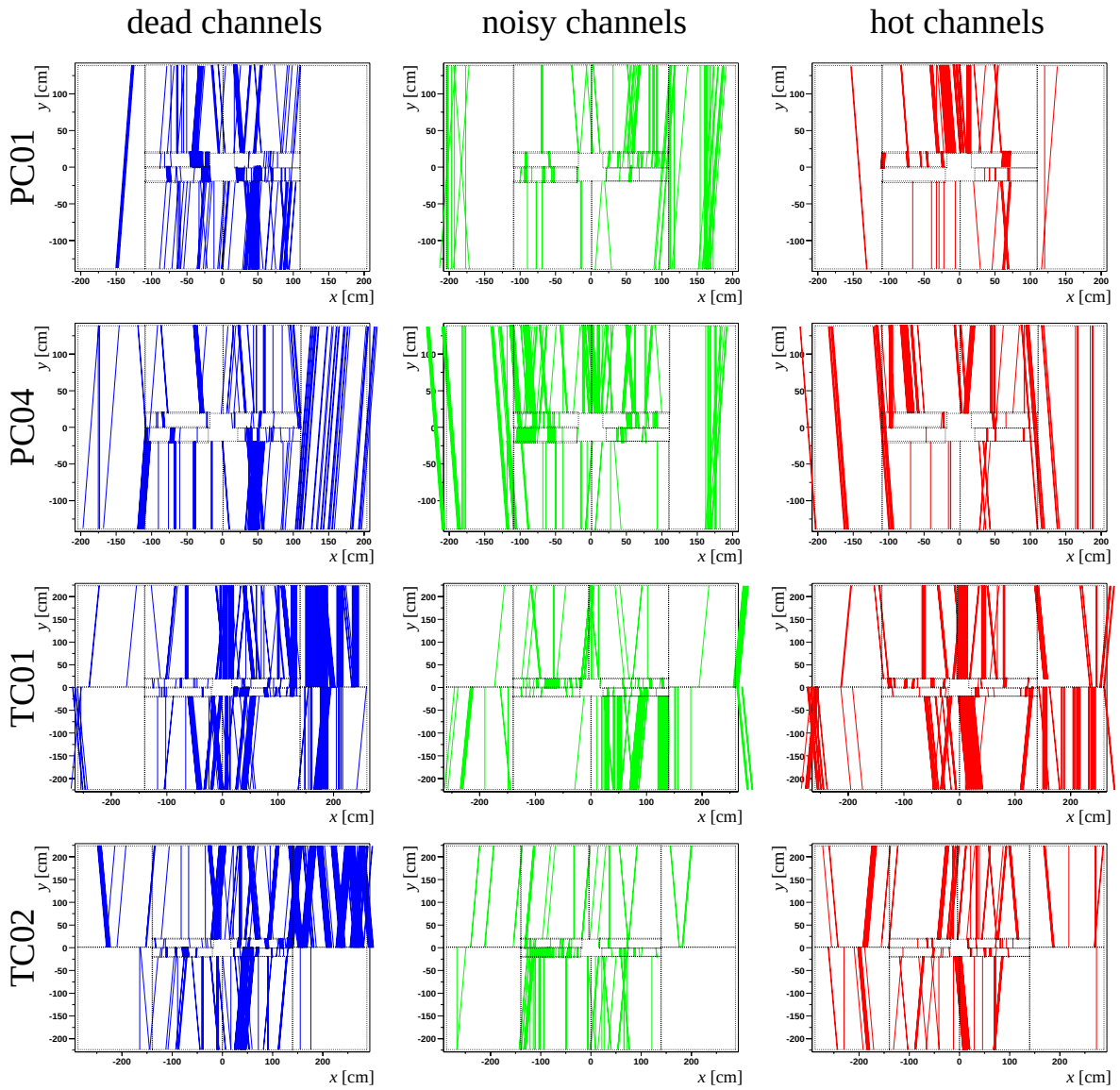

Fig. 3.10: Map of channels which are dead, noisy, or hot in the data quality histograms but not in the common data stream of run 17116. It is visible that the amount of noisy channels is higher than for dead and hot channels. Moreover, this figures make clear that the complete acceptance - with exception to the outermost regions - is covered by noisy channels in at least one superlayer.

17127 to 17134. The runs 17164-17166 are not included since they have higher target rates of 10 MHz and 15 MHz, which leads to an increase of the noisy channels. All other runs which are considered here have target rates of at maximum 5 MHz. Another observation is that the stability of the dead and hot channels is significantly higher that the stability of the noisy channels.

The conclusion from these results is that the dead and hot channels as observed in the

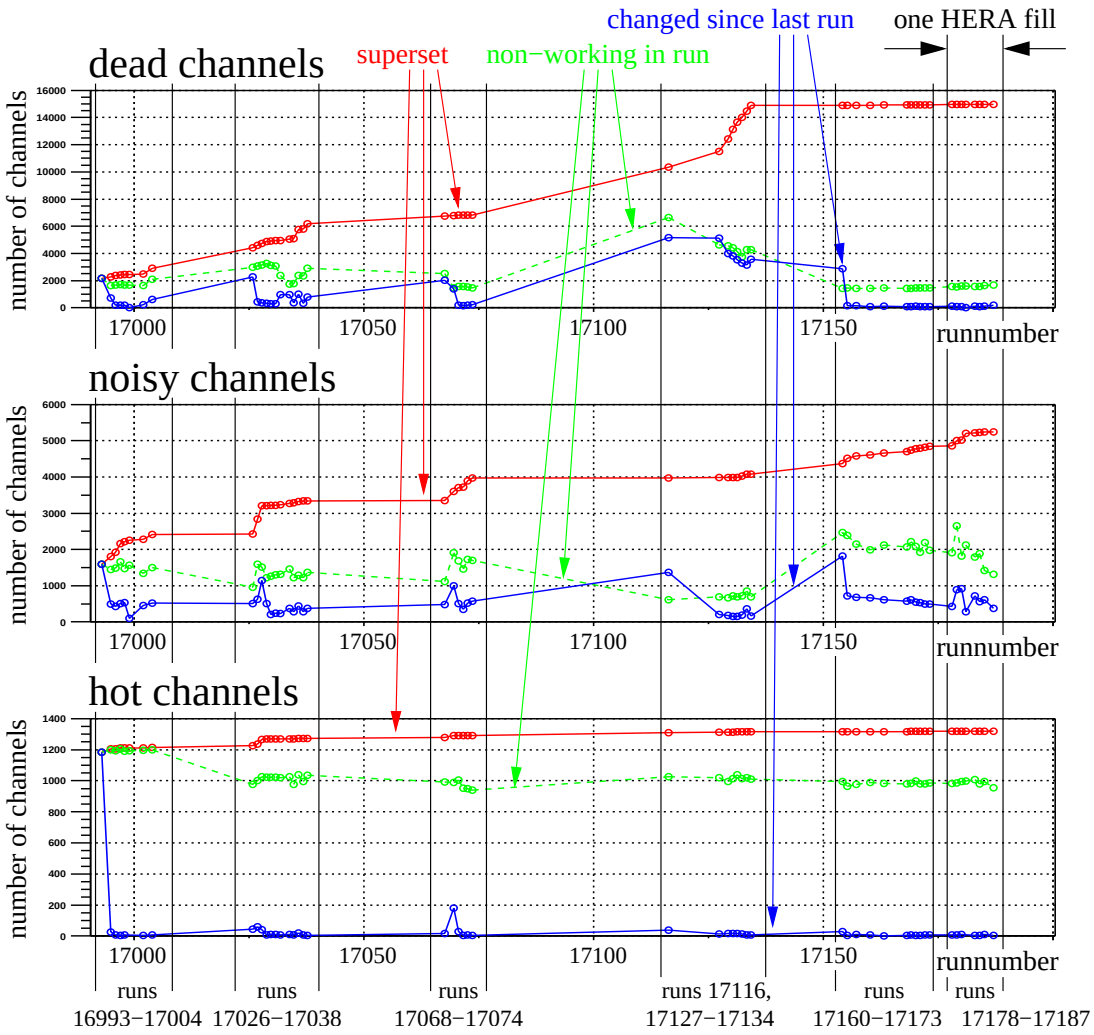

Fig. 3.11: Stability of defective channels as directly measured in the wire memories in the hardware. The three diagrams represent, from top to bottom, the dead, noisy and hot channels. The plots include all runs which provide information of the wire memory occupancies by the data quality histograms except for the runs 17164-17166. The three different entries in the plot show the number of defective channels, the accumulated superset of channels which appear defective in at least one run and the number of channels which have changed since the last regarded runs. At the bottom the length of the different HERA fills are indicated.

readout of the wire memories in the hardware are stable during several successive runs. This allows for the assumption that this is also true during each run. Moreover, the method of applying a masking which is based on the readout of the wire memories makes sense because of the observed stability. In contrast, the extrapolation to a run that does not belong to the same HERA fill is not acceptable since the defective channels change if longer time scales are regarded.

Stability of Defective Channels in the Data Acquisition

The result of the preceding section indicates that the set of defective channels stays constant within close boundaries as far it can be judged from the readout of the wire memories in the hardware which provide a snapshot of the occupancies at the begin of a run. An orthogonal test can be done by using the reconstructed wire memory occupancies based on the hit information of the common data stream. The stability — both within one run and between different runs — will be investigated in this section.
Fig. 3.12 gives an overview of the stability of the defective channels within the regarded runs. Moreover, the stability between the runs can be seen. From each of the runs 17036, 17037, 17160, and 17163 five slices are selected. The stability is defined by the ratio of channels which have changed their status (from defective to non-defective or vice versa) to the accumulated channels which have been defective at any time. Using this definition over the runs and the corresponding slices the stability is a monotonic decreasing

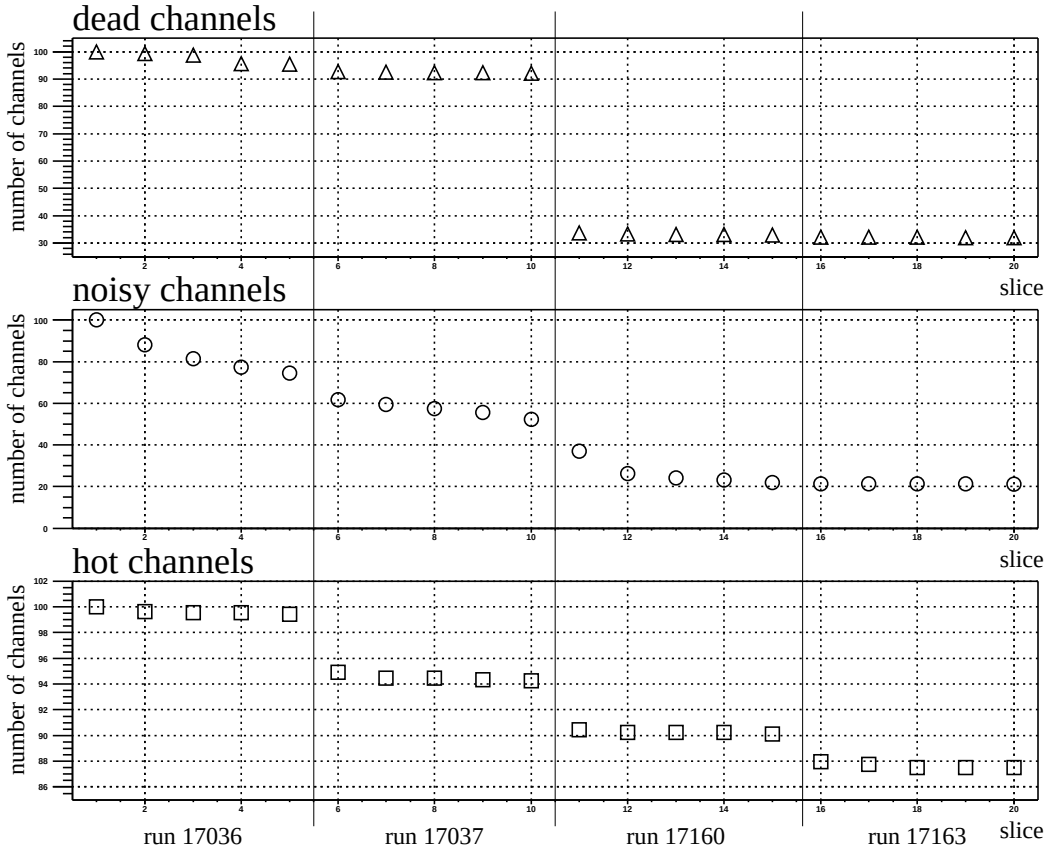

Fig. 3.12: Stability of defective channels in the common data stream. The histograms show the ratio of defective channels which have not changed their status. For the runs 17036, 17037, 17160 and 17163 time slices are used to estimate the stability of the defective channels within a run. Please note the different scales for the different channel categories.

run	stability of		
	dead	noisy	hot
17036	95.0%	68.8%	98.9%
17037	97.8%	63.5%	98.7%
17160	97.9%	68.2%	99.3%
17163	96.5%	56.8%	98.4%

Table 3.3: Stability of dead, noisy, and hot channels within the runs 17036, 17037, 17160, and 17163. The stability is defined as the ratio of the number of defective channels which appear in all regarded slices of a given run to the number of defective channels which are observed in at least one slice of the run.

function. The development of the stability shown in Fig. 3.3 proves that the stability of dead, noisy, and hot channels is on a high level since it does not change significantly during one run (except for the noisy channels whose definition is much more sensitive to statistical fluctuations). This is shown more precisely in Table 3.3 which displays the stability for each run separately under consideration of all slices of each run. The stability of the dead and hot channels within each run is at a level of 97% and 99%, respectively. The stability of the noisy channels is significantly lower but this can be again understood by the sensitivity of the definition of the noisy channels.
The conclusion from this result is that the choice of the cuts on the defective channels is reliable and selects a well-defined set of channels. The results of the investigations of the defective channels based on the data quality histograms and on the hit information stored by the data acquisition agree with each other.

Comparison of Defective Channels in WiM Readout and Common Data Stream

Finally, the maskings which are gained from the wire memory readout and the common data stream are combined in order to obtain the masking which can be applied to the simulation of the FLT on data. The procedure of the generation of the combined masking has been described in Sect. 3.3.
Table 3.4 gives an overview of the maskings which have been obtained by the described methods. For the runs which will be used in the remaining chapters of this thesis the masking is characterized by the number of masked channels. The maskings of the runs 17036, 17037 and 17160, 17163 will be used in Chapter 4 for the comparison of recorded and simulated FLT tracks. In that case the simulation will be run on data and the masking which is used is based on the difference of the defective channels which are observed in the common data stream and in the wire memory readout.
The runs 17116 to 17134 will be analyzed further in Chapter 5. The masking which is used on Monte Carlo is only based on the wire memory readout. The influence of the fluctuations of the masking on the FLT tracking efficiency will be studied using the series

run	WiM readout			difference of common data stream and WiM readout		
	dead	noisy	hot	dead	noisy	hot
17036	2290	1461	1039	459	1132	239
17037	2258	1370	995	484	1020	233
17116	1768	1201	1026	652	992	232
17127	1875	1304	1022	579	1087	237
17129	1694	1214	997	469	897	236
17130	1675	1321	1015	549	1106	233
17131	1686	1259	1039	581	1045	235
17132	1730	1255	1013	648	1041	234
17133	1716	1489	1022	629	1281	232
17134	1729	1246	1012	636	1030	232
17160	1518	1553	989	471	1104	233
17163	1538	1525	984	487	1070	237

Table 3.4: Number of masked channels in the maskings for runs 17036, 17037, 17160 and 17163 for each category. They correspond the the number of channels which are found to be defective in the data quality histograms but not in the common data stream. Comparing the numbers of masked dead and hot channels indicates the stability of the masking. The channel masking which is based on the wire memory readout is used in the Monte Carlo studies in Chapter 5. The masking which uses the difference of common data stream and the wire memory readout is used for the comparison of recorded and simulated FLT tracks in Chapter 4.

of maskings which are obtained from these runs.

Masking of the Channels of the Muon Tube System

Since the wire memory occupancies which are measured at the beginning of each run are only available for the outer tracker TFUs there is no possibility to generate an equivalent masking for the muon tube system as is done for the outer tracker. For the processing of real data only the defects of the muon detector itself are taken into account since they are present in the hit information. On the other hand for the processing of Monte Carlo the only way to take into account these defects is to use a masking file that is provided by the muon group. Both ways of processing inevitably do not take account of defects in the transmission of the hit information from the muon front end drivers to the TFUs. Nevertheless, the problems in the transmission of the muon tube hit information are expected to be smaller that in the outer tracker case. First, the mapping of the muon

chambers to the wire memory channels is simpler since there is only one granularity. Second, the result of the survey of the performance of the optical links showed that the links of the muon system work more reliably than those which are assigned to the outer tracker.

Chapter 4

Matching Efficiency of Online and Simulated FLT Records

This chapter discusses the reproducibility of the trigger decision of the FLT during data taking. The tracks which are reconstructed online by the FLT are compared to the result of the FLT simulation which is performed using the detector data which is stored by the data acquisition system. The analysis of the online reconstructed tracks and the comparison to the result of the simulation makes it possible to detect erroneous behavior of the system during data taking. The comparison of reconstructed tracks of both the hardware and the simulation allows an estimation of the reliability of the system. Since the algorithm of the FLT has been proven to perform identically in hardware and simulation, the observed discrepancies have to be assigned to shortcomings in the hit data transmission.

4.1 Used Runs and Event Selection

For the comparison of online and simulated FLT records the runs 17036, 17037, 17160, and 17163 are used, see Table 4.1. These are FLT efficiency runs. During data taking the FLT was turned on and the FLT record was stored by the data acquisition but not used for triggering. In contrast, the SLT was running an ECAL pretrigger emulation and its own track finding in order to enrich the sample. The usage of the ECAL pretrigger emulation on the level of the SLT was necessary since the FLT during the year 2000 was only capable to either operate in the regular tracking mode or in bypass mode which just forwards the pretrigger messages to the SLT[1].
During the simulation, the following event classes are ignored:

- The hit information in the wire memories is associated to the events using the bunch crossing number. Within the FLT network the bunch crossing number has values

[1] In the future, this changes since a second TDU is foreseen to send the pretrigger messages to the SLT. In this setup the SLT and the data acquisition receives both the pretrigger messages and the FLT record which will save computing time on the level of the SLT and allow a more detailed testing of the FLT tracking.

run	date	rate	number of events				
			all	bx zero	wrong bx	out of time	used
17036	13.08.00	4 MHz	29317	127	603	3063	26035 (89%)
17037			24940	148	338	1966	22832 (92%)
17160	19.08.00	5 MHz	19454	57	332	1599	17799 (91%)
17163			51141	208	18	2056	48887 (96%)

Table 4.1: FLT efficiency runs used in this analysis. The difference of the number of events and the number of used events is defined by a event selection which rejects events that have a physical bunch crossing number of zero or of an empty bunch and events that are probably coasting beam events due to an exceptional outer tracker timing. The first and second two runs are taken during two different HERA fills.

of 0 to 255. It has been observed that the wire memory content is not correctly filled for events which have the bunch crossing number zero. Such events are therefore not taken into account.

- Events which belong to empty bunches. They are suppressed in this study since the timing of the outer tracker is most likely not usable. In the case of the FLT, which only uses the hit information, the assignment of the hit data to a certain bunch crossing may be ambiguous.

- In events that belong to filled bunches the outer tracker timing may indicate that the interaction was not caused by the main bunch but by a satellite bunch or coasting beam. Also these events are not used.

Especially for the comparison of the FLT record to the simulated FLT tracks, the cuts have to be applied since a vague timing information may lead to additional discrepancies in the wire memory content in the TFUs during the data taking and in the simulation. In total 4% to 11% of the events are discarded, depending on the run in question. The statistics of these event classes, as well as the number of used events, are listed in Table 4.1.

4.2 The Test Vector Test

One way to verify to correspondence of hardware and simulation is the *test vector test* [mic02]. The test vector test was done during the HERA shutdown in the year 2001 after the acquisition of the runs which are considered in this thesis. The test allows one to put and process the same hit information and the same pretrigger messages in the hardware and in the simulation. The pipeline contents of the boards can be set to arbitrary values and read out again after the processing. Interpreting the pipeline content as a vector gives the notion of *test vectors*. Afterwards the output of the FLT hardware can be compared to the simulation. This procedure offers the opportunity to fix possible

discrepancies of hardware and simulation on a bit level given that all information which the FLT receives are identical in hardware and simulation. Later in this chapter we will focus in addition to the problems arising from data transmission errors both in the internal FLT data transmission and in the transmission of hit information from the detector to the FLT.
The differences which were observed during the test vector test were removed and the final conclusion of the test is that the simulation and the hardware work identically at the bit level with the exception of the following points:

- The coincidence matrix (see Sect. 2.4.3), which is part of the TFU, searches the coincidences in the hit patterns of the three stereo views. As described in Sect. 2.3.5 there are in general channels at the beginning and the end of the wire memory which are not used for geometrical reasons. In the simulation these channels are set to zero while in the hardware it happens that these channels contain arbitrary values. This leads to unphysical coincidences and, in case of a message corresponding to a region of interest reaching into these areas of the wire memory, unphysical messages are produced. Most likely these artificial messages are not updated in the following superlayers. But some fake tracks may survive the tracking algorithm. The result are additional tracks in the hardware which cannot be reproduced in the simulation.

- The message boards send the messages asynchronously from the TFUs of one superlayer to the TFUs of the next superlayer. The inevitable phase differences of clocks of the message boards lead to an unpredictable ordering of the messages. Only a rough estimation of the latency of the messages can be simulated which allows an estimation of the delay of messages in very busy events. In both the TPU and the TDU all incoming tracks are compared to the preceding tracks of the event in order to reject clones. At this point the order of the messages becomes important since the order of two similar tracks decides about which track will be rejected and which survives the clone removal. This results in an irreproduceable rejection of similar tracks in the TPU and TDU in the simulation. Nevertheless, tracks which survive the clone removal are similar to the rejected tracks. Thus a comparison of tracks of the hardware processing and of the simulation may fail on a bit level but succeed if less strict matching criteria are applied.

Except for these two points it has been proven that the simulation reproduces on the bit level the messages which are observed in the hardware given that the same hit information is fed into the wire memories and that the same pretrigger messages[2] are applied.
In the following we assume that the correspondence that was shown in the test vector test also holds during the running of the FLT network during triggering, i.e. that the lookup tables and the logic of the boards and their simulation match.

[2]The pretrigger hardware was not included in the test vector test.

4.3 Bit Errors in the FLT Record

Before we focus on the clone removal a basic comparison of tracks of one FLT record is performed. In order to avoid double counting of clones the analysis is restricted to events that contain exactly two tracks. Most probably these tracks are clones but they may of course also be different. A kinematical cut on the momentum of $P > 5.0\,\mathrm{GeV}$ and on the transverse momentum of $p_\mathrm{T} > 1.0\,\mathrm{GeV}$ of the tracks is applied. This is done in order to improve the quality of the tracks which are used in this test.

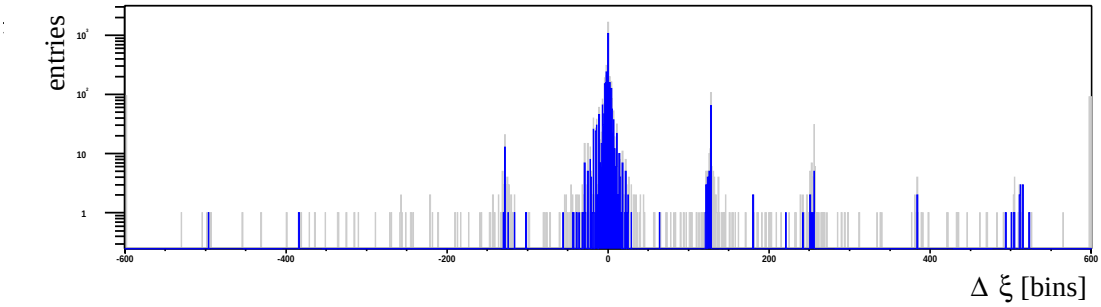

Fig. 4.1: Histogram of the difference in the digital parameter ξ of FLT online electron tracks using run 17160. The events are restricted to those which contain exact two FLT online electron tracks. The light shaded entries denote all comparisons, the dark shaded entries show the differences under the constraint of a match in the variables $d\xi$, $dd\xi$ and η. Satellite peaks at the positions $\pm 2^7$, $\pm 2^8$ and $\pm 2^9$ point to possible bit errors.

As described in Sect. 2.4.2 the four digital parameters ξ, $d\xi$, $dd\xi$ and η describe the track position and slope. If one looks at the differences in these parameters of different tracks of the same event, one observes beside the expected peaks at zero (due to similar tracks) additional satellite peaks in the difference histogram of the parameter ξ, i.e. the difference $\Delta\xi = \xi_{\text{first track}} - \xi_{\text{second track}}$ in the events that contain two recorded tracks, see Fig. 4.1. The satellite peaks occur at the positions ± 128, ± 256 and ± 512 or, written in powers of two, $\pm 2^7$, $\pm 2^8$ and $\pm 2^9$. If the bit number n of a given parameter of the FLT message is flipped during the data transmission from one processor board to the next, this shows up in form of a difference of 2^n in the value of that parameter. Most likely such messages are not updated but it is possible that they survive the complete chain of superlayers because of noise hits.

In order to quantify the satellite peaks we cut in the distributions of $d\xi$, $dd\xi$ and η in order to select most likely clones and to suppress track pairs which are different. This selection enhances the satellite peaks compared to the *combinatorial background* as shown in Fig. 4.1. The combinatorial background in the differences plots arises from track pairs which do not belong to the same physical track (from all combinatorial possibilities) and are therefore different. The difference in the track parameters of such tracks does not peak at zero but is equally distributed. This allows one to count the ratio of messages

difference of	ratio			
	run 17116	run 17160	run 17163	
	muons	electrons	electrons	muons
$-2^9 \pm 1$	(0.0)%	(0.0)%	(0.0)%	(0.0)%
$-2^8 \pm 1$	(0.0)%	(0.0)%	(0.0)%	(0.0)%
$-2^7 \pm 1$	(0.4 ± 0.1)%	(0.9 ± 0.2)%	(1.7 ± 0.9)%	(1.4 ± 0.5)%
$-2^6 \pm 1$	(0.0)%	(0.0)%	(0.0)%	(0.4 ± 0.2)%
0 ± 1	(96.9 ± 1.3)%	(94.2 ± 2.5)%	(93.0 ± 7.2)%	(94.6 ± 4.1)%
$+2^6 \pm 1$	(0.0)%	(0.1 ± 0.1)%	(0.0)%	(0.0)%
$+2^7 \pm 1$	(2.7 ± 0.2)%	(4.5 ± 0.5)%	(4.4 ± 1.6)%	(3.5 ± 0.8)%
$+2^8 \pm 1$	(0.0)%	(0.4 ± 0.2)%	(0.0)%	(0.0)%
$+2^9 \pm 1$	(0.0)%	(0.3 ± 0.1)%	(0.0)%	(0.0)%

Table 4.2: Fraction of tracks that suffer from bit errors in the runs 17116, 17160 and 17163 in recorded FLT electron and muon tracks. The frequency of errors in bit 7 of the parameter ξ is noticeable. The frequencies of bit failures are within the statistical errors comparable for both runs and both particle types.

which suffer from bit errors. The following cuts are applied on the quantities $d\xi$, $dd\xi$, and η:

parameter	cut
$d\xi$	± 20
$dd\xi$	± 5
η	± 5

The quite relaxed cut on $d\xi$ takes into account the fact that this parameter is updated in each superlayer (as described in Sect. 2.4.3) and thus differs significantly between clones. After applying these cuts we count the entries in the ξ-plot at 0 ± 1 and from $\pm 2^6 \pm 1$ up to $\pm 2^9 \pm 1$. The bits corresponding to deviations in the value of ξ from $\pm 2^0$ to $\pm 2^5$ are not regarded here since those deviations lie within the central peak of the ξ-difference histogram. The results are given in Table 4.2. The table shows that the observed effect does not stem from the pretriggers or the muon tracking since the effect occurs within the statistical errors at the same frequency in electron and muon tracks. The effect is concentrated on bit 7 of the parameter ξ while there are no satellite peaks visible in the difference histograms of the parameter η.
A priori the probability of a bit error is the same for each bit of the parameters ξ and η since both values are not updated in the TFU network after superlayer TC02. The high frequency of errors in bit 7 of ξ points to the possibility that the observed errors are caused by a localized problem in the transmission of the FLT messages and do not indicate a general shortcoming of the system. In order to follow up this possibility we plot the impact points of the tracks in superlayer PC01 which enter the satellite peaks of

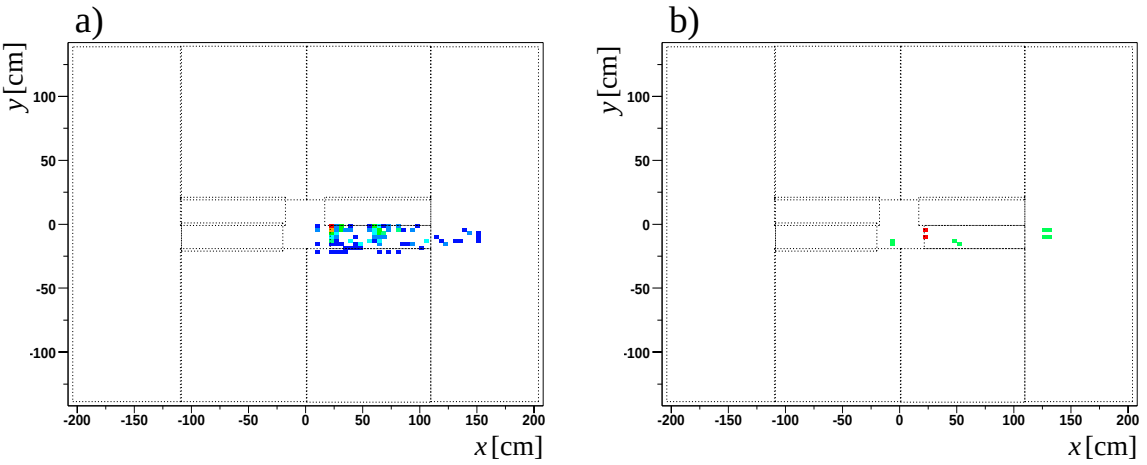

Fig. 4.2: Positions in x and y of tracks in superlayer PC01 that are identified to suffer from bit error by the method described in the text. Figure a) shows tracks that suffer from errors in bit 7, figure b) such that suffer from errors in bit 8 of the digital parameter ξ. Please notice that there are not only entries from the erroneous but also from the correct tracks in this histograms because the used method is only able to judge on a pair of tracks.

the ξ-difference histogram. The result for electron tracks of run 17160 is given in Fig. 4.2. A clear accumulation of impact points is visible in the FLT sector 7. This leads to the assumption that a message board in this sector did not work correctly during the data taking of the year 2000. It is most probable that the observed bit errors stem from that localized error.

The projection of the tracks that differ in bit 9 of ξ into the superlayer TC02 shows that those tracks lie at $x \approx 0$. This indicates no error since bit 9 serves as sign bit in the ξ parameter and the deviations just reflect clones that lie close to each other at $x \approx 0$.

For a cross-check all tracks which pass the TFU of sector 7 (FLT notation) are discarded and the difference histograms of the parameters are reevaluated. As is obvious from Fig. 4.3 (for electrons in run 17160) and Fig. 4.5 (for muons in run 17116) the satellite peaks in the difference histogram of the parameter ξ at $\xi = \pm 2^7$ are still present. The selection of tracks pairs that differ by $\Delta\xi \pm 2^7 \leq \pm 5$ show no correlation in the other parameters $d\xi$ and η ($dd\xi$ is anyhow restricted to a small range so that it cannot be used as a matching criterion). This is a different effect compared to what was described above since in this case not only some bits of ξ are flipped but additionally the values of $d\xi$ and η are uncorrelated. This may indicate that in some areas the transmission of the parameters $d\xi$ and η is corrupted while the parameter ξ suffers under bit-flipping which was already observed above. In order to trace back the origin of this effect again the x- and y-coordinates of the tracks are plotted which show up in the satellite peaks defined by $\Delta\xi \pm 2^7 \leq \pm 5$. In contrast to Fig. 4.2 we do not constrain the other parameters of the tracks but we cut out the region of FLT sector 7. The resulting distribution of

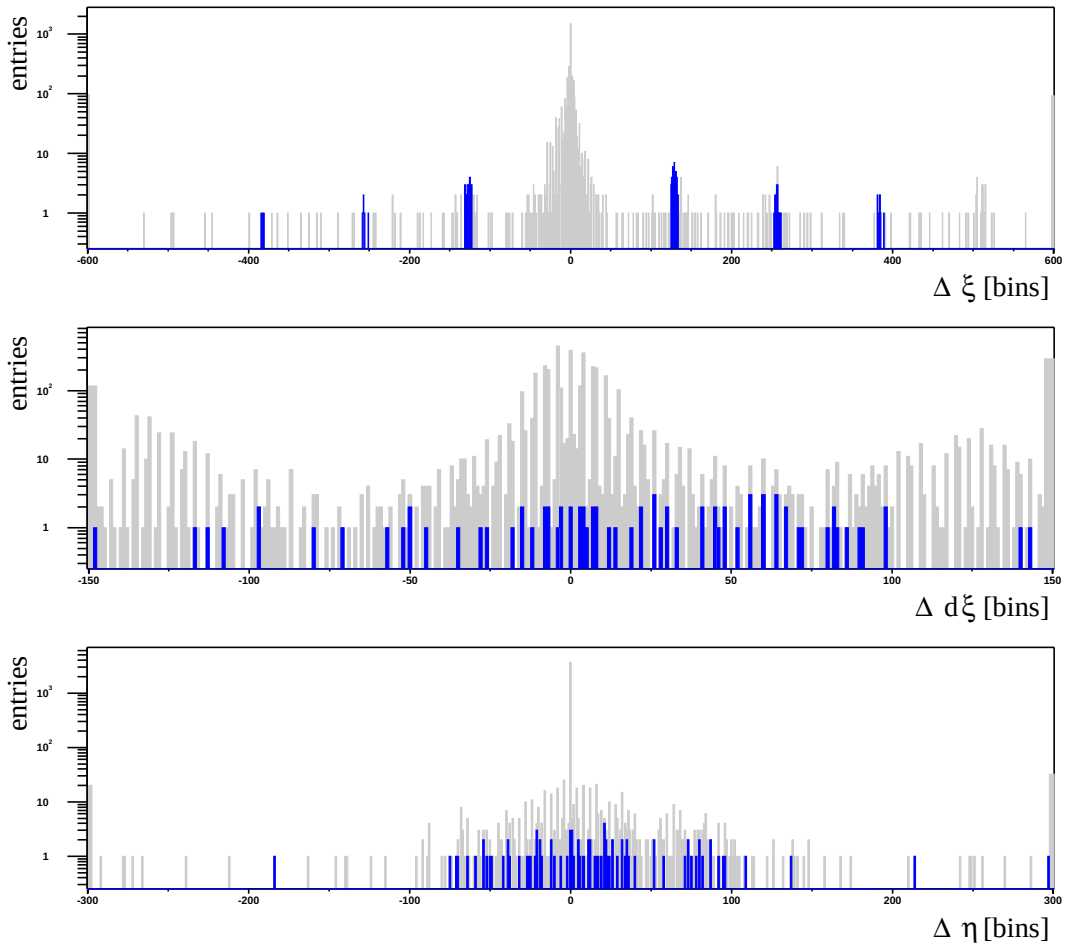

Fig. 4.3: Difference histograms of the digital parameters ξ, $d\xi$ and η of recorded FLT electron tracks in run 17160. The events are restricted to those which contain exactly two FLT online electron tracks. Tracks which pass FLT sector 7 are discarded. The light shaded entries denote all comparisons, the dark shaded entries show the differences under the constraint of a match in ξ of $\Delta\xi \pm 2^7 \leq \pm 5$. There is no constraint on the other parameters of the FLT track.

tracks is given in Fig. 4.4. The tracks which enter the satellite peaks exclusively pass the $-x$-$-y$-region of the outer tracker. This region corresponds to the FLT sector 3 which are assigned to superlayer PC01.

We have therefore to suspect also the message transmission in one of the superlayers PC01 or PC04 (or both) to behave erroneously. Again, as a cross-check, the difference histograms are reevaluated after discarding tracks which pass one of the FLT sectors 33, 37, or 41 or — to take into account the problem described above — sector 7. The resulting difference histogram is shown in Fig. 4.7. The satellite peaks have vanished completely which proves that they are caused exclusively by malfunctions of the data transmission

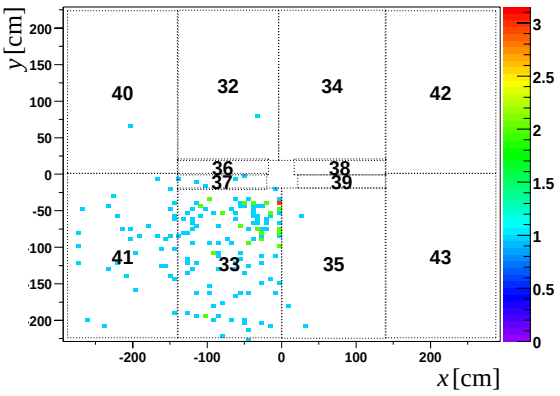

Fig. 4.4: Distribution in x and y of recorded electron FLT tracks that are found in the satellite peaks at $\Delta\xi \pm 2^7 \leq \pm 5$ shown in Fig. 4.3. The numbers indicate the corresponding FLT sectors of superlayer TC02. All those tracks pass the $-x$-$-y$-region of the outer tracker which is (in superlayer TC02) assigned to the FLT sectors 33, 37 and 41.

which lie in the projectivity of the FLT sectors 7, 33, 37 and 41. In the following we have to compare the recorded FLT tracks to the simulated tracks. We have to pay attention to the matching efficiencies of the areas which have shown problems in order to disentangle the matching inefficiencies which are based on the bit error phenomenona described here, and other effects.
The result of this section seems at first to contradict to the result of the test vector test which was presented in Sect. 4.2. As discussed in this section there are indications that the data transmission of messages in the FLT network suffers from bit errors and corrupted messages in localized parts of the acceptance. The test vector test did not indicate such effects. But one has to take into account that the full electronics that is used for the data transmission within the FLT network has been exchanged after the data taking in 2000 and before the test vector test in the year 2001. This involved, besides the cabling, the repeater and the message boards, see Sect. 2.4.2. Moreover, the message boards have been reprogrammed in order to carry out an error-check of the message transmission during the operation of the system. If the boards do not receive messages at the input they generate special test patterns which are marked using the value zero for the destination identifier. The boards which receive those test patterns are able to check if the test pattern is valid and can in this way look for bit errors. Using this new feature after the installation no such bit errors were measured which is in agreement with the result of the test vector test [schwi02]. We have to conclude from this that the localized errors which we have discussed in this section have been removed during the recabling and reprogramming of the message transmission system.

4.4 Matching by Comparing Track Parameters in the Electron Channel

The goal of this chapter is to give an estimate of the reliability of the FLT simulation. Although the test vector test has shown that the hardware and the simulation of the FLT deliver identical results on a bit level if they are fed with identical data, during the data

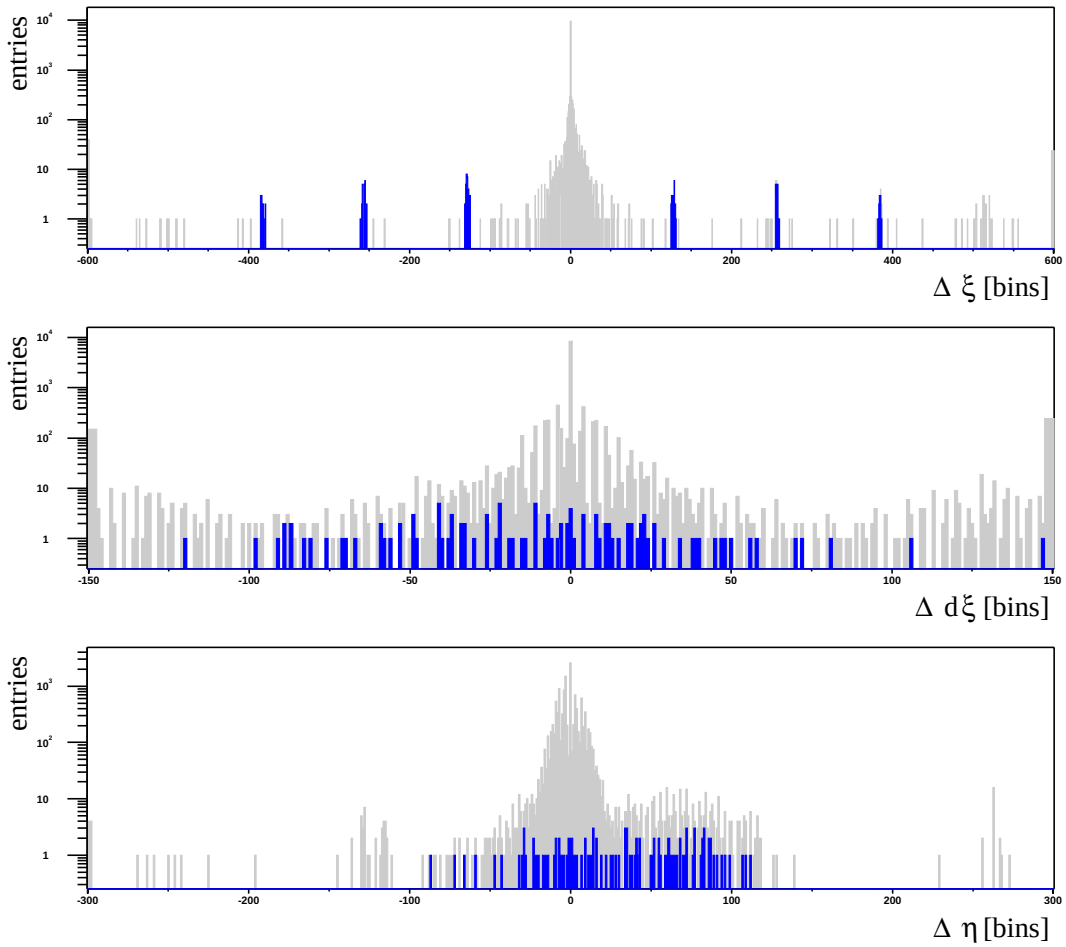

Fig. 4.5: Difference histogram of the digital parameters ξ, $d\xi$ and η of recorded FLT muon tracks in run 17116. The events are restricted to those which contain exactly two FLT online electron tracks and the tracks which pass FLT sector 7 are discarded. The light shaded entries denote all comparisons, the dark shaded entries show the differences under the constraint of a match in ξ plus a bit flip in bits 7 or 8. There is no constraint on the other parameters of the FLT track.

taking this prerequisite is not met. Erroneous transmission of the hit information, as discussed in Chapter 3, and bit errors in the inter FLT message transmission, as observed in Sect. 4.3, are the reasons for discrepancies of the FLT record gained by the hardware during the data taking and the simulation which is applied on the same data.

To investigate the reliability of the FLT simulation two things were done. On one hand, the tracks are used that were found by the FLT hardware for a given event. On the other hand, the data that was kept by the data acquisition for the same event is passed to the FLT simulation. In order to include the shortcomings of the detector performance and the data transmission the masking of the bad links and defective channels as described in

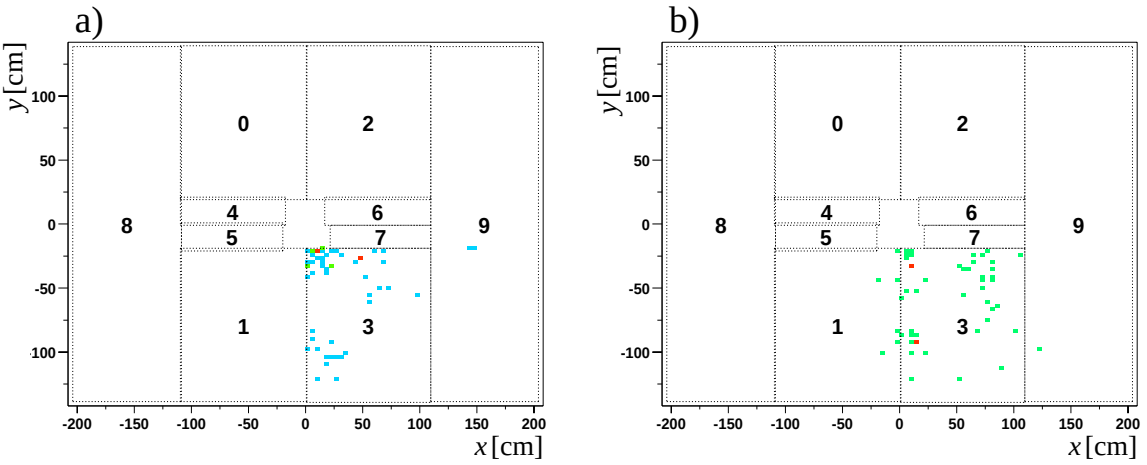

Fig. 4.6: Distribution in x and y of recorded muon FLT tracks that are found in the satellite of the parameter ξ shown in Fig. 4.5. Diagram a) refers to the errors in bit 7 and diagram b) to errors in bit 8. The numbers indicate the corresponding FLT sectors of superlayer PC01.

Sect. 3.3 is applied. The number of masked channels is given in Table 3.4. The comparison of the tracks of the FLT record of the hardware and the simulation allows one to quantify the correspondence of hardware and simulation on an event level.

The recorded FLT tracks are compared to the simulated tracks using their track parameters. The tracks are defined by the four parameters ξ, $d\xi$, $dd\xi$ and η which code the track position and slope of the FLT tracks. The parameter ξ embodies the x-position of the track in the superlayer TC02, $d\xi$ represents the slope of the track by quantifying the deviation from a track that has infinite momentum. $dd\xi$ denotes the width of the region of interest in PC01 and η stands for the slope in y-direction. For a more detailed description see Sect. 2.4.2.

In the first step, the differences of the tracks parameters are evaluated in order to choose appropriate cuts. In the second step, the cuts are applied in order to match the recorded and simulated FLT tracks. For each event two sets of tracks are the basis of the matching procedure, the *reference tracks* and the *test tracks*. The reference tracks represent the tracks which are expected to be found. For each reference track a matching track is searched among the test tracks. In the following only events are selected which contain exactly one reference track. This avoids the bias of clone tracks. The number of test tracks is varied as described below. Both tracks reconstructed by the hardware and the simulation are used as reference tracks. The other track kind is used for test tracks in each case. The *matching efficiency* is the ratio of reference tracks which are matched by a similar test track. Moreover, the systematic error is estimated by studying the variation of the matching efficiency under variation of the cuts. The influence of the regions that show erroneous performance as discovered in Sect. 4.3 is also considered.

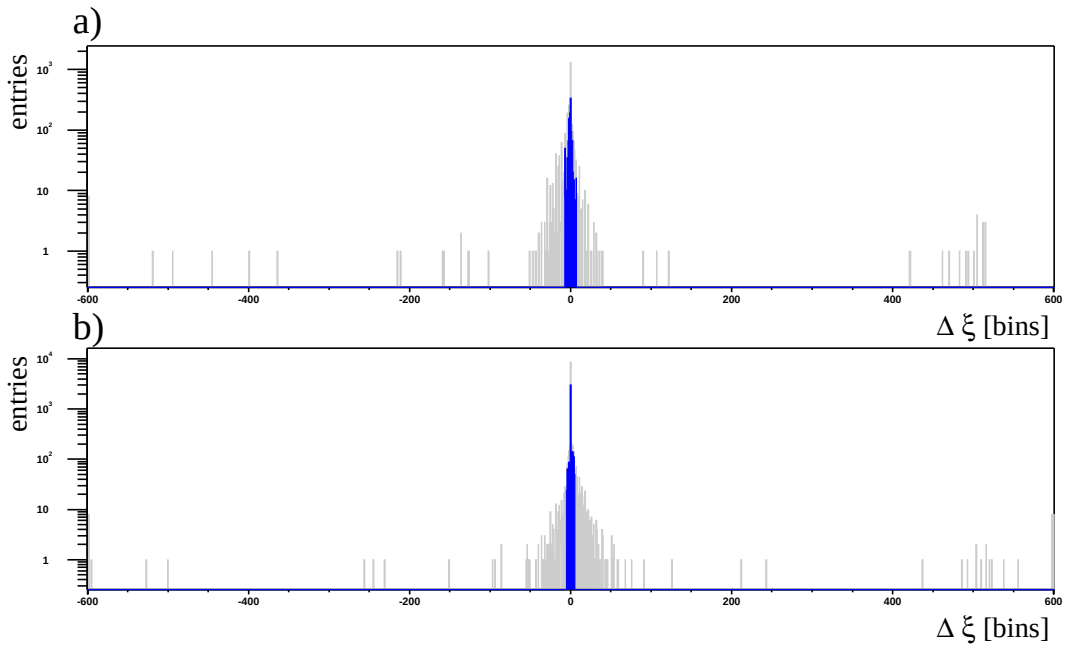

Fig. 4.7: Difference histogram of the digital parameter ξ of a) recorded FLT electron tracks in run 17160 and b) recorded muon tracks in run 17116. The events are restricted to those which contain exactly two recorded FLT electron or muon tracks, respectively. For the electron case tracks which pass FLT sectors 7, 33, 37 or 41 are discarded. For the muon case tracks passing sectors 3 or 7 are discarded. The light shaded entries denote all comparisons, the dark shaded entries show the differences under the constraint of a match in the track parameters $d\xi$, $dd\xi$ and η.

Justification of Cuts

In the first step, the cuts on the track parameters are established. Pairs of recorded and simulated tracks are selected which have a high probability to belong to the same physical track. We apply a kinematical cut of $P > 5.0\,\mathrm{GeV}$ on the momentum and of $p_\mathrm{T} > 1.0\,\mathrm{GeV}$ on the transverse momentum of the tracks in order to gain in track quality. In order to select tracks which belong to the same physical track only events which contain exactly one recorded and one simulated FLT electron track are selected. On one hand, this avoids a bias that could arise from the double counting of clones. On the other hand, it should be most probable that both tracks are similar which suppresses the combinatorial background. Moreover, for the difference histograms of each track parameter ξ, $d\xi$, $dd\xi$, and η, the remaining three parameters are constrained to be identical. This again reduces the combinatorial background and favors tracks which belong to the same physical track. The result of this selection is shown in Fig. 4.8. Based on the difference histograms we choose the following cuts. On the parameter ξ a cut of ± 7 is applied which corresponds to the full width of the peak of all combinations.
The difference histogram of $d\xi$ is hard to interpret since it shows a quite broad distribution. The reason for this is that the message multiplication during the tracking in the successive

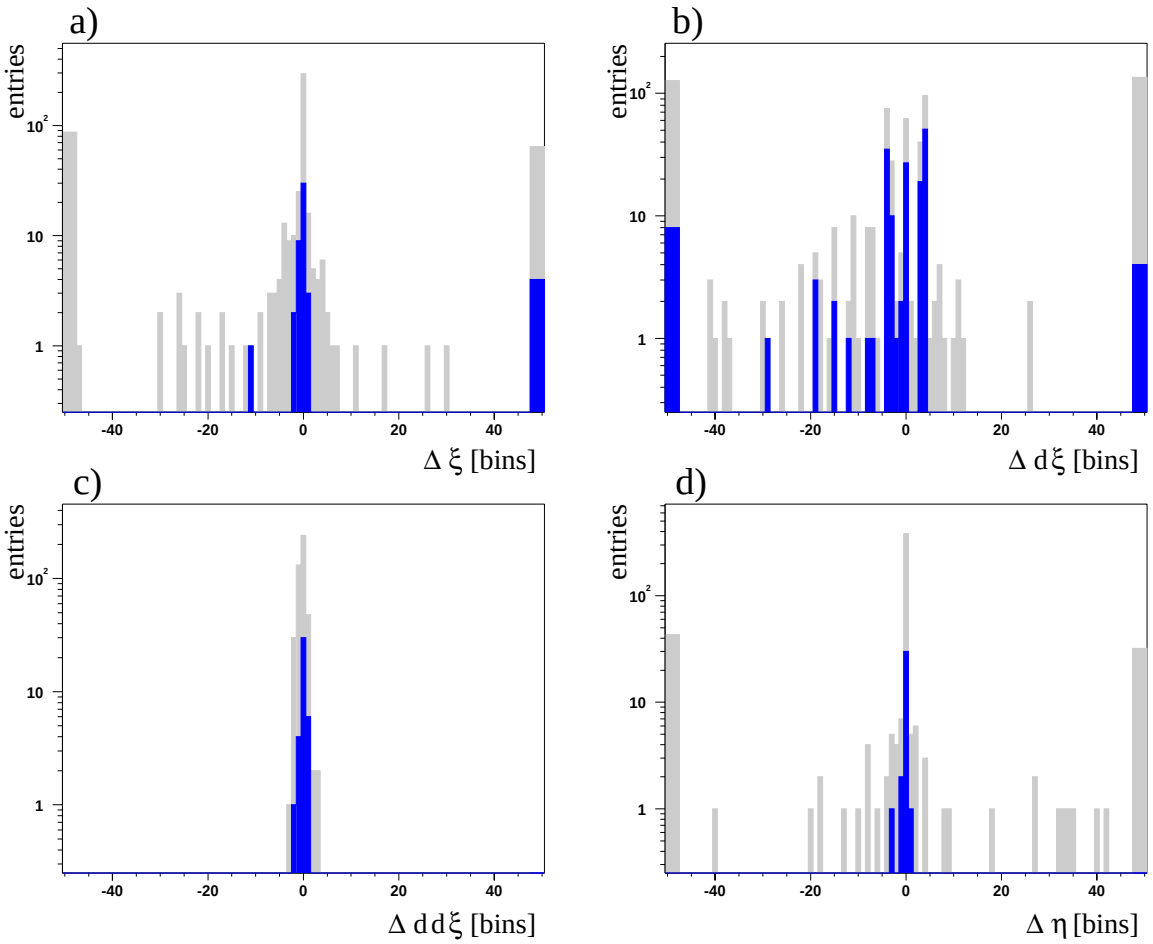

Fig. 4.8: Difference histograms of the track parameters ξ, $d\xi$, $dd\xi$ and η (in the figures a) to d) respectively) of recorded and simulated electron FLT tracks of run 17163. Only events that contain exactly one recorded and one simulated electron track are regarded. Entries which do not belong to the central peak are due to the combinatorial background, the peaks indicate the matched tracks. The light shaded entries denote all entries while the dark shaded entries mark the tracks which could be matched exactly in the three remaining parameters. The broad entries on the left and right sides of the plots represent the under- and overflow-bin, respectively.

superlayers generate clone tracks which are identical in the parameters ξ and η since these parameters are not updated after the TFUs of TC02 (holds for ξ) or even after the ECAL pretrigger (valid for η). In contrast, the parameter $d\xi$ is updated in every superlayer. Therefore clones differ in that parameter. The decision on the cut of the track parameter $d\xi$ has to take this into account. For the following a cut of ± 20 is used which allows one to match tracks that originated from the same pretrigger message but which got slightly different updates in the last superlayers PC01 and PC04.

For the parameter $dd\xi$ one observes one compact peak without any outliers. While in

general $dd\xi$ codes the width of the region of interest for the track finding algorithm in superlayer PC01 it reflects the width of the found cluster. The maximum cluster width which the FLT algorithm uses is 4 which is coded by the parameter $dd\xi$. If a broader cluster is found the algorithm generates multiple messages. Thus in the difference peak only values of at maximum ± 3 enter. Because of this a cut on $dd\xi$ is of no use to distinguish tracks and thus, no cut is applied.

parameter	cut
ξ	± 7
$d\xi$	± 20
$dd\xi$	none
η	± 5

Table 4.3: Cuts which are used for the matching of recorded and simulated FLT tracks.

Finally, the difference peak of the parameter η shows a width of ± 5 so the cut is set to that value. The cuts are summarized in Table 4.3. Using cuts for the selection of matching tracks introduces a systematic error since tracks may differ more than allowed by this cuts regardless of whether they belong to the same physical track. This error is estimated in the following by evaluating the matching efficiencies not only using the cuts shown in Table 4.3 but additionally for the doubled values.

Matching Efficiency of Electron Tracks

After establishing the cuts for the selection of similar tracks, they are used in order to evaluate the matching efficiency of recorded and simulated electron tracks. First, only events which contain exactly one recorded and one simulated track are regarded. In this way the events contain one reference and one test track. This is done in order to select events which most probably contain matching tracks and in order not to be biased by the double counting of clones. After that, events which contain zero or one and events that contain up to four test tracks are considered. The number of reference tracks is always fixed to one.
The reference tracks have to fulfill a cut of $P > 5.0\,\mathrm{GeV}$ on the momentum and of $p_\mathrm{T} > 1.0\,\mathrm{GeV}$ on the transverse momentum. There is no kinematical cut applied on the test tracks. In this way a test track can be matched to a reference track which is similar but has a slightly lower momentum which is below the applied cuts. Both the recorded tracks and the simulated tracks are alternatively used as reference tracks. For each reference track of one kind — recorded or simulated — matching test tracks of the other kind — simulated of recorded — are searched. In this way both the probabilities for a given recorded track to be reconstructed by the simulation and for a given simulated track to be found among the recorded tracks are evaluated.

event selection: exactly one reference track and exactly one test track					
applied cuts	run	reference tracks			
		recorded tracks		simulated tracks	
		simple cuts	relaxed cuts	simple cuts	relaxed cuts
no acceptance cut	17036	$(76.8 \pm 2.2)\%$	$(78.7 \pm 2.1)\%$	$(77.6 \pm 2.2)\%$	$(79.2 \pm 2.1)\%$
	17037	$(80.4 \pm 1.9)\%$	$(82.3 \pm 1.9)\%$	$(80.8 \pm 1.9)\%$	$(82.9 \pm 1.8)\%$
	17160	$(70.5 \pm 1.6)\%$	$(75.7 \pm 1.5)\%$	$(77.4 \pm 1.4)\%$	$(83.6 \pm 1.3)\%$
	17163	$(79.1 \pm 1.9)\%$	$(81.1 \pm 1.0)\%$	$(80.7 \pm 1.9)\%$	$(82.3 \pm 1.8)\%$
cut of outer ECAL	17036	$(78.7 \pm 2.2)\%$	$(80.6 \pm 2.1)\%$	$(79.5 \pm 2.1)\%$	$(81.1 \pm 2.1)\%$
	17037	$(84.8 \pm 1.8)\%$	$(86.8 \pm 1.7)\%$	$(85.6 \pm 1.8)\%$	$(87.8 \pm 1.6)\%$
	17160	$(74.5 \pm 1.6)\%$	$(79.8 \pm 1.5)\%$	$(79.1 \pm 1.5)\%$	$(85.2 \pm 1.3)\%$
	17163	$(79.9 \pm 2.0)\%$	$(81.9 \pm 1.9)\%$	$(82.1 \pm 1.9)\%$	$(83.6 \pm 1.8)\%$
additional cut on	17036	$(91.6 \pm 1.7)\%$	$(92.3 \pm 1.7)\%$	$(91.6 \pm 1.7)\%$	$(92.4 \pm 1.6)\%$
sectors 7, 33, 37, 41	17037	$(92.2 \pm 1.7)\%$	$(93.4 \pm 1.6)\%$	$(93.0 \pm 1.6)\%$	$(94.2 \pm 1.5)\%$
	17160	$(81.3 \pm 1.8)\%$	$(86.6 \pm 1.6)\%$	$(83.6 \pm 1.7)\%$	$(88.3 \pm 1.5)\%$
	17163	$(85.4 \pm 2.0)\%$	$(87.3 \pm 1.9)\%$	$(86.4 \pm 1.9)\%$	$(87.7 \pm 1.9)\%$
additional cut on	17036	$(94.7 \pm 1.5)\%$	$(95.1 \pm 1.4)\%$	$(94.7 \pm 1.5)\%$	$(95.2 \pm 1.4)\%$
sectors 2 and 3	17037	$(95.3 \pm 1.4)\%$	$(96.3 \pm 1.3)\%$	$(95.8 \pm 1.4)\%$	$(96.7 \pm 1.2)\%$
	17160	$(84.4 \pm 2.1)\%$	$(89.9 \pm 1.7)\%$	$(87.3 \pm 1.9)\%$	$(91.2 \pm 1.6)\%$
	17163	$(89.1 \pm 2.0)\%$	$(91.5 \pm 1.8)\%$	$(89.9 \pm 1.9)\%$	$(91.5 \pm 1.8)\%$

Table 4.4: Matching efficiencies of recorded and simulated FLT electron tracks. Only events which contain one recorded and one simulated track are regarded. Besides the matching efficiency for the full acceptance we also cut on the acceptance of the outer ECAL and, furthermore, restrict ourselves to the regions which have proven not to show bit errors. Moreover, the FLT sectors 2 and 3 are excluded since they also show a problematic behavior, as discussed in the following. In order to estimate the systematic error, the efficiencies using relaxed cuts are shown.

Matching One Reference Track to One Test Track

The summary of results for the events which contain one track of each kind is given in Table 4.4. Using the full acceptance the matching efficiency varies — depending on the run — from 70% up to 80% to find a simulated track for a given recorded track and from 77% to 81% to find a recorded track which matches a given simulated track.
The matching efficiencies for matching a recorded track to a simulated track and vice versa do not coincide for a given run. In events that contain just one track of each kind one could expect this since the matching of tracks is — as defined here — a symmetric relation. The reason for the difference is that the kinematical cuts are only applied on the reference tracks but not on the test tracks. The counting of tracks in each event which we use for selecting events that contain one recorded and one simulated track also only takes

tracks into account which fulfill this kinematical cut. For the test tracks we do not apply this cut in order not to suffer from edge effects in the case that the matching test track is just slightly below the kinematical cut. Therefore, the matching efficiencies of matching recorded tracks to simulated tracks and vice versa differ even when selecting events of one recorded and one simulated track. Nevertheless, the efficiencies are compatible within the statistical error.

As will be demonstrated in the following, the coverage of used ECAL readout boards and of used ECAL pretrigger boards varies over the regarded runs. The runs were taken during the commissioning phase of the detector and frequent changes in the detector setup were done. Therefore, one observes simulated electron tracks in areas that are not covered by ECAL pretrigger boards which, of course, cannot be matched by recorded tracks in that case. This happens especially in the acceptance of the outer ECAL as discussed in the following. In order to factorize out this effect we discard all tracks that pass the acceptance of the outer ECAL. The corresponding matching efficiencies are given in Table 4.4. The matching efficiencies increase by 5% to 11% compared to the matching using the full acceptance.

The influence of the regions which behave erroneously as found in the study of bit errors becomes visible if one discards the tracks passing through these regions. The matching efficiencies are significantly higher if the defective regions are not used and reach a level of 85%-91%. In events that contain exactly one recorded and one simulated track one would expect the tracks to be similar. Nevertheless, the presence of bit errors may corrupt the parameters of the recorded track such that it cannot be matched to the simulated track. This explains why the cut on the sectors which have shown bit errors in the parameter ξ improves the matching efficiency.

As it will be shown in the next section tracks which pass the FLT sectors 2 and 3 suffer from additional problems. A cut on these areas further increases the matching efficiencies to a level of 85% to 96%.

Table 4.4 shows the systematic error which is introduced by the matching criterion. Two tracks are regarded as matched if their track parameters do not differ by more than the cuts which are listed in Table 4.3. The bias introduced by these cuts is estimated by reevaluating the matching efficiencies using doubled values for the cuts. The matching efficiencies rise by about 2%. This is the same level as the statistical error which is between 1% and 2%.

Constraining the analysis to events which have one reference track and one test track and restricting the used acceptance to regions of the detector which show no erroneous behavior results in matching efficiencies of up to 95% (in the runs 17036 and 17037). This shows that, given that both reference track and test track are present, the matching efficiency is close to unity and that the system is working in agreement between hardware and simulation as soon as the problematic regions of the acceptance are removed.

Matching One Reference Track to up to One Test Track

In the next step, the study is expanded to all events that contain at most one recorded and one simulated track. In this way not only events which contain most likely a pair of matching tracks are regarded but also those that have recorded tracks that are not found by the simulation and those that have simulated tracks that are not in the FLT record. Thus we are able to obtain the probability for reconstructing a recorded FLT track by the simulation and to find a simulated track among the recorded tracks.

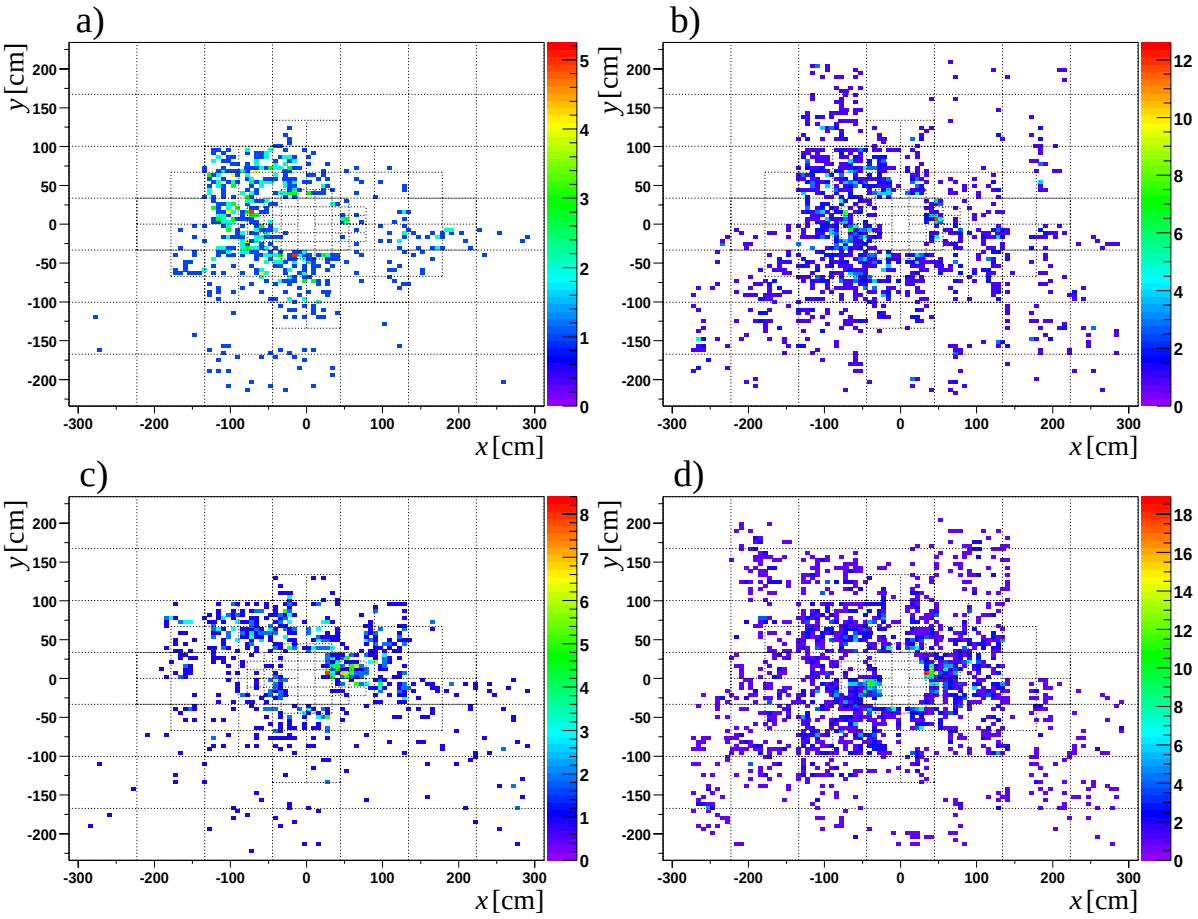

Fig. 4.9: Positions in x and y evaluated at the ECAL plane of recorded FLT tracks are shown in figure a) and c). The same is given for simulated FLT tracks in figures b) and d). The plots are based on the data of the runs 17037 (a) and b)) and 17163 (c) and d)).

Looking into those events we encounter mismatches of tracks which pass the outer ECAL. Fig. 4.9 proves that the pretrigger boards belonging to the outer ECAL were not or only partly used for the FLT input, see Fig. 4.9 a) for run 17037 and Fig. 4.9 c) for run 17163 which show the recorded FLT tracks projected to the ECAL plane. Only the $-y$-half of the acceptance of the outer ECAL is partly covered by the tracks. Moreover, the coverage

has changed during the two runs. The same is true for the coverage of ECAL readout which is reflected in the coverage of the simulated FLT tracks in both runs, see Fig. 4.9 b) and d) for run 17037 and 17163, respectively. The ECAL readout is also partly available for the $+y$-part of the outer ECAL which, nevertheless, has changed between the two runs. The changing coverage of the ECAL readout and the ECAL pretrigger boards is due to continuous commissioning during the selected period of data taking.

event selection: exact one reference track and zero or one test track					
applied cuts	run	reference tracks			
		recorded tracks		simulated tracks	
		simple cuts	relaxed cuts	simple cuts	relaxed cuts
no acceptance cut	17036	$(45.5 \pm 2.0)\%$	$(47.3 \pm 2.0)\%$	$(21.2 \pm 1.0)\%$	$(22.3 \pm 1.0)\%$
	17037	$(51.5 \pm 1.9)\%$	$(53.1 \pm 1.9)\%$	$(29.5 \pm 1.2)\%$	$(30.7 \pm 1.2)\%$
	17160	$(35.5 \pm 1.1)\%$	$(39.2 \pm 1.2)\%$	$(66.4 \pm 1.2)\%$	$(73.3 \pm 1.2)\%$
	17163	$(42.8 \pm 1.7)\%$	$(44.2 \pm 1.7)\%$	$(19.3 \pm 0.8)\%$	$(20.2 \pm 0.8)\%$
cut of outer ECAL	17036	$(47.3 \pm 2.0)\%$	$(49.2 \pm 2.0)\%$	$(28.2 \pm 1.2)\%$	$(29.6 \pm 1.3)\%$
	17037	$(54.6 \pm 1.9)\%$	$(56.2 \pm 1.9)\%$	$(38.8 \pm 1.4)\%$	$(40.4 \pm 1.4)\%$
	17160	$(40.2 \pm 1.2)\%$	$(44.3 \pm 1.2)\%$	$(66.3 \pm 1.3)\%$	$(73.2 \pm 1.2)\%$
	17163	$(44.6 \pm 1.8)\%$	$(46.0 \pm 1.8)\%$	$(23.0 \pm 1.0)\%$	$(24.1 \pm 1.0)\%$
additional cut on	17036	$(58.7 \pm 2.4)\%$	$(59.9 \pm 2.4)\%$	$(41.5 \pm 1.8)\%$	$(42.5 \pm 1.8)\%$
sectors 7, 33, 37, 41	17037	$(61.5 \pm 2.5)\%$	$(62.5 \pm 2.5)\%$	$(43.9 \pm 1.9)\%$	$(45.0 \pm 1.9)\%$
	17160	$(49.6 \pm 1.7)\%$	$(54.4 \pm 1.7)\%$	$(66.6 \pm 1.6)\%$	$(72.8 \pm 1.5)\%$
	17163	$(49.5 \pm 2.1)\%$	$(50.7 \pm 2.1)\%$	$(31.2 \pm 1.4)\%$	$(32.5 \pm 1.5)\%$
additional cut on	17036	$(67.0 \pm 2.6)\%$	$(67.9 \pm 2.6)\%$	$(59.0 \pm 2.2)\%$	$(60.1 \pm 2.2)\%$
sectors 2 and 3	17037	$(73.4 \pm 2.6)\%$	$(74.4 \pm 2.6)\%$	$(58.5 \pm 2.3)\%$	$(59.9 \pm 2.3)\%$
	17160	$(53.0 \pm 2.0)\%$	$(57.2 \pm 2.0)\%$	$(69.4 \pm 1.9)\%$	$(75.7 \pm 1.8)\%$
	17163	$(57.4 \pm 2.4)\%$	$(59.0 \pm 2.4)\%$	$(41.5 \pm 1.9)\%$	$(43.3 \pm 1.9)\%$

Table 4.5: Matching efficiencies of recorded and simulated FLT electron tracks. Only events which contain at maximum one recorded and/or one simulated track are regarded. Beside the matching efficiency for the full acceptance we also restrict ourselves to the regions which have proven not to show bit errors. Moreover, the matching efficiency is recalculated using relaxed cuts in order to estimate the systematic error.

Table 4.5 shows the results that are received for the events that contain at maximum one recorded and one simulated track for the runs 17036, 17037, 17160, and 17163 with various geometrical cuts. After applying the cut on the outer ECAL the efficiency to find a reconstructed track matched by a simulated track is $40 - 50\%$ and the probability to have a recorded track that matches a given simulated track varies from 23% to 67%. These numbers rise to 48%-60% and 40%-65%, respectively, if we discard the areas in which we found bit errors in the data transmission. The matching efficiency to find a

recorded track reconstructed by the simulation rises, depending on the run, by up to 8%. This can be understood by the fact that the messages that suffer from bit errors cannot be reconstructed by the simulation, which has no handle to reproduce these effect. This can also be visualized by the x-y-distributions of the simulated tracks that can be matched compared to those that cannot be matched, see Fig. 4.10. There is a large amount of non-matched simulated tracks in the sectors 7, 1, 5, and 8 (which lie in the projectivity of the sectors 33, 37, and 41). This is in agreement with the observation of bit errors in these sectors. If the messages are corrupted by bit errors there is no way for the simulation to reconstruct them.

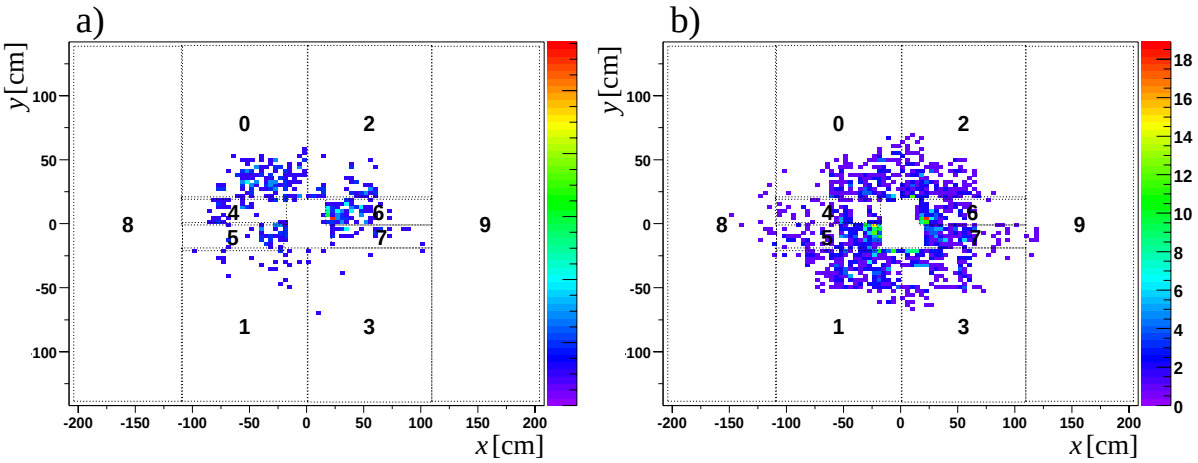

Fig. 4.10: Position in x and y of simulated tracks which a) can or b) cannot be matched by recorded tracks in run 17163. The numbers denote the corresponding FLT sectors. On the one side one observes a lack of matched tracks in the sections 7, 1, 5, and 8 (which lie in the projectivity of the sectors 33, 37, and 41) which have shown bit errors. Also noticeable are the regions of the FLT sector 3 ($+x$-$-y$-region) and sector 2 ($+x$-$+y$-region) where one observes a significant surplus of non-matched tracks. This leads to the presumption that these regions are not modeled by the simulation.

Additionally, the impact points in the superlayer PC01 of matched and non-matched simulated tracks indicate that two more FLT sectors do not match in the hardware and the simulation, see Fig. 4.10. The FLT sector 3, which is the a sector in the $+x$-$-y$-region, has a huge amount of non-matched tracks but very few matched tracks. This shows that almost none of the simulated tracks of that region is found in the FLT record. The corresponding plot showing the impact points of non-matched recorded tracks presents a similar effect. Moreover the sector 2, which is situated in the $+x$-$+y$-region, shows the same effect in the left half of its acceptance. The reason that problems in these regions were not observed during the first part of the determination of the matching efficiency is due to the fact that by selecting events that contain exactly one recorded and one simulated track it is unlikely to select two independent tracks. Thus selecting events containing one plus one track suppresses tracks in regions of low matching efficiency. We have therefore to presume the FLT sector 2 and 3 also to suffer from defects that

result in a low matching efficiency. Since these sectors were not conspicuous during the investigations of the bit errors in Sect. 4.3, the shortcomings do not arise from the same type of bit errors. At least no bit flip related correlation in the values of clones was observed. In contrast, the corruption of messages in the $-x$-$-y$-part of the acceptance was only detected by selecting messages that are different in the bit 7 of the parameter ξ. In contrast, in the same messages the values of $d\xi$ and η are uncorrelated which indicates that there might be more severe problems in the transmission of the messages than the flipping of a single bit.

In order to evaluate the matching efficiency without the influence of this effect, in addition to the FLT sectors 7, 33, 37, and 41, tracks which pass the sectors 2 and 3 are discarded. The matching efficiencies in the remainder of the acceptance are given in Table 4.5. They amount to 49%-72% for matching a recorded track by the simulation and to 42%-65% for matching a simulated track by a recorded track.

The systematic error due to the matching criteria is again estimated by using doubled values for the cuts. The matching efficiencies increase by 1% to 2% for the runs 17036, 17037, and 17163, and by about 5% for run 17160.

The numbers which are shown in Table 4.5 are the probabilities that a track which is reconstructed by the FLT hardware is also found in the simulation, and vice versa. Restricting the study to areas which show no obvious erroneous behavior, the matching efficiency for finding a simulated track which matches to a given track of the FLT hardware varies between $(53.0 \pm 2.0\,(\text{stat}) \pm 4.0\,(\text{syst}))\%$ and $(73.4 \pm 2.6\,(\text{stat}) \pm 1.0\,(\text{syst}))\%$, depending on the run. The probability to find a simulated track in the recorded FLT tracks varies between $(41.5 \pm 1.9\,(\text{stat}) \pm 1.8\,(\text{syst}))\%$ and $(69.4 \pm 1.9\,(\text{stat}) \pm 6.3\,(\text{syst}))\%$. The significant variations in the matching efficiency have to be seen in the context of the continuous commissioning during the data taking of the year 2000. The low level of the matching efficiencies have to be assigned to the data transmission problems. This will be discussed at the end of this chapter.

Matching One Reference Track to up to Four Test Tracks

In the last step, all events that contain at maximum four test tracks are selected. This allows the investigation of whether the presence of clones enlarges the efficiencies since there are more combinatorial possibilities for matching a given reference track. This cut still rejects high multiplicity events containing more then four tracks in the FLT. This is done because the main focus is the single track efficiency. Table 4.6 gives an overview of the matching efficiencies. Compared to the efficiencies in the case of at maximum one track of either kind the matching efficiencies in this last case have not changed significantly. The efficiencies increase by 1% to 3% compared to Table 4.5 which shows the efficiencies for at maximum one test track.

event selection: exact one reference track and up to four test tracks					
applied cuts	run	reference tracks			
		recorded tracks		simulated tracks	
		simple cuts	relaxed cuts	simple cuts	relaxed cuts
no acceptance cut	17036	$(50.2 \pm 1.8)\%$	$(52.1 \pm 1.8)\%$	$(23.4 \pm 1.0)\%$	$(24.7 \pm 1.0)\%$
	17037	$(57.4 \pm 1.7)\%$	$(59.4 \pm 1.6)\%$	$(31.9 \pm 1.2)\%$	$(33.3 \pm 1.2)\%$
	17160	$(48.6 \pm 0.9)\%$	$(52.6 \pm 0.9)\%$	$(71.1 \pm 0.9)\%$	$(76.6 \pm 0.8)\%$
	17163	$(48.8 \pm 1.5)\%$	$(51.7 \pm 1.5)\%$	$(22.0 \pm 0.8)\%$	$(23.0 \pm 0.8)\%$
cut of outer ECAL	17036	$(52.2 \pm 1.8)\%$	$(54.1 \pm 1.8)\%$	$(30.7 \pm 1.2)\%$	$(32.3 \pm 1.2)\%$
	17037	$(60.2 \pm 1.7)\%$	$(62.3 \pm 1.7)\%$	$(41.4 \pm 1.4)\%$	$(43.1 \pm 1.4)\%$
	17160	$(52.8 \pm 1.0)\%$	$(57.1 \pm 1.0)\%$	$(71.2 \pm 0.9)\%$	$(76.6 \pm 0.8)\%$
	17163	$(50.4 \pm 1.5)\%$	$(53.5 \pm 1.5)\%$	$(26.0 \pm 1.0)\%$	$(27.3 \pm 1.0)\%$
additional cut on	17036	$(64.2 \pm 2.1)\%$	$(65.2 \pm 2.1)\%$	$(43.9 \pm 1.8)\%$	$(45.0 \pm 1.8)\%$
sectors 7, 33, 37, 41	17037	$(65.9 \pm 2.1)\%$	$(68.2 \pm 2.1)\%$	$(46.2 \pm 1.9)\%$	$(47.4 \pm 1.9)\%$
	17160	$(61.3 \pm 1.2)\%$	$(66.1 \pm 1.2)\%$	$(72.0 \pm 1.1)\%$	$(76.7 \pm 1.1)\%$
	17163	$(55.1 \pm 1.8)\%$	$(57.7 \pm 1.8)\%$	$(34.7 \pm 1.4)\%$	$(36.2 \pm 1.4)\%$
additional cut on	17036	$(71.4 \pm 2.3)\%$	$(72.2 \pm 2.3)\%$	$(61.4 \pm 2.1)\%$	$(62.6 \pm 2.1)\%$
sectors 2 and 3	17037	$(76.8 \pm 2.2)\%$	$(78.4 \pm 2.1)\%$	$(60.3 \pm 2.2)\%$	$(61.8 \pm 2.2)\%$
	17160	$(64.2 \pm 1.5)\%$	$(68.5 \pm 1.4)\%$	$(74.3 \pm 1.4)\%$	$(78.9 \pm 1.3)\%$
	17163	$(62.2 \pm 2.1)\%$	$(65.3 \pm 2.0)\%$	$(45.2 \pm 1.9)\%$	$(47.1 \pm 1.9)\%$

Table 4.6: Matching efficiencies of recorded and simulated FLT electron tracks. Events which contain at maximum four recorded and four simulated track are regarded. Besides the matching efficiency for the full acceptance we also restrict ourselves to the regions which have proven not to show bit errors. Moreover, the matching efficiency is recalculated using relaxed cuts in order to estimate the systematic error.

Conclusions

The analysis of this chapter shows that the matching efficiency of the FLT hardware and simulation strongly depends on the selected running period and detector area. Even after cutting various regions of the geometrical acceptance the matching efficiency varies significantly in the regarded runs.
If the analysis is restricted to events that contain exactly one reference and one test track, the matching efficiencies reach values of up to $(95.3 \pm 1.4\,(\text{stat}) \pm 1.0\,(\text{syst}))\%$ to reconstruct a track of the FLT record in the simulation and up to $(95.9 \pm 1.4\,(\text{stat}) \pm 0.9\,(\text{syst}))\%$ to find a simulated track among the recorded tracks. These values are close to unity which shows that the tracking algorithm performs in agreement between hardware and simulation. Also the test vector test supports this result as one did not observe any discrepancies in the performance of the tracking algorithm in hardware and simulation (except for the two points mentioned in Sect. 4.2). The ne-

cessity of the restriction to selected runs and selected detector regions to obtain these values shows that the detector performance was unstable during the data taking of the year 2000. But the algorithm of the FLT has proven to be able to operate.
If the restriction to events which contain exactly one reference track and one test track is relaxed to events which contain at maximum four test tracks, the matching efficiencies change.
The highest matching efficiencies are found to reach $(76.8 \pm 2.2\,(\text{stat}) \pm 1.6\,(\text{syst}))\%$ in run 17037 for recorded tracks used as reference tracks and $(74.3 \pm 1.4\,(\text{stat}) \pm 4.6\,(\text{syst}))\%$ in run 17160 for simulated tracks used as reference tracks. These numbers mark only the best observed performance in selected areas. Nevertheless they prove that it is possible to describe the FLT hardware by the simulation on a level of 75%. The lower efficiencies in other areas and other runs are due to shortcomings in the performance and changes in the setup of the detector during the last days of data taking in the year 2000.
The analysis of the defective channels in Chapter 3 indicates that the hit data transmission was problematic during the year 2000 data taking. While the dead and hot channels behave relatively stable, the noisy channels are a source of uncertainty. In a given event it is not possible to make sure whether a certain noisy channels was active or not, the wire memory content remains doubtful in that cases. The large amount of noisy channels does not allow to cut areas of noisy channels since they are present everywhere in the FLT acceptance, see Fig. 3.10.
Since the FLT algorithm has been proven to operate identically in the test vector test, the comparatively low matching efficiencies of Table 4.6 have to be assigned to the uncertainties of the reproduction of the wire memory contents in the simulation compared to the contents in the FLT hardware during the data taking.

Chapter 5

Tracking Efficiency of the FLT on Monte Carlo

In this chapter, we will investigate the tracking efficiency of the First Level Trigger using Monte Carlo generated events. After the analysis of the efficiencies for toy-generated tracks (using a quite simple track model) and GEANT based tracks in a perfect detector we will regard the influence of defective channels, cell efficiency and misalignment on the tracking efficiency. Moreover, the items of wrong mapping in the outer tracker and the impact of bremsstrahlung radiation in the case of electron tracking will be investigated.
The Monte Carlo used for this section consists of 10000 $J/\psi \to e^+e^-$and 10000 $J/\psi \to \mu^+\mu^-$events. Each event contains an inelastic interaction comprising a $J/\psi \to l^+l^-$ decay. However, only the two lepton tracks are used by the the digitization and the remaining particles are ignored.

5.1 Tracking Efficiency for Toy-Tracks

First, we investigate the tracking efficiency of the FLT for toy-generated tracks. The toy-tracks are based on the same $J/\psi \to l^+l^-$ track data set that we also use later in this chapter. However, in these studies, we do not use the detector digitalization which is provided by GEANT. Only the information of the impact points in the superlayers PC01 and TC02 is used to construct a straight track which represents an idealized particle trajectory. These straight tracks are projected in the logical planes of the wire memories of the TFUs and the corresponding channels are set.
This is done by the following simple digitalization model: it assumes that the hexagonal outer tracker cells are 100% sensitive within a circle enclosed by the hexagon of the cell, see Fig. 5.1. Because of the width of the active area being slightly higher than the pitch of the cells a particle is able to hit two adjacent cells.
Using the base length a of the hexagon structure the pitch p results to

$$p = (1 + \sin 30^\circ)\, a \tag{5.1}$$

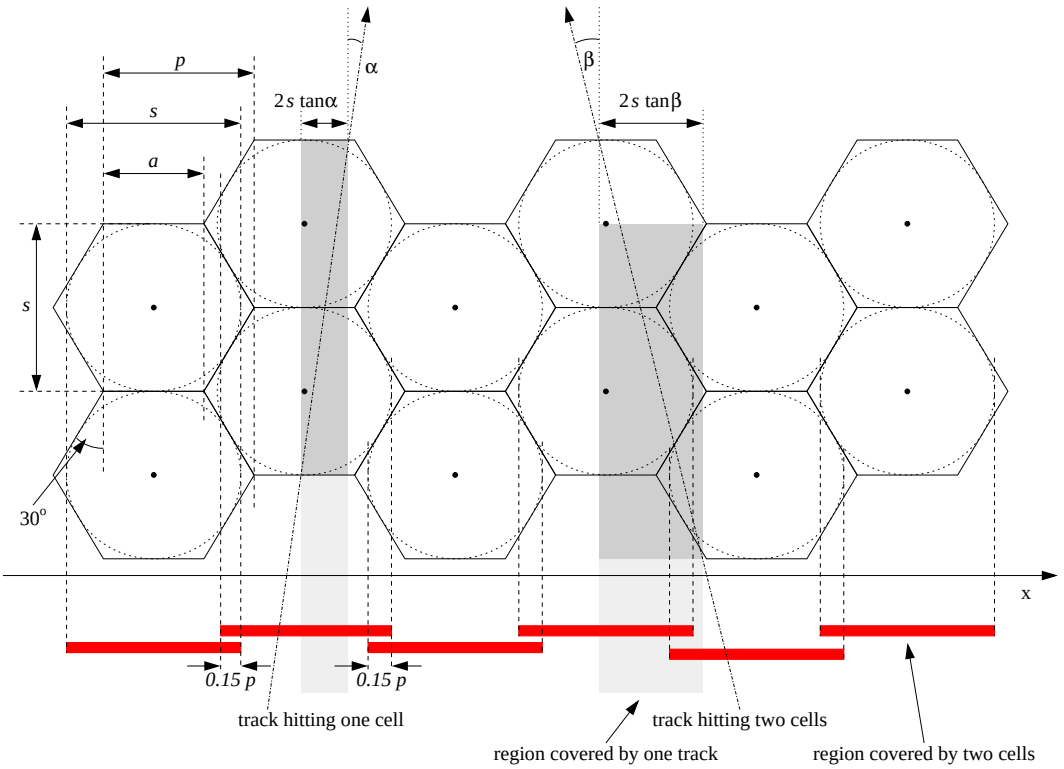

Fig. 5.1: Calculation of the hits of the toy-tracks. Because of the hexagonal structure of the OTR cells the pitch p differs from the width of the cells. The width of the sensitive areas $s = 1.15 \cdot p$ of the cells is estimated by a circle which is enclosed in one hexagonal cell. The sensitive areas of neighboring cells overlap so that a particle may hit two adjacent cells. Moreover, the slope α of the tracks introduce a virtual extension of the tracks of $2s \tan \alpha$.

The radius of the circle which is enclosed in the hexagon is $r = \sin 60° a$ and hence the sensitive area in this model has a width of

$$s = 2 \sin 60° a \tag{5.2}$$

Therefore the overlap of adjacent cells is given by

$$\frac{s}{p} = \frac{2 \sin 60°}{1 + \sin 30°} \approx 1.15 \tag{5.3}$$

which means that the sensitive area is 1.15 times larger than the pitch. Thus measuring the sensitive area from 0 to $1.15 \cdot p$ one obtains the overlap of adjacent cells: if a track hits the sensitive area in the interval from 0 to $0.15 \cdot p$ also the preceding cell is hit. Moreover the following cell is also hit if the track hits the sensitive area in the interval from p to $1.15 \cdot p$. Besides this, the sensitive area is virtually further enlarged due to the slope of the track. Because of the double layer structure, the depth of the sensitive area amounts

to $2s$, see Fig. 5.1. Thus a track of slope α in the xz-plane has an extension of $2s \tan\alpha$ in the x-direction
The mapping is simplified such that one wire memory channel is assigned to one idealized outer tracker cell. A further simplification is incorporated by assigning only cells of one cell diameter to each TFU, ignoring the fact that in reality there exist TFUs working with 5 mm and 10 mm cells. For the minus-degree channels, the or-ing of adjacent cells is considered.

Definition of the Geometrical Acceptance

One necessary condition for a track to be found by the FLT is that the track has to be within the *geometrical acceptance* of the FLT. Accordingly the tracking efficiency is given by the ratio of the tracks found by the FLT and of the tracks which are inside the acceptance.

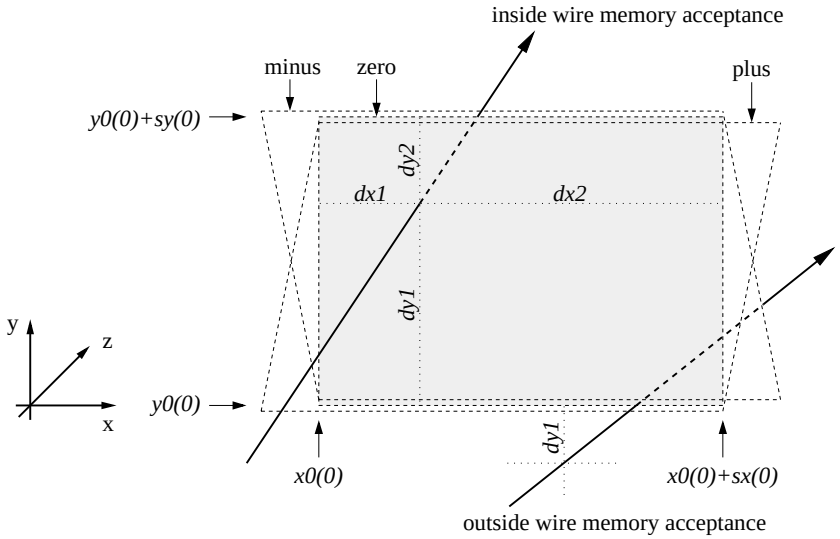

Fig. 5.2: Definition of the geometrical acceptance. The distances *dx1* and *dx2* denote the distance of the impact point of a track to the left and right border of the active area of the zero degree wire memory, respectively. Similarly, *dy1* and *dy2* denote the distances to the lower and upper border. The distances are positive if the track passes the sensitive area and negative if the track passes outside the area.

In order to determine whether a track is inside the acceptance, we define a distance of a track to the area which is assigned to the wire memory of a given TFU. Since the wire memory of the zero-degree layer defines the sensitive area of a TFU we use the geometry of the zero-degree layer for the definition of the distance, see Fig. 5.2. The distance is defined by the minimum of the distances of the track at the z-position of the plane to the four boarders of the sensitive area. These four distances are signed such that the minimum of the distances is positive if a track passes inside the area and negative if it passes outside. A track is assumed to be within the geometrical acceptance of the FLT

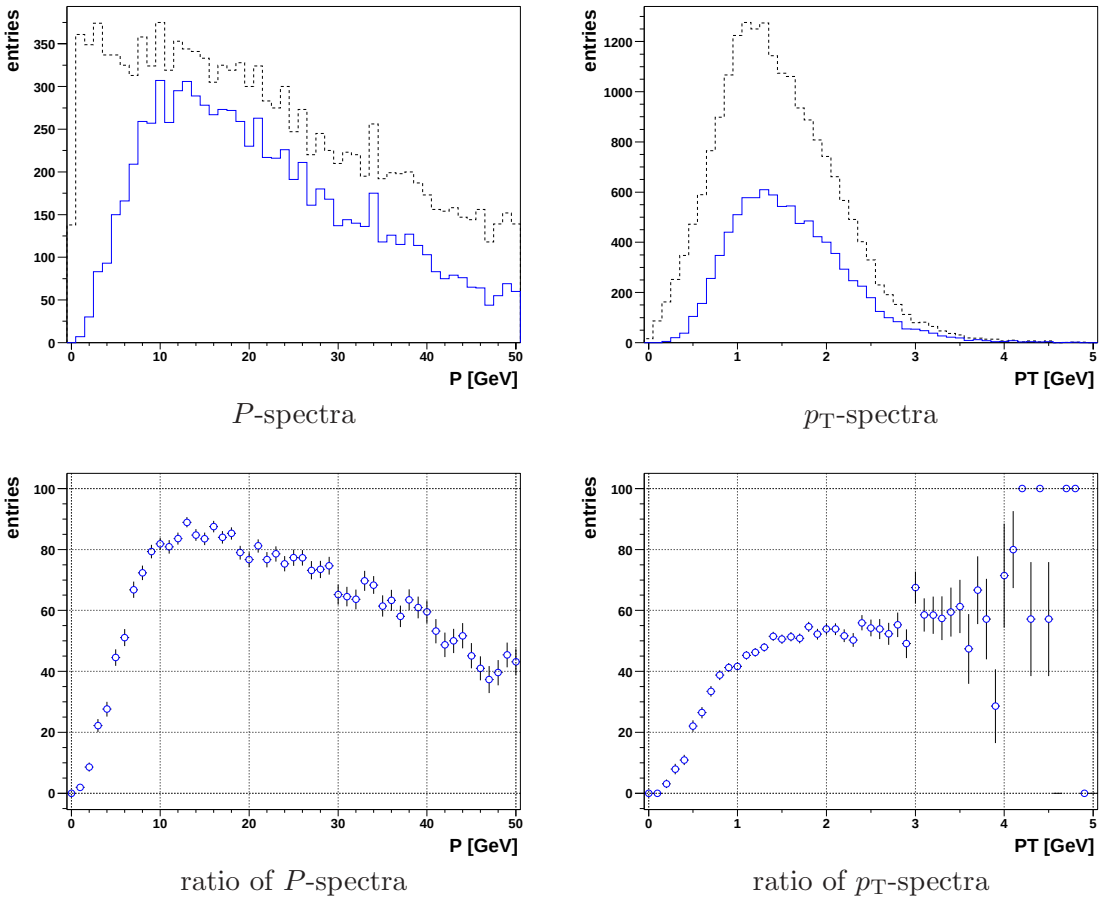

Fig. 5.3: Spectra of the momentum P and the transverse momentum p_T of the muons originating from a J/ψ-decay. The dashed curves indicate the full set of J/ψ-leptons while the solid lines show the leptons which are inside the geometrical FLT acceptance. Moreover, the ratio of the full set and the tracks within the acceptance are shown as a function of the momenta.

if there is in each superlayer at least one TFU that has a distance of more than 1 cm to the track. We do not apply a cut on the momentum of the track at this point in order to investigate first the dependence of the tracking efficiency on the momentum and transverse momentum.

Fig. 5.3 shows the spectra of momentum and transverse momentum of all muons of the J/ψ decays in the Monte Carlo and of those which pass the cut on the geometrical acceptance as well as the ratio of both track categories. The plots for electrons look similar and are thus not shown here. Note that only the TFUs which are assigned to the outer tracker are considered while the inner tracker TFUs are ignored. The ratio of the spectra of tracks before and after the geometrical cut reveal the influence of the acceptance. On one hand tracks, which pass the proton beam pipe or the acceptance of the inner tracker are discarded. On the other hand, tracks which exit the outer bounds

of the detector are also not regarded as reference tracks in the following.
The latter happens for tracks of low momentum which are bent heavily and thus exit the detector acceptance. This can be seen in the ratio of the momentum spectra of the tracks inside the acceptance and all tracks. The ratio decreases towards low momenta. In contrary, tracks of high momentum more likely pass the proton beam pipe and the inner tracker and therefore show an decreasing ratio towards higher momenta.
A similar result can be seen regarding the ratio of the spectra of the transverse momentum for tracks that are inside the acceptance and all tracks. Below a transverse momentum of $p_{\mathrm{T}} < 1.0\,\mathrm{GeV}$ the probability of a track to be inside the geometrical acceptance decreases. Below $p_{\mathrm{T}} < 0.5\,\mathrm{GeV}$ less than 10% of the tracks are within the acceptance.

Dependence of the Tracking Efficiency on the Momentum and Transverse Momentum

After applying the geometrical cut on the Monte Carlo generated tracks, we have a look on the tracking efficiency using the toy tracks. At this stage, we still do not apply a cut on the momentum, since we want to investigate the efficiency as a function of the momentum and transverse momentum.
We will use two different kinds of toy-tracks. Beside the toy-tracks which are based on the impact points of electron tracks in the superlayer PC01 and TC02 we additionally regard toy-tracks that use the Monte Carlo truth of muon tracks. Since we use them alternatively to estimate the FLT tracking efficiency in the outer tracker by generating electron pretrigger seeds from the muon tracks, we denote them as *muons 'faking' electron tracks* or shortly *'faked' electron tracks*.
The motivation for the consideration of the 'faked' electron tracks is the fact that electrons

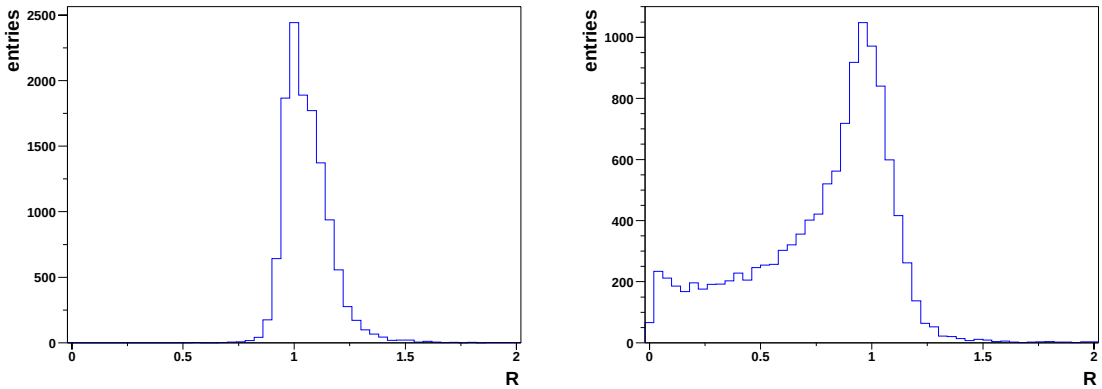

muon tracks electron tracks

Fig. 5.4: Distribution of the ratio of the *observed momentum* and the Monte Carlo truth momentum $R = P_{\mathrm{obs}}/P_{\mathrm{MC}}$ for muon and electron tracks. Due to the bremsstrahlung losses of the electrons one observes a tail towards low values of the *observed momentum*.

suffer a comparable high loss of energy due to bremsstrahlung radiation. The amount of energy which is lost before traversing the spectrometer magnet introduces a systematic error on the measurement of electron momenta based on the bending of the tracks in the magnetic field.

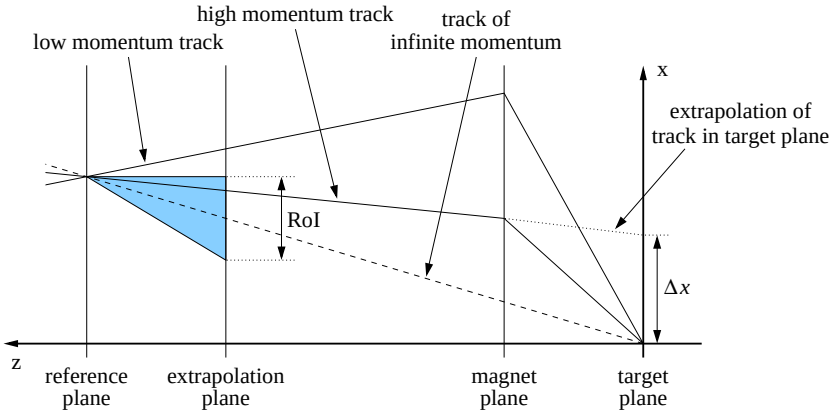

Fig. 5.5: Intrinsic momentum cut of the FLT algorithm. The FLT codes the region of interest (RoI) with respect to a track with infinite momentum. Therefore tracks of low momentum are not covered by the RoI and are not found. The x-position Δx of the track which is extrapolated into the target plane is used for the estimation of the track momentum in (Eq. 5.4).

To illustrate this, we compare the momentum of electron and muon tracks that one gets, first by regarding the Monte Carlo truth and second, by estimating the momentum by the magnet kick approach which was introduced in Sect. 2.5.1. If one extrapolates the track as observed behind the magnet into the target plane, the impact point Δx of the extrapolated track gives a measure for the momentum of the track according to

$$P = \frac{302.4\,\mathrm{GeV}\cdot\mathrm{cm}}{\Delta x} \tag{5.4}$$

see Fig. 5.5. We denote this momentum the *observed momentum* P_{obs} since this is the momentum which one observes by measuring the slope of the track behind the magnetic field. Fig. 5.4 shows the ratio $R = P_{\mathrm{obs}}/P_{\mathrm{MC}}$ of the observed momentum P_{obs} and the momentum of the Monte Carlo truth P_{MC} for both muon and electron tracks. In the muon case the distribution peaks at $P_{\mathrm{obs}}/P_{\mathrm{MC}} = 1$ and shows a shoulder towards higher ratios. This is just the inaccuracy which we introduce by using (Eq. 5.4). However this accuracy is more than sufficient to demonstrate the impact of the bremsstrahlung losses of the electron tracks. The histogram of the ratio $P_{\mathrm{obs}}/P_{\mathrm{MC}}$ for electron tracks shows a noticeable tail towards lower values reaching down to zero. Thus using the slope of the electron track as a measure of its momentum introduces a systematic error due to the

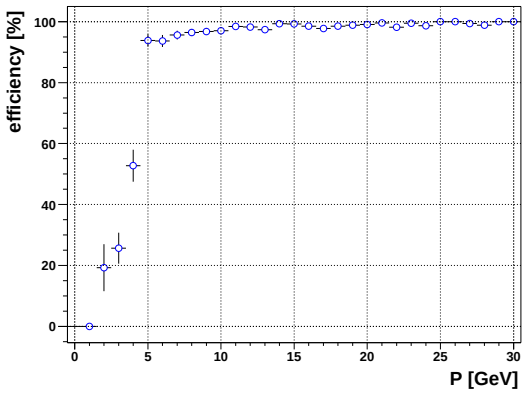

efficiency as a function of P_{MC} in TC01

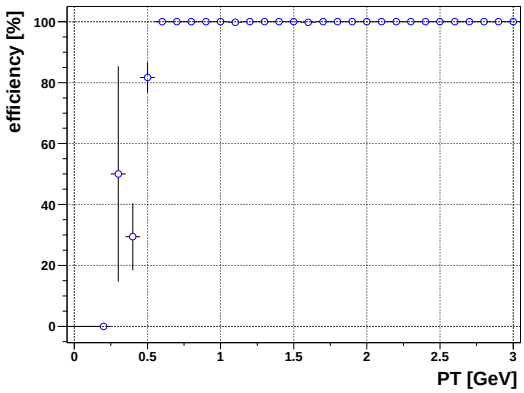

efficiency as a function of $p_{\mathrm{T,MC}}$ in the TPU

Fig. 5.6: Efficiency for message forwarding in the superlayer TC01 and the TPU as function of the Monte Carlo momentum P_{MC} and transverse momentum $p_{\mathrm{T,MC}}$, respectivly. The tracks used in these plots are muons 'faking' electron tracks. One observes clearly the drop in the efficiency in TC01 for tracks which have a momentum below 5.0 GeV due to the intrinsic momentum cut of the FLT tracking algorithm and the drop in the TPU for tracks of a transverse momentum below 0.5 GeV due to the cut which is performed in the TPU. For higher momenta the efficiencies reach almost 100%.

bremsstrahlung losses[1]. In order to illuminate the influence of this systematic error we will evaluate in the following the efficiencies for both electron tracks and 'faked' electron tracks.

Fig. 5.6 shows the probability for a message update in the superlayer TC01 as a function of the momentum of the track and the probability of passing the TPU in terms of the transverse momentum. For these plots the electron pretrigger messages are calculated based on the Monte Carlo truth of muon tracks and only the outer tracker part of the tracking is regarded starting with the generated electron pretrigger message.

The electron pretrigger simulation is not used here since it does not generate pretrigger messages for the muon tracks which are used for 'faking' electron tracks and in order to separate the influence of the pretrigger efficiency from the tracking efficiency of the FLT.

In Fig. 5.6 the efficiency stays constant at a level of nearly 100% but decreases drastically at momenta below 5.0 GeV. This is due to an intrinsic momentum cut of the FLT algorithm which is illuminated in Fig. 5.5. The region of interest (RoI) is coded with respect to a track of a hypothetical particle of infinite momentum. While tracks of high momentum pass close to the trajectory of infinite momentum tracks of low momentum hit the plane in a larger distance and thus are not covered by the RoI and get lost. This intrinsic momentum cut is determined by the maximum width of the RoI and leads to a

[1] As already discussed in Sect. 2.5.1, the FLT has incorporated the possibility to take the energy of bremsstrahlung clusters into account at the level of the TPU which carries out the momentum calculation. However, this feature was not used in the running of the year 2000 and is therefore not regarded in this thesis.

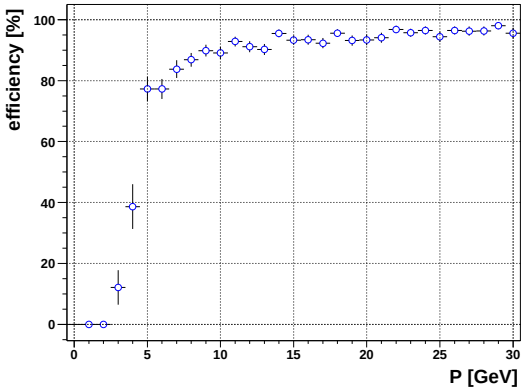

efficiency as a function of P_{MC} in TC01

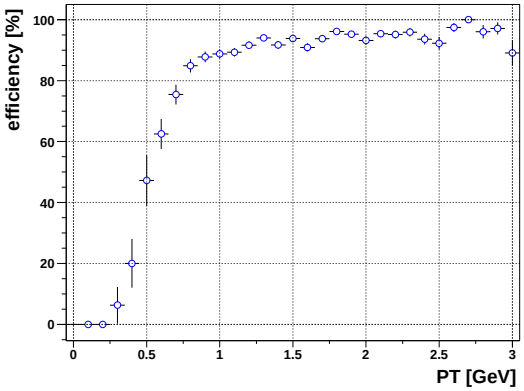

efficiency as a function of $p_{\mathrm{T,MC}}$ in the TPU

Fig. 5.7: Efficiency for message forwarding in the superlayer TC01 and the TPU as function of the Monte Carlo momentum P_{MC} and transverse momentum $p_{\mathrm{T,MC}}$, respectivly. In contrast to Fig. 5.6, in these plots electron tracks are used. One observes clearly the same drop in the efficiency in TC01 for tracks which have a momentum below 5.0 GeV and the drop in the TPU for tracks of a transverse momentum below 0.5 GeV as for the muons 'faking' electrons tracks. But in contrast, the cuts are more smooth and even for high values of P_{MC} and $p_{\mathrm{T,MC}}$, the efficiency stays below 100%.

cut of $P > 5.0\,\mathrm{GeV}$. Therefore we will cut on the momentum of the reference tracks for the efficiency determination in order to factor out this effect.

Another cut is performed by the algorithm of the TPU. The TPU calculates the momentum and transverse momentum of a found track based on the track parameters which have been obtained by the FLT tracking. Therefore the TPU is the natural place to apply a direct cut on the transverse momentum. In the simulation the cut on the transverse momentum in the TPU is set to $p_{\mathrm{T}} > 0.5\,\mathrm{GeV}$ which can be observed in the efficiency of message forwarding in the TPU as a function of of the transverse momentum, see Fig. 5.6. Above a transverse momentum of $p_{\mathrm{T}} > 0.5\,\mathrm{GeV}$ the efficiency reaches unity, below that value it decreases significantly and goes down to zero for values of $p_{\mathrm{T}} < 0.2$.

Please note that the momenta shown in the plots are taken from the Monte Carlo truth while the cuts in the simulation are performed on the FLT internal estimations of the momenta which are calculated by lookup tables and have therefore a limited precision. Because of this tracks which have a momentum which does not exceed the cuts of the TPU and the tracking algorithm may nevertheless pass the FLT.

In contrary to Fig. 5.6, Fig. 5.7 shows efficiencies of Monte Carlo electron tracks (no 'faked' tracks) which are also based on pretrigger messages which are calculated using the Monte Carlo truth, not the pretrigger simulation. In this case, the cuts show up more smoothly than for the 'faked' electron tracks and, additionally, the efficiency does not reach unity even for higher values of the momentum and the transverse momentum. To understand this, we have to remember that the momenta shown in Fig. 5.7 are based on the Monte

muons 'faking' electrons			
superlayer	efficiency		
	no momentum cut	$P_{MC} > 5.0\,\text{GeV}$ $p_{\text{T,MC}} > 0.8\,\text{GeV}$	$P_{obs} > 5.0\,\text{GeV}$ $p_{\text{T,obs}} > 0.8\,\text{GeV}$
PC01	$(95.0 \pm 0.2)\%$	$(96.7 \pm 0.2)\%$	$(96.7 \pm 0.2)\%$
TDU	$(94.6 \pm 0.2)\%$	$(96.7 \pm 0.2)\%$	$(96.7 \pm 0.2)\%$
electrons			
superlayer	efficiency		
	no momentum cut	$P_{MC} > 5.0\,\text{GeV}$ $p_{\text{T,MC}} > 0.8\,\text{GeV}$	$P_{obs} > 5.0\,\text{GeV}$ $p_{\text{T,obs}} > 0.8\,\text{GeV}$
PC01	$(89.0 \pm 0.3)\%$	$(91.0 \pm 0.3)\%$	$(96.1 \pm 0.3)\%$
TDU	$(81.3 \pm 0.4)\%$	$(84.5 \pm 0.4)\%$	$(95.9 \pm 0.3)\%$

Table 5.1: The FLT tracking efficiency for toy-generated tracks. Both the efficiencies for muons 'faking' electrons and electrons are reported at the superlayer PC01 and at the TDU. The latter efficiency comprises the kinematical cuts of the TPU. Moreover, the efficiencies are separated for different momentum cuts. The first column shows the efficiencies without momentum cut, in the second and third column cuts on the Monte Carlo momenta and the *observed momenta* are applied.

Carlo information of the tracks. As already discussed, unlike muons, electrons may lose a significant amount of energy when traversing the detector material by the production of bremsstrahlung. In this way the electron has a lower energy during the passage of the magnet and thus also the measured momentum of the track is lower compared to the production time.

Since the intrinsic momentum cut of the FLT algorithm is applied to the *observed momentum* as defined by the slope of the track, tracks may be discarded even if they have a momentum above the threshold of the algorithm. This can be seen in the smooth turn-on of the momentum and transverse momentum cut in Fig. 5.7. Moreover the efficiency does not reach unity even for high values of the momentum or transverse momentum as it was observed in the 'muons faking electron' case. In contrast, the efficiency stays at about 95%, since high momentum tracks happen to be cut due to high bremsstrahlung losses. The cuts on momentum and transverse momentum that we will perform on the reference tracks in the following sections will not raise the tracking efficiency to the optimal value which one gets using muon tracks. The influence of the bremsstrahlung loss will lower the efficiency in the electron case[2].

[2]There is of course the alternative to cut on the momentum not at the production time of the electrons but on the *observable momentum* which is relevant for the tracking efficiency. But since we are interested in the total efficiency for detecting a lepton originating from a J/ψ decay, we cut at the production of the lepton which allows a direct comparison of the efficiencies.

The tracking efficiencies of the FLT using toy-tracks in the outer tracker superlayers are summarized in table 5.1. It displays the ideal tracking efficiency of the FLT for outer tracker tracking. We regard toy-generated tracks that are inside the geometrical acceptance and that surpass the intrinsic momentum cut of the tracking algorithm of $P > 5\,\mathrm{GeV}$ and the cut on transverse momentum of $p_\mathrm{T} > 0.8\,\mathrm{GeV}$ to take the transverse momentum momentum cut if the TPU into account[3]. Using muon tracks in the outer tracker FLT tracking the efficiency inside the geometrical acceptance reach a value of $(94.6 \pm 0.2)\%$ if no momentum cut is applied and $(96.7 \pm 0.2)\%$ if the cuts are used which were just mentioned. The efficiencies of the tracking (at superlayer PC01) and of the entire FLT (after the TDU) differ only marginally, since the kinematical cuts on the reference tracks are similar to the cut of the TPU. The remarkable result is that even for idealized toy-track inside the geometrical acceptance the FLT tracking efficiency does not reach unity. The efficiency of $(96.7 \pm 0.2)\%$ in the outer tracker indicates thus the intrinsic efficiency of the FLT that cannot be assigned to detector inefficiencies or data transmission problems but just to the implementation of the tracking algorithm.
The efficiencies for the electron tracks reveal the influence of the bremsstrahlung energy loss. If one applies the cuts of $P > 5.0\,\mathrm{GeV}$ and $p_\mathrm{T} > 0.8\,\mathrm{GeV}$ on the observed momenta of the electron reference tracks, the efficiencies reach almost the level of the muon 'faking' electron tracks. If one cuts on the Monte Carlo truth momenta which correspond to the electron momenta at production time the efficiencies drop to $(91.0 \pm 0.3)\%$ at PC01 showing the influence of the intrinsic momentum cut of the tracking algorithm and to $(84.5 \pm 0.4)\%$ at the TDU which takes the kinematical cuts of the TPU into account. Thus one has to remember that even for an ideal detector and an ideal data transmission the electron tracking efficiency is highly reduced compared to muon tracking because of the bremsstrahlung radiation.

5.2 Tracking of GEANT Generated Tracks

After the investigation of the FLT tracking efficiency using toy-tracks which are idealized in the sense that they are straight tracks inside the detector volume and that the hits are generated geometrically, this section draws the attention on the tracking efficiency using GEANT generated tracks. GEANT [gea94] is a software package which is used in the Monte Carlo studies to simulate the passage of elementary particles through matter. The simulated particle trajectories take into account, for example, the effect of multiple scattering in different detector materials. Moreover the usage of GEANT simulated tracks introduces the usage of the FLT mapping. We use the hit information of the detector cells which is gained by the digitization. This information has to be transfered to the channels of the wire memories in the FLT simulation. This procedure requires the FLT mapping. The resulting effects on the tracking efficiency are subject of this section.

[3] As already mentioned we cut at a transverse momentum of $p_\mathrm{T} > 0.8\,\mathrm{GeV}$ in contrast to the cut of $p_\mathrm{T} > 0.5\,\mathrm{GeV}$ which is applied in the TPU in order to avoid the influence of binning uncertainties which are introduced by the momentum calculation of the FLT.

Generation of GEANT Tracks

When using GEANT generated tracks within the analysis software framework ARTE of HERA-*B*, one receives the digitized detector information in a decoded format which allows an easy implementation of the analysis software. In contrast, the data which is delivered from the detector is given in a raw format which has to be decoded and to be combined with the detector calibration. We denote this raw format as *daq format* since it is the format which is delivered by the data acquisition. As the FLT operates at an early stage of the event processing, the FLT simulation relies on this raw data format. Therefore when processing the FLT simulation on Monte Carlo, this daq format has to be constructed on the base of the Monte Carlo digitized detector information, see section 2.6. The software package DaqIf provides this functionality and has been developed by the SLT group for the SLT software which also needs the daq format for a realistic Monte Carlo processing.

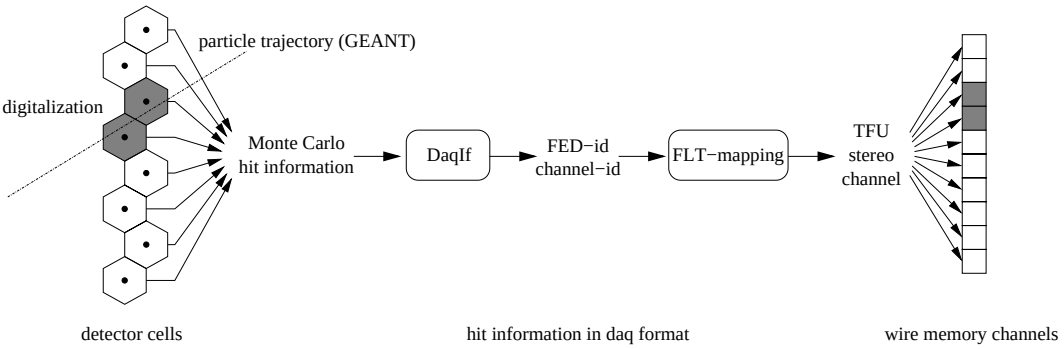

Fig. 5.8: Processing of GEANT generated tracks. The detector response is calculated by the detector specific digitization software. For the FLT the interesting output are the FED and channel numbers of the hit wires which are provided by the DaqIf software. The FLT mapping has to translate these numbers into the corresponding wire memory addresses.

Fig. 5.8 illustrates the processing of Monte Carlo hit information using GEANT, the detector digitization and DaqIf. The passage of the particles is simulated by GEANT, which delivers the impact points of the particles in the detector volumes. This information is used by the detector digitization routines which compute the detector response on the traversing particles. The hit efficiency of the outer tracker is assumed to be $\epsilon_{\text{hit}} = 100.0\%$ in this section. If a response is assumed by the digitization software, corresponding hits are used by the DaqIf software package to represent the detector response in the daq format, which can be used by the FLT simulation. At that point, the hits are represented by the front end driver identifier (FED-id) and the channel identifier (id). This information is used by the FLT mapping, which maps the FED- and channel-id to the channels of the wire memories of the TFUs which are used in the setup under investigation.
This is in contrast to the toy-tracks which were discussed in the previous section and which are generated by directly projecting straight tracks into the frame of the wire memory channels. In this way the realistic detector acceptance is taken into account, since a

hit in the wire memory has been generated by a hit of a specific wire of the detector. Moreover the effects of the FLT mapping procedure are taken into consideration. In the following section we will discuss the FLT tracking efficiency having special regard to the hit generation and the mapping. We first evaluate the efficiency of the muons 'faking' electron tracks after the TDU. This is done because the muon tracks show no losses due to bremsstrahung and therefore, the effects which we are interested in are seen more clearly. In the conclusion of the section we additionally state the results for original electron tracks.

Wire Memory Acceptance

First, we state the efficiencies for reference tracks which are selected by the same cut on the geometrical acceptance as it was done in the case of toy-generated tracks, i.e. they are within the idealized wire memory defined acceptance. In the following two more restrictive definitions of the acceptance will be regarded, too.
The efficiency for muon 'faking' electron tracks at the level of the TDU and using reference tracks which are within the acceptance defined by the wire memory geometry is $(79.3 \pm 0.5)\%$. A cut on the momentum of $P > 5.0\,\mathrm{GeV}$ and on the transverse momentum of $p_\mathrm{T} > 0.8\,\mathrm{GeV}$ is applied for the reference tracks. Comparing this to the corresponding efficiency of toy-generated tracks $(96.7 \pm 0.2)\%$ as stated in Table 5.1 shows that the efficiency for the GEANT generated tracks is considerably lower. For the only difference between the determination of both efficiencies is the method of setting the hits in the wire memory, we have to follow up the way how the hits are set in the simulation. In contrast to the toy-method which we discussed in the previous section and which directly sets the channels in the wire memory according to an idealized geometry, the way used in this section is more complicated, see Fig. 5.8.
According to the complexity of the mapping there are several sources of problems. We will take care in the following of two aspects in order to understand the difference of the efficiencies shown in Table 5.2 compared to the numbers obtained by the tracking efficiency of toy generated tracks, see Table 5.1.

Hit Relations

In order to trace back the origin of the loss of efficiency of GEANT generated tracks compared to toy-generated tracks, we introduce a more stringent condition for the acceptance which takes the mapping between detector cells and wire memory channels into account. One has to consider a cut on the geometrical acceptance which does not only take into account the idealized geometrical coverage of the wire memories.
Therefore we do not only require the particle trajectory to be within the idealized geometry of the wire memories, but additionally that the hits in the outer tracker cells are mapped into at least one TFU in each superlayer. A necessary condition for a message update is a triple coincidence which can be recognized by one TFU. Therefore we follow the relation of the Monte Carlo generated particle to the hits in the outer tracker and further

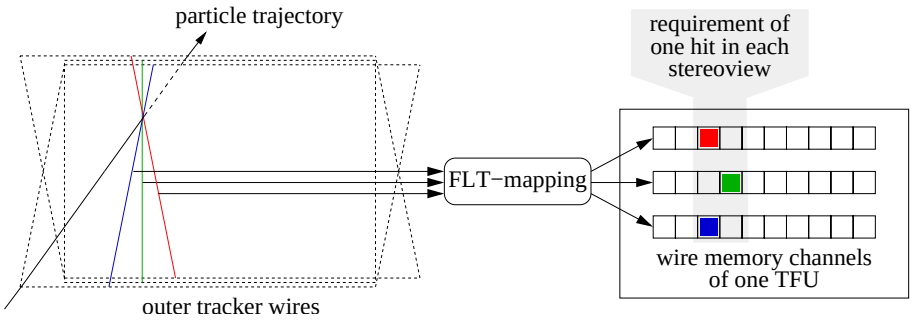

Fig. 5.9: Acceptance definition based on hit relations. A particle has to hit wires of the outer tracker such that in each superlayer there is at least one TFU which receives in the wire memories of each stereo view at least one hit which can be related to the particle in question.

the mapping of these hits into the wire memories of the TFUs. In order to fulfill the necessary condition for a message update in each superlayer there has to be at least one TFU which has hits in all three stereo view which can be related to the particle under consideration, as illustrated in Fig. 5.9.
Using this restriction on hit relations of the reference tracks, the tracking efficiency for muons 'faking' electron tracks increases from $(79.3 \pm 0.5)\%$ to $(85.0 \pm 0.4)\%$, measured to the level of the TDU. Still this is significantly less than the efficiency which was observed on toy-generated tracks which amounts to $(96.7 \pm 0.2)\%$. In fact there is an additional effect which will be discussed in the following section.

Wrong Mapping

Even if the hits of one particle have been transmitted to the wire memories of all three stereo views of one TFU, it may happen that no coincidence is found due to an additional effect. The mapping from the outer tracker wires to the wire memory channels may be wrong because of erroneous programming of the trigger link boards or due to incorrect connections from the ASD8 chips to the TDC boards which happened in fact at several places in the setup of the year 2000.
Fig. 5.10 illustrates the origin of this effect. If two cables connecting the hit information of two ASD8 chips to the trigger link boards are swapped, two times eight channels (two cables carrying the hit information of eight wires) are exchanged. The FLT mapping is based on the outer tracker cabling schemes as discussed in section 2.3.6. Thus if the cabling changes, the mapping becomes incorrect. Since the hits within such a region occur about eight channels shifted, the corresponding TFU has no possibility to find coincidences in that area. Areas of two times two swapped cables with or without correctly connected cables inbetween have likewise been observed.
In order to quantify the effect of wrong mapping, the requirement of acceptance is further restricted. For a given reference track the distance between the x-positions of all hit outer tracker wires to all x-positions of the corresponding wire memory channels in the virtual

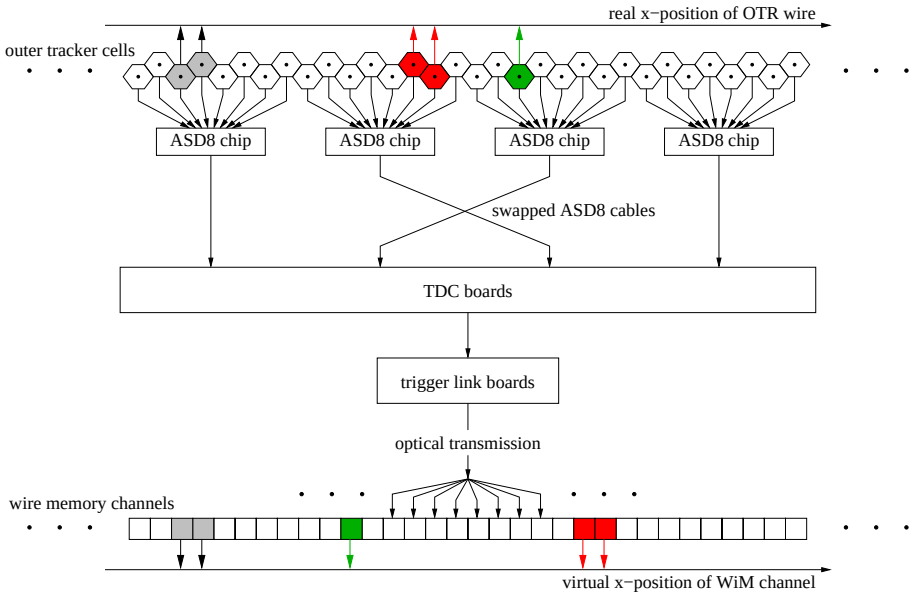

Fig. 5.10: Wrong mapping due to swapped ASD8-cables. In this exemplary flow chart two ASD8 cables are swapped leading to the mismapping of two times eight channels (the 'red hits' and the 'green hit' occur in reversed order in the outer tracker and in the wire memory). In order to detect those mismappings we evaluate the x-position of the OTR-wire using the OTR data base and compare it to the virtual positions of the corresponding wire memory channels given by the geometry information of the FLT data base.

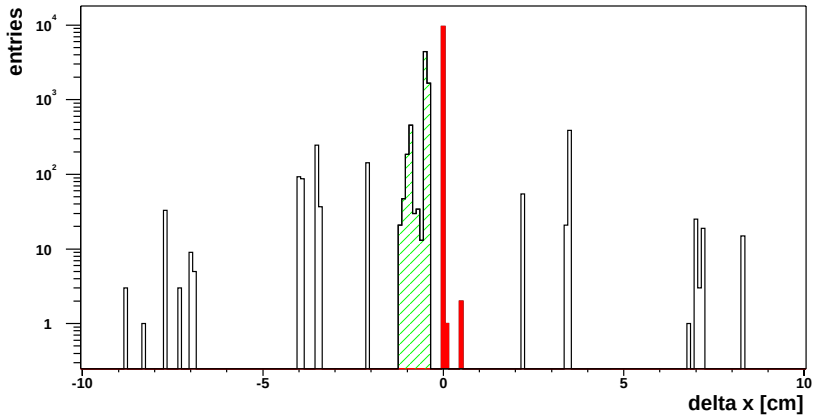

Fig. 5.11: Histogram of the differences of the real x-position of the wire of the outer tracker as reported by the OtrI software and the expected virtual x-positions of the corresponding wire memory channels. The correctly mapped wires show up in the central bin (solid red) while the side-peak in the interval $-1.0\,\mathrm{cm} \leq \Delta x \leq -0.5\,\mathrm{cm}$ is an artefact of the or-ing of adjacent channels in the minus stereo view (hatched green).

space of the idealized geometry are calculated. The x-positions of the outer tracker wires are provided by the outer tracker data base via the software package OtrI, while the virtual x-positions of the wire memory channels are defined by the FLT data base. For the plus- and minus-degree wires we evaluate the distance in the rotated space in which the wires are vertically aligned. Since an outer tracker wire may be mapped to several channels in different wire memories, we take the maximum distance in order to detect the maximum mismapping of that wire.
In case that all detector channels which are hit by the reference track in question are correctly mapped into the wire memories of the TFUs, the maximum distance of all x-positions of the hit wires to the virtual x-positions of the mapped channels in the wire memory frame does not exceed a fraction of the cell diameter. As soon as, due to cable-swapping, the distance in x of a wire in the detector and a wire memory channel which is assigned to it by the mapping becomes significantly larger, the wire is not correctly mapped.
A histogram of the differences found for all reference tracks which are used for the muons 'faking' electrons Monte Carlo is given in Fig. 5.11. First beside the sharp central peak at $\Delta x = 0\,\mathrm{cm}$ there is a broad side peak in the interval $-1.0\,\mathrm{cm} \leq \Delta x \leq -0.5\,\mathrm{cm}$. This side peak is an artefact of the or-ing of adjacent wires in the minus-degree view which shows up here in the mapping. The remaining satellite peaks are caused by mismappings which are introduced by the swapping of ASD8 cables. If any of the outer tracker wires which are hit by a given reference track have a maximum distance to the corresponding wire memory channels of more than $\Delta x >= 1.5\,\mathrm{cm}$ we regard that track as suffering under wrong mapping.
We are able to observe the effect of this criterion by plotting the x- and y-coordinates of messages in a certain superlayer depending on whether there was no update of that message in that superlayer. Areas of poor efficiency accumulate in these plots and show up as non-uniform structures in the x-y-view. Fig. 5.12 a) shows such structures which are related to regions of wrong mapping. It depicts the impact points of not updated messages in superlayer PC04. The structures vanish if one rejects tracks which suffer from wrong mapping, as defined by the method just described. The non-uniformities which are visible in Fig. 5.12 a) do not show up in Fig. 5.12 b) which depicts only impact points of tracks which are not updated in superlayer PC04 but have proven to be correctly mapped. Since they appear uniformly one can associate the non-updating of these messages to the intrinsic inefficiency of the FLT tracking algorithm.
Using this cut on correctly mapped reference tracks additionally to the cuts on geometrical acceptance and given hit relations — actually the first implies the two latter cuts — we reevaluate the FLT tracking efficiency for GEANT generated tracks. The tracking efficiency which amounts to $(79.3 \pm 0.5)\%$ for tracks within the acceptance of the wire memory geometry increases to $(85.0 \pm 0.4)\%$ if hit relations are required. If one demands reference tracks which are within areas of correct mapping the efficiency increases further to $(96.9 \pm 0.3)\%$ which is comparable to the efficiency for toy-generated tracks $\eta = (96.7 \pm 0.2)\%$, see Table 5.1.
Provided that the FLT mapping is correct and restricting to tracks which hit detector

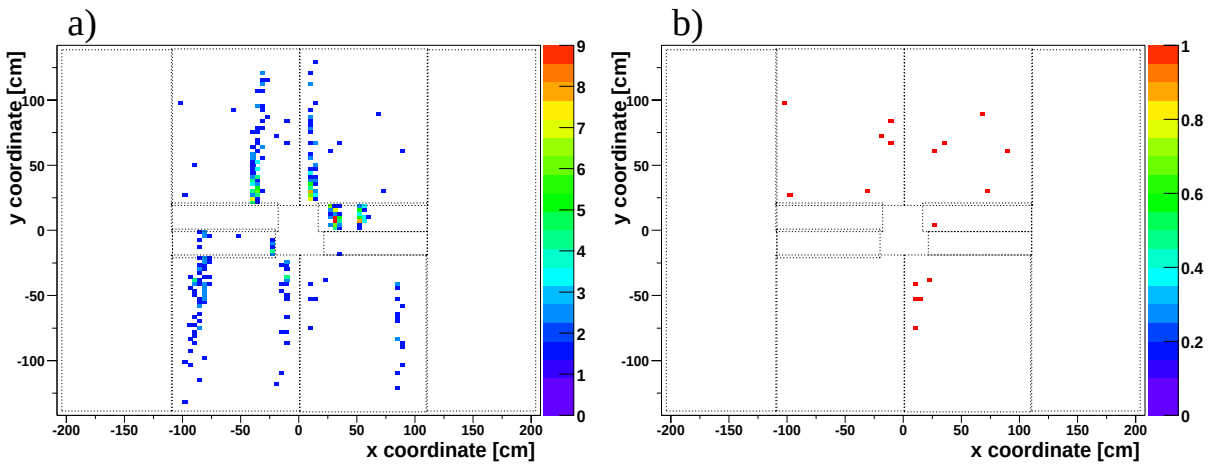

Fig. 5.12: Figure a) depicts the impact points of messages in superlayer PC04 which do not get an update. The structures visible in that plot, indicating regions of low efficiency are due to the areas of wrong mapping as described in the text. Figure b) shows the same impact points of the same sample of tracks but discarding tracks which traverse areas of wrong mapping according to the test described in the text. The noticeable structures of figure a) have vanished proving that they are caused by wrong mapping.

wires such that hits are present in at least one TFU of each superlayer the FLT tracking efficiency in the outer tracker is the same for toy-tracks and GEANT generated tracks.

Conclusion on the OTR Tracking Efficiency of GEANT Generated Tracks

After regarding the influence of the hit relations and the issue of correct mapping we summarize the discussion of the efficiencies of GEANT generated track. Additionally to the efficiencies for muon 'faking' electron tracks the numbers for original electron tracks will be regarded. The efficiency is evaluated at two points of the system, at superlayer PC01 which represents the pure tracking efficiency and after the TDU representing the additional influence of the kinematical cuts of the TPU. Moreover the efficiencies are given for two types of kinematical cuts: using the cut on the Monte Carlo truth momenta and on the observed momenta as introduced in Sect. 5.1.
The results for muons 'faking' electron tracks were already given during the discussion of the influence of the hit relations and the correct mapping on the tracking efficiency. They were evaluated after the TDU using a cut on the Monte Carlo truth momentum and transverse momentum of $P_{\mathrm{MC}} > 5.0\,\mathrm{GeV}$ and of $p_{\mathrm{T,MC}} > 0.8\,\mathrm{GeV}$, respectivly. In Table 5.2, besides these results, the efficiencies at the stage of the TPU and for the kinematical cuts on the observed momenta, are stated. Since the muon tracks do not loose energy by bremsstrahlung radiation, the observed momentum of the muons 'faking' electron tracks does not differ significantly to the Monte Carlo truth momenta. Because of

muons 'faking' electrons			
cut	superlayer	$P_{\mathrm{MC}} > 5.0\,\mathrm{GeV}$ $p_{\mathrm{T,MC}} > 0.8\,\mathrm{GeV}$	$P_{\mathrm{obs}} > 5.0\,\mathrm{GeV}$ $p_{\mathrm{T,obs}} > 0.8\,\mathrm{GeV}$
none	PC01	$(79.4 \pm 0.5)\%$	$(79.4 \pm 0.5)\%$
	TDU	$(79.3 \pm 0.5)\%$	$(79.4 \pm 0.5)\%$
on hit	PC01	$(85.0 \pm 0.4)\%$	$(85.0 \pm 0.4)\%$
relations	TDU	$(85.0 \pm 0.4)\%$	$(85.0 \pm 0.4)\%$
on correct	PC01	$(96.9 \pm 0.3)\%$	$(97.0 \pm 0.3)\%$
mapping	TDU	$(96.9 \pm 0.3)\%$	$(97.0 \pm 0.3)\%$
electrons			
cut	superlayer	$P_{\mathrm{MC}} > 5.0\,\mathrm{GeV}$ $p_{\mathrm{T,MC}} > 0.8\,\mathrm{GeV}$	$P_{\mathrm{obs}} > 5.0\,\mathrm{GeV}$ $p_{\mathrm{T,obs}} > 0.8\,\mathrm{GeV}$
none	PC01	$(72.9 \pm 0.5)\%$	$(78.0 \pm 0.5)\%$
	TDU	$(68.1 \pm 0.5)\%$	$(77.8 \pm 0.5)\%$
on hit	PC01	$(78.6 \pm 0.5)\%$	$(83.8 \pm 0.5)\%$
relations	TDU	$(73.3 \pm 0.6)\%$	$(83.6 \pm 0.5)\%$
on correct	PC01	$(89.3 \pm 0.5)\%$	$(94.1 \pm 0.4)\%$
mapping	TDU	$(83.8 \pm 0.6)\%$	$(94.0 \pm 0.4)\%$

Table 5.2: Tracking efficiencies for Monte Carlo tracks using GEANT digitization. Both the efficiencies for muons 'faking' electrons and electron tracks are shown at the superlayer PC01 and the TDU. The kinematical cuts (5.0 GeV on the momentum and 0.8 GeV on the transverse momentum) on the reference tracks are performed on the Monte Carlo momenta (P_{MC}, $p_{\mathrm{T,MC}}$) and on the *observed momenta* (P_{obs}, $p_{\mathrm{T,obs}}$).

this, the results for cutting on the Monte Carlo truth momenta and on observed momenta are similar. Moreover, the kinematical cuts of the TPU also do not lower the efficiencies since the momentum calculation of the TPU again is not influenced by bremsstrahlung radiation of the measured tracks.

The picture changes when regarding the tracking efficiencies for electron tracks because of their significant loss of energy introduced by bremsstrahlung radiation. As shown in Sect. 5.1 the implementation of the FLT tracking algorithm leads to an implicit cut on the track slope which results in a momentum cut of about $P > 5.0\,\mathrm{GeV}$. Because of the loss due to bremsstrahlung this implicit cut on momentum affects electron tracks of even higher production momenta that $P > 5.0\,\mathrm{GeV}$ which leads to a decreased tracking efficiency. This can be observed by comparing the efficiencies at superlayer PC01 in Table 5.2 which represent the efficiencies of the tracking algorithm without the kinematical cuts of the TPU for muon 'faking' electron tracks and electron tracks. The efficiency for electron tracks at superlayer PC01 is about 5% below the efficiency of muon 'faking' electron

tracks which do not underlie the bremsstrahlung radiation.
After the TDU, the efficiency is further decreased by about 5% compared to the efficiency at PC01 because of the cut on transverse momentum in the TPU, which is also influenced by the energy loss due to bremsstrahlung.
In order to avoid this artefact of the electron tracking we alternatively do not cut on the momentum and transverse momentum which is provided by the Monte Carlo truth but on the *observed momentum* as introduced using (Eq. 5.4). The *observed momentum* measures the particle energy as a function of the bending inside the magnetic field and is thus similar the method used by the FLT. Using this method we get in the case of muon 'faking' electron tracks the same results as performing the cut on the Monte Carlo momenta, see Table 5.2, which is expected because the muon tracks do not emit bremsstrahlung. In contrary, the tracking efficiencies of the electron tracks increase significantly using the cut on the observed momenta and reach — within errors — the same values of the muon 'faking' electron tracks.
Using the cut on correct mapping one gets the same tracking efficiencies for toy-tracks and for GEANT-generated tracks. The difference in the tracking efficiencies for toy and GEANT generated tracks can be therefore reduced to the problems of the correct geometrical acceptance (which is taken into account by the cut on the hit relations) and to the problems of wrong mapping.
To conclude we record that the FLT tracking efficiency in the outer tracker using the superlayers TC02, TC01, PC04 and PC01 and the kinematical cuts in the TPU reaches a level of 97% for both GEANT generated and toy-generated tracks using muon tracks in a idealized detector without dead or hot channels, assuming 100% cell efficiency and nominal alignment. For electron tracks the efficiencies are lower because of the energy loss due to bremsstrahlung which results in decreased efficiencies of about 85% for both toy-tracks and GEANT generated tracks. All these numbers are based on a momentum cut of $P_{\mathrm{MC}} > 5.0\,\mathrm{GeV}$ and a transverse momentum cut of $p_{\mathrm{T,MC}} > 0.8\,\mathrm{GeV}$. If one cuts on the momenta as observed behind the magnet the efficiencies for electron tracks rise to the values of muon tracks.
In the following sections we will take care of items introducing inefficiencies such as defective channels, outer tracker cell efficiency and misalignment.

5.3 Influence of Alignment on the Tracking Efficiency

The FLT tracking algorithm requires an aligned detector. The Monte Carlo efficiency estimations as presented in the preceding sections are made using the nominal chamber positions, implying an ideal aligned detector. But since the tracking algorithm of the FLT requires well located triple coincidences which have to be within a region of interest, the tracking efficiency sensitively depends on the actual position of hits. This can only be guaranteed if the geometry of the detector is well known.
The positioning accuracy of the detector is limited by practical reasons and, therefore, one has to correct for the differences of the nominal and the actual detector positions. This correction is called *alignment* and has to be determined directly by measuring the detector positions (which has a limited accuracy) and indirectly by the analysis of data. In this section, the impact of a limited knowledge of the detector position of the FLT tracking efficiency is investigated. Moreover the efficiencies for the nominal positions and the OTR alignment of the year 2000 data taking are compared.

Tracking Efficiency as a Function of Alignment Accuracy

In order to estimate the sensitivity of the tracking efficiency of the FLT with respect to the positioning accuracy of the detector, the efficiency for the electron and muons 'faking' electron sample is evaluated after application of randomly generated shifts in the outer tracker module positions. This is done in order to simulate a limited positioning accuracy of the modules. The values of the module shifts follow a Gaussian distribution and the efficiencies are evaluated for different standard deviations.
Fig. 5.13 a) shows the relative decrease of tracking efficiency of electron tracks as a function of the standard deviation σ_x of the randomly generated module shifts in x. Figure b) shows the same for muons 'faking' electron tracks. For $\sigma_x = 0.5\,\text{cm}$ the drop in efficiency is in both cases about 1% and for $\sigma_x = 1.0\,\text{cm}$ it amounts already about 4%. For higher standard deviations of the module positions the efficiency decreases rapidly.
The alignment dependence of the FLT is determined by two constrains. First, the requirement of having a triple coincidence implies a huge sensitivity on the hit efficiency. Since the shift of a hit may lead to either the loss of a triple coincidence or losing the overlap of the hits and the region of interest, already the shift of one hit may result in the loss of a track. Second, the granularity of the detector (mainly 5 mm-cells in the OTR) defines the scale at which a shift in the geometry of the detector influences the tracking algorithm.
Taking these two factors together the shapes of the alignment accuracy dependences of the tracking efficiency in Fig. 5.13 can be understood. The width of the cells of 5 mm makes the FLT insensitive to small deviations of the detector positions up to values of $\sigma_x = 0.5\,\text{cm}$. In contrast, the strict requirement of triple coincidences in each superlayer is reflected by the fact, that starting at $\sigma_x = 1.0\,\text{cm}$ the relative tracking efficiency decreases by approximately 10% for each cm of increasing standard deviation of the position uncertainty.

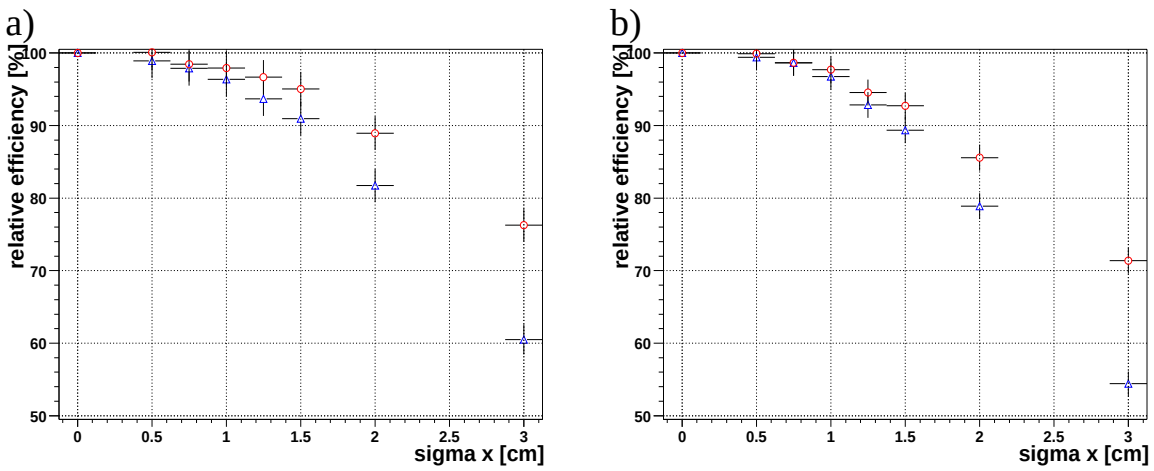

Fig. 5.13: Relative FLT tracking efficiency (compared to having no misalignment) at the TDU as a function of the misalignment σ_x (sigma x) of outer tracker modules. Figure a) shows the relative efficiencies for electron tracks while figure b) depicts muons 'faking' electron tracks. The blue triangles give the values using the nominal FLT geometry while the red circles indicate the improvements which are gained by using a dedicated FLT geometry which is based on the random misalignment.

The FLT has the possibility to correct for shifted detector positions by using a corresponding modified geometry. This method is limited to shifts of the positions of entire wire memories representing one stereo view of one TFU. Because several detector modules are mapped into one such wire memory it is possible only to correct for the average shift of the detector modules. However common shifts of groups of modules which are mapped into one TFU can be corrected.

We discuss the impact of shifted detector positions on the FLT by regarding Fig. 5.14 which depicts three different cases. In the first case both the OTR module positions and FLT geometries are at their nominal values. Thus, if a particle hits a cell of number a at x_{hit}, the FLT mapping associates the corresponding wire memory channel m which again is situated at x_{hit} in the virtual wire memory frame. A region of interest (RoI) which covers the area of the particle trajectory also covers the hit in the wire memory in this case (for simplicity reasons, we regard only one stereo view here).

This situation changes if the detector is shifted with respect to its nominal position by Δx. In this case another cell of number b of the detector is hit by the particle and correspondingly another channel in the wire memory receives the hit signal. Because of the shift of the detector by Δx the wire memory channel which receives the hit information is correspondingly shifted by $-\Delta x$ which respect to the real particle trajectory. In case the extrapolation of the particle trajectory into the wire memory is correct, the RoI misses the hit in the wire memory by Δx and therefore the track gets lost.

In order to fix this problem one has the possibility to use an aligned FLT geometry. This geometry takes into account the shifts of the detector positions which respect to the nominal positions. The aligned FLT geometry can be built on the basis of an OTR alignment

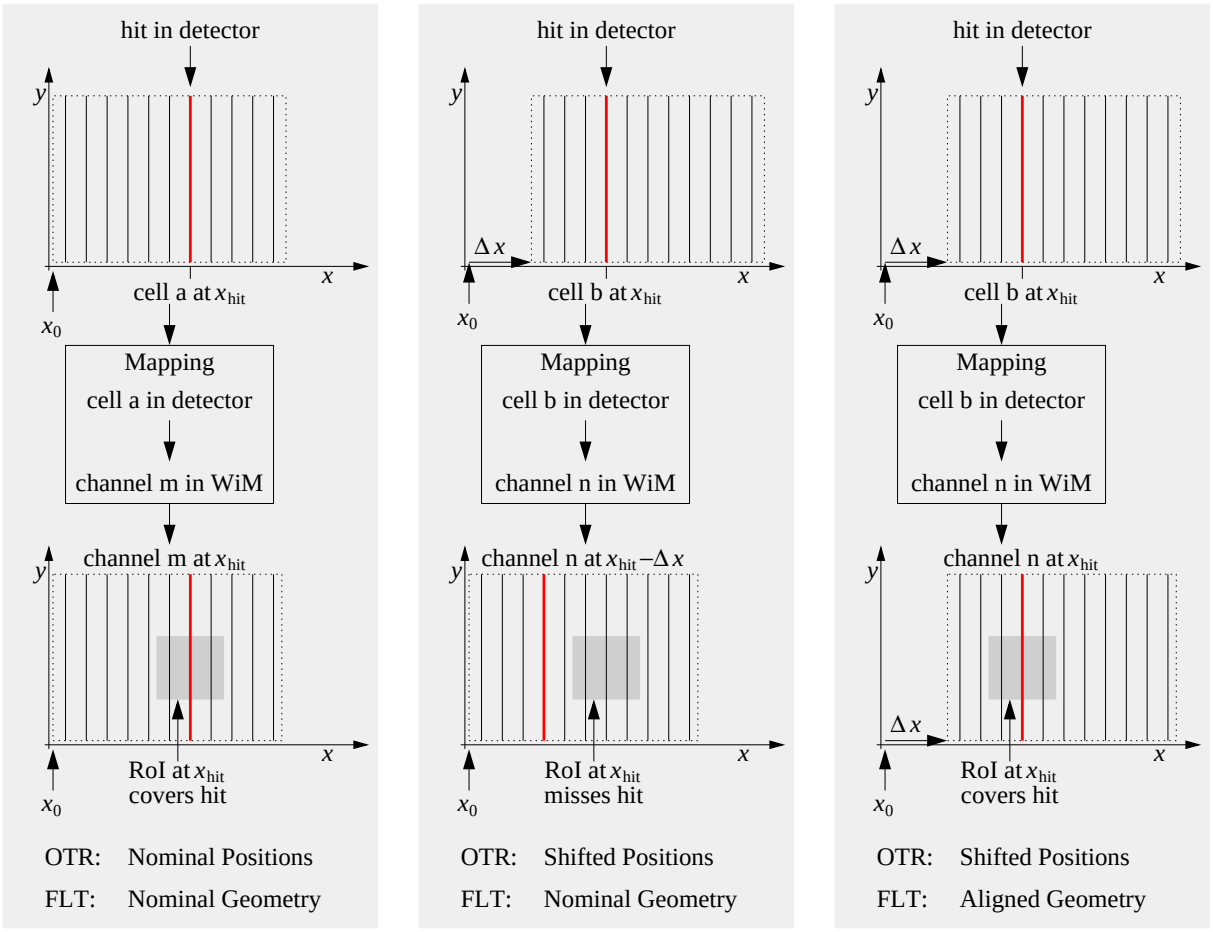

Fig. 5.14: Geometry relations for nominal and shifted positions of the OTR modules and nominal and aligned geometries of the FLT. For simplicity, only one stereo view is shown here.

which reports the shifts of each detector module[4]. This alignment of the FLT geometry is limited by two factors: first the OTR alignment is only known to a limited accuracy. During the year 2000 the OTR alignment was known to a precision of about 1.0 cm to 1.5 cm [krü02] which limits the accuracy of the aligned FLT geometry. Moreover each stereo view of each TFU receives the hit information of several detector modules. In contrast only the position for the entire stereo view averaging over all modules used in that stereo view can be corrected. Shifts among the modules cannot be taken into account.

In order to estimate the capabilities of an aligned FLT geometry for some of the random generated outer tracker shifts according FLT geometries are produced. This is done by averaging the shifts of all detector modules which are mapped into one wire memory and applying this average shift to the geometry of the wire memory. Running the FLT

[4]Although the FLT is able to correct in addition for shifts in y and z as well as corrections for the stereo angle, only shifts in the x-direction are regarded here.

simulation using the randomly shifted outer tracker modules and taking the corresponding FLT geometries into account the results shown in Fig. 5.13 are obtained.
Compared to the tracking efficiencies that are received for the randomly shifted detector modules, the usage of a corresponding aligned FLT geometry, improves the efficiency significantly. Nevertheless, the original efficiency is not reached. For example, for random shifts of $\sigma_x = 1\,\text{cm}$ only about 60% of the efficiency loss can be 'recovered' by the usage of the correspondingly FLT geometry. As already mentioned, this is unavoidable, since the FLT geometry is not able to take into account shifts among different modules that are mapped into one wire memory of one TFU stereo view.
Nevertheless, shifts of whole superlayers can be corrected completely. Shifts of the two halfs of one superlayer (minus-x and plus-x side) can be corrected except for the overlap region of the minus-x side which is mapped to the plus-x TFUs. This is because of the different borders of both detector halfs: the outer tracker borders are defined by the electron beam pipe while the border of the TFUs was chosen to be at $x = 0$. All further corrections are limited for the reasons just mentioned.

Tracking Efficiency for a Realistic Alignment

After the inspection of the relation of the FLT tracking efficiency and the accuracy of the detector position, the interplay of the outer tracker alignment of the year 2000 and the FLT geometry has to be regarded. By reporting the deviation of the measured detector positions compared to the nominal positions, the OTR alignment opens the possibility to take into account these deviations in the event reconstruction. In the case of the FLT this can be done by deriving a modified FLT geometry from the OTR alignment.

OTR positions	FLT geometry	tracking efficiency	
		electrons	muons 'faking' electrons
nominal	nominal	$(68.1 \pm 0.5)\%$	$(79.2 \pm 0.5)\%$
shifted	nominal	$(62.0 \pm 0.5)\%$ (-9.0%)	$(70.4 \pm 0.5)\%$ (-11.1%)
shifted	aligned	$(65.7 \pm 0.5)\%$ (-3.5%)	$(76.1 \pm 0.5)\%$ (-3.9%)

Table 5.3: FLT tracking efficiency for electron and muon 'faking' electron tracks for nominal OTR positions and FLT geometry, shifted OTR positions (corresponding to the alignment of the OTR in 2000) but nominal FLT geometry, and shifted OTR positions and accordingly aligned FLT geometry.

In this section the influence of the OTR detector positions during the year 2000 running is estimated. This estimation is based on the outer tracker alignment that was available during 2000 and that was the basis of the corresponding aligned FLT geometry. During that running period, the real outer tracker detector positions and therefore the outer tracker alignment was known by an accuracy of $\sigma_x \approx 1.0...1.5\,\text{cm}$ [krü02]. For the estimation of the influence of the outer tracker detector positions first the FLT simulation is run using the OTR alignment of the year 2000 but taking the nominal FLT geometry.

This simulates the shifts of the detector modules during this period and gives the loss in tracking efficiency. Second, additionally, the corresponding FLT geometry that was used for the creation of the lookup tables during the year 2000 data taking is applied.
The results are shown in Table 5.3. Compared to the nominal detector positions, the tracking efficiency drops by about 10% if one applies the OTR module positions as reported by the OTR alignment. Using the corresponding FLT geometry improves the efficiency again such, that the drop of efficiency decreases to about 3.5%. This is the loss in FLT tracking efficiency due to the outer tracker misalignment which cannot be improved by changes in the FLT geometry.

5.4 Influence of Hit Efficiency on the Tracking Efficiency

Up to now, we idealized the detector assuming a hit efficiency of 100%. In reality this ideal efficiency is not reached and one has to take the influence of the real hit efficiency into account for the estimation of the FLT tracking efficiency. In Sect. 2.3.1 it was claimed that the dependence of the FLT tracking efficiency in the OTR $\epsilon_{\mathrm{FLT,\,OTR}}$ and the single cell hit efficiency $\epsilon_{\mathrm{single\,cell}}$ is given by

$$\epsilon_{\mathrm{FLT,\,OTR}} = \epsilon^{12}_{\mathrm{double\,cell}} = (1 - (1 - \epsilon_{\mathrm{single\,cell}})^2)^{12} \tag{5.5}$$

This equation is based on two assumptions. First, the efficiency of a double layer is estimated using the or-ing of two single layers $\epsilon_{\mathrm{double\,cell}} = 1 - (1 - \epsilon_{\mathrm{single\,cell}})^2$. Second, the cell hit efficiency is assumed to be the probability that a track which geometrically traverses the sensitive region of a detector cell generates a measurable signal. The second assumption is a matter of definition and one has to remember that the cell efficiency is in general defined differently, while the first assumption is only approximately valid. In the following both assumptions are rendered more precisely in order to give a form of (Eq. 5.5) which is in agreement to Monte Carlo.

Outer Tracker Hit Efficiency

The hit efficiency of a drift cell, as used in this analysis, is the probability that a hit is found if a charged particle geometrically traverses that particular cell. This efficiency is defined for working cells, it does not cover dead, noisy or hot detector cells which will be treated separately in Sect. 5.5.
When specifying the hit efficiency one has to consider that the hit efficiency of a cell depends on the length l of the track segment in the cell, i.e. the length of the path that the particle traverses geometrically inside the cell. The dependence of the track segment l on the probability of a signal is called *efficiency profile* and can be estimated by the relation

$$\epsilon_{\text{hit}}(l) = 1 - e^{-\alpha_{\text{eff}} \cdot l} \tag{5.6}$$

The *effective cluster density* α_{eff} which is used in this equation is given by the plateau efficiency ϵ_{plt} which corresponds to the hit efficiency for the maximal track segment length

$$\epsilon_{\text{plt}} = 1 - e^{-\alpha_{\text{eff}} \cdot l_{\max}} \quad \Longrightarrow \quad \alpha_{\text{eff}} = -\frac{1}{l_{\max}} \ln(1 - \epsilon_{\text{plt}}) \tag{5.7}$$

Therefore the efficiency profile can also be expressed in terms of the plateau efficiency

$$\epsilon_{\text{hit}}(l) = 1 - e^{-\alpha_{\text{eff}} \cdot l} = 1 - (1 - \epsilon_{\text{plt}})^{\frac{l}{l_{\max}}} \tag{5.8}$$

To get the probability that a hit is generated if a particle traverses the cell geometrically one has to integrate over the efficiency profile. If s is the distance of the track to the wire after normalizing $l_{\max} = 1$, see Fig. 5.15 a), the length of the track segment is given by

$$l(s) = \begin{cases} 1 & \text{for} \quad |s| < \frac{1}{2} \\ \sqrt{3} - \frac{1}{2} - |s| & \text{for} \quad \frac{1}{2} < |s| < \sqrt{3} - \frac{1}{2} \\ 0 & \text{for} \quad \sqrt{3} - \frac{1}{2} < |s| \end{cases} \tag{5.9}$$

For this we assume the track passing without slope, which gives a sufficient precision for our purposes. Thus the average hit efficiency as a function of the plateau efficiency $\epsilon_{\max}$ is given by integration over the geometrical cell acceptance

$$\begin{aligned} \epsilon_{\text{avg}}(\epsilon_{\text{plt}}) &= 1 - \tfrac{1}{2\sqrt{3}-1} \left((1 - \epsilon_{\text{plt}}) + 2 \int_{\frac{1}{2}}^{\sqrt{3}-\frac{1}{2}} (1 - \epsilon_{\text{plt}})^{\frac{1}{\sqrt{3}-1}\left(\sqrt{3}-\frac{1}{2}-s\right)} ds \right) \\ &= 1 - \tfrac{1}{2\sqrt{3}-1} \left((1 - \epsilon_{\text{plt}}) + \tfrac{2(\sqrt{3}-1)}{\ln(1-\epsilon_{\text{plt}})} \left((1 - \epsilon_{\text{plt}})^{\frac{1}{-\sqrt{3}+1}} - (1 - \epsilon_{\text{plt}})^{\frac{\sqrt{3}}{-\sqrt{3}+1}} \right) (1 - \epsilon_{\text{plt}})^{\frac{\sqrt{3}}{\sqrt{3}-1}} \right) \end{aligned} \tag{5.10}$$

This dependence of the average hit efficiency ϵ_{avg} as a function of the plateau efficiency ϵ_{plt} is visualized in Fig. 5.15 b). First, ϵ_{avg} is almost proportional to ϵ_{plt} for $\epsilon_{\text{plt}} < 0.5$, ϵ_{avg} always $< \epsilon_{\text{plt}}$. For $\epsilon_{\text{plt}} \sim 1$, ϵ_{avg} increases very fast and meets ϵ_{plt} at $\epsilon_{\text{plt}} = 1$. A list of values for the plateau efficiency and corresponding average efficiencies is given in Table 5.4.

Tracking Efficiency as a Function of the Hit Efficiency

We want to understand the dependence of the FLT tracking efficiency as a function of the average hit efficiency of the OTR, as introduced in the previous section. This is done using muon 'faking' electron tracks as introduced in Sect. 5.1. The particle trajectories are generated by GEANT and the digitization is done by the HERA-*B* analysis framework ARTE. It is possible to specify the plateau hit efficiency $\epsilon_{\text{plt}}^{\text{hit}}$ which is used by the digitization routine for each detector plane separately. In this section the plateau hit efficiency

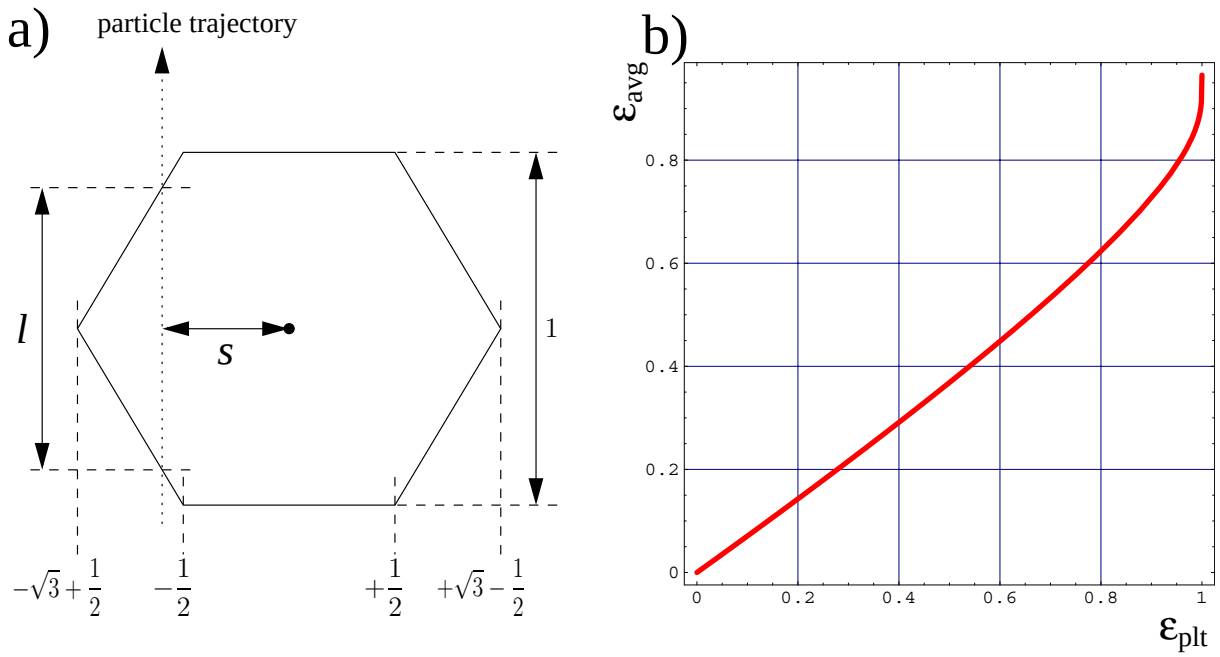

Fig. 5.15: Plot of (Eq. 5.10). Figure a) indicates the integration limits which are used to compute the average hit efficiency in (Eq. 5.10). Figure b) depicts the result of this equation. The average hit efficiency ϵ_{avg} is ploted as a function of the plateau efficiency ϵ_{plt}.

is uniformly set to values ranging from 80.0% to 100.0%, while the FLT simulation is evaluated for the same Monte Carlo multiple times.

The dependence of the tracking efficiency on the plateau efficiency is illustrated in Fig. 5.16. The tracking efficiency is given at each of the four superlayers which are used by the FLT outer tracker tracking. One discrepancy becomes visible comparing the tracking efficiency for an adjusted plateau hit efficiency of $\epsilon_{\text{plt}}^{\text{hit}} = 100.0\%$ to the values of lower plateau hit efficiencies. The tracking efficiency for $\epsilon_{\text{plt}}^{\text{hit}} = 100.0\%$ is significantly higher than the asymptotic value for the remaining hit efficiency range.

The reason of this behaviour can be found in the relation of the plateau hit efficiency and the average hit efficiency. As shown in Fig. 5.15 b) the average hit efficiency shows a quite non-linear dependence of the plateau hit efficiency. Even for values near to unity of the plateau efficiency the average hit efficiency stays significantly lower. This results in the low tracking efficiency values for plateau efficiencies below unity.

This behaviour changes when plotting the tracking efficiency as a function of the average hit efficiency rather than the plateau hit efficiency, see Fig. 5.17. The tracking efficiency develops continually for changes of the average hit efficiency. In the following a suitable fitting function will be developed which allows to describe the dependence of Fig. 5.17.

In Sect. 2.3.1 we already used the relation

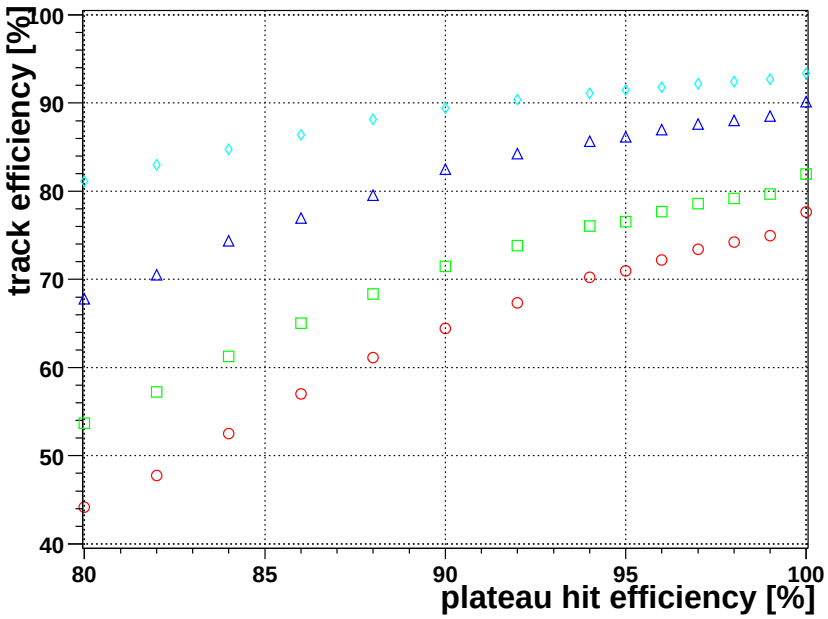

Fig. 5.16: Tracking efficiency as a function of the plateau hit efficiency $\epsilon_{\text{plt}}^{\text{hit}}$ evaluated at the OTR superlayers TC02 (cyan diamonds), TC01 (blue triangles), PC04 (green squares) and PC01 (red circles).

$$\epsilon_{\text{track}} = (1 - (1 - \epsilon^{\text{hit}})^2)^{12} \tag{5.11}$$

for estimating the FLT tracking efficiency ϵ_{track} in the outer tracker as function of the hit efficiency ϵ_{hit}. The or-ing of the double layers increases the single layer hit efficiency ϵ^{hit} to the value $1-(1-\epsilon^{\text{hit}})^2$. Taking this value to the 12th power reflects the requirement of having a triple coincidence in all four superlayers. Based on the data of Fig. 5.16 one can test the validity of (Eq. 5.11). The result is that (Eq. 5.11) is able to describe the data only roughly (resulting in a $\chi^2/ndf = 121.2/13$). Therefore an alternative description will be developed in the following.

For the estimation of the tracking efficiency we assume that the tracking efficiency in the four superlayers of the outer tracker ϵ^{track} is made up by multiplication of the probability ϵ^{update} of an update in one of the superlayers

$$\epsilon^{\text{track at superlayer } n} = (\epsilon^{\text{update}})^n \tag{5.12}$$

The probability of an update in one superlayer depends on the probability of having at least one hit in the wire memory for each stereo view. Moreover, the update probability depends on the cluster widths in the wire memory. In order to keep things simple, we compose the update probability of a component which is proportional to the probability of having at least one hit in the wire memories of each stereo view and a component which

hit efficiency		track efficiency in superlayer			
$\epsilon_{\text{plt}}^{\text{hit}}$	$\epsilon_{\text{avg}}^{\text{hit}}$	TC02	TC01	PC04	PC01
100.0%	100.0%	$(93.4 \pm 0.3)\%$	$(90.2 \pm 0.3)\%$	$(82.0 \pm 0.4)\%$	$(77.7 \pm 0.5)\%$
99.9%	91.4%	$(93.0 \pm 0.3)\%$	$(89.3 \pm 0.3)\%$	$(80.8 \pm 0.4)\%$	$(76.2 \pm 0.5)\%$
99.5%	88.6%	$(92.9 \pm 0.3)\%$	$(88.9 \pm 0.4)\%$	$(80.2 \pm 0.4)\%$	$(75.6 \pm 0.5)\%$
99.0%	86.8%	$(92.7 \pm 0.3)\%$	$(88.5 \pm 0.4)\%$	$(79.7 \pm 0.4)\%$	$(75.0 \pm 0.5)\%$
98.5%	85.5%	$(92.5 \pm 0.3)\%$	$(88.3 \pm 0.4)\%$	$(79.6 \pm 0.4)\%$	$(74.7 \pm 0.5)\%$
98.0%	84.3%	$(92.4 \pm 0.3)\%$	$(88.0 \pm 0.4)\%$	$(79.2 \pm 0.5)\%$	$(74.3 \pm 0.5)\%$
97.0%	82.3%	$(92.2 \pm 0.3)\%$	$(87.6 \pm 0.4)\%$	$(78.6 \pm 0.5)\%$	$(73.4 \pm 0.5)\%$
96.0%	80.7%	$(91.8 \pm 0.3)\%$	$(87.0 \pm 0.4)\%$	$(77.7 \pm 0.5)\%$	$(72.2 \pm 0.5)\%$
95.0%	79.1%	$(91.5 \pm 0.3)\%$	$(86.1 \pm 0.4)\%$	$(76.5 \pm 0.5)\%$	$(71.0 \pm 0.5)\%$
94.0%	77.7%	$(91.1 \pm 0.3)\%$	$(85.7 \pm 0.4)\%$	$(76.0 \pm 0.5)\%$	$(70.3 \pm 0.5)\%$
92.0%	75.1%	$(90.4 \pm 0.3)\%$	$(84.2 \pm 0.4)\%$	$(73.8 \pm 0.5)\%$	$(67.3 \pm 0.5)\%$
90.0%	72.7%	$(89.4 \pm 0.3)\%$	$(82.5 \pm 0.4)\%$	$(71.5 \pm 0.5)\%$	$(64.4 \pm 0.5)\%$
88.0%	70.5%	$(88.2 \pm 0.4)\%$	$(79.6 \pm 0.4)\%$	$(68.4 \pm 0.5)\%$	$(61.2 \pm 0.5)\%$
86.0%	68.3%	$(86.4 \pm 0.4)\%$	$(76.9 \pm 0.5)\%$	$(65.0 \pm 0.5)\%$	$(57.0 \pm 0.6)\%$
84.0%	66.3%	$(84.8 \pm 0.4)\%$	$(74.4 \pm 0.5)\%$	$(61.3 \pm 0.5)\%$	$(52.5 \pm 0.6)\%$
82.0%	64.3%	$(83.0 \pm 0.4)\%$	$(70.5 \pm 0.5)\%$	$(57.2 \pm 0.5)\%$	$(47.8 \pm 0.6)\%$
80.0%	62.3%	$(81.1 \pm 0.4)\%$	$(67.8 \pm 0.5)\%$	$(53.7 \pm 0.6)\%$	$(44.2 \pm 0.6)\%$

Table 5.4: FLT tracking efficiency for muon 'faking' electron tracks at the four outer tracker superlayers as function of the plateau hit efficiency $\epsilon_{\text{plt}}^{\text{hit}}$ and the average hit efficiency $\epsilon_{\text{avg}}^{\text{hit}}$.

is proportional of having no double hits, i.e. in none of the three wire memories having more than one single hit:

$$\epsilon^{\text{update}} \propto \alpha \cdot p_{3\,\text{hits}} + \beta \cdot p_{3\,\text{single hits}} \tag{5.13}$$

The probability of single and double hits depends, first, on the geometrical coverage of the tracks and, second, on the average hit efficiency. Using Monte Carlo the probabilities of a track within the geometrical acceptance and obeying the momentum cuts $P > 5.0\,\text{GeV}$ and $p_{\text{T}} > 0.8\,\text{GeV}$ to hit a certain number of outer tracker cells is obtained. The relative frequencies of hits for the number of cells which are traversed by the track are given in Table 5.5. Using these frequencies $p_{n\,\text{hits}}^{\text{geo}}$ of having n hits in a double layer, the probability of having at least one hit in all three stereo views amounts to

$$p_{3\,\text{hits}} = \left(\sum_{n=2}^{4} p_{n\,\text{hits}} \right)^3 = \left(\sum_{n=2}^{4} p_{n\,\text{hits}}^{\text{geo}} \cdot (1 - (1 - \epsilon_{\text{hit}}^{\text{avg}})^n) \right)^3 \tag{5.14}$$

number of hits	relative frequency
2	0.5885
3	0.1450
4	0.2648

Table 5.5: Relative frequencies of number of cells which are hit by tracks which are in the FLT acceptance.

Based on the geometry of the outer tracker and the maximal slope of the tracks, one can deduce that one track either hits two back-to-back cells of the double layer which are or-ed for the FLT mapping and, therefore, generate exactly one hit in the corresponding wire memory. In contrast, if a track hits three or four cells always one pair of adjacent cells is affected that are mapped to a double hit of two adjacent channels in the wire memory. Therefore the probability for having just single hits in the wire memory is given by

$$p_{3\,\text{single hits}} = \left(p^{\text{geo}}_{2\,\text{hits}} \cdot (1 - (1 - \epsilon^{\text{avg}}_{\text{hit}})^2)\right)^3 \tag{5.15}$$

Taking (Eq. 5.13), (Eq. 5.14) and (Eq. 5.15) together we get the following relation for the dependence of the FLT tracking efficiency after tracking in n superlayers

$$\begin{aligned}\epsilon^{\text{track}}(n) &= (\epsilon^{\text{update}})^n = (\alpha \cdot p_{3\,\text{hits}} + \beta \cdot p_{3\,\text{single hits}})^n \\ &= \left(\alpha \cdot \left(\sum_{n=2}^{4} p^{\text{geo}}_{n\,\text{hits}} \cdot (1 - (1 - \epsilon^{\text{avg}}_{\text{hit}})^n)\right)^3 + \beta \cdot (p^{\text{geo}}_{2\,\text{hits}} \cdot (1 - (1 - \epsilon^{\text{avg}}_{\text{hit}})^2))^3\right)^n\end{aligned} \tag{5.16}$$

This equation can be fitted to the data shown in Table 5.4. The fit results are summarized in Table 5.6 for all four superlayers. The data is not described by (Eq. 5.16) in all details. In order to obtain fit results which can be compared to each other one has to enlarge the errors of the data such, that the χ^2/ndf is similar for all fits. This is done be multiplying the errors by suitable enlargement factors f_{error}. The used factors are given in Table 5.6.

n	α	β	f_{error}	χ^2/ndf
1	2.33 ± 0.02	-6.47 ± 0.10	0.85	15.6/15
2	2.32 ± 0.02	-6.43 ± 0.11	1.40	14.6/15
3	2.33 ± 0.02	-6.48 ± 0.09	1.40	15.0/15
4	2.32 ± 0.02	-6.44 ± 0.09	1.65	15.0/15

Table 5.6: Fit results of fitting (Eq. 5.16) to the data of Table 5.4. n is the number of superlayers, α and β are the fit variables used in (Eq. 5.16), f_{error} indicates the error enlargement as explained in the text and χ^2/ndf gives the χ^2 divided by the number of degrees of freedom of the fit.

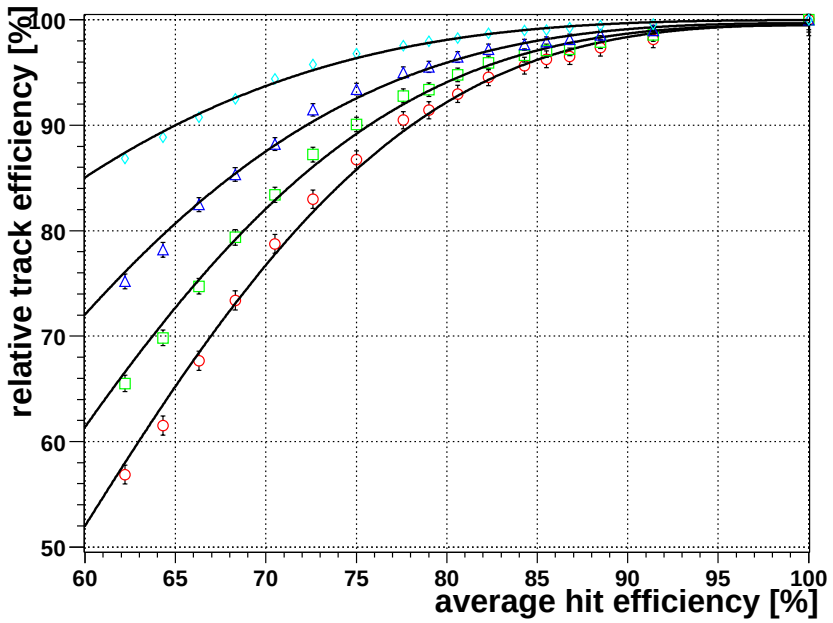

Fig. 5.17: Relative tracking efficiency (compared to the efficiency for $\epsilon_{\text{avg}}^{\text{hit}} = 100.0\%$) as a function of the average hit efficiency $\epsilon_{\text{avg}}^{\text{hit}}$ evaluated at the OTR superlayers TC02 (cyan diamonds), TC01 (blue triangles), PC04 (green squares), and PC01 (red circles). The data is taken from Table 5.4 and fitted by the function given in (Eq. 5.16) resulting in the fit results of Table 5.6. The errors are enlarged by the factors as listed in Table 5.6.

The results for the fit parameters α and β are equal within errors for the four superlayers. The necessity of enlarging the errors indicates that (Eq. 5.16) does not describe all effects which make up the tracking efficiency as function of the average hit efficiency $\epsilon_{\text{avg}}^{\text{hit}}$. Nevertheless the fits describe the dependence much more accurately than (Eq. 5.11) which factorizes the hit efficiencies of all twelve stereo views independently in contrast to (Eq. 5.13) which combines the hits of the three stereo views of one superlayer.

Measured Hit Efficiencies of 2000

Table 5.7 gives an estimation of the measured hit efficiencies of the outer tracker cells in the superlayers used by the FLT. Basis of this estimation is a run (run 14577) taken on the 12.4.2000 at 5.0 MHz target rate.
In [hul02], which is the source of the efficiency numbers in Table 5.7, it is reported that the efficiencies underlie a systematical error which is caused by the circumstance that the hits are used both for the efficiency measurement and for building the reference tracks. This introduces a bias which can be estimated by predefining a hit efficiency in Monte Carlo and running the same plateau hit efficiency evaluation on it, as used for data. The results are given in Table 5.8.

superlayer	hit efficiency (measured in data)			
	minus-x side		plus-x side	
	5 mm cells	10 mm cells	5 mm cells	10 mm cells
PC01	0.9505(6)	0.954(3)	0.9132(12)	0.925(3)
PC04	0.9509(6)	0.9582(13)	0.9377(11)	0.934(2)
TC01	0.961(2)	0.962(2)	0.947(2)	0.935(2)
TC02	0.906(2)	0.919(2)	0.942(3)	0.940(2)

Table 5.7: Measured outer tracker plateau hit efficiencies of the superlayers which are used by the FLT. The numbers in parenthesis denote the statistical uncertainty in the last digit. The values are taken from [hul02].

superlayer	hit efficiency (measured in Monte Carlo)			
	minus-x side		plus-x side	
	5 mm cells	10 mm cells	5 mm cells	10 mm cells
PC01	0.91106(6)	0.921(3)	0.9134(12)	0.917(3)
PC04	0.9158(10)	0.918(2)	0.9177(13)	0.919(2)
TC01	0.935(2)	0.930(3)	0.937(3)	0.931(4)
TC02	0.933(3)	0.927(4)	0.936(4)	0.930(4)

Table 5.8: Measured outer tracker plateau hit efficencies for Monte Carlo assuming a predefined hit efficiency of 0.90. The numbers in parenthesis denote the statistical uncertainty in the last digit. The values are taken from [hul02].

Although the hit efficiency is set to $\epsilon_{\text{MC,defined}} = 0.90$ the measured efficiencies in Monte Carlo $\epsilon_{\text{MC,measured}}$ are higher by about $1 - 2\%$ for the PC and 3% for the TC region. Since this indicates a substantial deviation we have to include this bias in the measured hit efficiencies $\epsilon_{\text{measured}}$ of Table 5.7. In [hul02] it is stated that the deviation is in good approximation proportional to the inefficiency $1 - \epsilon_{\text{hit}}$. Therefore the corrected hit efficiency $\epsilon_{\text{corrected}}$ amounts to

$$\epsilon_{\text{corrected}} = 1 - \left((1 - \epsilon_{\text{measured}}) \cdot \frac{1 - \epsilon_{\text{MC,defined}}}{1 - \epsilon_{\text{MC,measured}}} \right) \tag{5.17}$$

The efficiencies given in Table 5.7 underlie, apart from the statistical error given in the table, an additional systematical error. In [hul02] an additional estimation of the efficiency based on Monte Carlo is presented assuming a hit efficiency of 0.90.
Table 5.9 presents the corrected outer tracker hit efficiencies which take the bias of using the hits twice for tracking and for efficiency measurement into account[5]. The outer tracker

[5]The values of Table 5.9 for superlayers PC01 and PC04 are also given in [hul02] while the corrected efficiencies for superlayers TC01 and TC02 are not. For this reason the motivation and the method of the correction is presented here although it is subject of [hul02].

superlayer	hit efficiency (measured in data, corrected)			
	minus-x side		plus-x side	
	5 mm cells	10 mm cells	5 mm cells	10 mm cells
PC01	0.9446(8)	0.942(4)	0.900(2)	0.910(5)
PC04	0.9417(9)	0.949(2)	0.9243(18)	0.919(3)
TC01	0.940(2)	0.946(2)	0.916(2)	0.906(2)
TC02	0.860(2)	0.889(2)	0.909(3)	0.914(2)

Table 5.9: Corrected outer tracker hit plateau efficencies for data using (Eq. 5.17). The numbers in parenthesis denote the statistical uncertainty in the last digit. The values are based on [hul02].

hit efficiencies which are significantly below unity and moreover differ in the different regions of the outer tracker show that the FLT efficiency has to be evaluated as function of the hit efficiency. The tracking efficiency using the measured hit efficiency as given in Table 5.9 are investigated in the next section.

Tracking Efficiency Using the Measured Hit Efficiencies

In the last section the measurement of the outer tracker hit efficiencies during the year 2000 were summarized. In this section these numbers are used in order to investigate the impact of the hit efficiencies on the FLT tracking efficiency. In contrast to Sect. 5.4 which regarded the tracking efficiency as a function of a hit efficiency uniformly applied in the entire outer tracker, here, for the different detector regions, the corresponding hit efficiencies are used.

hit efficiency	tracking efficiency			
	electrons		muons faking electrons	
ideal (100.0%)	$(68.1 \pm 0.5)\%$		$(79.3 \pm 0.5)\%$	
measured	$(62.2 \pm 0.5)\%$	(-8.7%)	$(71.3 \pm 0.5)\%$	(-10.1%)
measured (MC corrected)	$(60.2 \pm 0.6)\%$	(-11.6%)	$(67.9 \pm 0.5)\%$	(-14.4%)

Table 5.10: FLT tracking efficiency using an ideal hit efficiency of 100.0% and using the measured hit efficiencies without and with Monte Carlo correction as given in Table 5.7 and Table 5.9. Both the efficiencies for electron and for muons 'faking' electron tracks are listed.

In order to be able to estimate the error margin which is introduced by the uncertainties of the determination of the hit efficiencies, the FLT simulation is run using the measured hit efficiencies, as reported in Table 5.7, as well as using the Monte Carlo corrected efficiencies given in Table 5.9. Due to the uncertainties of the measurement and the correction method using Monte Carlo, it is expected that the numbers of Table 5.7 overestimate the

hit efficiencies while the numbers of Table 5.9 underestimate the hit efficiencies. Thus evaluating the tracking efficiencies gives an interval of the expected values.
Table 5.10 shows the result on running the FLT simulation of the measured hit efficiencies. Both electron tracks and muons 'faking' electron tracks are listed. For electron tracks the loss in tracking efficiency is in the interval -8.7% to -11.6% while for the muons 'faking' electron tracks the loss amounts -10.1% to -14.4%. The difference for electron and muons 'faking' electron tracks is caused by the different efficiencies for the ideal tracking efficiency.
Comparing to Table 5.4, the loss in efficiency in the muon 'faking' electrons case is comparable to a plateau hit efficiency of about $\epsilon_{\mathrm{plt}}^{\mathrm{hit}} \approx 90\%...94\%$ which is in agreement to the values listed in Table 5.7 and Table 5.9.

5.5 Influence of Defective Channels and Link Masking on the Tracking Efficiency

In Chapter 3, the performance of the hit data transmission from the detector cells to the wire memories of the TFUs was investigated. This study resulted in maskings which reflect the presence of dead, noisy and hot detector channels as well as non-working links. By using the corresponding maskings, it is possible to estimate the impact of the defective channels on the FLT tracking performance.
In this section, we first investigate the effect of dead, noisy and hot channels separately in order to see which importance the different kinds of channel maskings have. After this study the FLT tracking efficiency is regarded using the complete masking but under variation of the runs which were used to generate the masking. This will give an estimation of the uncertainty of the efficiency drop which is introduced by the defective channels in the regarded run period.

Tracking Efficiency as a Function of Defective Channels

The influence of the different channel maskings and of the link masking on the tracking efficiency is investigated in this section. First we recapitulate the notion of defective channels which are subject of Chapter 3. Second the results of the application on the FLT simulation on Monte Carlo are presented.
The channel masking is based on the wire memory occupancies which were recorded before the starting of a run in the year 2000. The observation of an exceptional high or low occupancy of a channel compared to the Monte Carlo expectation is used to classify wire memory channels. A channel of low occupancy is regarded as 'dead channel' while channels of high occupancy are classified as 'noisy' or 'hot'. The consideration of the wire memory occupancies has the advantage that both, effects of the detector, as well as of the data transmission, are regarded. Applying a corresponding masking of the wire memory contents for Monte Carlo data makes sure that the same dead, noisy and hot channels are

present as during the data taking. In this way, the estimation of the tracking efficiency on Monte Carlo takes the channel defects into account.
The optical links which have shown a problematic performance before the start of a run have not been used during the data taking. In order not to loose efficiency, the channels of the wire memories which are related to the links that were not used are switched to one. This means that the corresponding channels are assumed to have received hits in each event such that a coincidence is found if hits in the other stereo views are given. The same is done in the simulation, i.e. the wire memory channels which correspond to a link that was not used in the run are switched to one.
The expected influence of the defective channels on the FLT tracking efficiency depends on the type of defectiveness. While dead channels result in missing hits and, therefore, decrease the tracking efficiency, noisy and hot channels increase the tracking efficiency by introducing additional hits. Also the link masking which switches entire regions to one which are associated to a malfunctioning optical link increases the tracking efficiency.
However the strength of the impact on the efficiency differs for the different kinds of defective channels. Moreover it is depending on the hit efficiency of the detector. Assuming a high hit efficiency, the addition of hits due to noisy or hot channels or due to link-masking cannot increase the hit efficiency too much, since the hits which are needed for a successful track search are already set. This argument changes for lower hit efficiencies because in that case the additional hits may replace hits that were lost due to low hit efficiency. In this way, the noisy and hot channels may 'recover' hits which are lost due to a lower hit efficiency.
Dead channels, in contrast, lower the tracking efficiency in any case. They delete hits and therefore have the same effect like a decreased hit efficiency. The effect of the dead channels dominates the influence of the defective channels because the probability to lose a track because of missing hits is higher that recovering tracks which are lose due to a low hit efficiency.
Table 5.11 gives the result of applying the different kinds of channel masking. The numbers are shown differentiating electron and muons 'faking' electron tracks and for an ideal hit efficiency as well as for the measured hit efficiencies which where introduced in Sect. 5.4. The channel and link masking was taken from run 17127. The FLT simulation is evaluated for 10000 Monte Carlo events of the channels $J/\psi \to e^+e^-$ and $J/\psi \to \mu^+\mu^-$, respectivly. The results support the considerations which were just mentioned. Applying only the dead channel masking reduces the tracking efficiency by 35% to 40%. Just using the noisy or hot channel masking, or the link masking, increases the efficiencies in the order of 2% to 3%. The relative increase is higher for the sample using the measured hit efficiency of the year 2000. This is because it opens the possibility that hits which are lost due to the low hit efficiency are removed.
It becomes clear that the dead channels have the largest impact on the tracking efficiency. The influence of the dead channels dominates if all three kinds of channel masking and the link masking are applied together. The tracking efficiency is lowered by 26.7% in the electron and by 28.5% in the muon 'faking' electron case, independent on the used OTR hit efficiency.

ideal hit efficiency					
channel masking	link masking	tracking efficiency			
		electrons		muons faking electrons	
none	no	$(68.1 \pm 0.5)\%$		$(79.3 \pm 0.5)\%$	
none	yes	$(69.6 \pm 0.5)\%$	$(+2.2\%)$	$(81.4 \pm 0.4)\%$	$(+2.6\%)$
only dead channels	no	$(44.2 \pm 0.6)\%$	(-35.1%)	$(49.1 \pm 0.6)\%$	(-38.1%)
only noisy channels	no	$(69.6 \pm 0.5)\%$	$(+2.2\%)$	$(80.9 \pm 0.4)\%$	$(+2.0\%)$
only hot channels	no	$(69.2 \pm 0.5)\%$	$(+1.6\%)$	$(80.5 \pm 0.4)\%$	$(+1.5\%)$
full masking	yes	$(50.6 \pm 0.6)\%$	(-25.7%)	$(56.8 \pm 0.6)\%$	(-28.4%)
measured hit efficiency					
channel masking	link masking	tracking efficiency			
		electrons		muons faking electrons	
none	no	$(62.2 \pm 0.5)\%$		$(71.3 \pm 0.5)\%$	
none	yes	$(64.0 \pm 0.5)\%$	$(+2.9\%)$	$(73.6 \pm 0.5)\%$	$(+3.2\%)$
only dead channels	no	$(39.2 \pm 0.6)\%$	(-37.0%)	$(42.7 \pm 0.5)\%$	(-40.1%)
only noisy channels	no	$(64.1 \pm 0.5)\%$	$(+3.1\%)$	$(73.1 \pm 0.5)\%$	$(+2.5\%)$
only hot channels	no	$(64.1 \pm 0.5)\%$	$(+3.1\%)$	$(73.3 \pm 0.5)\%$	$(+2.8\%)$
full masking	yes	$(46.2 \pm 0.6)\%$	(-25.7%)	$(51.0 \pm 0.6)\%$	(-28.5%)

Table 5.11: Tracking efficiency of electron and muons 'faking' electron tracks under variation of the applied channel masking. Both ideal and measured hit efficiencies are used. Besides the absolute tracking efficiencies, the relative loss or gain in efficiency compared to the case without any masking are given.

Stability of Efficiency for Different Runs

After the consideration of the impact of the masking of defective channels as well as the link masking, in this section, the stability of this influence should be investigated. Therefore the FLT simulation is run under variation of the maskings of dead, noisy and hot channels which are based on a set of the runs which were regarded in Chapter 3.

Fig. 5.18 shows the tracking efficiency for both electron and muons 'faking' electron tracks using eight different channel maskings and with and without link masking. The channel maskings are based on the data quality information of the runs 17116, 17127, 17129...17134. These are runs of the end of the year 2000 data taking. The link masking is used from the same runs.

For each efficiency shown in Fig. 5.18, the FLT simulation is run over 4000 events $J/\psi \to e^+e^-$ and $J/\psi \to \mu^+\mu^-$ Monte Carlo events, respectivly[6]. The hit efficiency is

[6]Please note that this is a lower statistics that for the other efficiencies given in this chapter which are based on 10000 events.

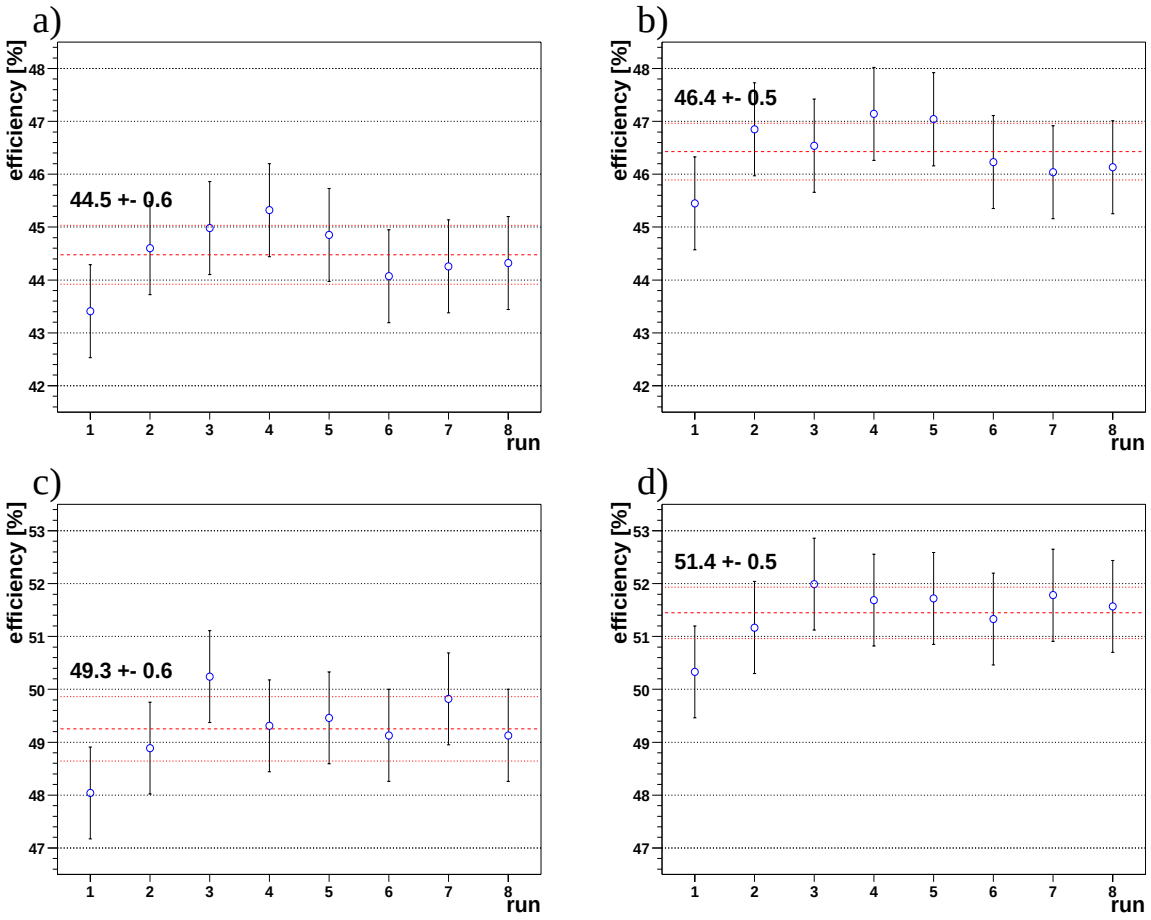

Fig. 5.18: FLT tracking efficiency as a function of the masking of the runs 17116, 17127, 17129...17134 (mapped to the indices 1...8). Figure a) shows the efficiencies for electron tracks without and figure b) with link masking. Figures c) and d) depict the efficiencies for muons 'faking' electron tracks without and with link masking, respectivly. The dashed red lines indicate the mean value and the dotted red lines the standard deviation.

set to the measured values of the year 2000 as noted in Sect. 5.4.

The average tracking efficiency is $(44.5 \pm 0.6)\%$ and $(46.5 \pm 0.5)\%$ for electron tracks without and with link masking, respectivly. For muon 'faking' electron tracks, the efficiencies are $(49.3 \pm 0.6)\%$ without link masking and $(51.4 \pm 0.5)\%$ using link masking. The fluctuation of the efficiency over the different runs is comparable to the statistical error of the efficiencies.

Comparing Fig. 5.18 a) and c) the influence of the link masking can be estimated. The link masking adds about 2% to the efficiency by recovering tracks which are lost due to the low OTR hit efficiency. The same can be observed comparing Fig. 5.18 b) and d) which show the efficiencies for muons 'faking' electron tracks.

5.6 Realistic Tracking Efficiency on Monte Carlo

We want to summarize the influences on the FLT tracking efficiency which arise from the realistic treatment of the Monte Carlo. All aspects that were discussed in this chapter are put together in order to get a conclusion on the efficiency.

	tracking efficiency	
	electrons	muons faking electrons
toy-tracks	$(84.5 \pm 0.4)\%$	$(96.7 \pm 0.2)\%$
ideal detector	$(68.1 \pm 0.5)\%$	$(79.3 \pm 0.5)\%$
OTR alignment and FLT geometry	$(65.7)\%$ (-3.5%)	$(76.1)\%$ (-3.9%)
alignment uncertainty	$(65.6 \pm 1.0\,(\text{syst}))\%$ $(-3.6 \pm 1.4\,(\text{syst}))\%$	$(75.4 \pm 2.0\,(\text{syst}))\%$ $(-4.8 \pm 2.5\,(\text{syst}))\%$
measured hit efficiency	$(62.2)\%$ (-8.7%)	$(71.3 \pm 0.5)\%$ (-10.1%)
ditto (MC corrected)	$(60.2)\%$ (-11.6%)	$(67.9 \pm 0.5)\%$ (-14.4%)
full channel and link masking	$(50.6 \pm 0.6\,(\text{syst}))\%$ $(-25.7 \pm 0.9\,(\text{syst}))\%$	$(56.8 \pm 0.5\,(\text{syst}))\%$ $(-28.4 \pm 0.6\,(\text{syst}))\%$
realistic detector	$(42.9 \pm 0.5\,(\text{stat}) \pm 1.5\,(\text{syst}))\%$	$(47.5 \pm 0.5\,(\text{stat}) \pm 2.5\,(\text{syst}))\%$
ditto (MC corrected)	$(41.8 \pm 0.5\,(\text{stat}) \pm 1.5\,(\text{syst}))\%$	$(45.3 \pm 0.5\,(\text{stat}) \pm 2.5\,(\text{syst}))\%$

Table 5.12: Tracking efficiency of electron and muons 'faking' electron tracks under variation of the applied channel masking. The left hand side numbers denote the absolute efficiencies while the right hand side number give the relative loss compared to the efficiency of the ideal detector. If not marked otherwise, the errors are statistical.

Table 5.12 gives the summary of all numbers which were considered here. The momentum cut for the reference tracks which are gained from the Monte Carlo truth is $P > 5.0\,\text{GeV}$ while the transverse momentum is required to be $p_\text{T} > 0.5\,\text{GeV}$. Moreover the tracks are required to be within the acceptance, which is defined by the FLT geometry, see Sect. 5.2. For toy-generated tracks, the tracking efficiencies reach values of $(84.5 \pm 0.4)\%$ for electron tracks and $(96.7 \pm 0.2)\%$ for muons 'faking' electron tracks. This is the intrinsic efficiency of the FLT tracking algorithm. The lower efficiency of electron tracks is caused by the bremsstrahlung energy loss. This reduces the momentum of the electron tracks. Since there is an implicit momentum cut of the tracking algorithm and the cut on the transverse momentum, the reduced momenta of the electron tracks lead to an reduced tracking efficiency.

The tracking efficiency for GEANT generated tracks using an ideal detector simulation amounts to $(68.1 \pm 0.5)\%$ for electron and $(79.3 \pm 0.5)\%$ for muons 'faking' electron tracks. As already discussed in Sect. 5.2, the tracking efficiency is dominated by the effects of a partially wrong mapping of detector cells of the outer tracker to the wire memory channels

of the FLT. The mapping which is applied in the simulation is the same which was used during the data taking of the year 2000. In this way the efficiencies of $(68.1 \pm 0.5)\%$ for electron and of $(79.2 \pm 0.5)\%$ for muons 'faking' electron tracks reflect the simulation of an ideal detector and ideal hit data transfer, but take into account the effects of the wrong mapping.

The tracking efficiency for electron tracks is lower compared to the muons 'faking' electron tracks because of the bremsstrahlung losses of the electrons. Therefore the intrinsic momentum cut of the FLT tracking algorithm and the p_{T}-cut of the TPU decrease the efficiency as discussed in Sect. 5.1.

The next effect which is taken into consideration in Table 5.12 is the alignment of the detector. The shift of the detector modules with respect to their nominal positions introduces a loss in tracking efficiency, since coincidences may get lost due to non-uniform shifts of modules of the three stereo views and due to coincidences which do not hit the region of interest. This leads to a loss of 9% to 11% in tracking efficiency, assuming the detector positions which were determined in the year 2000. This loss can partially be compensated by the usage of a modified FLT geometry, as discussed in Sect. 5.3. The efficiency loss amounts -3.5% to -3.9% after the application of a corresponding FLT geometry. However one has to take into account that the OTR alignment during the running of the year 2000 was known with a accuracy of about 1.0 cm to 1.5 cm. Therefore an additional efficiency loss of 3.5% for electron tracks and of 3.9% for muons 'faking' electron tracks has to be taken into account, see Sect. 5.3.

Moreover the hit efficiency of the detector has to be considered. In Sect. 5.4 the OTR hit efficiencies of the year 2000 are cited, as presented by [hul02]. The evaluation of the FLT efficiency using these hit efficiencies results in a decrease of about 9% to 10%. The used hit efficiencies are overestimated because of the method to use the same hits for both track reconstruction and hit efficiency measurement. The correction using an additional Monte Carlo study leads to tracking efficiencies which are 11.6% to 14.4% lower compared to an ideal hit efficiency. However in [hul02] it is stated that the efficiencies which are obtained with the Monte Carlo correction underestimate the real efficiencies. Therefore we have to estimate the loss in tracking efficiency by the interval which is defined by both methods.

The last influence which was considered in this chapter is the masking of defective channels and of non-working links. Although the introduction of additional hit by the noisy and hot channels as well as by the link masking increases the tracking efficiency, the impact of the dead channels is dominating. The tracking efficiency drops by 25.7% for electron and by 28.5% for muons 'faking' electron tracks as soon as the maskings are applied in the FLT simulation. However the stability of this impact over a set of several successive runs is comparable to the statistical error on the efficiency.

The various effects correlate with each other. Therefore it is not possible to summarize all effects by simply multiplying the different factors. The efficiencies number which take all effects into account in Table 5.12 are therefore obtained by rerunning the simulation taking all the effects into consideration.

5.7 Influence of the ECAL Pretrigger

The analysis of this chapter has, up to now only, taken into account the FLT tracking efficiency in the outer tracker. Instead of using the ECAL pretrigger simulation, the pretrigger messages were generated using the Monte Carlo truth information. Thus, an idealized pretrigger of ideal efficiency was simulated. The pretrigger messages were generated without a cut on the particle momentum or the acceptance. This was done in order to disentangle the FLT tracking and the pretrigger efficiencies.
In this last section, the ECAL pretrigger simulation is included in order to get a summarizing value for the single track efficiency of the FLT in the electron channel. The ECAL pretrigger simulation is run in the mode of the data taking of the year 2000. This comprises the choice of the lookup tables and the usage of the the nonett-cluster scheme, see p. 39, Fig. 2.2. In contrary, the full ECAL readout and pretrigger board coverage is used in the simulation. Moreover no masking of problematic ECAL channels is applied. This is because the ECAL and the ECAL pretrigger performance was changing on a run by run basis due to continuous commissioning activities during the year 2000 data taking. A study about the ECAL pretrigger performance during the year 2000 can be found in [fla01c]. The efficiency loss due to masking of non-used readout boards and pretrigger boards in the ECAL is estimated to be $(20.7 \pm 0.1)\%$[7]. This number is valid for the response of the ECAL pretrigger on a single electron.

settings	efficiency		
	pretrigger	tracking	both
no pretrigger simulation (seeds based on MC truth)	—	$(65.3 \pm 0.5)\%$	$(65.3 \pm 0.5)\%$
using ECAL pretrigger simulation	$(55.9 \pm 0.5)\%$	$(75.8 \pm 0.6)\%$	$(42.4 \pm 0.5)\%$
channel and link masking alignment, hit efficiency	$(55.9 \pm 0.5)\%$	$(47.0 \pm 0.5)\%$	$(26.3 \pm 0.5)\%$
using MC correction for hit efficiency	$(55.9 \pm 0.5)\%$	$(45.7 \pm 0.5)\%$	$(25.5 \pm 0.5)\%$

Table 5.13: Single track efficiencies of the FLT including the ECAL pretrigger.

The cut on the transverse energy (see p. 38, (Eq. 2.1)) which is used by the ECAL pretrigger simulation is set to 1.0 GeV. This is a value commonly used during the data taking of the year 2000. Table 5.13 shows the FLT tracking efficiencies including the ECAL pretrigger simulation. Since the ECAL pretrigger performs a cut on the transversal energy, no cut on the momentum or transverse momentum of the reference tracks is applied. The only cut on the reference tracks is the requirement that the tracks passes the geometrical acceptance of the FLT. In this case, the tracking efficiency using pretrigger seeds which are

[7] The study is based on run 17195 which was taken after the runs which are regarded in this thesis.

based on Monte Carlo truth drops to (65.3±0.5)%, Table 5.13. Using a cut of $P > 5.0\,\mathrm{GeV}$ and $p_\mathrm{T} > 0.8\,\mathrm{GeV}$ the same efficiency is $(68.1 \pm 0.5)\%$, Table 5.12.
As soon as the pretrigger messages are generated by the ECAL pretrigger simulation instead of using the Monte Carlo truth, the tracking efficiency increases to $(75.8 \pm 0.6)\%$. The reason is that the cut on the transverse energy of $E_\mathrm{T} > 1.0\,\mathrm{GeV}$ is equivalent to a cut on the observed momentum as introduced in Sect. 5.1. The cut in the ECAL pretrigger restricts the sample to tracks of high observed momentum, which increases the efficiency of the tracking algorithm and the p_T cut which is applied in the TPU.
The efficiency of the ECAL pretrigger is $(55.9 \pm 0.5)\%$. This number is dependent on the used threshold of the transversal energy and rises as soon as the threshold is lowered. Combining the pretrigger efficiency and the tracking efficiency, the probability to trigger on a lepton of a $J/\psi \to e^+e^-$ decay which passes the FLT acceptance is $(42.4 \pm 0.5)\%$.
Using the link and channel masking, the alignment and the measured hit efficiencies, the FLT tracking efficiency is $(47.0 \pm 0.5)\%$ or $(45.7 \pm 0.5)\%$, respectivly, if the Monte Carlo corrections on the hit efficiencies are taken into account. These values are higher than the corresponding numbers given in Table 5.12 again because of the influence of the cut on the transversal energy of the pretrigger. Including the pretrigger efficiency yields a track finding efficiency of $(26.3 \pm 0.5)\%$ or $(25.5 \pm 0.5)\%$, respectivly, depending on the used hit efficiencies.
The systematical errors are the following (see Table 5.12):

- The uncertainty in the OTR alignment. For the year 2000 detector the alignment is known at a precision of 1.0 cm to 1.5 cm [krü02]. This yields an systematic error of ±0.8% on the tracking efficiency.

- The outer tracker hit efficiencies are measured and given in Table 5.7 [hul02]. A Monte Carlo study shows that these values may be overestimated. A lower limit on the efficiencies is given in Table 5.9. This effect introduces a systematic error on the FLT tracking efficiency of −0.8%.

- The variation of the link and channel masking as analyzed in Sect. 5.5. It introduces an systematic error of ±0.3.

Taking all systematic errors into account, the efficiency that the FLT triggers on an electron which originates from a $J/\psi \to e^+e^-$ decay and which pass the FLT outer tracker acceptance is

$$\epsilon = \left(26.3 \pm 0.5\,(\mathrm{stat})\ {}^{+0.9}_{-1.2}\ (\mathrm{syst})\right)\%$$

This includes the ECAL pretrigger simulation using a cut on the transversal energy of $E_\mathrm{T} > 1.0$. A masking of ECAL readout or pretrigger boards as well as of ECAL channels is not included. In contrary, the FLT outer tracking performance is simulated describing the situation of the data taking in the year 2000.

Chapter 6

Summary and Conclusions

The experiment HERA-B has been designed to measure CP violation in the decay of neutral B mesons produced using an internal wire target at the proton ring of HERA. In order to collect B decays in the gold-plated channel $B^0 \to J/\psi K^0_S$, the FLT is designed to select $J/\psi \to l^+l^-$ decays. It provides a reduction factor of 200 of the hadronic background and allows the implementation of a software trigger at the second trigger level.
The FLT is built from a network of about 80 custom designed processor boards which allow an online reconstruction of $\mathcal{O}(10^7)$ tracks per second, including the calculation of momenta of tracks and invariant masses of track pairs. A dedicated data transmission system sends the hit information of selected detector regions to the processor boards.
In this thesis, the performance of the FLT during the data taking of the year 2000 has been analyzed. This running period was used for the commissioning of the experiment. The main results are summarized in the following.
The analysis of the hit data transmission reveals that a noticeable number of channels show different occupancies in the stored detector readout and the FLT hardware. Based on a Monte Carlo study, criteria for dead, noisy, and hot channels are defined. The occurrence of these defective channels in the wire memories of the FLT hardware as well as in the detector hit information in the common data stream has been analyzed.
Using these criteria, the time evolution of defective channels in the wire memories of the FLT was investigated. It turns out that on the time scale of one HERA fill, the defective channels are stable. Major changes appear only between different HERA fills. This can be understood in the context of the continuous commissioning activities which were done during the data taking of the year 2000. A similar result is obtained in the analysis of the stability of defective channels in the common data stream. The set of defective channels remains stable during one HERA fill. In addition, the stability of the link masking has been investigated.
The investigation of the channel behaviour makes it possible to generate channel maskings, which can be applied in the simulation of the FLT. In this way, erroneous behaviour of defective channels can be taken into account. Two different types of masking are presented, depending on whether the simulation is used on data or Monte Carlo.
Using the channel maskings, the matching probability of FLT tracks which are recorded

in the common data stream and which are obtained by the FLT simulation is evaluated. The test vector test which was done during the HERA shutdown in the year 2001 proves that the FLT hardware is exactly described by the simulation. The exceptions in some details do not affect the matching efficiency. In contrast to the result of the test vector test, the investigation of the recorded FLT tracks of the data taking in the year 2000 reveals the existence of bit errors in the transmission of the FLT messages. The errors occur in localized areas of the FLT acceptance. Since these errors are not observed in the test vector test, it is assumed that the cause of the bit errors was repaired during the exchange of the message transfer system of the FLT which was done before the test vector tests took place.

Restricting to areas which do not show bit errors, the matching efficiency between recorded and simulated FLT tracks is at a high level. Events which contain exactly one recorded and one simulated track show a matching efficiency of up to $(95.3 \pm 1.4\,(\text{stat}) \pm 1.0\,(\text{syst}))\%$ and $(95.9 \pm 1.4\,(\text{stat}) \pm 0.9\,(\text{syst}))\%$ using recorded and simulated tracks as reference, respectivly. This proves that the tracking algorithm performs identical in the hardware and the simulation.

If the constraint of just one track of each kind is not required, the matching efficiencies are lower. The highest values which are observed are $(76.8 \pm 2.2\,(\text{stat}) \pm 1.6\,(\text{syst}))\%$ and $(74.3 \pm 1.4\,(\text{stat}) \pm 4.6\,(\text{syst}))\%$ for using recorded and simulated tracks as reference, respectivly. Since the tracking algorithm in hardware and simulation performs identical, these lower efficiencies have to be assigned to the limited performance of the hit data transmission of the FLT in the year 2000. Especially the presence of noisy channels in the entire FLT acceptance makes it impossible to reconstruct the wire memory content in the simulation such that it exactly matches the situation during the data taking.

The analysis of the FLT tracking efficiency in the outer tracker shows that even for an idealized detector using simplified 'toy-generated' tracks, the efficiency does not reach unity. The maximal tracking efficiency is $\epsilon_{\text{toy}} = (96.7 \pm 0.2)\%$ which is the intrinsic efficiency of the FLT tracking algorithm. The calculation of this value involves a cut on the momentum of the tracks of $P > 5.0\,\text{GeV}$ since the FLT tracking algorithm contains an implicit momentum cut. In case of electron tracks the efficiency is affected by the energy loss due to bremsstrahlung. An electron that radiates a fraction of its energy before the spectrometer magnet, has a lower momentum behind the magnet. This effect decreases the tracking efficiency in the FLT due to the implicit momentum cut of the algorithm.

When Monte Carlo analysis is repeated using GEANT generated tracks, the tracking efficiency is reduced by two effects. On one hand, the geometrical acceptance becomes critical. The evaluation of the FLT acceptance has to take into account the relations of detector cells to the wire memory channels of the FLT in order to obtain conclusive results. On the other hand, the mapping of detector cells to wire memory channels is erroneous in certain areas, both in the hardware and the simulation. This effect also lowers the tracking efficiency. For tracks which are not affected by these two problems, the tracking efficiency for GEANT generated tracks and toy-tracks is the same.

For a realistic estimation of the tracking efficiency for Monte Carlo events, the alignment of the outer tracker, the hit efficiencies, and the channel and link masking of the data

taking in the year 2000 are included in the analysis.
The efficiency loss due to the outer tracker misalignment is investigated. The uncertainty of the alignment measurement is also taken into account. The alignment, which can be only partially corrected by corresponding changes in the FLT geometry, introduces a loss in the electron tracking efficiency of 3.5%. The uncertainty on the alignment introduces an additional efficiency loss of $(3.6 \pm 1.4\,(\text{syst}))\%$.
The influence of the tracking efficiency on the outer tracker hit efficiency has been analyzed. Using the measured plateau hit efficiencies in the year 2000, the corresponding loss in the tracking efficiencies for electron tracks is in the range between 8.7% and 11.6%.
The systematic influence of the masking of defective channels and non-working links is estimated. The tracking efficiency of electron tracks is lowered by $(25.7 \pm 0.9\,(\text{syst}))\%$. The main influence is introduced by the masking of dead channels.
Taking all effects together and using a simulation of the ECAL pretrigger with a cut on the transverse energy of a cluster in the ECAL of $E_{\text{T}} > 1.0\,\text{GeV}$, the efficiency that the FLT triggers on an electron which originates from a $J/\psi \to e^+e^-$ decay and which passes the FLT outer tracker acceptance is

$$\epsilon = \left(26.3 \pm 0.5\,(\text{stat}) \begin{smallmatrix}+0.9\\-1.2\end{smallmatrix}\,(\text{syst})\right)\%$$

The analysis has shown that the FLT hardware is correctly described by the simulation. The correspondence of the FLT tracking in hardware and simulation is demonstrated. However, the problems of the detector and hit data transmission of the data taking in the year 2000 have a serious impact on the FLT tracking efficiency. For the future, the event-by-event comparison between the hit data in the detector readout and the FLT hardware should allow an analysis of the hit data transmission in more detail. This is the remaining key measurement to understand the FLT system.

Acknowledgments

After the completion of the thesis it is my desire to thank all people who supported me during the last years and who made this thesis come true. First I want to thank my parents and my sister for the support not only during my time at HERA-B, but also for making it possible to study physics.
This thesis would not have been possible without the careful attention of my supervisor Andreas Schwarz. During our meetings the basis of the thesis was laid. Moreover I would like to thank Walter Schmidt-Parzefall for the discussions and the help he offered me.
I want to thank Ekkehard Gerndt who primary motivated me to start the PhD thesis and made sure that everything was going into the right direction. Later Cristóbal Padilla took over the responsibility of the day-by-day supervision. Many thanks for his efforts, especially for continuing the supervision after his move to CERN.
Special thanks to all who read the thesis in its various stages. M. Bräuer, H. Fleckenstein, and B. Schwingenheuer als well as my supervisors had many critical looks on the text and put the thesis onto its right path. Especially I want to thank K. Reeves for cross-reading my thesis, regarding the english language.
The thesis is about the First Level Trigger and therefore I like to thank all the members of the FLT-group. E. Gerndt, A. Michetti, I. Négri, F. Ratnikow, D. Reßing, I. Riu, B. Schwingenheuer, and A. Somov supported me whith countless discussions and immediate support in case of questions or problems. Moreover, there are many people of the HERA-B collaboration who helped me during my time at the experiment and to whom I thank for every hint and discussion.
I would like to thank my office mates. During my time as PhD student I had the pleasure to work together with J. Flammer, H. Fleckenstein, D. Kahnert, P. Kreuzer, Ch. Rothe, and L. Sözüer. The nice atmosphere in our office and the possibility for direct questions and answers, helped with all the tiny problems during the daily work.
During the time at HERA-B some of my colleagues became good friends and made not only my work easier but also my life more cheerful. I want to mention G. Baki, M. Bräuer, A. Hamel, S. İşsever, T. Jagla, S. Keller, M. Symalla and many others who not only shared my time at DESY but also on the Kiez, in England, Spain and Greece.

Bibliography

[aba02] A. Abashian et al.,
Improved Measurement of Mixing-induced CP Violation in the Neutral B Meson System,
Belle Preprint 2002-30, hep-ex/020825

[abr00] M. C. Abreu et al.,
Evidence for deconfinement of quarks and gluons from the J/ψ suppression pattern measured in Pb-Pb collisions at the CERN-SPS,
Phys. Lett. B477 (2000) 28

[abt97] I. Abt et al.,
The H1 Detector at HERA,
Nucl. Instr. Methods **A 386** (1997) 310

[ack98] K. Ackerstaff et al.,
The HERMES Spectrometer, Nucl. Instr. Methods **A 417** (1998) 230

[ada01] M. Adams,
Study of the muon pretrigger acceptance for muon tracks from $J/\psi \to \mu^+\mu^-$,
HERA-B Note 01-057, Trigger Note 01-009

[ada02] M. Adams,
Entwicklung eines Simulationsprogrammes für das Myon-Pretrigger-System des HERA-B Experimentes und Untersuchungen zum Systemverhalten,
Ph.D. Thesis, Universität Dortmund, 2002

[alb95] H. Albrecht et al.,
HERA-B - An Experiment to Study CP Violation in the B System Using an Internal Target at the HERA Proton Ring, Technical Design Report,
DESY-PRC 95/01 (1995)

[alb97] V. Alberico et al.,
The HERA-B electromagnetic calorimeter pre-trigger system,
Il Nuovo Cimento **110 A** (1997) 1453

[ale99a] R. Aleksan,
Quark Mixing and CP Violation,
T. Ferbel (ed.), Techniques and Concepts of High Energy Physics X, 487-596

[ale99b] T. Alexopoulos et al.,
Measurement of the $b\bar{b}$ cross section in 800 GeV *p-Si interations*,
Phys. Rev. Lett. **B 492** (2000) 259

[art96] HERA-*B* Software Group,
ARTE, The Event Reconstruction and Analysis Tool for HERA-B,
HERA-*B* internal document, 1996

[aub02] B. Aubert et al.,
Measurement of CP-Asymmetry Amplitude $\sin 2\beta$,
BaBar-PUB-02/008, hep-ex/0207042

[ber00] S. Bergmann et al.,
Lessons from CLEO and FOCUS measurements of $D^0 - \bar{D}^0$ mixing parameters,
Physics Letters B 486 (2000) 418 – 425

[böck01] M. Böcker et al.,
The Muon Pretrigger System of the HERA-B Experiment,
IEEE Trans. Nucl. Sci. **48** (2001) 1270

[bou95] D. Boutigny et al. (The BaBar Collaboration),
BaBar technical design report,
SLAC-R-0457 (1995)

[bra96] E. Braaten, S. Fleming, T. C. Yuan,
Production of Heavy Quarkonium in High Energy Colliders,
Ann. Rev. Nucl. Part. Sci. **46** (1996) 197-235

[bräu01] M. Bräuer,
Die Alignierung des HERA-B Vertexdetektors,
PhD. Thesis, Ruprecht-Karls-Universität Heidelberg, 2001

[bre94] S. Brenner et al.,
Performance of a LHC Front-End Running at 67 MHz,
Nucl. Instr. Methods **A 339** (1994) 477

[bru98] M. Bruinsma, J. Hogenbirk and O. Steinkamp 1998,
Documentation on the First Level Trigger Linkboard,
`http://www.nikhef.nl/pub/experiments/bfys/herab/FLTLBdoc.ps`

[bru02] M. Bruinsma,
Performance of the First Level Trigger of HERA-B and Nuclear Effects in J/ψ Production,
Ph.D. Thesis, Utrecht University, 2002

[bru01] M. Brushi et al.,
The electromagnetic calorimeter of the HERA-B experiment,
Nucl. Instr. Methods **A 461** (2001) 332-336

[buc99] M. Buchler et al.,
Design and Operation of Frond-End Electronics for the HERA-B Muon Detector,
IEEE Trans. Nucl. Sci. **46** (1999) 126

[che95] M. T. Cheng et al. (The Belle Collaboration),
A Study of CP Violation in B Meson Decays: Technical Design Report,
BELLE-TDR-3-95 (1995)

[chr64] J. H. Christenson et al.,
Evidence for the 2π Decay of the K_L Meson,
Phys. Rev. Lett. 13 (1964), 138

[con89] J. S. Conway et al.,
Experimental study of muon pairs produced by 252 GeV *pions on tungsten*,
Phys. Rev. D 39 (1989) 92

[duj01] D. Dujmic,
Open Charm Production at HERA-B,
Ph.D. Thesis, University of Texas at Austin, 2001

[ehr00] K. Ehret,
Commissioning of the HERA-B internal target: using the HERA proton ring as a B-factory,
Nucl. Instr. Methods **A 446** (2000) 190-198

[eig00] V. Eiges,
High-p_{T} trigger for HERA-B experiment,
Nucl. Instr. Methods **A 453** (2000) 412-416

[fla01a] J. Flammer,
EcalSIM - The Ecal Pretrigger Simulation,
HERA-B Note 01-054, Software Note 01-008

[fla01b] J. Flammer,
Track Parameter Unit - Documentation,
HERA-B Note 01-055, Trigger Note 01-008

[fla01c] J. Flammer,
Entwicklung der Simulation des ECAL Pretrigger Systems für das Experiment HERA-B und Analyse der Effizienzen des Zerfalls $J/\psi \to e^+e^-$,
Ph.D. Thesis, Universität Hamburg, 2001

[fle01] H. Fleckenstein, D. Ressing,
Track Finding Unit Calcuations,
FLT internal note

[fle02] H. Fleckenstein,
Performance of the TFU network of the First Level Trigger of HERA-B and determination of efficiencies for $J/\psi \to \mu^+\mu^-$,
Ph. D. Thesis, Universität Hamburg, 2002

[frü87] R. Frühwirth,
Application of Kalman Filtering to Track and Vertex Fitting,
Nucl. Instr. Methods **A 262** (1987) 444-450

[ful99] Th. Fuljahn,
Aufbau und Charakterisierung des schnellen Kontrollsystems fuer das Experiment HERA-B,
Ph. D. Thesis, Universität Hamburg, 1999

[gea94] *GEANT Detector Description and Simulation Tool*,
Application Software Group, Computing and Networks Division, CERN Geneva, Switzerland, March 1994

[ger98] E. K. E. Gerndt et al.,
Description of Messages and Process-Logic for the First Level Trigger of HERA-B,
FLT internal note, 1998

[ger00] E. K. E. Gerndt,
HERA-B Pretrigger and FLT Latency,
HERA-*B* internal note 00-013, HERA-*B* trigger note 00-001

[gla61] S. Glashow,
Partial-Symmetries Of Weak Interactions,
Nucl. Phys. **22** (1961) 579-588

[glae02] J. Glaess,
HERA-B FLT Message Transfer Module LVDS,
FLT internal note, 2002

[gol58] M. Goldhaber, L. Grodzins, A. W. Sunyar,
Helicity of Neutrinos,
Phys. Rev. **109** (1958) 1015

[gra01] W. Gradl,
The Readout of the HERA-B Inner Tracker and Prospects of HERA-B in the Field of Drell-Yan Physics,
Ph.D. Thesis, Ruprecht-Karls-Universität Heidelberg, 2001

[gro00] D. E. Groom et al. [Particle Data Group],
Review of Particle Physics,
Eur. Phys. J. C15 (2000), 1-878

[her01] J. M. Hernández,
PC Farms for Triggering and Online Reconstruction at HERA-B,
Proc. of CHEP 2001: Computing On High-Energy Physics And Nuclear, Beijing, 2001

[hb95] The HERA-*B* Collaboration,
HERA-B Design Report,
DESY-PRC 95/01

[hb00] The HERA-*B* Collaboration,
HERA-B physics in 2001/2002,
Letter to the DESY Directorate, 2000

[hq98] P. F. Harrison and H. R. Quinn (editors),
The BABAR Physics Book,
SLAC-R-504 (1998)

[hul02] W. D. Hulsbergen,
A Study of Track Reconstruction and Massive Dielectron Production in HERA-B,
Ph.D. Thesis, Universiteit van Amsterdam, 2002

[jan95] D. M. Jansen,
Measurement of the Bottom-Quark Production Cross Section in 800 GeV/c *Proton-Gold Collisions*, Phys. Rev. Lett. **74** (1995) 3118

[kal60] R. E. Kalman,
A New Approach to Linear Filtering and Prediction Problems,
Transactions of the ASME-Journal of Basic Engineering, 82 (Series D) (1960) 35-45

[knö01] K. T. Knöpfle et al.,
Performance of the HERA-B Vertex Detector System,
submitted for publication to Nucl. Instr. Methods, 2001

[kol99] H. Kolanoski et al.,
Large-System Experience with the ASD-8 Chip in the HERA-B Experiment,
Proceedings of the 5th Workshop on Electronics for the LHC, Snowmass 1999

[kra01] C. Krauss et al.,
Inner Tracker Performance in 2000,
HERA-*B* internal note 01-060, HERA-*B* ITR note 01-001

[kri00] P. Križan et al.,
The HERA-B RICH,
Nucl. Instr. Methods **A 453** (2000) 289-295

[krü02] D. Krücker,
private communication, 2002

[loh94] T. Lohse et al. (The HERA-*B* Collaboration),
HERA-B. An Experiment to Study CP Violation in the B System Using an Internal Target at the HERA Proton Ring. Proposal.,
DESY-PRC 94/02 (1994)

[lue57] G. Lueders,
Proof of the TCP theorem,
Annals Phys. 2 (1957), 1-15

[mic02] A. Michetti, D. Ressing, I. Riu,
Hera-B First Level Trigger Test Vector Test,
HERA-*B* internal note 02-027, HERA-*B* trigger note 02-001

[neg00] I. Négri,
Mapping of the OTR and the Muon detectors for the First Level Trigger,
FLT internal note, 2000

[nir99] Y. Nir 1999,
CP Violation In and Beyond the Standard Model,
SLAC Summer Institute, July 7-16, 1999, Prelecture Notes

[noe16] E. Noether,
Der Endlichkeitssatz der Invarianten endlicher Gruppen,
Mathe. Ann. **77** (1916) 89-92

[noe99] M. Nörenberg,
Objektorientierte Simulation der Trigger Decision Unit des HERA-B First Level Triggers,
Diploma Thesis, Universität Hamburg, 1999

[per98] R. Pernack 1998,
Untersuchung von Gasmischungen mit Blick auf die im Spurkammersystem des HERA-B-Detektors erreichbare Effizienz und Auflösung,
Diploma Thesis, Universität Rostock, 1998

[per01] R. Pernack 2001,
Private communication.

[pyr98] J. Pyrlik,
Schematic drawing of the HERA-B detector,
`http://www-hera-b.desy.de/subgroup/pictures/detector_schematic.eps`

[rat96] F. Ratnikov,
First Level Trigger Track Kinematics Reconstruction,
talk given in the HERA-*B* week of October 1996, HERA-*B* internal note 96-200, HERA-*B* trigger note 96-015

[ress97] D. Ressing and R. Wurth,
Implementation of the SLB using SHARCs,
HERA-*B* internal document, 1997

[sav98] V. Saveliev,
The HERA-B Transition Radiation Detector,
Nucl. Instr. Methods **A 408** (1998) 289-295

[scha98] S. Schaller,
Untersuchung der Beiträge einzelner Protonenbündel zur Wechselwirkungsrate des HERA-B Experimentes,
Diploma Thesis, Ruprecht-Karls-Universität Heidelberg, 1998

[schwa99] A. J. Schwartz et al.,
Development of a straw tube chamber with pickup-pad readout,
Nucl. Instr. Methods **A 427** (1999) 465-486

[schwa00] U. Schwanke,
Trigger and Reconstruction Farms in the HERA-B Experiment and Algorithms for a Third Level Trigger,
Ph.D. Thesis, Humboldt-Universität Berlin, July 2000

[schwi02] B. Schwingenheuer 2002,
private communication

[slt02] The HERA-*B* Second Level Trigger Group,
The Second Level Trigger Algorithm,
to be published in Nucl. Instr. Methods

[söz01] L. Sözüer,
private communication

[ste00] Ch. Stegmann,
The Outer Tracker for HERA-B,
Nucl. Instr. Methods **A 453** (2000) 153-158

[str98] U. Straumann et al.,
Operation of a large GEM-MSGC detector in a high intensity hadronic test beam using fully pipelined readout electronics,
LHCb internal note TRAC-98/060, HERA-*B* internal note 98-149, HERA-*B* inner tracker note 98-020

[sym99] M. Symalla,
Vorbereitende Untersuchungen zur Bestimmung der Wechselwirkungsraten und deren Zeitstruktur an einem Drahttarget mit Hilfe der Energieinformation des HERA-B elektromagnetischen Kalorimeters,
Diploma Thesis, Universität Dortmund, 1999

[tit00] M. Titov,
The Muon System in the HERA-B experiment,
Nucl. Instr. Methods **A 446** (2000) 355-365

[wag00] G. Wagner,
Aufbau und Test der mit Digitalen-Signal-Prozessoren realisierten Komponenten des Datennahmesystems von HERA-B,
Ph.D. Thesis, Universität Hamburg, 2000

[wei67] S. Weinberg,
A Model Of Leptons,
Phys. Rev. Lett. **19** (1967) 1264-1266

[wu57] C. S. Wu et al.,
Experimental Test of Parity Conservation in Beta Decay,
Phys. Rev. 105 (1957), 1413-1414

[zeu93] The ZEUS Collaboration,
The ZEUS Detector,
Status Report 1993, DESY-PRC 93/05

[zeu00] T. Zeuner,
The MSCG-GEM Inner Tracker for HERA-B,
Nucl. Instr. Methods **A 446** (2000) 324-330

[zim99] R. Zimmermann,
Zeitmeßelektronik für den HERA-B-Detektor,
Ph.D. Thesis, Universität Rostock, 1999

[zoc00] A. Zoccoli,
The electromagnetic calorimeter of the HERA-B experiment,
Nucl. Instr. Methods **A 446** (2000) 246-252

[zoc01] A. Zoccoli,
HERA-B Physics Program in 2001/2002,
plenary talk given at the HERA-*B* collaboration meeting, 2001, HERA-*B* internal note 01-045

Index

Erklärung

Ich versichere hiermit, die vorliegende Arbeit selbstständig verfaßt und nur die angegebenen Quellen und Hilfsmittel verwendet zu haben.

Hamburg im Dezember 2002

(Michael Nörenberg)